University of Sussex

Data-driven mathematical modelling and simulation of Rho-Myosin dynamics

Victor Ogesa Juma

Supervisors:

Prof. Anotida Madzvamuse Prof. Stephanie Portet

A thesis submitted in partial fulfilment of the degree of Doctor of Philosophy in Mathematics

University of Sussex

22nd May 2019

Declaration

I hereby declare that this thesis has not been and will not be submitted in whole or in part to another University for the award of any other degree.

Signature:

Victor Ogesa Juma

UNIVERSITY OF SUSSEX

Victor Ogesa Juma, Doctor of Philosophy

Data-driven mathematical modelling and simulation of Rho-Myosin dynamics

Summary

In this thesis, a full repertoire of model formulation, model analysis, numerical analysis, sensitivity analysis and Bayesian method for parameter identification are presented, that seek to describe faithfully the temporal dynamics of GEF–Rho–Myosin signalling pathway as observed experimentally. The thesis is based on rigorous mathematical and numerical analysis to provide robust models and numerical results that exhibit the temporal dynamics as observed in experiments. We also explore the effect of spatial inhomogeneity on two of the models formulated. The modelling is based on experimental observations, and therefore three different mathematical models are formulated from first principles depending on the constitutive laws for the interaction between chemical species, entailing that new mathematical models are obtained. Detailed mathematical analysis of the stability of uniform steady states using nullcline theory, linear stability theory and sign pattern analysis is carried out, to characterise mathematically the key temporal dynamics of stability, oscillations, excitability and bistability as observed in experiments. Numerical bifurcation analysis using *Matcont* and numerical simulations carried using MATLAB illustrate theoretical analytical results through parameter variations for the key temporal dynamics. Rigorous sensitivity analysis provides a powerful tool for investigating the effects of parameter variations through local and global sensitivity.

In particular, we use local sensitivity theory to characterise the limit cycle behaviour of an oscillatory dynamical system in terms of parameter variations and therefore, the thesis provides premises to characterise or study amplitude and period sensitivity to parameter variations. A full Bayesian approach is applied to the model for the identification of parameters that best-fits the model to experimental results. Therefore, the thesis provides a new framework for incorporating prior knowledge about parameters, which results in obtaining full probability distribution for parameters. Finally, the thesis explores and studies the spatially extended version on the ODE models. We analyse the existence of Turing instability for some parameter values. This proof-of-concept set premises to extend the temporal models to include spatial variations in the form of coupled bulk-surface reaction-diffusion systems through compartmentalisation of the spatial domain.

Acknowledgements

First and foremost, I wish to thank my supervisors Prof. Anotida Madzvamuse and Prof. Stephanie Portet for their guidance and continued support towards the quality of my research. I also wish to thank Prof. Perihan Nalbant and Dr. Leif Dehmelt, and their respective lab members at the University of Duisburg-Essen and Max Planck Institute of Molecular Physiology in Dortmund. They provided the necessary support towards the biological understanding of my research problem. I am indebted to the European Union for funding my research. This project received funding from the European Union's Horizon 2020 research and innovation programme under the Marie Skłodowska-Curie grant agreement No 642866. I also wish to thank all the InCeM (Research Training Network on Integrated Component Cycling in Epithelial Cell Motility) members for their support, particularly the project manager, Christine Kempchen and the coordinator, Prof. Rudolf Leube. I also wish to thank each and everyone of my family members for their continued support, love and unending sacrifice towards me. The list is endless, I just mention Faustine Juma, Caroline Mugeni, Sofia Achieng, Annet Obondo, Brantone, Cheryl, Ivan, Rayan, Millicent, Edwin, Osman and Mourine. I offer my gratitude to the staff of the Department of Mathematics, University of Sussex for facilitating a resourceful environment necessary for research. Finally I would like to thank all my great friends at the department of mathematics for their continued support. Many thanks to Kipchumba, Cusseddu, Farzad, Matteo, Eduard, Fanzon and many others. To God be the glory.

Contents

List of Tables

List of Figures

Chapter 1

Introduction

1.1 Biological motivation

Cell migration plays a very crucial role in the development and maintenance of multicellular organisms. Many processes in the body require the migration of cells, i.e. wound healing, germ cell migration during embryonic development and angiogenesis. The migrating cell is highly polarised with complex regulatory pathways that spatially and temporally integrate its components (Drubin and Nelson, 1996; Ridley et al., 2003; Guilluy et al., 2011). In the polarisation process, the cellular symmetry is broken, causing the cell to have a well defined front and back. This process might be spontaneous or caused by external stimuli (Andrew and Insall, 2007; Graessl et al., 2017; Cusseddu et al., 2018). Failure of cells to migrate may lead to many effects like ineffective wound repair. Cell migration also drives disease progression in cancer, mental retardation, atherosclerosis, metastasis of tumours and arthritis (Ridley et al., 2003). Therefore, understanding and controlling cell migration will have major clinical impacts.

Cell migration is a cyclic multi-step process. This process consists of: Actin polymerization dependent pseudopod protrusion at the leading edge of the cell; integrin-mediated adhesion to extracellular matrix (ECM); contact-dependent ECM cleavage by cell surface proteases; actomyosin-mediated contraction of the cell body which increases longitudinal tension; and rear retraction and translocation of the cell body (Ridley et al., 2003; Friedl and Alexander, 2011; Wolf et al., 2013). Cells migrate in

several different ways depending on their environment. The environment includes ECM composition, interactions with other cells, and the chemical stimuli (Ridley, 2015). Migration occurs either as single cells or groups of cells (Friedl et al., 2012). For all types of cell migration, Rho GTPases play a key role, but the relative contribution of each Rho GTPase depends on the environment, cell type and nature of migration (Ridley, 2015). Rho GTPases were first identified to have key roles in cell migration around 1995 (Ridley et al., 1995). In this thesis we study the activity dynamics of Ras homolog gene family member A, also called *RhoA* (hence *Rho*) linked to cellular contractility. Rho GTPases have been identified to play a key role in cell migration, particularly Rho plays a key role in cellular contractility. In the next section, we discuss the contributions of Rho GTPases to cell migration.

1.1.1 The role of Rho GTPases

The Rho family of small GTPases are key regulators of several cellular processes. These processes include cytoskeleton organisation, cell adhesion, migration, polarity and division (Etienne-Manneville and Hall, 2002; Jaffe and Hall, 2005; Heasman and Ridley, 2008; Yi et al., 2016). There are 20 Rho GTPase genes in humans, but the best studied Rho GTPases are Rho, Rac and Cdc42, which are the most highly conserved Rho family members across eukaryotic species, being found in plants, fungi and animals (Boureux et al., 2006). During cell migration, Rac and Cdc42 mostly concentrate their activities at the cell front and control the protrusive actin network. Rho, on the other hand, is mostly active at the rear and regulates focal adhesion dynamics, stress fibre assembly and cellular contractility (Ohashi et al., 2017; Wu et al., 2012; Mayor and Carmona-Fontaine, 2010). See Figure 1.1 (Wu et al., 2012), for roles of GTPases in cell migration. The figure shows a migrating cell and contributions of Rho, Cdc42 and Rho to the migration.

RhoA is a small GTPase protein of Rho family, that exists in guanosine diphosphate (GDP)-bound (inactive) and the guanosine triphosphate (GTP)-bound (active) conformal states. The Rho family members act as molecular switches, cycling between active and inactive conformal states. The cycling is mediated by guanine nucleotide exchange factors (GEFs) and GTPase-activating proteins (GAPs) (Raftopoulou and Hall, 2004). GEFs activate Rho while GAPs inactivate them. Both active and inact-

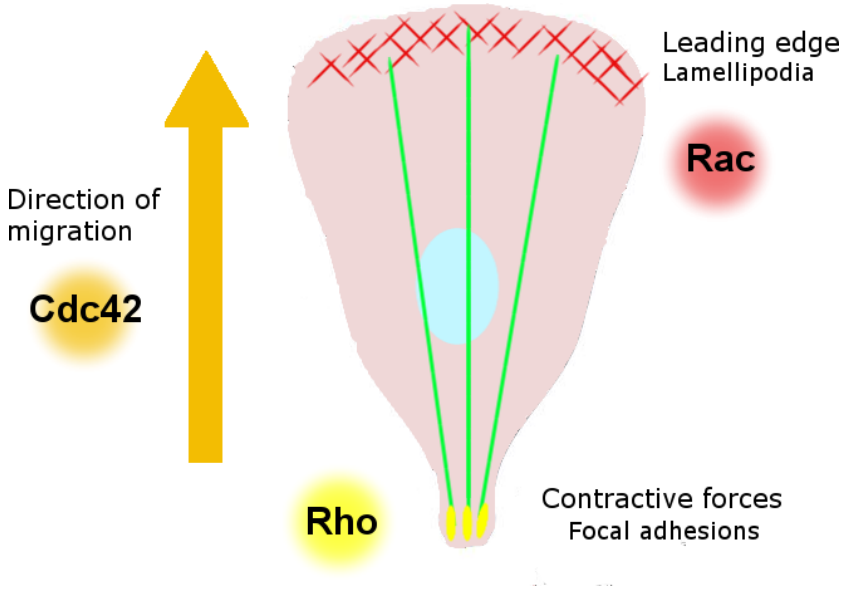

Figure 1.1: Roles of Rho GTPases; Rho, Rac and Cdc42 in cell migration.

ive conformal states of Rho GTPases reside on the cell membrane, but sometimes the inactive molecule is found in the cell cytosol attached to guanosine nucleotide dissociation inhibitor (GDI). They prevent Rho GTPases' association with cell membrane (DerMardirossian and Bokoch, 2005; Garcia-Mata et al., 2011; Hodge and Ridley, 2016).

Figure 1.2 shows cycling of GTPases between the active and inactive conformal states. While GAPs inactivates RhoA by enhancing the intrinsic GTP-hydrolysis activity. Some RhoA family members are GTPase deficient and hence bind GTP constitutively, but little is known about their regulation. The figure also shows the positive feedback loop between GEF and GTPases, which shows that Rho GTPases increase their activities by activating their activators. The inactive GTPases are also attached to the GDI which prevents them from attaching to the cell membrane.

We discuss some of the roles of Rho GTPases in relation to cell migration:

Lamellipodia-driven cell migration. The plasma membrane extension in lamellipodia is predominantly driven by Rac induced actin polymerisation, and therefore local Rac activation is sufficient for cell to migrate in *vivo* (Montell et al., 2012; Faroudi et al., 2010). For effective cell migration, the protrusions have to be limited to one part of the cell membrane (Ridley, 2015).

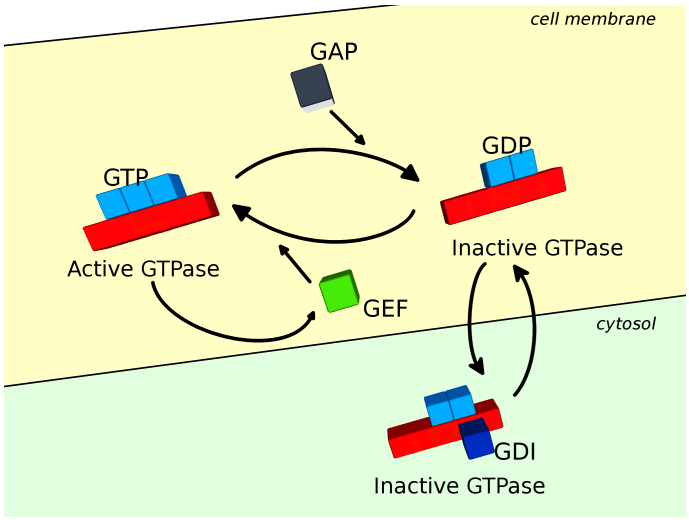

Figure 1.2: Rho GTPase dynamics. Rho GTPases cycle between active and inactive states. Both active and inactive conformal states reside on the cell membrane, but sometimes the inactive molecule is found in the cell cytosol attached to GDI.

RhoA and Cdc42 contribute to lamellipodia extension (Machacek et al., 2009; Heasman et al., 2010). RhoA is activated at the front of lamellipodium (Heasman et al., 2010), it is thought that it activates formins which nucleates actin filaments at the leading edge of the lamellipodium but this is yet to be proved (Ridley, 2015). Cdc42 contributes to establishing cell migratory polarity and migratory persistence. It can localise Rac activity through multiple potentially synergistic pathways (Etienne-Manneville, 2004). Feedback loops involving Rho/Rho-associated protein kinase (ROCK) and actomyosin contractility are believed to turn off lamellipodia in other regions of the cell, and therefore reducing RhoA or ROCK activity can lead to multiple or larger lamellipodia formation (Vega et al., 2011).

Filopodia and cell migration. Cdc42 is the best characterised Rho GTPase involved in filopodium formation, they act predominantly through formins (Kühn and Geyer, 2014). Several other Rho GTPases can induce filopodia formation under different conditions and contexts, examples are shown in (Bornschlögl, 2013; Fan and Mellor, 2012; Gad et al., 2012).

Filopodia are implicated in directed cell migration and neuronal guidance (Moshfegh et al., 2014). They can also mediate initial cell–cell contact when epithelial cells move towards each other (Khurana and George, 2011), and are

observed in the leading cells during angiogenesis (Wakayama et al., 2015). Recent studies have shown that filopodia are important for both lamellipodium-driven and bleb-driven migration in vivo, see examples discussed (Mayor and Theveneau, 2013; Boer et al., 2015).

Blebbing and cell migration. Bleb-based migration is driven by cortical actomyosin contractility, and is associated with RhoA/ROCK signalling (Charras and Paluch, 2008). Bleb-based migration is rarely observed in 2D culture conditions, but is frequently observed in vivo and in confined environments or on low-adhesion 3D systems in vitro (Ridley, 2015). In vivo, cells can transform quickly between bleb-based migration and filopodium-based migration. This reflects their adaptation to variation in the ECM structure, for example as shown in Row et al. (2011).

Collective cell migration. Many cells migrate collectively during development. They include epithelial cells, endothelial cells and neural crest cells (Etienne-Manneville, 2014). This is driven by lamellipodia and filopodia in the leading cell and their suppression on all the rest of the follower cells (Cai et al., 2014).

Besides Rho GTPases, the other contributors to cellular migration are Myosins, composed of Myosin-IIA and MYO9B. Therefore, in the next section we discuss the role of Myosin to cellular migration, particularly in relation to cellular contractility.

1.1.2 The role of Myosin in cell migration

Myosins are a large family of structurally diverse molecular motors (Togo and Steinhardt, 2004). In this thesis, our focus is on Myosin-IIA and Myosin-9b (MYO9B). These two myosins inhibit Rho activities. Myosin-IIA inhibit GEF-H1 activities (Nalbant et al., 2009), thereby inhibiting RhoA, while MYO9B is a GAP for RhoA (see Figure 1.2) (Hanley et al., 2010; Kong et al., 2015; Yi et al., 2016).

The role of Myosin-IIA in cell migration

Non muscle Myosin-II is composed of three distinct isoforms, referred to as *Myosin-IIA, Myosin-IIB and Myosin-IIC* (Simons et al., 1991; Togo and Steinhardt, 2004; Even-Ram et al., 2007). They have distinct roles in cell contractility, cytokinesis

and locomotion. However, the specific contribution of each of the isoforms is not yet classified. Myosin-II contains pairs of myosin heavy chains (MHCs), regulatory myosin light chains (MLCs), and essential MLCs that assemble into bipolar filaments with actin-stimulated ATPase activity (Lee et al., 2010). Myosin-IIA is associated with Rho kinase-dependent functions (Sandquist et al., 2006). Myosin-II has been shown to bind and inhibit the Dbi family GEFs (these are GEFs characterised by the presence of a Dbi homology (DH) catalytic domain, followed by an adjacent pleckstrin homology (PH) domain) (Lee et al., 2010). The study in there shows that binding to GEFs required the assembly of Myosin-II into filaments and actin-stimulated ATPase activity. Binding to Myosin-II suppressed GEF activity and accordingly inhibition of Myosin-II ATPase activity caused the release of GEFs and hence activating RhoA.

Rho GTPases regulate Myosin-II through multiple pathways (Somlyo and Somlyo, 2000), for example ROCK activates Myosin-II and increase contractility whereas Rac1 and its effector PAK negatively regulate Myosin-II and decrease contractility (Lee et al., 2010). We have described Myosin-II in general, however in this thesis we only consider Myosin-IIA which is used in experiments (Graessl et al., 2017).

The role of Myosin-9b in cell migration

Mammalian class IX myosins consist of MYO9A and MYO9B, they are single-headed molecular motors which contain a Rho-specific GAP domain in the tail region. MYO9B is predominantly expressed in the immune system (Wirth et al., 1996). Therefore, it contributes to the regulation of rapid cell shape changes and motility, this is paramount for host defence. MYO9B has been shown to turn off RhoA in vitro and therefore this Rho GAP, MYO9B is required for spatially co-ordinated membrane protrusions and retractions, the elementary events underlying shape changes and directional motility (Hanley et al., 2010).

We have seen that Rho GTPases are activated by GEFs, in particular GEF-H1 is a candidate molecule for cellular contractility, it activates RhoA (Rho) as well as being inhibited Myosin-IIA. In the next subsection, we therefore discuss on the contribution of GEF-H1 to cellular contractility.

1.1.3 Guanine nucleotide exchange factor-H1 (GEF-H1)

There are several GEFs in the human genome. They are encoded into two distinct gene families, called the Dbi and the DOCK families (Rossman et al., 2005; Meller et al., 2005). The Dbi family is characterised by the presence of a Dbi homology (DH) catalytic domain, followed by an adjacent pleckstrin homology (PH) domain (Rossman et al., 2005).

GEF-H1 belongs to the Dbi family of GEFs. They activate RhoA by phosphorylation and they promote the exchange of GTP for GDP. The studies in Rossman et al. (2005); Nalbant et al. (2009) found that RhoA is activated at the leading edge of motile cells by an unknown mechanism to control stress fibres assembly, contractility and focal adhesion dynamics. RhoA is activated by the microtubule-associated guanine nucleotide exchange factor GEF-H1 when they are released from microtubules to initiate RhoA/Rho kinase/Myosin light chain signalling pathway. This pathway controls cellular contractility. GEF-H1 has also been shown to be a component in tight junctions, and hence its importance in the integrity of cell to cell adhesions (Benais-Pont et al., 2003; Nalbant et al., 2009).

GEF-H1 activates RhoA when they are in active form, in their inactive form, GEF-H1 are bound to microtubules, and the microtubule disassembly results in their activation hence leading to the activation of RhoA. Catalytic activity of GEF-H1 is negatively regulated when bound to microtubules (Ren et al., 1998; Krendel et al., 2002) and therefore microtubule depolymerisation mediates cellular contractility. Regulation of GEF-H1 is a complex process involving a multitude of phosphorylation on the activating and inactivating sites, several kinases have been shown to inhibit GEF-H1 by phophorylating its inhibitory sites. GEF-H1 is inhibited by Myosin-IIA and in turn activated by RhoA. From Lee et al. (2010), it is revealed that Myosin regulates multiple Dbi family members through direct binding, which controls their activity and localisation in migrating cells.

1.2 Experimental observations and results

In this section, we describe the experimental observations carried out in the laboratories of our collaborators from the University of Duisburg-Essen (UDE) and Max Planck Institute of Molecular Physiology (MPI). These results are presented in Graessl et al. (2017) and Kamps et al. (2019). Their experimental set up focuses on the role of Rho in regulating contraction in adherent cells by simultaneous imaging of endogenous Rho activity and Myosin-II dynamics.

First to investigate the casual link between Rho and GEF-H1, a light pulse was used to uncage a chemical dimerizer which is covalently linked to a plasma membrane anchor. This technique is used to induce targeting of Escherichia coli dihydrofolate reductase (eDHFR) fusion proteins of Rho to plasma membrane and then use Total Internal Reflection Fluorescence (TIRF) microscopy to measure how plasma membrane targeting of these eDHFR fusion proteins affect Rho activity. In this analysis, it was observed that GEF-H1 was co-recruited together with Rho constructs and the Rho activity sensor, which demonstrates the existence of a clear casual link between Rho activity and GEF-H1 membrane localisation. This means that local increase in Rho activity leads to increased plasma membrane recruitment of GEF-H1.

To investigate the mechanism of Rho self-inhibition, actin and Myosin were hypothesised to be potential candidates which act as platforms to recruit inhibitors due to their significant delays. Indeed there exists a strong spatio-temporal cross-correlation between Rho activity and localisation of inactive mutants of the actin-associated Rho-specific GAP, Myo9b. Using those mutants, they observed significant delays in the plasma membrane association of the GAPs after Rho activity peaks, suggesting that they act downstream of Rho activity. Based on these experimental observations and the known interaction activity with Myosin-IIA (Nalbant et al., 2009; Lee et al., 2010), it was hypothesised that GEF, Rho and Myosin self reorganise to form an activator-inhibitor network as shown in Figure 1.3. The figure shows basic interactions of GEF, Rho and Myosin. In this set up, Rho recruits both its activator (GEF), and its inhibitor (Myosin). For the model formulation in Chapter 2, we consider both active and inactive molecules of GEF-H1, RhoA and Myosin.

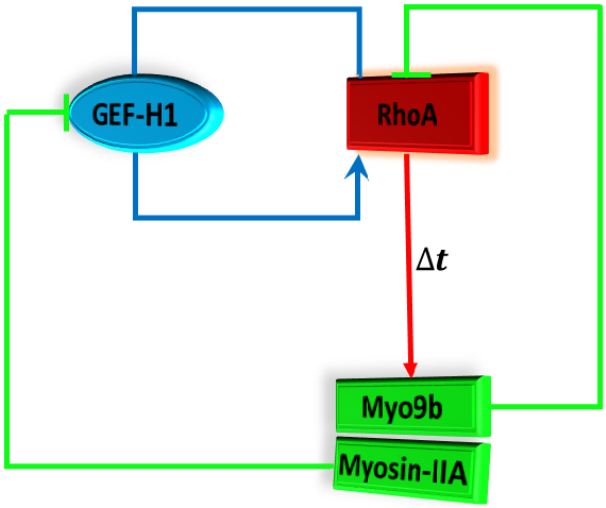

Figure 1.3: An activator-inhibitor network for RhoA-Myosin signaling pathway. Red represents activation of Myosin by RhoA, green represents inhibition of RhoA activity by myosin and blue represents RhoA positive feedback loop through GEF-H1.

1.3 Review of mathematical models of activator-inhibitor type

This section focusses on the review of mathematical models composed of positive and slow negative feedback mechanism which are characterised by the excitable dynamics. It was shown that an excitable medium is composed of a component that regulates its activities by recruiting both its activator and inhibitor. Such systems when coupled spatially via diffusion can generate propagating wave fronts of excited signal activity (Iglesias and Devreotes, 2012). Activator provides positive feedback loop while the inhibitor provides negative feedback loop. We will review some models that exhibit these dynamics.

Local contractile forces are generated by the cells to probe and react to changes in mechanical properties of their environments, it has been revealed that those contractile forces are regulated by Rho/Myosin-based signal networks (Graessl et al., 2017). These networks can generate excitable system dynamics via a combination of positive and negative feedback mechanism. In Graessl et al. (2017), it was found that a combination of Rho self-amplification through GEF-H1 and Myosin inhibition leads to pulsatile and cell contraction dynamics. This is the characteristic of an excitable medium which is composed of a component that regulates its activities by

recruiting both its activator and an inhibitor (Murray, 2002; Iglesias and Devreotes, 2012).

In multicellular organisms, cell migration involves coordinated cell protrusions and contraction (Burnette et al., 2011). There have been several studies which show that an excitable signaling network controls cellular protrusion (Xiong et al., 2010; Yang et al., 2015; van Haastert et al., 2017; Miao et al., 2017; Barnhart et al., 2017). However, the role of excitability in controlling cellular contractions is still not clear (Graessl et al., 2017). It has been suggested that Rho is the key candidate in spatio-temporal regulation of the signaling pathway that drives cellular contractility (Graessl et al., 2017). The study here-in suggests an existence of an activator-inhibitor network that is coupled to matrix elasticity to control cell contraction dynamics; in this network Rho amplifies its activity via a positive feedback loop through the GEF-H1, this module is coupled to a negative feedback loop composed of MYO9B or Myosin-IIA (collectively called Myosin) associated Rho inhibition as shown in Figure 1.3. The experimental results of this signalling network show spontaneous emergence of pulses and propagating waves of RhoA(Rho) activity (Graessl et al., 2017; Kamps et al., 2019). Furthermore it has been shown that the dynamics of this network are regulated by the associated regulators (GEF-H1). It was also shown that reactions involving GEF-H1 occur more rapidly than Myosin activation which occurs with delay of between 3–40 seconds. Therefore these Myosin activities provide a slow negative feedback. The analysis of GEF–Rho–Myosin signalling network and experimental results showed that the GEF activity and also interaction between GEF-H1 and GTP RhoA are key for generating Rho activity dynamics (Graessl et al., 2017), this confirms that the GEF-H1 parameters are responsible for having Rho observed dynamics.

Since many years ago, ordinary differential equations (ODEs) have been used in physical and life sciences to describe the temporal dynamics of a dynamical system (Murray, 2002, 2003; Edelstein-Keshet, 1988). There have been several research that used ODEs to model regulatory networks, An example can be found in Tyson et al. (2001, 2003). Differential equations provide a convenient way of expressing the meaning of molecular wiring diagram in a computer readable form (Bray, 1995; Csikász-Nagy et al., 2006). This method has been used in many areas to create

mathematical models of cell eukaryotic cycle (Novak and Tyson, 1993, 1995; Gonze and Goldbeter, 2001). An example can be found in Tyson et al. (2003) about the activator-inhibitor model network that was used to describe a response element R that auto-catalytically amplifies itself by phosphorylating an enzyme, E and it also inhibits itself by activating its inhibitor, X. This model shows an activator-inhibitor system equivalent to GEF–Rho–Myosin signalling pathway.

An activator-inhibitor system may exhibit wave generation when coupled spatially (Ryan et al., 2012; Inagaki and Katsuno, 2017). The activator-inhibitor system when coupled spatially belongs to the class of reaction-diffusion models (Murray, 2002, 2003). These models may generate spatial patterns under certain conditions, in which a steady state which is locally stable in the absence of diffusion becomes unstable when diffusion is added. This phenomenon is called diffusion-driven instability or Turing instability (Turing, 1952; Murray, 2003). Models that explain wave generation (spatial and temporal) involve an activator-inhibitor mechanism. This concept is driven by a combination of auto-catalytic positive and slow negative feedback mechanism. However, the details of molecular network controlling such networks are unclear (Ryan et al., 2012; Allard and Mogilner, 2013; Graziano and Weiner, 2014; Inagaki and Katsuno, 2017). Wave generation results when a system having local excitable dynamics is coupled spatially. Excitability results from a steady state in which small perturbations decay but perturbations which are larger than a threshold result in a larger excursion but later return to the steady state indirectly (Allard and Mogilner, 2013). In excitability, increasing the replenishment of an inhibitor further increases the steady state of an activator above the threshold and this causes the system to be in oscillatory region. Further increasing perturbation beyond the threshold converges the system to another steady state. This implies the system is in a bistable region and the steady state to which it goes to depends on the perturbation. This is illustrated in Figure 1.4.

FitzHugh-Nagumo model is a classic model of excitable dynamics that derives from self-amplifying positive feedback loop coupled to a delayed negative feedback loop, in which an activator and inhibitor diffuse over the leading edge of the cell membrane (FitzHugh, 1961, 1969).

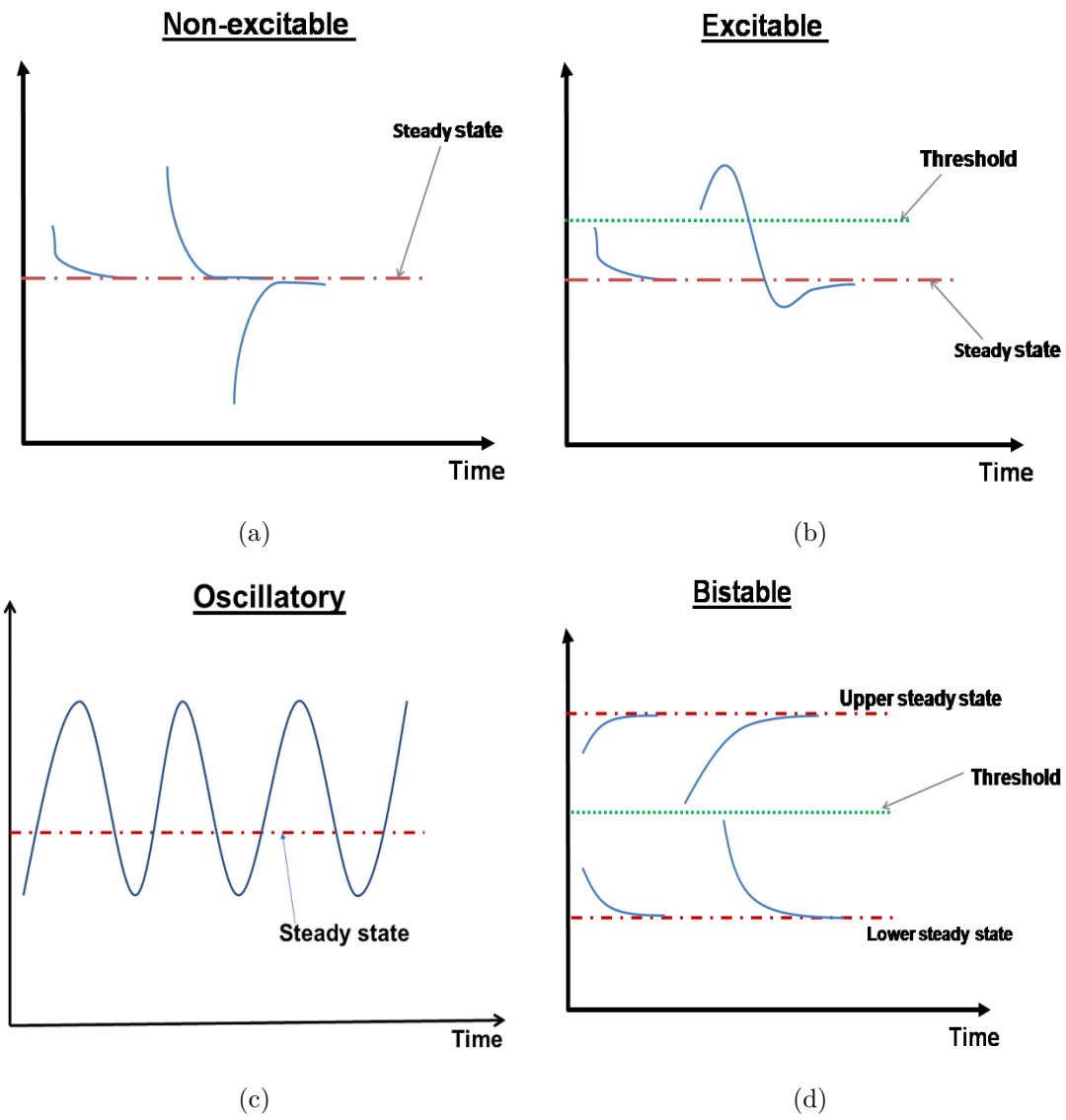

Figure 1.4: Schematic representation of an activator-inhibitor dynamics. The type of behaviour achieved depends on parameters and also the threshold. The blue curves represent the behaviour of the solutions for different scenarios.

The activity dynamics of cell migration is controlled by complex signalling networks of interacting species. This network that control migration displays a number of behaviours such as oscillations and cortical wave propagation (excitability) (Devreotes and Horwitz, 2015). Previous studies suggested that the cross-talk between Rho GTPases can control their activity dynamics (Machacek et al., 2009; Guilluy et al., 2011), and several migration dynamics. For example, the mutual antagonism between Rac and Rho has been observed in many cell types (Huang et al., 2014; Byrne et al., 2016; Holmes and Edelstein-Keshet, 2016) and accounts for cell contraction and polarization (Holmes et al., 2017). In Byrne et al. (2016) it

was suggested that the bistability of Rho-Rac network translates into bistability of actin dynamics and cell migration. However, Graessl et al. (2017) has showed that the Rho activity was never preceded by neither Rac nor Cdc42 and therefore did not trigger Rho activity pulses. This shows that Rho activity dynamics (in relation to cellular contractility) are not dependent on mutual antagonism with other GTPases.

Holmes et al. (2017) focussed on Rho-Rac antagonism and its influence on the extracellular matrix. Three models were constructed based on experimental observations by Park et al. (2016). The difference between the models stem from different biological assumptions used and the type of feedback as discussed below; first the general model is divided in two subsystems one responsible for bistability and the subsystem responsible for negative feedback so as to achieve experimentally observed coexistence, bistable and oscillatory lamellipodia dynamics (Influence of ECM is modelled using lamellipodia dynamics).

Model 1: It assumes that ECM is the source of bistability, and GTPases dynamics is the source of negative feedback that drives oscillations observed in some cells. This model predicts experimental observations (when GTPases are conserved) but was rejected since oscillations are possible when GTPases operate on smaller time scales. This is not biologically plausible.

Model 2: It is adjusted so that bistability results from GTPases dynamics, and ECM signalling provides slow negative feedback. The model also assumes that GTPases are abundant. This system behaves as a toggle switch studied in (Gardner et al., 2000; Tyson et al., 2003). This model was not considered good due to the high sensitivity of the strength of Rac activation which is not consistent with biological data.

Model 3: It is a modification of Model 2 by dropping the fact that GTPases are abundant and instead assume that GTPases are conserved (Edelstein-Keshet et al., 2013; Holmes and Edelstein-Keshet, 2016). This model agrees with experimental observations with suitable range of parameters. This study suggests that conservation of GTPases dynamics plays a key role in signalling dynamics as also shown in other studies (Mori et al., 2008, 2011; Holmes and Edelstein-Keshet, 2016). It was assumed in Holmes and Edelstein-Keshet

(2016) that the total GTPase concentration is conserved since its activation and inactivation happens in order of seconds compared to the gene expression which occurs in time scales of hours.

An activator-inhibitor network can make cell plasma membrane and its cortex act as an excitable medium (Bement et al., 2015; Barnhart et al., 2017; Miao et al., 2017), this excitable behaviour can account for the spontaneous migration of cells (Iglesias and Devreotes, 2012).

Barnhart et al. (2017) considered mechanical and biochemical interactions among adhesions, actin, VASP and cell membrane. They formulated a model (activator-inhibitor reaction-diffusion type model) consisting of local positive feedback (actin branching), global negative feedback (protrusion dependent membrane tension) and local negative feedback (adhesion dependent depletion of VASP). Their model predicts the existence of travelling waves of actin dynamics. It was shown that excitable waves were dependent on local positive feedback and local negative feedback. In principle, it has been shown that combining positive feedback and slow negative feedback produces excitable dynamics (Allard and Mogilner, 2013).

Miao et al. (2017) also considered an activator-inhibitor reaction diffusion model which is coupled to a polarization model, the activator-inhibitor consist of three interacting species; the first two species are mutually inhibitory and provide a positive feedback loop and this loop initiates a slow negative feedback loop through the third species. Their model shows that altering the threshold of an excitable network changes cell migratory modes. It has also been shown in others (Huang et al., 2013; Xiong et al., 2010; Shi et al., 2013) that changing the threshold alters wave dynamics which leads to distinct pattern behaviour in a cell.

Bement et al. (2015) used an activator-inhibitor reaction-diffusion model to show that Rho signalling and F-actin assembly makes cell cortex an excitable medium. In their model Rho activates itself by activating the RhoGEF, Ect2 which forms a positive feedback loop while F-actin dependent Rho inhibition forms slow negative feedback. Their model shows propagating waves, which undergo self annihilation on collision suggesting the existence of excitable dynamics (Allard and Mogilner, 2013). In their model, Rho was suggested to be a good candidate for an activator as

Rho GTPases have been shown to indirectly activate themselves forming a positive feedback loop (Goryachev and Pokhilko, 2008).

Cusseddu et al. (2018) considered a spatial model for the Rho-GTPase cycle between active and inactive form. This model was described in three-dimensional domains. In this work a conceptual one-dimensional model first proposed by Mori et al. (2008) was extended to a bulk-surface setting, in which membrane and cytosolic activities were naturally linked to the surface and bulk of the geometric domain. The non-linearity of the reaction term generates propagation of the membrane-bound GTPase, related to the initial conditions and geometric shape, while the interplay with cytosolic component eventually halts the spreading, leading to two well defined regions respectively characterised by high and low concentration of protein.

The work in Bement et al. (2015); Barnhart et al. (2017); Miao et al. (2017) focuses on the study of excitable dynamics in relation to cellular protrusion dynamics. However, this thesis focuses on the study of activator-inhibitor signalling network in relation to cell contractility dynamics.

Similarly to the models reviewed here, this thesis focuses also on studying the GEF–Rho–Myosin network that organises itself to form activator-inhibitor network. The system of interaction described to explore GEF–Rho–Myosin dynamics is similar to the one applied to the activator-inhibitor model network that was initially described and studied in Tyson et al. (2003). Originally this model was used to describe a response element R that auto-catalytically amplifies itself by phosphorylating an enzyme, E and it also inhibits itself by activating its inhibitor, X. As observed experimentally the activator-inhibitor signal network described in Tyson et al. (2003) is equivalent to the GEF-H1–RhoA–Myosin dynamics. This model lacks GTPases conservation as discussed by Mori et al. (2008, 2011); Holmes and Edelstein-Keshet (2016); Holmes et al. (2017). We draw insight from the activator-inhibitor system in Tyson et al. (2003) for the formulation of GEF–Rho– Myosin models, but our model is derived from first principles based on experiments (Graessl et al., 2017). It is shown experimentally (Graessl et al., 2017) that the Rho activity dynamics are mediated by the expression levels of the positive feedback mediator, GEF-H1. It was also shown that if on assumption that GEF-H1 does not act as a feedback mediator

and instead consider it as the background GEF activity (constitutive activation) or other Rho GEFs, then there would be no excitability, hence it has an opposing effect when its concentration is increased. This shows that the model dynamics are determined by the feedback mediator through GEF-H1 and not through the background GEF activity (Graessl et al., 2017).

1.4 Thesis outline

The focus of this thesis is to study from first principles the temporal Rho activity dynamics linked to cellular contractility based on experimental observations. Different mathematical models were formulated from first principles to describe GEF–Rho–Myosin interaction and then validated through a rigorous Bayesian approach. Hence, the thesis is structured as follows: In Chapter 2 we formulate from first principles a set of mathematical models based on different biological assumptions and their mathematical translations. The main assumption is the use of law of mass action or enzymatic activity to translate the GEF-H1 activity and the quasi-equilibrium approximation on GEF-H1 or Rho activities. Chapter 3 explores the asymptotic behaviour of the models formulated in Chapter 2, in order to understand their long term behaviour. Therefore, motivated by the experimental observation that this network manifests distinct dynamic states depending on the expression level of the positive feedback mediator GEF-H1, the stability analysis of the equilibrium state is investigated with respect to the GEF total concentration, G_T. Also motivated by the experimental observation that the system exhibit periodic pulses, we used sign pattern analysis and nullcline theory to study the existence of periodic solutions arising from Hopf bifurcations in the ODE models formulated. These results are complemented by detailed numerical bifurcation analysis of the models with respect to G_T. In Chapter 4 we investigate the model sensitivity to parameter variations. Two approaches are described, first the local sensitivity method is described which seeks to determine the influence of parameters on the oscillatory dynamics and the global method is thereafter described to determine the influence of parameters in a global sense. Chapter 5 explores numerical simulations of the models formulated in Chapter 2. First the region within which the three models exhibit excitable dy-

namics is identified, and then the variation of response amplitude of Rho activity dynamics with respect to G_T obtained and lastly we plot the phase planes and temporal profiles of Rho and Myosin to illustrate the theoretical findings of the mathematical analysis in Chapter 2. In Chapter 6 we present a detailed comparison of results corresponding to all the three models. This is done with respect to their formulation, asymptotic behaviour, and how sensitive they are to parameter variations and the numerical simulation results. In Chapter 7 we formulate a model with perturbation from experimental observations, which is used to fit the unknown kinetics. The Bayesian approach to parameter identification is described and applied to the model to approximate the parameters which satisfy the perturbation kinetics as well the oscillatory dynamics with only varying GEF total concentration. Chapter 8 explores th effect of spatial inhomogeneity on the models formulated in Chapter 2, we present the mathematical analysis for the existence of diffusion-driven instability and illustrate the mathematical analysis with numerical simulations. Chapter 9 concludes the thesis with some possible extensions of the study contained in this thesis. The study in this thesis follows the schematic representation shown in Figure 1.5. This forms a cyclic loop. We formulate models based on experimental data, these models are analysed and then linked back to the data, through the Bayesian parameter identification.

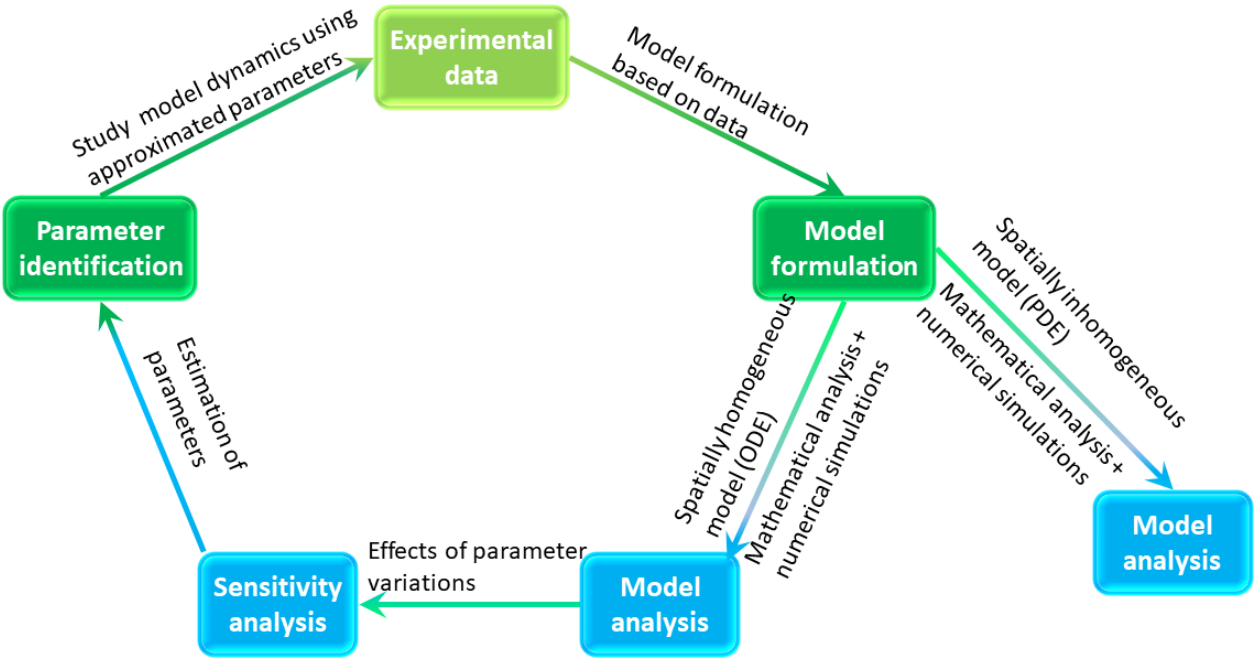

Figure 1.5: A schematic representation of the thesis structure. The focus of the thesis presents a novel approach to data-driven mathematical modelling whereby experimental observations are translated into mathematical models which in turn are rigorously analysed. Model analysis is followed by sensitivity analysis which includes local and global sensitivity analysis. Finally, to fit models back to data, parameter identification is carried out through a Bayesian approach that allows us to reject models that do not fit or describe the data very well and to select the model that best-fit experimental observations.

Chapter 2

Model formulation of Rho-Myosin temporal dynamics

2.1 Introduction

This chapter focusses on the formulation of mathematical models that represent the GEF–Rho–Myosin network to describe the temporal Rho activity dynamics linked to cellular contractility. The models formulated are broadly categorised into two, depending on how the GEF activities are interpreted mathematically. Detailed biological and mathematical assumptions used in formulating the models are described in each section. Given the experimental observations as depicted in Figure 1.3, we embark on formulating from first principles a set of three mathematical models based on different biological assumptions. These assumptions are: first, GEF activities are translated using the Michaelis-Menten kinetics based on the work in Tyson et al. (2003) and then this is modified and hence translated using the law of mass action based on experimental observations (Kamps et al., 2019). The other major assumption is the quasi-steady state approximation on either GEF activity or the Rho activity. In each case Goldbeter-Koshland (Goldbeter and Koshland, 1981) function is derived to implicitly define, respectively, GEF or Rho activities. To model reaction rates, we used the law of mass action, Michaelis-Menten kinetics and the Hill function. These laws are introduced and described in Appendix A.

2.2 Model formulation

In Appendix A, the general theory underpinning different biological assumptions and their mathematical translations has been introduced, which will be used in the following sections to develop from first principles a set of three mathematical models based on experimental observations (Graessl et al., 2017; Kamps et al., 2019). It was suggested that coupled positive and negative feedback loops form essential signal transduction motifs in cellular signalling systems (Kim et al., 2007). It is also known that positive feedback induces a switch-like behaviour and bistability (Ferrell Jr, 2002; Tyson et al., 2003), and that negative feedback suppresses noise effects (Tyson et al., 2003; Stelling et al., 2004). We derive a model of positive and negative feedback systems (Hartwell et al., 1999; Tyson et al., 2003; Kamps et al., 2019), which represents the GEF-H1–Rho–Myosin signalling pathway linked to cellular contractility (Graessl et al., 2017).

The modelling assumptions are simplified by requiring that all the underlying biochemical reactions are integrated into three main modules. We define a module as *a discrete entity whose function is separable from those of others* (Hartwell et al., 1999). These modules represent the activities of Rho module and the regulators of positive and negative feedback which act on the Rho module. The positive feedback module represents the activities of GEF-H1 (which activates Rho) while the negative feedback module represents the activities of Myosin (comprising Myosin-IIA and the actin associated GAPs such as MYO9B (Graessl et al., 2017; Kamps et al., 2019)), that acts to inhibit Rho activities.

The three modules considered are summarised in Figure 1.3 in Chapter 1 such that

1. **Rho module** represents Rho or RhoA activities
2. **Myosin module** represents either Myosin-IIA or MYO9B activities
3. **GEF module** represents GEF-H1 activities.

Recent experimental observations (Graessl et al., 2017; Kamps et al., 2019) have shown that Rho-Myosin network can be represented by an activator-inhibitor regulatory network as shown in Figure 1.3. Within this set-up, Rho up-regulates its activity through a positive feedback loop mediated by GEF-H1. Up-regulation of

Rho GTPases through a positive feedback mechanism has also been shown in (Medina et al., 2013). This formed a basis for mathematical models described in Mori et al. (2008); Rätz and Röger (2012); Cusseddu et al. (2018). The activator-inhibitor type of network has been described and studied for example in Tyson et al. (2003), where they described the interaction of three species X, Y, Z. In their framework, it is assumed that the interacting species are in plenty and therefore no conservation of mass. Our modelling framework draws inspiration from this work for the formulation of GEF-H1–Rho–Myosin models based on experimental work (Graessl et al., 2017; Kamps et al., 2019). The activation and inhibition of Rho module is based on GEF and GAP activities which are implemented via constant functions or via the GEF and Myosin modules.

In Nalbant et al. (2009), it is shown that Rho is activated by the microtubule associated guanine nucleotide exchange factor (GEF-H1), when they are released from the microtubules to initiate Rho/ROCK/Myosin light chain signalling pathway that controls cellular contractility. In turn, regulation of GEF-H1 activity is a complex process involving a multitude of phosphorylation on the activating and inactivating sites. There are several kinases which have been shown to inhibit GEF-H1 activities by phosphorylation of its inhibitory sites (Lee et al., 2010). They show that Myosin-II binds to GEF to suppress GEF activities, the binding required Myosin-II assembly into filaments and actin stimulated ATPase activity. They, in turn, showed that inhibition of Myosin-II ATPase activity caused the release of GEFs and in turn activation of Rho. We therefore postulate that GEF-H1 is inhibited by Myosin and in turn activated by Rho.

MYO9B has been shown to turn off RhoA in vitro (Hanley et al., 2010). Mammalian class IX myosins consist of MYO9A and MYO9B, they are single headed molecular motors containing a Rho specific GAP domain in the tail region. Therefore this motorised Rho GAP is a candidate signal molecule for regulating rapid cell shape changes and motility for the host defence. They are predominantly expressed in the immune system.

The basic interactions of GEF-H1, RhoA and Myosin are summarised in Figure 1.3. This takes the form of an activator-inhibitor system. The activator is RhoA,

while inhibitor is Myosin (Myosin-IIA and MYO9B), collectively called Myosin, whose activities occur with time delay, Δt of between 3-40 seconds (Graessl et al., 2017; Kamps et al., 2019). GEF-H1 provides a positive feedback loop for RhoA self amplification. In this work we do not consider a delay differential equation. The ODE models formulated accounts for the delay by using slower time scales in the Myosin activities. In Figure 2.1 an explicit reaction for each molecule is considered. The models will follow the structure in Figure 2.1, which represents the interaction of the active and inactive molecules of GEF, Rho and Myosin. Myosin inhibits Rho

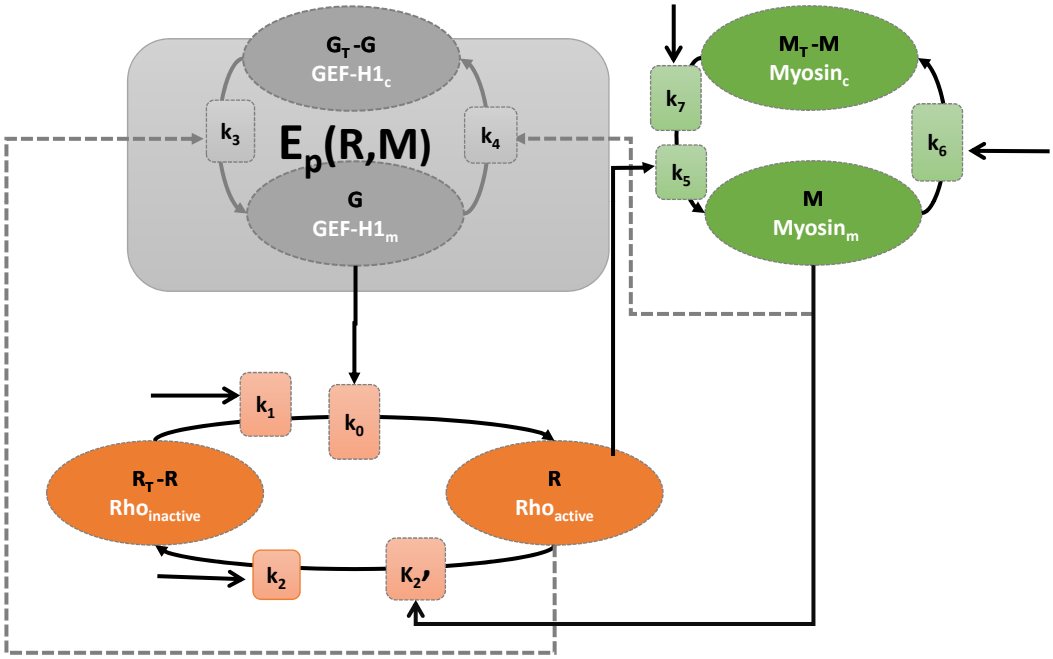

Figure 2.1: Flow diagram representing the interaction between active and inactive molecules of GEF-H1, RhoA and Myosin. $E_p(R, M)$ represents the steady state approximation of GEF-H1.

via two processes:

- Myosin-IIA inhibits Rho by inactivating GEF-H1 activities (Lee et al., 2010),
- It may inhibit Rho activities directly via MYO9B GAP (Hanley et al., 2010).

We consider the following species:

- GEF-H1 is composed of GEF-H1$_c$ in the cytosol and GEF-H1$_m$ in the cortex plasma-membrane. The active part GEF-H1$_m$ is denoted by G. The total

concentration is constant such that

$$\text{GEF-H1}_c(t) + \text{GEF-H1}_m(t) = G_T = \text{const.}$$

The state variable $G(t)$ denotes the concentration of GEF-H1$_m$ at time t in the models.

- RhoA is composed of RhoA$_a$ active (in cortex plasma-membrane) and RhoA$_i$ inactive (cytosol + cortex). The inactive RhoA$_i$ in the cortex is quickly replenished from the cytosolic pool and we therefore have both RhoA$_a$ and RhoA$_i$ in the cell cortex. The total concentration is constant such that

$$\text{RhoA}_a(t) + \text{RhoA}_i(t) = R_T = \text{const.}$$

The state variable $R(t)$: denotes the concentration of RhoA$_a$ at time t

- Myosin is composed of Myosin-IIA and MYO9B and we first consider just Myosin. There are Myosin$_c$ (inactive) in cytosol and Myosin$_m$ (active) in cortex plasma-membrane. The total concentration is constant such that

$$\text{Myosin}_c(t) + \text{Myosin}_m(t) = M_T = \text{const.}$$

The state variable $M(t)$ denotes the concentration of Myosin$_m$ at time t in the models.

Using the conservation of mass, the general model is of the form:

$$\begin{aligned}
\frac{dG}{dt} &= f_1(G, R, M), \\
\frac{dR}{dt} &= f_2(G, R, M), \\
\frac{dM}{dt} &= f_3(G, R, M).
\end{aligned}$$

The explicit definition of the functions f_1, f_2 and f_3 are determined by different assumptions used hence resulting into different mathematical models being formulated. To this end we consider two main categories of models depending on how GEF module activities are interpreted. This interpreted via enzymatic activity (Michaelis-Menten kinetics) or the law of mass action. In the next section, we first consider two models in which GEF activities are translated using Michaelis-Menten kinetics.

In Chapters 1-7, we only consider the ODE models, which represent the temporal activities of GEF, Rho and Myosin, and not spatially extended model. However, in Chapter 8, we formulate and analyse the spatially extended version of the ODE models. The ODE models are used to approximate kinetic dynamics that represent behaviour at a particular point of the cell body, from the experimental data. The data is obtained by dividing the cell body into several frames of reference and observations are recorded for each frame and then averaged over the whole cell body. This experimental data shows temporal evolutions of GEF, Rho and Myosin averaged over the whole cell body and averaged for all the cell population (35 to 68 cells), which is used to fit the ODE model in Chapter 7. However other data is also available for spatial distributions of GEF, Rho and Myosin that will be used in the analysis of spatially extended model (Graessl et al., 2017; Kamps et al., 2019).

Due to lack of precise mechanism on how different reactions occur, different assumptions are considered such as binding and enzymatic activity. Furthermore we also consider different translations for enzymatic activity such as Michaelis-Menten kinetics or Hill function, hence resulting in different mathematical models (GRM-1, GRM-2 and GRM-3). In the analysis we then study similarities and differences between the models.

2.3 Enzymatic activity and quasi-equilibrium assumption on GEF module

In the previous section, we have introduced the general principles and assumptions underlying the models to be formulated. In this section we consider only the models in which the GEF activities are translated via Michaelis-Menten kinetics. The main assumptions considered for these models are;

1. Michaelis-Menten kinetics on GEF module,

2. Quasi-equilibrium assumption on GEF module, and

3. Activities of Myosin-IIA and MYO9B are combined together and collectively referred to as Myosin, which inhibits both Rho and GEF as shown in Figure 2.1.

The models formulated in this section are respectively referred to as: *GRM-1* and *GRM-2*.

2.3.1 Formulation of model GRM-1

First, we formulate the mathematical models describing the temporal dynamics of the three species, $G(t)$, $R(t)$ and $M(t)$ by using the enzyme kinetics on GEF-H1 (Rowlands et al., 1988; Sakumura et al., 2005). For this model, the biological assumptions are translated using the following assumptions.

1. GEF activation by Rho and its inhibition by Myosin are modelled using Michaelis-Menten kinetics.

2. The activation of Rho by GEF and its inhibition by Myosin are modelled using the law of mass action, while the constitutive activity of Rho (self activation and deactivation of Rho) are modelled by using a Hill function with $n = 2$, to describe kinetics with saturation. This approach is similar to the one used in (Simon et al., 2013) to model the signalling between Abr (GEF) and RhoA. In this work, it was shown that $n \geq 2$ is necessary for the system to exhibit bistability.

3. The activation of Myosin by Rho, and its constitutive activation and inhibition are all modelled by the law of mass action.

Therefore, the time-evolution of $G(t)$, $R(t)$ and $M(t)$ are described by the following system of ordinary differential equations

$$\frac{dG}{dt} = \underbrace{\frac{k_3 R\,(G_T - G)}{K_{g3} + (G_T - G)}}_{\text{Activation of GEF by Rho}} - \underbrace{\frac{k_4\, M\, G}{K_{g4} + G}}_{\text{Inhibition of GEF by myosin,}} \tag{2.1a}$$

$$\frac{dR}{dt} = \underbrace{\alpha\, G\,(R_T - R)}_{\text{Rho Activation by GEF}} + \underbrace{\frac{k_1\,(R_T - R)^2}{K_{r1}^2 + (R_T - R)^2}}_{\text{Rho baseline activation}} - \underbrace{k_2' M R}_{\text{Rho Inhibition by myosin}} - \underbrace{\frac{k_2 R^2}{K_{r2}^2 + R^2}}_{\text{Rho baseline inhibition,}} \tag{2.1b}$$

$$\frac{dM}{dt} = \underbrace{k_5 R\,(M_T - M)}_{\text{Myosin activation by Rho}} + \underbrace{k_7\,(M_T - M)}_{\text{myosin baseline activation}} - \underbrace{k_6 M}_{\text{myosin decay.}} \tag{2.1c}$$

In the above equations, α, k_1, k_2, k_2', k_3, k_4, k_5, k_6 and k_7, are positive reaction rates while K_{g3}, K_{g4}, K_{r1} and K_{r2} are Michaelis-Menten constants which are also positive, and G_T, R_T, M_T are, respectively, the total concentrations of GEF, Rho and Myosin. It has been shown experimentally that Myosin activation occurs with a time delay of about 3-40 seconds with respect to RhoA and GEF-H1 activities (Graessl et al., 2017; Kamps et al., 2019). That means that RhoA and GEF-H1 activities are much faster than Myosin activities, and we therefore assume a fast pre-equilibrium on GEF module. With this effect, we may assume a quasi-steady state approximation of GEF-H1 reaction. This is mathematically written by setting Equation (2.1a) equal to 0:

$$0 = \frac{k_3 R\,(G_T - G)}{K_{g3} + (G_T - G)} - \frac{k_4\, M\, G}{K_{g4} + G}. \tag{2.2}$$

To simplify calculations we work with the non-dimensional form corresponding to (2.2) where we let $u = k_3 R$, $v = k_4 M$, $J = K_{g3}/G_T$, $K = K_{g4}/G_T$ and $g = G/G_T$. Substituting this in (2.2) we have

$$(v-u)g^2 - (v - u + vJ + uK)g + uK = 0. \tag{2.3}$$

This quadratic equation has two roots given by

$$g = \frac{2uK}{v - u + vJ + uK \pm \sqrt{(v - u + vJ + uK)^2 - 4(v-u)uK}}. \tag{2.4}$$

We require a biophysically feasible root, that satisfies $0 < g < 1$. We show that the root with a negative sign is either negative or if it is positive, then it is such that $g > 1$. Since all the other parameters in Equation (2.3) are positive, we consider signs of $v - u$.

If $v - u \leq 0$, it can be easily seen by using Descartes' rules of sign on (2.3), that there exist exactly 1 positive and 1 negative real root. The positive real root is given by (2.7).

If $v - u > 0$, it can be easily seen using Descartes' rule of sign that (2.3) has two real roots or two complex conjugates. We are only interested in real roots. We show that if two real roots exist, then

$$\frac{2uK}{v - u + vJ + uK - \sqrt{(v - u + vJ + uK)^2 - 4(v-u)uK}} > 1. \tag{2.5}$$

Assume by contradiction that it is less than 1, we get

$$\frac{2uK}{v-u+vJ+uK-\sqrt{(v-u+vJ+uK)^2-4(v-u)uK}}<1,$$

this is equivalent to

$$2uK<v-u+vJ+uK-\sqrt{(v-u+vJ+uK)^2-4(v-u)uK}.$$

Simplifying this inequality, we obtain

$$\sqrt{(v-u+vJ+uK)^2-4(v-u)uK}<v-u+vJ-uK.$$

Squaring both sides and simplify we have

$$(vJ+uK)^2<(vJ-uK)^2,$$

which is not possible since the parameters are positive, and therefore inequality (2.5) holds. Similarly, consider the second root

$$\frac{2uK}{v-u+vJ+uK+\sqrt{(v-u+vJ+uK)^2-4(v-u)uK}}. \tag{2.6}$$

Following similar procedure as before we obtain

$$(vJ-uK)^2<(vJ+uK)^2.$$

Therefore, the only physically meaningful root which satisfies $0<g<1$ is:

$$g=\frac{2uK}{v-u+vJ+uK+\sqrt{(v-u+vJ+uK)^2-4(v-u)uK}}. \tag{2.7}$$

The solution is the known Goldbeter-Koshland function (Goldbeter and Koshland, 1981) that represents the steady state fraction of G namely G^*/G_T and denoted $E_p(\cdot)$, which is given by:

$$\frac{G^*}{G_T}=E_p\left(k_3R, k_4M, K_{g3}/G_T, K_{g4}/G_T\right), \tag{2.8}$$

where in non-dimensional form

$$E_P(u,v,J,K)=\frac{2uK}{v-u+vJ+uK+\sqrt{(v-u+vJ+uK)^2-4(v-u)uK}}. \tag{2.9}$$

Therefore, we obtain the dimensional model

$$\frac{dR}{dt} = \alpha G_T E_p\left(k_3 R, k_4 M,\ K_{g3}/G_T,\ K_{g4}/G_T\right)\left(R_T - R\right) + \frac{k_1\left(R_T - R\right)^2}{K_{r1}^2 + \left(R_T - R\right)^2} - k_2' M R - \frac{k_2 R^2}{K_{r2}^2 + R^2}, \tag{2.10a}$$

$$\frac{dM}{dt} = k_5 R\left(M_T - M\right) - k_6 M + k_7\left(M_T - M\right), \tag{2.10b}$$

where $E_p\left(k_3 R, k_4 M,\ K_{g3}/G_T,\ K_{g4}/G_T\right)$ is given in equation (2.9).

In equation (2.10a), the parameter αG_T can be aggregated in such a way that one can define $k_0 = \alpha G_T$ where the parameter k_0 is the maximum rate of activation of $R(t)$ by $G(t)$. Hence, the new system of ordinary differential equations for Equation (2.10), which is referred to as model *GRM-1* can be stated as:

$$\frac{dR}{dt} = k_0 E_p\left(k_3 R, k_4 M,\ K_{g3}/G_T,\ K_{g4}/G_T\right)\left(R_T - R\right) + \frac{k_1\left(R_T - R\right)^2}{K_{r1}^2 + \left(R_T - R\right)^2} - k_2' M R - \frac{k_2 R^2}{K_{r2}^2 + R^2}, \tag{2.11a}$$

$$\frac{dM}{dt} = k_5 R\left(M_T - M\right) - k_6 M + k_7\left(M_T - M\right), \tag{2.11b}$$

with initial conditions

$$R(t_0) = R_0 \text{ and } M(t_0) = M_0, \tag{2.12}$$

and positive constant parameters.

Mathematical analysis of this model will be provided in Chapter 3. In the next subsection, we describe the formulation of model GRM-2. The parameters of model GRM-1 and their corresponding units are shown in Table 2.1.

2.3.2 Formulation of model GRM-2

In the previous subsection, we have formulated model GRM-1, in this section we describe the formulation of model GRM-2. The following assumptions are used to formulate model GRM-2.

1. GEF activation by Rho and its inhibition by Myosin are modelled using Michaelis-Menten kinetics similar to model GRM-1.

2. The activation of Rho by GEF and its self inhibition are modelled by Michaelis-Menten kinetics, which is different from model GRM-1 in which they are modelled by the law of mass action. Similarly its self activation and inhibition by Myosin are modelled by the law of mass action, different from model GRM-1 in which these reactions are modelled by a Hill function.

3. The activation of Myosin by Rho is modelled by Michaelis-Menten kinetics, different from model GRM-1 in which this reaction was modelled by mass action. Myosin self activation and inhibition are modelled by the law of mass action which is similar to model GRM-1.

Therefore the temporal dynamics of the three species are governed by the following system of ordinary differential equations:

$$\frac{dG}{dt} = \underbrace{\frac{k_3 R\,(G_T - G)}{K_{g3} + (G_T - G)}}_{\text{Activation of GEF by Rho}} - \underbrace{\frac{k_4\, M\, G}{K_{g4} + G}}_{\text{Inhibition of GEF by myosin,}} \tag{2.13a}$$

$$\frac{dR}{dt} = \underbrace{\alpha G \frac{(R_T - R)}{K_{r0} + (R_T - R)}}_{\text{Rho Activation by GEF}} + \underbrace{k_1 (R_T - R)}_{\text{Rho baseline activation}} - \underbrace{k_2' M R}_{\text{Rho Inhibition by myosin}} - \underbrace{\frac{k_2 R}{K_{r2} + R}}_{\text{Rho baseline inhibition,}} \tag{2.13b}$$

$$\frac{dM}{dt} = \underbrace{\frac{k_5 R (M_T - M)}{K_{m5} + M_T - M}}_{\text{Myosin activation by Rho}} + \underbrace{k_7\,(M_T - M)}_{\text{myosin baseline activation}} - \underbrace{k_6 M}_{\text{myosin decay.}} \tag{2.13c}$$

Equations (2.13) are defined for positive constant parameters and bounded positive initial conditions defined by;

$$G(t_0) = G_0,\ R(t_0) = R_0 \text{ and } M(t_0) = M_0. \tag{2.14}$$

By quasi-steady state assumption on GEF-H1, the system of three ordinary differential equations (2.13) simplifies to a system of two ordinary differential equations given by

$$\frac{dR}{dt} = \alpha G_T E_p\left(k_3 R, k_4 M,\ K_{g3}/G_T,\ K_{g4}/G_T\right) \frac{(R_T - R)}{K_{r0} + (R_T - R)} + k_1 (R_T - R) - \frac{k_2 R}{K_{r2} + R} - k_2' M R, \tag{2.15a}$$

$$\frac{dM}{dt} = \frac{k_5 R (M_T - M)}{K_{m5} + (M_T - M)} - k_6 M + k_7 (M_T - M), \tag{2.15b}$$

where $E_p\left(k_3R, k_4M,\ K_{g3}/G_T,\ K_{g4}/G_T\right)$ is given in Equation (2.9). If we let $k_0 = \alpha G_T$, then system (2.15) reduces to what we refer to as model GRM-2 defined by;

$$\begin{aligned}\frac{dR}{dt} &= k_0 E_p\left(k_3R, k_4M,\ K_{g3}/G_T,\ K_{g4}/G_T\right)\frac{(R_T - R)}{K_{r0} + (R_T - R)} + k_1(R_T - R) \\ &\quad - \frac{k_2 R}{K_{r2} + R} - k_2' M R,\end{aligned} \tag{2.16a}$$

$$\frac{dM}{dt} = \frac{k_5 R(M_T - M)}{K_{m5} + (M_T - M)} - k_6 M + k_7(M_T - M), \tag{2.16b}$$

with initial conditions

$$R(t_0) = R_0 \text{ and } M(t_0) = M_0, \tag{2.17}$$

where $0 \leq R(t_0) \leq R_T$ and $0 \leq M(t_0) \leq M_T$. Model parameters and their corresponding units are listed in Table 2.1.

In summary, models GRM-1 and GRM-2 have been formulated from first principles based on the experimental work in Graessl et al. (2017), and following the modelling approach of an activator-inhibitor network described in Tyson et al. (2003). The main assumptions for these models are Michaelis-Menten kinetics and quasi-steady state approximation for GEF activities. The other reactions from Rho and Myosin modules were represented using different mathematical assumptions (Mass action, Michaelis-Menten kinetics and Hill function). These two models were refined, based on the experimental work in Kamps et al. (2019), which led to the formulation of a new model in the following section, referred to as GRM-3.

2.4 Mass action on GEF-H1 activity and quasi-equilibrium assumption on Rho module

In the previous section, we have derived two models in which the main assumptions were the use of Michaelis-Menten kinetics and the quasi-steady state approximation on the GEF module. These assumptions were modified based on the experimental work in Max Planck Institute of Molecular Physiology and the University of Duisburg-Essen (Kamps et al., 2019). The two main underlying assumptions in this model are:

(i) GEF module is translated via the law mass action

(ii) The quasi-steady-state approximation is assumed on the Rho module.

These assumptions are different from the ones used to formulate the first two models (GRM-1 and GRM-2), in which we assumed enzymatic activity on the GEF module implementation. The quasi-steady-state approximation was also assumed on the GEF module. Therefore, for this model, consider the wiring diagram in Figure 2.2. The definition of variables and mass conservation are considered as in the case of previous models. To formulate the model, we consider the following set of points;

1. The formation of stable complex between active Rho and GEF-H1 (Medina et al., 2013; Kamps et al., 2019) would imply non-enzymatic activity on the activation of GEF-H1 by Rho. Activation of GEF module by Rho activity is based on a direct protein interaction and therefore this is implemented via mass action. Similarly, the mechanism of GEF inhibition by Myosin module is based on direct binding of the two components and therefore also implemented via mass action (Graessl et al., 2017; Kamps et al., 2019).

2. The Rho activity module is based on enzymatically conversion between the active and inactive states, and therefore this will be implemented via Michaelis-Menten kinetics.

3. The activation of Myosin module by Rho activity is based on a multi-step enzymatic cascade. This process involves several kinases, phosphatase or actin polymerisation regulation. This will be implemented via Hill type equation.

3. Experimental analysis (Graessl et al., 2017; Kamps et al., 2019) shows that amplification of Rho occurs very rapidly and much faster than the activation of Myosins which occurs with a time delay of about 3 seconds for MYO9B, and a delay of about 30 to 40 seconds for Myosin-IIA. Therefore a fast pre-equilibrium is assumed on Rho amplification. From this Rho activity module which is based on enzymatic conversion between active and inactive states is implemented using Goldbeter-Koshland function (Goldbeter and Koshland, 1981).

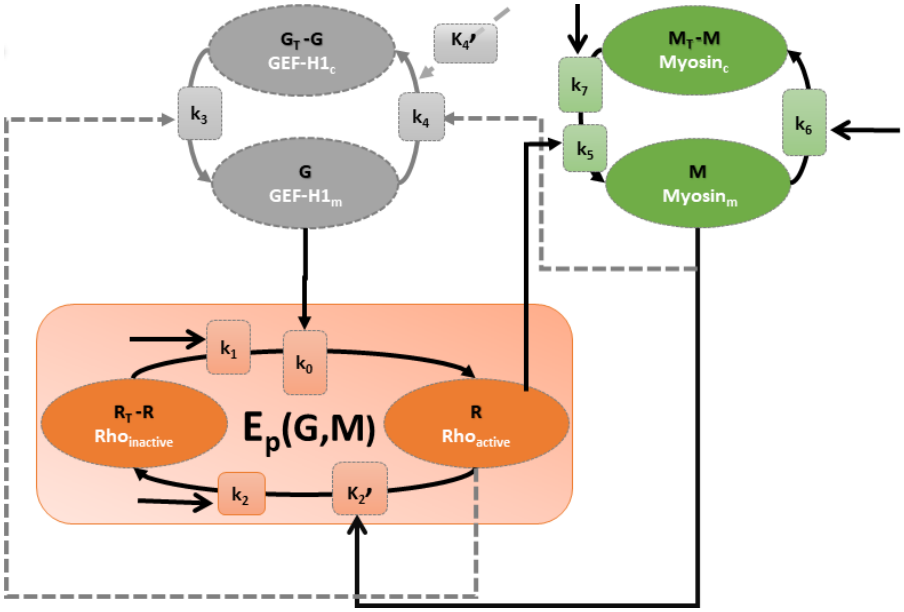

Figure 2.2: Interaction of GEF-H1, RhoA (Rho) and Myosin together with their inactive molecules. Quasi steady state approximation is assumed on the Rho module.

Based on interactions presented in Figure 2.2 and assuming the conservation of mass for each population, the evolution of G, R and M is governed by

$$\frac{dG}{dt} = \underbrace{k_3 R(G_T - G)}_{\text{Activation of GEF by Rho}} - \underbrace{k_4 MG}_{\text{Inhibition of GEF by myosin}} - \underbrace{k_4' G}_{\text{GEF decay,}} \tag{2.18a}$$

$$\frac{dR}{dt} = \underbrace{\frac{k_0 G(R_T - R)}{K_{r0} + (R_T - R)}}_{\text{Rho Activation by GEF}} + \underbrace{\frac{k_1 (R_T - R)}{K_{r1} + (R_T - R)}}_{\text{Rho baseline activation}} - \underbrace{\frac{k_2' MR}{K_{r2}' + R}}_{\text{Rho Inhibition by myosin}} - \underbrace{\frac{k_2 R}{K_{r2} + R}}_{\text{Rho baseline inhibition,}} \tag{2.18b}$$

$$\frac{dM}{dt} = \underbrace{\frac{k_5 R(M_T - M)^n}{K_{m5}^n + (M_T - M)^n}}_{\text{Myosin activation by Rho}} + \underbrace{\frac{k_7 (M_T - M)}{K_{m7} + (M_T - M)}}_{\text{myosin baseline activation}} - \underbrace{\frac{k_6 M}{K_{m6} + M}}_{\text{myosin decay.}} \tag{2.18c}$$

Equations (2.18) are defined for positive parameter values and with initial conditions

$$G(t_0) = G_0, \;\; R(t_0) = R_0 \text{ and } M(t_0) = M_0. \tag{2.19}$$

For model GRM-3, we only consider Myosin-IIA which inhibits Rho through GEF-H1. From Equation (2.18), since we do not consider MYO9B, we have that $k_2' = 0$. We also do not consider background GEF activity, therefore $k_4' = 0$. Therefore, from

system (2.18), we obtain;

$$\frac{dG}{dt} = k_3 R(G_T - G) - k_4 MG, \tag{2.20a}$$

$$\frac{dR}{dt} = \frac{k_0 G(R_T - R)}{K_{r0} + (R_T - R)} + \frac{k_1(R_T - R)}{K_{r1} + (R_T - R)} - \frac{k_2 R}{K_{r2} + R}, \tag{2.20b}$$

$$\frac{dM}{dt} = \frac{k_5 R(M_T - M)^n}{K_{m5}^n + (M_T - M)^n} + \frac{k_7(M_T - M)}{K_{m7} + (M_T - M)} - \frac{k_6 M}{K_{m6} + M}. \tag{2.20c}$$

Considering fast pre-equilibrium of R on system (2.20). Since there is no precise mechanism on how background GEFs activate *Rho*, we can assume they activate Rho in a similar way to GEF-H1, and thus, we have that $K_{r0} = K_{r1}$. This assumption helps us to derive the Goldbeter-Koshland function. Therefore from Equation (2.20b) we have:

$$\frac{(k_0 G + k_1)(R_T - R)}{K_{r0} + (R_T - R)} - \frac{k_2 R}{K_{r2} + R} = 0. \tag{2.21}$$

To simplify calculations, we work with the non-dimensional expression of (2.21) by letting

$$u = k_0 G + k_1,\ v = k_2,\ J = K_{r0}/R_T,\ K = K_{r2}/R_T \text{ and } r = R^*/R_T,$$

then Equation (2.21) reduces to

$$\frac{u(1-r)}{J + (1-r)} - \frac{v\, r}{K + r} = 0. \tag{2.22}$$

Simplifying (2.22) we obtain a quadratic equation of the form;

$$(v-u)r^2 - \underbrace{(v - u + uK + vJ)}_{\Phi} r + uK = 0. \tag{2.23}$$

The solution to (2.23) is given by

$$r = \frac{\Phi \pm \sqrt{\Phi^2 - 4(v-u)uK}}{2(v-u)} = \frac{2uK}{\Phi \pm \sqrt{\Phi^2 - 4(v-u)uK}}. \tag{2.24}$$

Since $u \geq 0$ and $K \geq 0$, from Equation (2.23) the only biologically feasible solution is given by

$$E_P(u, v, J, K) = \frac{2uK}{\Phi + \sqrt{\Phi^2 - 4(v-u)uK}}. \tag{2.25}$$

Therefore, model equations (2.20) reduce to

$$\frac{dG}{dt} = k_3 R_T E_P \left(k_0 G + k_1, k_2, \frac{K_{r0}}{R_T}, \frac{K_{r2}}{R_T}\right)(G_T - G) - k_4 MG, \tag{2.26a}$$

$$\frac{dM}{dt} = \frac{k_5 R(G, M)(M_T - M)^n}{K_{m5}^n + (M_T - M)^n} + \frac{k_7(M_T - M)}{K_{m7} + (M_T - M)} - \frac{k_6 M}{K_{m6} + M}. \tag{2.26b}$$

The asymptotic analysis of this model is provided in Chapter 3, model parameters and their corresponding units are listed in Table 2.1.

MODEL GRM-1								
Parameters	G_T	k_3	k_4	K_{g3}	K_{g4}	k_1	k_2	k_2'
Units	**M**	s^{-1}	s^{-1}	**M**	**M**	$\mathbf{M}^{-1}s^{-1}$	$\mathbf{M}^{-1}s^{-1}$	$\mathbf{M}^{-1}s^{-1}$
Parameters	R_T	K_{r1}	K_{r2}	k_0	M_T	k_5	k_6	k_7
Units	**M**	**M**	**M**	s^{-1}	**M**	$\mathbf{M}^{-1}s^{-1}$	s^{-1}	s^{-1}
MODEL GRM-2								
Parameters	G_T	k_3	k_4	K_{g3}	K_{g4}	k_1	k_2	k_2'
Units	**M**	s^{-1}	s^{-1}	**M**	**M**	s^{-1}	$\mathbf{M}\,s^{-1}$	$\mathbf{M}^{-1}s^{-1}$
Parameters	R_T	K_{r0}	K_{r2}	k_0	M_T	k_5	k_6	k_7 K_{m5}
Units	**M**	**M**	**M**	$\mathbf{M}s^{-1}$	**M**	s^{-1}	s^{-1}	s^{-1} **M**
MODEL GRM-3								
Parameters	G_T	k_3	k_4	k_0	K_{r0}	k_1	K_{r1}	k_2
Units	**M**	$\mathbf{M}^{-1}$ s^{-1}	$\mathbf{M}s^{-1}$	s^{-1}	$\mathbf{M}^{-1}$	$\mathbf{M}s^{-1}$	**M**	**M** s^{-1}
Parameters	K_{r2}	R_T	M_T	k_5	K_{m5}	k_6	K_{m6}	k_7 K_{m7}
Units	**M**	**M**	**M**	s^{-1}	**M**	$\mathbf{M}s^{-1}$	**M**	$\mathbf{M}s^{-1}$ **M**

Table 2.1: Table of parameters for models GRM-1, GRM-2 and GRM-3 together with their corresponding units. **M** represents units of concentration while s time.

2.5 Conclusion

In this chapter, we have derived from first principles a set of three mathematical models that represent the temporal GEF–Rho–Myosin signalling pathway, to describe the Rho activity dynamics linked to cellular contractility, based on the experimental observations (Graessl et al., 2017; Kamps et al., 2019). The models were broadly categorised into two classes, depending on the mathematical translation of the GEF activities. The first two models, which we called GRM-1 and GRM-2, were derived based on the assumption that the GEF activation and inhibition follows enzymatic activity and also the quasi-steady state approximation on the GEF module. The derivation of these models was motivated and guided by the activator-inhibitor network in the work of Tyson et al. (2003).

The third model, GRM-3 was a refinement of the first two models based on the experimental results in Kamps et al. (2019), with the assumption that activation

of GEF and its inhibition follow the normal binding and the quasi-steady state approximation of the Rho module in order to derive the equivalent of the Goldbeter-Koshland function (Goldbeter and Koshland, 1981). The detailed comparison of these models from their underlying mathematical assumptions will be presented in Chapter 6. In the next chapter, we explore the asymptotic behaviour of the models formulated in this chapter, in order to understand their long term behaviour. The analysis is motivated by the experimental observations in Graessl et al. (2017); Kamps et al. (2019) which show that this network manifests distinct dynamical states depending on the expression level of the positive feedback mediator GEF-H1. This motivates us to investigate the stability of equilibrium states of the model as G_T varies.

Chapter 3

Mathematical analysis of temporal models

3.1 Introduction

In the previous chapter, we have derived a set of three mathematical models of ODE type to describe the temporal dynamics of GEF–Rho–Myosin network. In this chapter, we first prove the positive invariance of the formulated models, by requiring that the total concentrations of GEF, Rho and Myosin are conserved. We also study the asymptotic behaviour of those models, in order to understand their long term behaviour. Motivated by the experimental observation that this network manifests distinct dynamic states depending on the expression level of the positive feedback mediator GEF-H1, the stability analysis of the equilibrium state is investigated with respect to the GEF total concentration, G_T. Also motivated by the experimental observation that the system exhibits periodic pulses. We use sign pattern analysis to study the existence of Hopf bifurcation points at some G_T values, and hence periodic solutions. We use nullcline configuration to explore the type of configurations for which the ODE models exhibit different dynamics. These results are complemented by detailed numerical bifurcation analysis of the models with respect to bifurcation parameter, G_T. We only consider the qualitative analysis and numerical bifurcation analysis of the models. The illustration of these results are presented in Chapter 5.

The three models introduced in Chapter 2 describe species namely R and M inter-

acting such that

$$\frac{dR}{dt} = f(R, M), \tag{3.1a}$$

$$\frac{dM}{dt} = g(R, M). \tag{3.1b}$$

We remark here that R represents the variable R in models GRM-1 and GRM-2, while it represents the variable G in Model GRM-3. Since here the analysis is general for the three models, we use generic variables R to refer to the first variable in models GRM-1, GRM-2 and GRM-3, while M refers to the second variable. Before investigating asymptotic behaviour of the models, we first prove the existence, uniqueness of solutions of models and the positive invariance of the flow of the systems defining models GRM-1, GRM-2 and GRM-3.

3.2 Preliminary properties

In this section, we prove the positive invariance of the three models GRM-1 (2.11), GRM-2 (2.16) and GRM-3 (2.26).

Theorem 3.2.1. *The set*

$$S = \{(R, M) \in \mathbb{R}^2_+ : 0 \leq R \leq R_T, \quad 0 \leq M \leq M_T\}. \tag{3.2}$$

is compact positively invariant with respect to the flow of systems (2.11)*,* (2.16) *and* (2.26)*.*

Proof. By using Bony–Brezis theorem (Redheffer, 1972), it is sufficient to check that the vector field induced by the system is either tangent or entering S on the boundary of S defined in Equation (3.2). In other words, the vector field does not allow the flow outside the domain. We therefore check the flow field close to the boundaries, $R = 0$, $R = R_T$, $M = 0$ and $M = M_T$ as illustrated in Figure 3.1.

Let $R = R_T$, it can be easily seen from equations (2.11a), (2.16a) and (2.26a) that

$$\lim_{R \to R_T} \frac{dR}{dt} \leq 0,$$

therefore R is non-increasing. Hence the flow is into S. Similarly, along the boundary $R = 0$, we have

$$\lim_{R \to 0} \frac{dR}{dt} \geq 0,$$

hence R is non-decreasing, and the flow is into the domain.

Along the boundary $M = M_T$, it can be seen from equations (2.11b), (2.16b) and (2.26b) that

$$\lim_{M \to M_T} \frac{dM}{dt} \leq 0,$$

therefore M is non-increasing, and the flow is into the invariant set S. Similarly, along the boundary $M = 0$,

$$\lim_{M \to 0} \frac{dM}{dt} \geq 0,$$

and therefore the flow is into the domain S. The proof has been illustrated in Figure 3.1. □

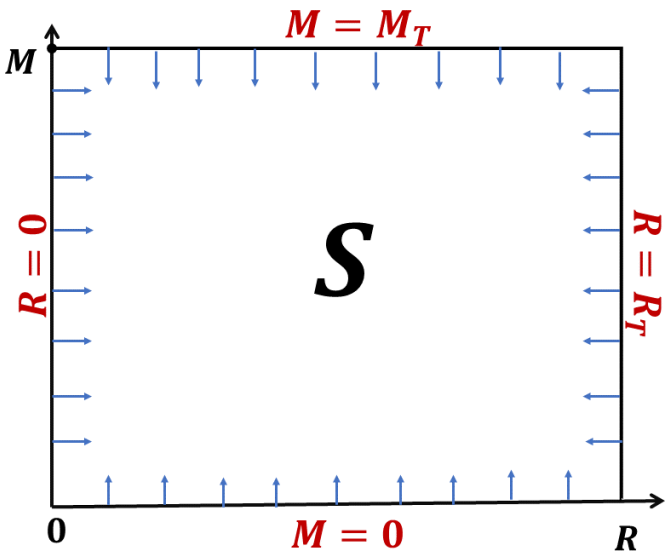

Figure 3.1: The flow of solutions when approaching the boundary of the invariant set S.

The functions f and g are the right-hand-side terms defined in models (2.11), (2.16) and (2.26). Systems are considered with non-negative initial conditions with $0 \leq R(t_0) \leq R_T$ and $0 \leq M(t_0) \leq M_T$. The solutions to systems defined in models GRM-1, GRM-2 and GRM-3 considered with non-negative initial conditions exist and are unique, since the vector field $(f, g) \in C^\infty(S)$, where $S = \{(R, M) \in \mathbb{R}^2_+ : 0 \leq R \leq R_T, \quad 0 \leq M \leq M_T\}$. Furthermore, the planar systems defined in models GRM-1, GRM-2 and GRM-3 have bounded solutions as proved in Theorem 3.2.1.

3.3 Asymptotic behaviour analysis

We have proved that the set (3.2) is positively invariant with respect to the flow of the systems defining models GRM-1 (2.11), GRM-2 (2.16) and GRM-3 (2.26). In this section, we analyse the asymptotic behaviour of the three models. This will entail the use of sign matrix of the Jacobian matrix that will be derived later in this section.

Motivated by the experimental results about the dynamics of GEF–Rho–Myosin network (Graessl et al., 2017; Kamps et al., 2019), we investigate the asymptotic behaviour of model equations (2.11), (2.16) and (2.26) at different expression levels of GEF-H1. Therefore we describe conditions of stability of the steady state with respect to the parameter of interest, G_T, which represents the total concentration of GEF-H1. To achieve this, we combine two approaches: sign pattern analysis of the Jacobian matrices as well as the local shape of the nature of nullcline configuration at the point of intersection.

A steady state $(R_*,\, M_*)$ of (3.1) satisfies the equation

$$f(R_*,\, M_*) = g(R_*,\, M_*) = 0,$$

and the curves defined as

$$f(R, M) = 0, \tag{3.3a}$$

$$g(R, M) = 0, \tag{3.3b}$$

are called R- and M-nullclines respectively.

To analyse stability of Equation (3.1), we linearise it around the steady state to obtain:

$$\begin{bmatrix} \frac{d(R-R_*)}{dt} \\ \frac{d(M-M_*)}{dt} \end{bmatrix} = J \begin{bmatrix} R - R_* \\ M - M_* \end{bmatrix}, \tag{3.4}$$

where J is the Jacobian matrix evaluated at $(R_*,\, M_*)$ and is given by

$$J = \begin{bmatrix} f_R & f_M \\ g_R & g_M \end{bmatrix}_{(R_*,\, M_*)}, \tag{3.5}$$

with subscripts $_R$ and $_M$ denoting partial derivatives $\frac{\partial}{\partial R}$ and $\frac{\partial}{\partial M}$ respectively. For the analysis, we shall consider the sign pattern corresponding to the Jacobian matrices that will be derived in the next subsection.

3.3.1 Jacobian matrices of the models

In this subsection we derive the Jacobian matrix of the three models. Model GRM-1 (2.11) has the Jacobian matrix, denoted J_1 which is given by:

$$J_1 = \begin{bmatrix} f_R & f_M \\ g_R & g_M \end{bmatrix}, \tag{3.6}$$

where

$$\begin{aligned} f_R &= k_0\left[E_{p,r}(R_T - R) - E_p\right] - k_2' M - \frac{2\,k_2 K_{r2}^2}{\left(K_{r2}^2 + R^2\right)^2} - \frac{2\,k_1 K_{r1}^2}{\left(K_{r1}^2 + (R_T - R)^2\right)^2}, \\ f_M &= k_0 E_{p,m}\left(R_T - R\right) - k_2' R, \\ g_R &= k_5(M_T - M) \geq 0, \\ g_M &= -k_5\, R - k_6 - k_7 < 0, \end{aligned}$$

with

$$E_{p,r} = \frac{2k_3 K\left[A - RA_r\right]}{A^2}, \quad A_r = \frac{\partial A}{\partial R},$$
$$E_{p,m} = \frac{-2k_3 K R A_m}{A^2}, \quad A_m = \frac{\partial A}{\partial M},$$
$$\Phi = k_4 M - k_3 R + k_4 M J + k_3 R K, \quad J = K_{g3}/G_T,\ K = K_{g4}/G_T,$$
$$A = \Phi + \sqrt{Z}, \quad Z = \Phi^2 - 4(k_4 M - k_3 R)k_3 R K.$$

Model GRM-2 (2.16) has the Jacobian matrix, evaluated at the steady state, denoted J_2 which is given by:

$$J_2 = \begin{bmatrix} f_R & f_M \\ g_R & g_M \end{bmatrix}, \tag{3.7}$$

where

$$\begin{aligned} f_R &= k_0\left[E_{p,r}\frac{(R_T - R)}{K_{r0} + (R_T - R)} - E_p\frac{K_{r0}}{(K_{r0} + (R_T - R))^2}\right] - \frac{k_1 K_{r1}}{(K_{r1} R_T - R)^2} \\ &\quad - \frac{k_2 K_{r2}}{(K_{r2} + R)^2} - \frac{k_2' K_{r2}' M}{(K_{r2}' + R)^2}, \\ f_M &= k_0 E_{p,m}\frac{(R_T - R)}{K_{r0} + (R_T - R)} - \frac{k_2' R}{K_{r2}' + R}, \\ g_R &= \frac{k_5(M_T - M)}{K_{m5+(M_T - M)}} \geq 0, \\ g_M &= \frac{-k_5 K_{m5} R}{(K_{m5+M_T - M})^2} - \frac{k_6 K_{m6}}{(K_{m6} + M)^2} - \frac{k_7 K_{m7}}{(K_{m7} + M_T - M)^2} < 0, \end{aligned}$$

with

$$E_{p,r} = \frac{2k_3K\,[A - RA_r]}{A^2}, \quad A_r = \frac{\partial A}{\partial R},$$

$$E_{p,m} = \frac{-2k_3KRA_m}{A^2}, \quad A_m = \frac{\partial A}{\partial M},$$

$$\Phi = k_4M - k_3R + k_4MJ + k_3RK,$$

$$J = K_{g3}/G_T, \;\; K = K_{g4}/G_T,$$

$$A = \Phi + \sqrt{Z}, \quad Z = \Phi^2 - 4(k_4M - k_3R)k_3RK.$$

Before calculating the Jacobian matrix of model GRM-3 (2.26), we find $\frac{\partial R(G,M)}{\partial G}$ and $\frac{\partial R(G,M)}{\partial M}$ denoted, respectively, as R_g and R_m. In order to simplify calculations, we define the following quantities:

$$\Phi = k_2 - (k_0G + k_1) + k_2J + (k_0G + k_1)K, \;\; J = K_{r0}/R_T, \;\; K = K_{r2}/R_T,$$

$$\Phi_g = -k_0 + k_0K \quad \text{and} \quad \Phi_m = 0.$$

$$Z = \Phi^2 - 4(k_2 - (k_0G + k_1))(k_0G + k_1)K,$$

$$Z_g = 2\Phi\Phi_g - 4\left[-k_0(k_0G + k_1) + k_0(k_2 - (k_0G + k_1))\right]K \quad \text{and} \quad Z_m = 0.$$

$$A = \Phi + \sqrt{Z}, \quad A_g = \Phi_g + \frac{Z_g}{2\sqrt{Z}} \quad \text{and} \quad A_m = 0.$$

$$R(G, M) = \frac{2\,R_T(k_0G + k_1)K}{A}.$$

Finally, we get

$$R_g = \frac{2\,R_TK\,[k_0A - A_g(k_0G + k_1)]}{A^2} \quad \text{and} \quad R_m = 0.$$

Therefore, model system (2.26) has the Jacobian matrix, denoted J_3 given by:

$$J_3 = \begin{bmatrix} f_R & f_M \\ g_R & g_M \end{bmatrix}, \tag{3.8}$$

where

$$\begin{aligned} f_R &= k_3\left[R_g(G_T - G) - R\right] - k_4 M, \\ f_M &= -k_4 G < 0, \\ g_R &= \frac{k_5 R_g (M_T - M)^n}{K_{m5}^n + (M_T - M)^n}, \\ g_M &= \frac{-k_5\, n\, K_{m5}^n R (M_T - M)^{n-1}}{\left(K_{m5}^n + (M_T - M)^n\right)^2} - \frac{k_6 K_{m6}}{(K_{m6} + M)^2} - \frac{k_7 K_{m7}}{(K_{m7} + M_T - M)^2} < 0. \end{aligned}$$

3.3.2 Sign pattern analysis

We consider sign pattern of the Jacobian matrices for the analysis. Sign pattern analysis explores the possibility of having periodic solutions arising from Hopf bifurcation, just by analysing if the sign matrix of the corresponding Jacobian matrix admits the refined inertia

$$\mathbb{H}_n = \{(0,\, n, 0, 0),\, (0, n-2, 0, 2),\, (2, n-2, 0, 0)\}.$$

$\mathbb{H}_n$ was introduced by Bodine et al. (2012) and it corresponds to the transition of eigenvalues as the pair of them with negative real part crosses the imaginary axis to have positive real part. It is therefore used to investigate the existence of periodic solutions as a parameter is varied. If a matrix allows $\mathbb{H}_n$ as a certain parameter varies, then there is a Hopf bifurcation at some value of the parameter and hence the possibility of linearly stable periodic solutions. We use this method for the analysis since the method does not involve quantitative analysis of the Jacobian matrix, but only signs of the corresponding entries of the Jacobian matrix. We make use of concepts, definitions and theorems regarding sign pattern analysis which are described in Appendix B and are necessary for a complete understanding of this section. The linear stability of the steady state $(R_*,\, M_*)$ is determined by the eigenvalues of its Jacobian matrix evaluated at the steady state. The solution may approach this steady state (when all eigenvalues have negative real part), oscillate around it, or move away from it (Culos et al., 2016). We study the asymptotic behaviour of models GRM-1 (2.11), GRM-2 (2.16) and GRM-3 (2.26) by considering the sign pattern of their respective Jacobian matrices evaluated at the equilibrium points.

2×2 sign pattern

It can be easily seen from Jacobian matrices (3.6), (3.7) and (3.8) that,

- f_R is not sign-definite.
- f_M is not sign-definite for models GRM-1 and GRM-2, but $f_M < 0$ for model GRM-3.
- $g_M < 0$ for all the three models and $g_R > 0$ for models GRM-1 and GRM-2, while it is not sign definite for model GRM-3.

Therefore, the Jacobian matrices J_i, with $i \in \{1, 2, 3\}$ have the sign pattern given by:

$$\mathcal{J} = \begin{bmatrix} \circledast & \circledast \\ \circledast & - \end{bmatrix}, \tag{3.9}$$

where $\circledast$ represents $-$, $+$ or 0 depending on the sign of the corresponding term. Recall the following theorem with regard to 2×2 sign patterns:

Theorem 3.3.1. *There is no 2×2 sign pattern that require $\mathbb{H}_2$. The sign pattern (sign pattern similar to)*

$$\begin{bmatrix} + & - \\ + & - \end{bmatrix},$$

is the only sign pattern that allows $\mathbb{H}_2$, since it is spectrally arbitrary [1] *(Drew et al., 2000; Bodine et al., 2012).*

We have seen that Jacobian matrices have sign pattern in the form of Equation (3.9). We know that $g_R > 0$ for models GRM-1 and GRM-2, and also GRM-3 might have $g_R > 0$. We also know that $f_M < 0$ for model GRM-3, this case is also possible for models GRM-1 and GRM-2. From this observation we therefore have the following particular case:

Theorem 3.3.2. *Provided that $f_M < 0$ and $g_R > 0$, for the systems (2.11), (2.16) and (2.26), we have the following:*

i) If $f_R \leq 0$, there exists an equilibrium point that is locally asymptotically stable and there is no possibility of periodic solutions.

[1] Matrix that allows all possible refined inertias

ii) Otherwise if $f_R > 0$ then the periodic solutions are possible and a Hopf bifurcation occurs at some parameter values.

Proof. Assume that $f_M < 0$ and $g_R > 0$.

Case 1 $f_R \leq 0$. The sign matrix takes the form

$$\mathcal{J} = \begin{bmatrix} \ominus & - \\ + & - \end{bmatrix}.$$

From this it can be easily seen that $tr(J_i) < 0$ and $det(J_i) > 0$. Therefore, the only possible refined inertia is $(0, 2, 0, 0)$, and the equilibrium point is locally asymptotically state is stable by Theorem B.1.4.

Case 2 $f_R > 0$. The sign matrix takes the form

$$\mathcal{J} = \begin{bmatrix} + & - \\ + & - \end{bmatrix}.$$

By Theorem 3.3.1, it allows

$$\mathbb{H}_2 = \{(0,\ 2,\ 0,\ 0),\ (0,\ 0,\ 0,\ 2),\ (2,\ 0,\ 0,\ 0)\},$$

and therefore, there is a possibility of periodic solutions arising from a Hopf bifurcation at some parameter values.

□

Due to magnitude restrictions (the terms in the Jacobian matrices are related, i.e. at least two terms depend on at least one common parameter), we cannot fully conclude on the asymptotic behaviour of the systems. Therefore the sign pattern analysis results will be combined with the nullcline configuration in the geometric approach to analyse the stability with respect to the parameter G_T. This allows full characterisation of model stability with respect to the parameter of interest. Therefore, in the following subsection, we analyse the qualitative intersections of the nullclines at the steady state. We refer to this approach as the *Geometric approach*.

3.3.3 Geometric approach to stability analysis

In the previous subsection we found some conditions for which models GRM-1, GRM-2 and GRM-3 may exhibit periodic solutions. These conditions are $f_R > 0$, $f_M < 0$ and $g_R > 0$.

To investigate the local stability of equilibrium we consider the local configuration of the nullcline at the intersection point defining the given equilibrium. We use the approach presented in Murray (2002), about the local configuration at the point of intersection of the two nullclines as G_T changes. In this case the qualitative behaviours of the solution can be deduced from a gross geometric study of nullclines, (Murray, 2002). For the three planar systems (2.11), (2.16) and (2.26) considered, the intersection of the nullclines might take one of the following forms depicted in Figure 3.2 as G_T is varied. The use of parameter G_T here is biologically motivated since it has been observed in experiments that GEF–Rho–Myosin network shows distinct dynamics depending on the expression levels of GEF-H1 (Graessl et al., 2017; Kamps et al., 2019). Since the solutions are bounded in S then, we have at least one equilibrium in S. In Figure 3.2 the possible configurations at the equilibrium point are listed. All the possible nullcline intersections of the three models are locally similar to the configurations presented in Figure 3.2. From Figure 3.2 as G_T varies we observe 1 or 3 equilibrium points, R-nullclines depend on G_T and behave as cubic curves for the three models. For models GRM-1 and GRM-2, M-nullcline do not depend on G_T.

The equilibria E_i, $i = 1, \cdots, 9$ in Figure 3.2 can be classified according to the local configuration of both nullclines at the point of intersection such that we have three different types grouped as:

$$E_1 \sim E_3 \sim E_4 \sim E_6 \sim E_7,\ E_2 \sim E_9 \text{ and } E_5 \sim E_8.$$

There exist only 3 different types of local configurations. Therefore, we will only analyse the local configurations at the steady states E_1, E_2 and E_5.

The nature of the steady state can be summarised in a theorem as follows:

Theorem 3.3.3. *The stability of the steady states E_i, for $i = 1, \ldots, 9$ defined in Figure 3.2 of models GRM-1 (2.11), GRM-2 (2.16) and GRM-3 (2.26) if they exist*

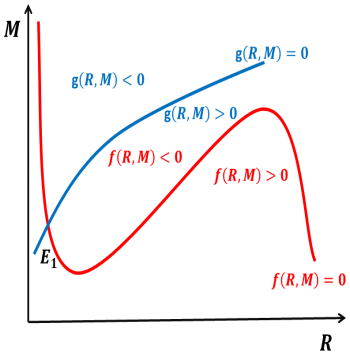

(a) Global asymptotic stability

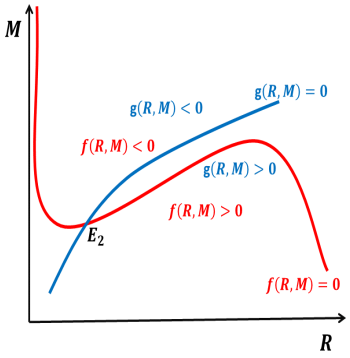

(b) **(i)** Stable limit cycle + unstable spiral (node) OR **(ii)** G.A.S. spiral (node)

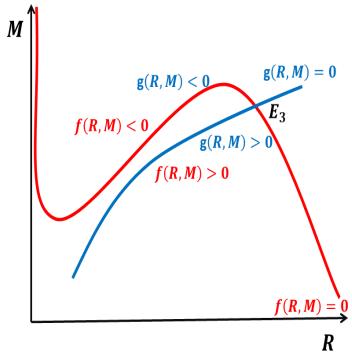

(c) Global asymptotic stability

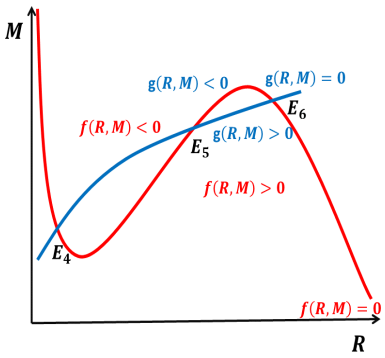

(d) Bistability (L.A.S. + saddle + L.A.S.)

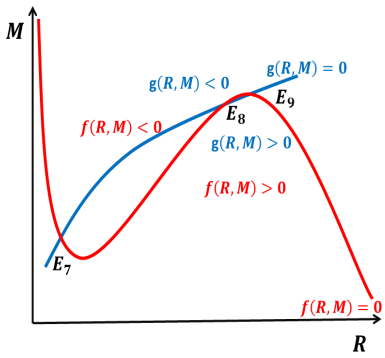

(e) L.A.S. + saddle + unstable (with or without limit cycle) or L.A.S. + saddle+ L.A.S. (with or without limit cycle)

Figure 3.2: Qualitative forms of nullcline intersection for Models GRM-1, (2.11), GRM-2, (2.16) and GRM-3, (2.26) as parameter G_T varies. Figure 3.2(e) is a special case of 3.2(d), in which the equilibrium point E_9 may be L.A.S as E_6 or unstable

.

can be categorised as follows:

Case 1 *Unique equilibrium point*

i) *Any equilibrium in the form of E_1, (Figure 3.2(a) similarly to E_3, Figure 3.2(c)) is globally asymptotically stable (G.A.S).*

ii) *For the case of equilibrium in the form of E_2, Figure 3.2(b),* $\det(J) > 0$ *and we have the following possibilities:*

- *If $tr(J) < 0$, E_2 is globally asymptotically stable;*

- *If $tr(J) > 0$, we have an unstable node for $tr(J)^2 > 4\det(J)$ or an unstable spiral for $tr(J)^2 < 4\det(J)$. In both cases, there exits a stable limit cycle, by Poincaré-Bendixson Theorem (Jordan and Smith, 1999).*

Case 2 *Three equilibrium points*

i) *For the case of E_4, E_5 and E_6, Figure 3.2(d) we have, respectively, locally asymptotically stable (L.A.S), a saddle point and L.A.S.*

ii) *For the case of E_7, E_8 and E_9, Figure 3.2(e) we have, respectively, L.A.S, saddle point and L.A.S (there exists a possibility of a limit cycle centred at E_9), or L.A.S., saddle point and unstable (there exists possibility of a limit cycle centred at E_9).*

Proof. The functions f_R, f_M, g_R and g_M are evaluated at the point of interest E_i.

(a) Steady state E_1

At the steady state E_1, the shape of the nullclines is shown in Figure 3.2(a). First we have

$$df = f_R dR + f_M dM \quad \text{and} \quad dg = g_R dR + g_M dM.$$

On the R-nullcline $f(R, M) = 0$, we have

$$df = f_R dR + f_M dM = 0,$$

and therefore get

$$\left.\frac{dM}{dR}\right|_{f=0} = -\frac{f_R}{f_M}. \tag{3.10}$$

Similarly along the M-nullcline $g(R, M) = 0$, we have

$$\left.\frac{dM}{dR}\right|_{g=0} = -\frac{g_R}{g_M}. \tag{3.11}$$

At the point E_1, we have that,

$$\left.\frac{dM}{dR}\right|_{f=0} < \left.\frac{dM}{dR}\right|_{g=0}.$$

Equivalently,

$$-\frac{f_R}{f_M} < -\frac{g_R}{g_M}.$$

This simplifies to

$$\frac{f_R}{f_M} > \frac{g_R}{g_M}. \tag{3.12}$$

We first find signs of entries of the Jacobian matrix. At E_1,

$$\left.\frac{dM}{dR}\right|_{f=0} = -\frac{f_R}{f_M} < 0,$$

therefore, f_R and f_M have the same sign. As we move parallel to the R–axis through the point of intersection E_1, we observe that $f(R, M)$ changes from positive to negative. This means $f(R, M)$ decreases and therefore, $f_R < 0$ which implies $f_M < 0$.

Similarly, at E_1,

$$\left.\frac{dM}{dR}\right|_{g=0} = -\frac{g_R}{g_M} > 0,$$

therefore, g_R and g_M have opposite signs. As we move parallel to the M-axis through the point of intersection E_1, we observe that $g(R, M)$ changes from positive to negative. This means $g(R, M)$ decreases and therefore, $g_M < 0$ which implies that $g_R > 0$. From the above we can write the sign pattern of the Jacobian matrix around the steady state E_1 and is given by

$$\mathcal{J}_{E_1} = \begin{bmatrix} - & - \\ + & - \end{bmatrix}. \tag{3.13}$$

From (3.13), the trace of the Jacobian matrix is such that tr $J(E_1) < 0$.

Back to equation (3.12) and since f_M and g_M are both negative, we have that

$$f_R\, g_M > g_R\, f_M$$

and therefore it follows that at E_1

$$\det J(E_1) = f_R\, g_M - g_R\, f_M > 0, \tag{3.14}$$

$$\mathrm{tr} J(E_1) = f_R + g_M < 0. \tag{3.15}$$

Conditions (3.14) and (3.15) are sufficient for stability, and, therefore, E_1 is L.A.S. Furthermore, the sign pattern $\mathcal{J}_{E_1}$ from (3.13) does not allow $\mathbb{H}_2$ (Bodine et al., 2012; Culos et al., 2016); therefore, a Hopf bifurcation leading to periodic solutions is not possible. There is no limit cycle centred at the equilibrium E_1.

In the case of E_1, the equilibrium is unique and L.A.S. (Figure 3.2(a)), if there is no limit cycle, the global asymptotic stability of the equilibrium can be concluded by invoking Poincaré-Bendixson theorem (Jordan and Smith, 1999). Hence, E_1 is globally asymptotically stable (G.A.S).

At E_3, nullclines exhibit the same local configuration as at E_1 (Figure 3.2(c)). Then a similar analysis can be carried out for equilibrium E_3. When the equilibrium E_3 exists, it is unique and L.A.S. and there is no limit cycle. Therefore, E_3 is G.A.S. At E_4 and E_6, the nullclines exhibit the same local configuration as that at E_1 (see Figure 3.2(d)). Hence, conclusions drawn for E_1 hold for E_4 and E_6: E_4 and E_6 are L.A.S. and there is no limit cycle neither centred at E_4 nor at E_6. Moreover, the equilibria E_4 and E_6 co-exist with E_5. The nature of the stability of E_5 is investigated later.

In Figure 3.2(e), equilibrium E_7 co-exits with E_8 and E_9. At E_7, the nullcline exhibit the same local configurations as that at E_1, therefore equilibrium of the form E_7 is L.A.S. and there is no limit cycle centred there. The nature of stability of E_8 and E_9 will be investigated later.

(b) Steady state E_2

To analyse the steady state E_2 we will consider Figure 3.2(b). At the point E_2 we have that

$$\left.\frac{dM}{dR}\right|_{f=0} < \left.\frac{dM}{dR}\right|_{g=0}.$$

Equivalently

$$-\frac{f_R}{f_M} < -\frac{g_R}{g_M}.$$

This simplifies to

$$\frac{f_R}{f_M} > \frac{g_R}{g_M}. \tag{3.16}$$

We also find the signs of entries of the corresponding Jacobian matrix. At E_2,

$$\left.\frac{dM}{dR}\right|_{f=0} = -\frac{f_R}{f_M} > 0,$$

therefore, f_R and f_M have opposite signs. As we move parallel to the R-axis through the point of intersection E_2, we observe that $f(R, M)$ changes from negative to positive. This means $f(R, M)$ increases and therefore, $f_R > 0$,

this implies that $f_M < 0$. Similarly at E_2,

$$\left.\frac{dM}{dR}\right|_{g=0} = -\frac{g_R}{g_M} > 0,$$

therefore g_R and g_M have opposite signs. As we move parallel to the M-axis through the point of intersection E_2, we observe that $g(R, M)$ changes from positive to negative. This means $g(R, M)$ decreases and therefore $g_M < 0$, which implies that $g_R > 0$. From the above we can write the sign pattern of the Jacobian matrix around the steady state E_2 which is given by

$$\mathcal{J}_{E_2} = \begin{bmatrix} + & - \\ + & - \end{bmatrix}. \tag{3.17}$$

From (3.17), we find that the trace of the Jacobian matrix is such that tr $J(E_2)$ is not sign definite. Back to equation (3.16) and since f_M and g_M are both negative, we have that

$$f_R\, g_M > g_R\, f_M,$$

and therefore it follows that at E_2

$$\det J(E_2) \quad = f_R\, g_M - g_R\, f_M > 0. \tag{3.18}$$

From the sign pattern analysis, this sign matrix allows $\mathbb{H}_2$ and therefore, it is possible to have a limit cycle and therefore, there is a possibility of linearly stable periodic solutions arising from a Hopf bifurcation (Bodine et al., 2012) as a parameter is varied. Summing up, for E_2, we can have:

(i) if $f_R + g_M > 0$, E_2 is an unstable (node or spiral). By the Poincaré-Bendixon criterion, as E_2 is a unique equilibrium point, there exists a stable limit cycle (Jordan and Smith, 1999).

(ii) if $f_R + g_M < 0$, E_2 is L.A.S. If there is no limit cycle, as E_2 is unique, by the Poincaré-Bendixon criterion, E_2 is G.A.S.

At E_9 (Figure 3.2(e)), nullclines exhibit the same local configuration as that at E_2 and therefore conclusions of E_2 can be drawn for E_9, which co-exists with E_7 and E_8. Therefore for E_9 we might have:

- If $f_R + g_M > 0$ then E_9 is unstable with or without a limit cycle centred at E_9.

- If $f_R + g_M < 0$ then E_9 is L.A.S. and there is possibility of a limit cycle centred at E_9.

(c) Steady state E_5

To analyse the nature of steady state E_5 we will consider Figure 3.2(d) and what happens locally around the intersection point E_5. At the point E_5 we have that

$$\left.\frac{dM}{dR}\right|_{f=0} > \left.\frac{dM}{dR}\right|_{g=0}.$$

Equivalently,

$$-\frac{f_R}{f_M} > -\frac{g_R}{g_M}.$$

This simplifies to

$$\frac{f_R}{f_M} < \frac{g_R}{g_M}. \tag{3.19}$$

At E_5,

$$\left.\frac{dM}{dR}\right|_{f=0} = -\frac{f_R}{f_M} > 0,$$

therefore f_R and f_M have the opposite signs. As we move parallel to the R-axis through the point of intersection E_5, observe that $f(R, M)$ changes from negative to positive. This means $f(R, M)$ increases and therefore $f_R > 0$. This implies that $f_M < 0$. Similarly at E_5,

$$\left.\frac{dM}{dR}\right|_{g=0} = -\frac{g_R}{g_M} > 0,$$

therefore g_R and g_M have opposite signs. As we move parallel to the M-axis through the point of intersection E_5, we observe that $g(R, M)$ changes from positive to negative. This means $g(R, M)$ decreases and therefore $g_M < 0$. This implies also that $g_R > 0$. From the above we can write the sign pattern of the Jacobian matrix around the steady state E_5 which is given by

$$\mathcal{J}_{E_5} = \begin{bmatrix} + & - \\ + & - \end{bmatrix}. \tag{3.20}$$

From (3.20), we find that the trace of the Jacobian matrix is such that tr $J(E_5)$ is not sign definite. Back to equation (3.19) and since f_M and g_M are both negative, we have that

$$f_R\, g_M < g_R\, f_M,$$

and therefore, at E_5

$$\det J(E_5) \quad = f_R\, g_M - g_R\, f_M < 0. \tag{3.21}$$

The steady state E_5 is a saddle point. A closed path cannot surround a region containing only a saddle (Jordan and Smith, 1999), and therefore no possibility for existence of a limit cycle.

The same local configuration occurs at E_8 (Figure 3.2(e)); therefore when they exist, E_5 and E_8 are saddle points.

In situations as in Figures 3.2(a) and 3.2(c), systems (2.11), (2.16) and (2.26) have a unique equilibrium that is globally asymptotically stable. In Figure 3.2(b), if $f_R > -g_M$ (trace is positive), then there exists a linearly stable limit cycle. If $f_R < -g_M$ (trace is negative), the unique equilibrium E_2 can be G.A.S. or L.A.S. and there exists a limit cycle centred around E_2. Therefore from Theorem 3.3.2, the conditions for the existence of periodic solution can now be refined to have the extra conditions that; $f_R > 0$, $f_R + g_M > 0$ and $\det(J) > 0$. The last condition, $\det(J) > 0$ excludes the possibility of having a limit cycle centred at a saddle point, which has the same sign matrix (3.17) as the equilibrium in the form of E_2.

In Figure 3.2(d), when the three steady states E_4, E_5 and E_6 exist: E_4 and E_6 are always L.A.S. (and no limit cycle exists) and E_5 is always a saddle point; there is a bistability (two stable steady states). In situations as in Figure 3.2(e), when the steady states E_7, E_8 and E_9 exist; E_7 is always L.A.S. and there is no limit cycle centred at E_7. E_8 is always a saddle point and E_9 could be unstable (with or without a limit cycle centred at E_9) or could be L.A.S. and surrounded by a limit cycle or not. □

All the three models have the Jacobian matrix with the same sign pattern. Models GRM-1 and GRM-2 admit all the nullcline configurations in Figure 3.2. Their dynamics are qualitatively similar as G_T varies. The dynamics transition from Figure 3.2(c) $\mapsto$ 3.2(b) $\mapsto$ 3.2(a) $\mapsto$ 3.2(e) and then to 3.2(d). On the other hand, model GRM-3 only admits three of the nullcline configurations in Figure 3.2. As G_T varies, the dynamics transition from Figure 3.2(a) $\mapsto$ 3.2(b) and then to 3.2(c). For biologically relevant parameters, model GRM-3 only exhibits one equilibrium.

We verified that model GRM-3 can also exhibit three equilibrium points with other parameter values, however we do not study this based on experimental observations. These transitions are verified from the bifurcation analysis results in the next section.

In this section we have considered qualitative stability analysis of the steady states of models GRM-1, GRM-2 and GRM-3, using the sign pattern analysis and the qualitative shape of nullcline configuration at the point of intersection. We have found out that all the models may exhibit periodic solutions arising from Hopf bifurcations for some parameter values. Models GRM-1 and GRM-2 may exhibit bistable dynamics for some parameter ranges. From the theoretical analysis, we summarised the results in two theorems, 3.3.2 and 3.3.3. These theoretical findings are complemented by numerical bifurcation analysis in the next section. Illustration of these results are provided in Chapter 5 where we provide both the temporal dynamics and phase planes describing the dynamics.

3.4 Bifurcation analysis

In the previous section, we presented theoretical analysis of the nature of the steady states of all the three models derived in Chapter 2. In this section we carry out numerical bifurcation analysis of all the models to complement the theoretical findings in the previous section. Throughout this section, we shall consider G_T as our bifurcation parameter.

The numerical bifurcation analysis provides a summary of the effect of the total concentration G_T on the value, the number and nature of the equilibrium points. The numerical bifurcation analysis is carried out with parameter values listed in Table 3.1. From the bifurcation analysis, the bifurcation values (values at which the models exhibit a change in their dynamics) of the bifurcation parameter G_T are obtained. Table 3.1 shows parameter values of the three models used for numerical bifurcation analysis.

The numerical bifurcation analysis was carried out using *Matcont* (Holmes et al., 2015; Dhooge et al., 2003, 2008). This is a MATLAB based software for interactive study of dynamical systems (Simon et al., 2013). It allows the computation of

Parameters	Model GRM-1	Model GRM-2	Model GRM-3
k_0	4	4	1
k_1	0.45	0.1	0.2
k_2	1	1	0.5
k_2'	1	1	NA
k_3	1	1	1
k_4	1	1	0.65
k_5	0.022	0.035	0.15
k_6	0.01	0.01	0.1
k_7	0.001	0.001	0.025
K_{r0}	NA	1	0.051
K_{r1}	0.05	NA	0.051
K_{r2}	0.05	1	0.05
$K_{r2'}$	NA	NA	NA
K_{m5}	NA	1	0.5
K_{m6}	NA	NA	0.75
K_{m7}	NA	NA	0.75
K_{g3}	0.3	0.15	NA
K_{g4}	0.2	0.1	NA

Table 3.1: Parameter values used for simulations and bifurcation analysis. Parameter values are taken from Tyson et al. (2003) and some of them adjusted to illustrate the qualitative dynamics hypothesised.

For total concentrations: $R_T = M_T = 1$ (NA refers to Not Applicable).

equilibrium solutions of the ODEs and their continuation with respect to the bifurcation parameter. It is able to detect bifurcation points such as; Hopf bifurcations, branching points and saddle-node bifurcations. For all the models, we take the total concentration of GEF-H1 (G_T) as a bifurcation parameter (this choice is biologically motivated). It was shown experimentally that the system dynamics changes with respect to different expression levels of the feedback mediator (Graessl et al., 2017; Kamps et al., 2019).

For all the bifurcation diagrams, we label; **HB**: Hopf bifurcation, **LP**: Fold bifurca-

tion. Bifurcation analysis of the models will be carried out separately. We can also consider other parameters for bifurcation analysis, here we only considered G_T and also k_1. k_1 is the parameter associated with the Rho constitutive activation, which represents the activity related to Rho activation by other background GEFs outside GEF-H1–RhoA–Myosin network.

3.4.1 Bifurcation analysis of model GRM-1

Bifurcation analysis of model GRM-1 was carried out with parameter values listed in the Table 3.1. One-parameter bifurcation diagrams were obtained by taking G_T the bifurcation parameter, they represent the value of equilibria of Rho and Myosin as G_T varies as shown in Figures 3.3(a) and 3.3(b). As the parameter G_T varies, the following observations are made:

1. $0 < G_T < 0.348546$ similar to $0.894942 < G_T < 8.115115$: situation as in Figure 3.2(a), a unique equilibrium which is G.A.S. (*stable regime*).

2. $0.348546 < G_T < 0.894942$: situation as in Figure 3.2(b), there is a unique equilibrium which is unstable and a stable limit cycle (*oscillatory regime*).

3. $8.115115 < G_T < 8.822280$: situation as in Figure 3.2(e) the model exhibit three equilibrium points; unstable, a saddle point and L.A.S.

4. $8.822280 < G_T$: situation as in Figure 3.2(d), two L.A.S equilibria and a saddle point (*bistable regime*).

a two-parameter bifurcation diagram was obtained by considering GEF concentration, G_T and k_1. This defines a region of plane where the model exhibit different dynamics as shown in Figure 3.3(c). The following regions are defined:

1. The red region is characterised by unstable steady state (node or spiral). The steady state is unique and therefore there exits a stable periodic obit (limit cycle). This region corresponds to red dashed lines in 3.3(a) and 3.3(b).

2. The uncoloured region in Figure 3.3(c) is characterised by the steady state which is unique and L.A.S., and therefore globally asymptotically stable.

3. The yellow region in Figure 3.3(c) is characterised by three steady states, two

locally asymptotically stable, separated by a saddle. The saddle acts as a switch which determines to which steady state the system converges to. This region is called the *bistable region*.

The results are summarised in Figure 3.3 and the bifurcation parameters listed in Table 3.2.

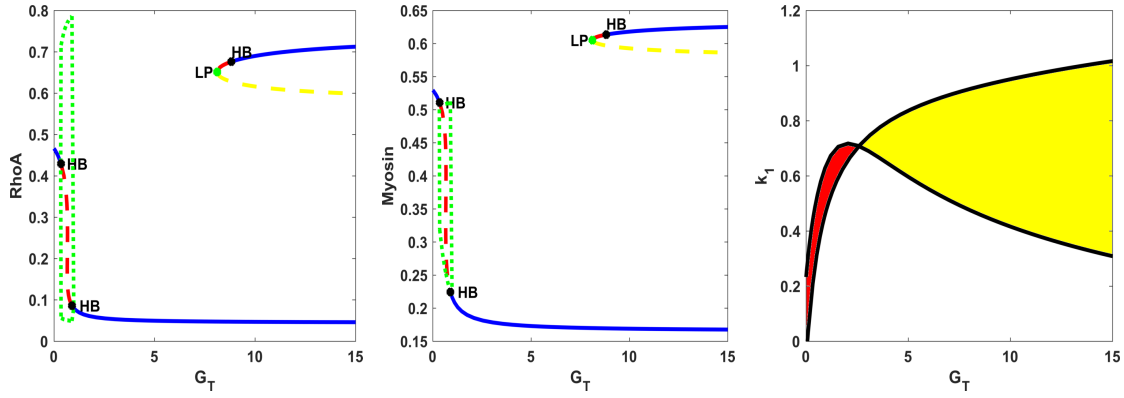

(a) (b) (c)

Figure 3.3: Bifurcation diagrams corresponding to model GRM-1. Figures 3.3(a) and 3.3(b) represent the value of equilibria of Rho and Myosin as G_T varies. Blue line represents the steady state values of Rho and Myosin in the stable region, red dashed line represents their values in the unstable region, yellow dashed line denotes their values at a saddle point while green dotted curve shows the maximum and minimum values of the resulting limit cycle. Hopf bifurcation points are labelled **HB** while fold bifurcations labelled **LP**. Figure 3.3(c) shows two-parameter bifurcation diagram. Red region shows the unstable region characterised by the stable periodic solutions, yellow region represents bistable region while uncoloured region represents the the region within which the steady state is stable.

Considering Figure 3.3(c), the following observations emerge: For $k_1 < 0.0338$, the steady state is always stable as G_T varies and no changes in its stability. The equilibrium point is unique and L.A.S., and therefore, G.A.S. For $0.0338 \leq k_1 \leq 0.2332$, model GRM-1 shows two distinct asymptotic behaviour (oscillatory and stable) as G_T varies. For small G_T values, the steady state is unstable characterised by periodic solutions, increasing G_T changes the steady state to stable. For $0.2332 < k_1 < 0.7116$, model GRM-1 has three distinct asymptotic behaviours, which can be characterised as follows: For small G_T values, the steady state is stable, which becomes unstable, characterised by periodic solutions as G_T increases. This steady state becomes stable again and further increase in G_T gives rise to three equilibrium points.

Lastly for $k_1 > 0.7176$, the model shows only two distinct asymptotic behaviour (stable and bistable regimes) as G_T is varied. This model has a narrow region characterised by periodic solutions. Bifurcation points are listed in Table 3.2, together with their corresponding Rho and Myosin values.

	Bifurcation points			
	HB	**HB**	**HB**	**LP**
G_T	0.348546	0.894942	8.822280	8.115115
Rho	0.429348	0.086142	0.676311	0.651325
Myosin	0.510899	0.224513	0.613584	0.605198

Table 3.2: Hopf bifurcation (**HB**) and Turning point/Limit point (**LP**) parameter values for model GRM-1.

3.4.2 Bifurcation analysis of model GRM-2

Bifurcation analysis of model GRM-2 was carried out in a similar way, using the parameter values listed in the Table 3.1, and G_T and k_1 are bifurcation parameters. Bifurcation analysis results are shown in Figure 3.4. As G_T varies, the following observations can be deduced from Figures 3.4(a) and 3.4(b):

1. $0 < G_T < 0.320114$ similar to $1.715645 < G_T < 18.097355$: situation as in Figure 3.2(a), a unique equilibrium which is G.A.S. (*stable regime*).

2. $0.320114 < G_T < 1.715645$: situation as in Figure 3.2(b), there is a unique equilibrium which is unstable and a stable limit cycle (*oscillatory regime*).

3. $18.097355 < G_T < 19.679276$: situation as in Figure 3.2(e), three equilibrium points; unstable, a saddle point and one L.A.S.

4. $19.679276 < G_T$: situation as in Figure 3.2(d), two L.A.S equilibria and a saddle point (*bistable regime*).

a two-parameter bifurcation diagram was obtained by considering GEF concentration and Rho constant activation parameter defined by k_1. This defines a region of the plane where the model exhibit different dynamics as shown in Figure 3.4(c). The following regions are defined:

1. The red region in Figure 3.4(c) is characterised by unstable steady state (node or spiral). The steady state is unique and therefore there exits a stable periodic obit (limit cycle). This region corresponds to red dashed lines in Figures 3.4(a) and 3.4(b).

2. The uncoloured region shown in Figure 3.4(c) is characterised by the steady state which is unique and stable, and therefore globally asymptotically stable.

3. The yellow region in Figure 3.4(c) is characterised by three steady states, two locally asymptotically stable with a saddle. The saddle acts as a switch which determines to which steady states the system converges to. This region is called the *bistable region*.

The results are summarised in Figure 3.4 and the bifurcation parameters listed in Table 3.3. For suitable values of k_1, Model GRM-2 shows similar qualitative

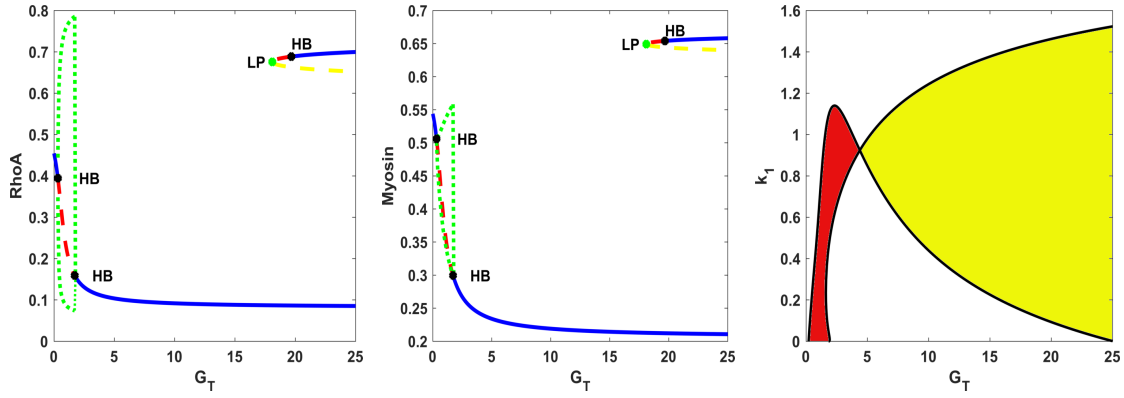

(a) (b) (c)

Figure 3.4: Bifurcation diagrams corresponding to model GRM-2. Figures 3.4(a) and 3.4(b) respectively represent the value of equilibria of Rho and Myosin as G_T varies. Blue represents the steady state values of RhoA and Myosin in the stable region, red dashed line represents their values in the unstable region, yellow dashed line denotes their values at a saddle point while green dotted curve shows the maximum and minimum values of the resulting limit cycle. Hopf bifurcation points are labelled **HB** while fold bifurcations labelled **LP**. Figure 3.4(c) shows two-parameter bifurcation diagram. Red region shows the unstable region characterised by a limit cycle, yellow region represents bistable region while uncoloured region represents the stable region.

dynamics to model GRM-1. Both of them show similar asymptotic behaviour as G_T is varied.

	Bifurcation points			
	HB	**HB**	**HB**	**LP**
G_T	0.320114	1.715645	19.679276	18.097355
Rho	0.394477	0.159106	0.688598	0.675676
Myosin	0.505957	0.299459	0.654055	0.649213

Table 3.3: Hopf bifurcation (**HB**) and Turning point/Limit point (**LP**) parameter values for Model GRM-2.

3.4.3 Bifurcation analysis of model GRM-3

Bifurcation analysis of model GRM-3 was carried out with parameters values shown in Table 3.1. The study is focussed on the analysis of Rho activity dynamics. For model GRM-3, the Rho activity is defined implicitly, by $R(G, M)$ and therefore we shall derive its bifurcation diagram from GEF and Myosin bifurcation diagrams. One-parameter bifurcation diagrams were obtained by taking G_T the bifurcation parameter, they represent the value of equilibria of Rho and Myosin as G_T varies, as shown in Figures 3.5(a) and 3.5(b). As G_T varies, the following can be deduced:

1. $G_T < 0.451118$ similar to $0.537857 < G_T$: situation as in Figure 3.2(a) or Figure 3.2(c), a unique equilibrium state which is G.A.S. (*stable regime*).

2. $0.451118 < G_T < 0.537857$: situation as in Figure 3.2(b), there is a unique equilibrium state which is unstable and therefore existence of a stable limit cycle (*oscillatory regime*).

Two parameter bifurcation diagram was derived from one parameter diagrams by considering G_T and k_1. This defines a region of the plane where the model exhibits different dynamics as shown in Figure 3.5(c). The following regions are defined;

1. The red region is characterised by an unstable steady state (node or spiral). The steady state is unique, and, therefore, there exits a linearly stable periodic obit (limit cycle). This region corresponds to red dotted lines in Figures 3.5(a) and 3.5(b).

2. The uncoloured region is characterised by the steady state which is unique and stable, and, therefore, globally asymptotically stable.

The results are summarised in Figure 3.5 and the bifurcation parameters listed in Table 3.4.

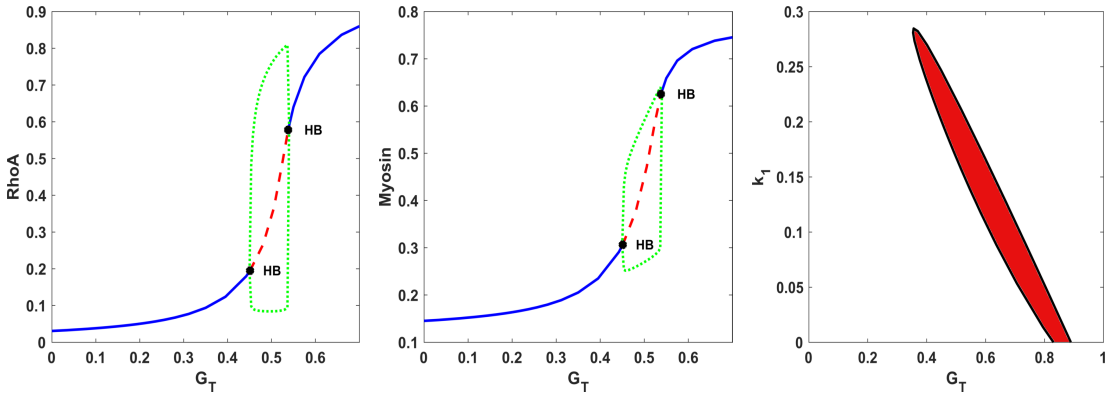

(a) (b) (c)

Figure 3.5: Bifurcation diagrams corresponding to model GRM-3 (2.26). G_T is the bifurcation parameter. In Figure 3.5(a) **HB** are Hopf bifurcation points, red dotted line represents respectively values of Rho and Myosin in the unstable region while blue line represent their values in the stable region. Green dotted line represents the maximum and minimum values of Rho and Myosin in the oscillatory regime. Figure 3.5(c) represents two-parameter bifurcation diagram, bifurcation parameters are G_T and k_1. Red region is the unstable region.

	Bifurcation points	
	HB	**HB**
G_T	0.451118	0.537857
Rho	0.223149	0.315769
Myosin	0.306405	0.625217

Table 3.4: Hopf bifurcation (**HB**) parameter values for model GRM-3.

3.5 Conclusion

In this chapter we performed the mathematical analysis of all the three mathematical models formulated in Chapter 2. The asymptotic behaviour of the models were analysed for different G_T values. The qualitative stability of the steady states of all the three models was analysed using sign pattern analysis, as well as geometric approach where the nullcline configuration was studied with respect to changes on the total GEF concentration, G_T. From these results, we were able to characterise the kind of configuration associated with stable steady states, and also the

configurations that admit periodic solutions. Based on experimental observations that GEF–Rho–Myosin network admit periodic pulses for intermediate expression levels of GEF-H1 (Graessl et al., 2017; Kamps et al., 2019). We also found that all the three models exhibit periodic solutions for some parameter values. In addition, models GRM-1 and GRM-2 have bistable regimes. It has also been shown in other published work (Cusseddu et al., 2018), that models with positive feedback may exhibit bistable dynamics for some parameter values.

To complement the qualitative analysis, we conducted bifurcation analysis of all the models. We investigated the change in model dynamics as G_T varies. The use of this parameter is justified as it has been observed experimental observations (Graessl et al., 2017; Kamps et al., 2019).

To summarise, models GRM-1 and GRM-2 show similar qualitative dynamics for suitable range of parameters; as G_T varies, they exhibit up to three distinct asymptotic behaviours (stable, oscillatory and bistable). On the other hand, model GRM-3 has only two distinct dynamic regimes. The change of dynamic behaviour of model GRM-3 corresponds to the change in distinct states of GEF–Rho–Myosin at different expression levels of GEF-H1 (Graessl et al., 2017; Kamps et al., 2019) and therefore, this model agrees qualitatively to the experimental results. Detailed comparison of mathematical analysis of all the models will be presented in Chapter 6.

In the next chapter, we want to investigate the response of all the models to parameter variations. This will be categorised into two: local sensitivity analysis which enables us to study the effect of parameter variations on oscillatory dynamics. Thereafter we will consider global sensitivity analysis. The findings of this chapter can help identify crucial parameters whose variations affect system dynamics.

Chapter 4

Sensitivity analysis

4.1 Introduction

In Chapter 3, we studied the asymptotic behaviour of the mathematical models, where we observed that the characteristic dynamics of the mathematical models are qualitatively similar to the experimentally observed dynamics of the biological network of GEF, Rho and Myosin interaction. Asymptotic theory does not tell us how these models will respond to variations in parameters, and therefore, due to the uncertainty of input factors associated with measurements, in this chapter we are interested to study how models respond parameter variations. We carry out the analysis in two parts: first, the local sensitivity is used to analyse the dependency of periodic dynamics (period and amplitude) on the parameter variations. This will be used to investigate how the amplitude and period change due to variations in the parameters. The global sensitivity analysis will be performed to analyse the effect of parameter variations to the model output in general.

The general features of a model system are well understood, but problems do arise if there exist some uncertainties in the input parameters. The inputs of a model are not always known with sufficient degree of certainty. This uncertainty in the input may be caused by natural variations, as well as errors or uncertainties associated with measurements (Ekström, 2005). The main reason for sensitivity analysis is to assess the variation in the model output derived from the variation in the input factors. The sensitivity analysis (SA) is defined according to Saltelli et al. (2000);

Ekström (2005) as the "study of how the variation in the model output can be apportioned qualitatively or quantitatively to different sources of variation and how the given model depends upon the information fed into it." The sensitivity analysis aims at determining how sensitive the output is to changes in the input factors. This may include model parameters and/or initial conditions. In this thesis we study the sensitivity of the models with respect to the model parameters, but not to initial conditions.

Sensitivity measure can be computed numerically by finding the partial derivative of the output function to the input factors, and by performing multiple simulations varying input parameters around the base value (nominal parameter), this enables to find the local impact of the input factors to the model output. Therefore, these methods are called *Local sensitivity analysis methods* (Ekström, 2005).

4.2 Local sensitivity analysis

In this section, we provide the local sensitivity analysis of all the models, we use local sensitivity analysis to characterise the limit cycle behaviour of an oscillatory dynamical system in terms of parameter variations, and therefore, it provides a premise to characterise or study amplitude and period sensitivity to parameter variations.

Sensitivity analysis provides a useful tool to investigate effect of variation of parameters and/or initial conditions on model dynamics (Lu and Yue, 2011; Zak et al., 2005). This may include system output and derived functions (Lu and Yue, 2011), which are respectively called *output sensitivity* and *objective sensitivity* (Lu and Yue, 2011; Varma et al., 2005). The local sensitivity analysis is used to investigate the how the model output is affected by parameter variations around base parameter values called the *nominal parameter* values.

The methods commonly used to compute local sensitivities are: *direct differential method (DDM)*, *Green's function method* and *finite difference method* (Lu and Yue, 2011). DDM is the most widely used since it provides a complete information on each sensitivity index as a function of the independent variable (Lu and Yue, 2010). For an oscillating dynamical system, the local sensitivity analysis can be used to

characterise the effect of parameter variation on the amplitude, period, and phase of a limit cycle. So the purpose of this work is to determine the parameter variations and how they affect oscillations in GEF–Rho–Myosin dynamics.

Oscillations are one of the most important non-linear behaviour widely observed in living cells. They are characterised by their amplitudes, phase and period. Areas where oscillatory behaviours are observed include cell division, circadian rhythms and also cell signalling pathways (Goldbeter, 1995; Kruse and Jülicher, 2005; Das et al., 2012). Oscillations can be crucial for biological functions like circadian rhythms (Bagheri et al., 2006), but in some cases they may not have a biological function, but simply reflect the dynamic properties of a system (Hu and Yuan, 2006; Yue et al., 2008). Consider a general ordinary differential equation model given by:

$$\dot{\mathbf{x}}(t) = \mathbf{f}\left(\mathbf{x}(t),\ \mathbf{p}\right), \qquad \mathbf{x}(t_0) = \mathbf{x}_0, \tag{4.1}$$

where $\mathbf{x} \in \mathbb{R}^{m_s}$ is the vector of dependent variables and $\mathbf{p} \in \mathbb{R}^{m_p}$ are the parameters of the model. The model depends on the variables themselves and the parameters.

If the solution of Equation (4.1) exists, then the sensitivity matrix is defined by:

$$\mathbf{S}(t) = \left(\frac{\partial \mathbf{x}}{\partial \mathbf{p}}\right)_{(\mathbf{x}(t,\mathbf{p}_0),\mathbf{p}_0)} = \{s_{ij}\}, \tag{4.2}$$

where $\mathbf{p}_0$ defines the nominal parameter values. To find the sensitivity matrix (4.2), differentiate Equation (4.1) with respect to parameter, $\mathbf{p}$, which gives;

$$\begin{aligned} \frac{\partial \dot{\mathbf{x}}}{\partial \mathbf{p}} &= \frac{\partial}{\partial \mathbf{p}}\left(\mathbf{f}(\mathbf{x},\mathbf{p})\right), \\ \frac{\partial}{\partial t}\underbrace{\left(\frac{\partial \mathbf{x}}{\partial \mathbf{p}}\right)}_{\mathbf{S}} &= \underbrace{\frac{\partial \mathbf{f}}{\partial \mathbf{x}}}_{A(t,\mathbf{p}_0)} \cdot \underbrace{\frac{\partial \mathbf{x}}{\partial \mathbf{p}}}_{\mathbf{S}} + \underbrace{\frac{\partial \mathbf{f}}{\partial \mathbf{p}}}_{B(t,\mathbf{p}_0)}, \end{aligned} \tag{4.3}$$

which can be written more compactly as

$$\dot{\mathbf{S}} = A(t,\mathbf{p}_0)\mathbf{S} + B(t,\mathbf{p}_0), \tag{4.4}$$

$$\mathbf{S}(t_0,\mathbf{p}_0) = \mathbf{S}_0.$$

Equations (4.1) and (4.4) can be solved simultaneously to obtain the sensitivity matrix $\mathbf{S}$ given initial conditions $\mathbf{x}(t_0) = \mathbf{x_0}$, nominal parameter values $\mathbf{p}(t_0) = \mathbf{p_0}$, and initial sensitivity, $\mathbf{S}(t_0) = \mathbf{S}_0$. Initial sensitivity to the initial conditions is taken

as 1 (Zak et al., 2005). In this thesis we only consider sensitivity to parameters, thus $\mathbf{S}_0 = [0]$. For an ODE system with convergent steady state, the direct differential method (DDM) solution is also convergent, which can be used to interpret the sensitivity analysis results in the case stable steady states. The aim of this work is to characterise the limit cycle of the ODE system (4.1) including amplitude and period in terms of the dependency on the parameters.

For a system of differential equations that is periodic in time with period τ, we have:

$$\mathbf{x}(t+\tau) = \mathbf{x}(t). \tag{4.5}$$

From (4.5), it is possible to express each of the state variables of $\mathbf{x}(t)$ expanded in Fourier series, (Tomovic and Vukobratovic, 1972; Larter, 1983; Zak et al., 2005; Lu and Yue, 2010) and we obtain:

$$x_i(t) = \sum_{n=0}^{\infty} \left[a_{n_i} \cos \frac{2n\pi t}{\tau} + b_{n_i} \sin \frac{2n\pi t}{\tau} \right]. \tag{4.6}$$

Fourier coefficients a_{n_i} and b_{n_i} are functions of parameters. We assume that the period of oscillation is dependent on at least one parameter and its sensitivity, $\mathbf{S}_\tau$ may be defined as:

$$\mathbf{S}_\tau = \left[\frac{\partial \tau}{\partial p_1}, \cdots, \frac{\partial \tau}{\partial p_{m_p}} \right]. \tag{4.7}$$

$\mathbf{S}_\tau$ contains individual sensitivity parameters and is a vector independent of time. From Equation (4.6) and using the fact that τ depends on $\mathbf{p}$, the sensitivity matrix may be defined as (details of derivation can be found in Appendix C):

$$\mathbf{S} = -\frac{t}{\tau} \mathbf{f}\, \mathbf{S}_\tau + \mathbf{S}_c. \tag{4.8}$$

$\mathbf{S}_c$ represents $\left[\frac{\partial x_i}{\partial p_j}\right]_\tau$ evaluated at a constant period, it is periodic in time and is an $m_s \times m_p$ matrix called *Cleaned-out sensitivity matrix* (Tomovic and Vukobratovic, 1972). It captures how parameter variations affect the shape of trajectory when period is constant (Zak et al., 2005; Lu and Yue, 2010, 2011).

From Equation (4.8) when $\mathbf{f} \neq 0$ and $\mathbf{S}_\tau \neq 0$, then the first term will grow unbounded as time increases and it will become the dominant term, and therefore, at higher time points, we have

$$\mathbf{S} \approx -\frac{t}{\tau} \mathbf{f}\, \mathbf{S}_\tau.$$

We thereafter make use of singular value decomposition method (SVD) as described in (Zak et al., 2005; Lu and Yue, 2011) to calculate period sensitivities. The description of SVD method and how it is applied to the state sensitivity matrix is described in the Appendix C. Applying SVD method to the state sensitivity matrix (4.8) and using Theorem C.1.2, we obtain the period sensitivity given by the formula

$$\mathbf{S}_\tau \approx -\frac{\tau}{\phi^2\, t}\mathbf{f}^T\, \tilde{\mathbf{S}}_1, \tag{4.9}$$

where the term $\tilde{\mathbf{S}}_1 = \sigma_1\, \mathbf{u}_1\, \mathbf{v}_1^T$ is the largest SVD term of the state sensitivity matrix $\mathbf{S}$. The cleaned-out sensitivity can be approximated using the sum of all the remaining SVD terms, i.e.

$$\mathbf{S}_c \approx \sum_{i=2}^{r} \tilde{\mathbf{S}}_i, \quad \text{where} \quad \tilde{\mathbf{S}}_i = \sigma_i\, \mathbf{u}_i\, \mathbf{v}_i^T. \tag{4.10}$$

To obtain amplitude sensitivity, we first define amplitude as

$$A_{mi} = x_i(t_{\max_i}) - x_i(t_{\min_i}), \tag{4.11}$$

where $t_{\max_i}$ and $t_{\min_i}$ are the time points where the local maximum and minimum occurs within the period. Amplitude sensitivity can be defined from Equation (4.11). Using the cleaned-out sensitivity, we can use the fact that at the local extrema of x_i, $f_i = 0$, and therefore, from Equation (4.8) we have that $\mathbf{S}_i = \mathbf{S}_{ci}$ and thus amplitude sensitivity is calculated using the formula

$$\mathbf{S}_{A_{mi}} = \mathbf{S}_{ci}(t_{\max_i}) - \mathbf{S}_{ci}(t_{\min_i}). \tag{4.12}$$

4.2.1 Local sensitivity results for models GRM-1, GRM-2 and GRM-3

The local sensitivity results for all the models are presented. These include the state sensitivity matrices, both in the stable and oscillatory regimes, followed by period and amplitude sensitivity results. The sensitivity matrix $\mathbf{S}$ is obtained by DDM approach to obtain the time profile of its components. $\mathbf{S}$ is then decomposed by SVD at each time point to obtain all the singular values and their corresponding SVD terms. In the models GRM-1, GRM-2 and GRM-3, the sensitivity matrix has rank $r = 2$.

Local sensitivity results for model GRM-1

Model GRM-1(2.11) is solved simultaneously with the corresponding sensitivity equation defined by Equation (4.4). We use parameter values $G_T = 1$ and $G_T = 0.5$ for oscillatory and stable regimes, respectively. The other parameter values are fixed as shown in Table 3.1. Results for simulations are shown in Figures 4.1 and 4.2.

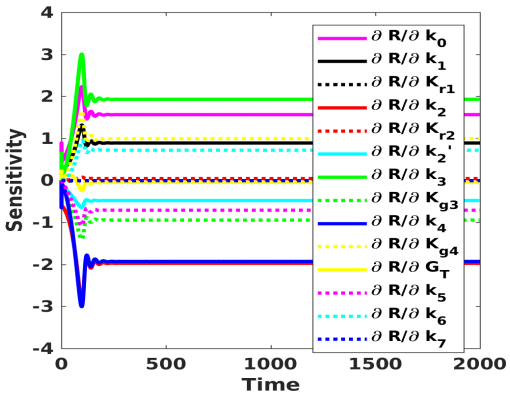

(a) Sensitivity of R to parameters in the stable region

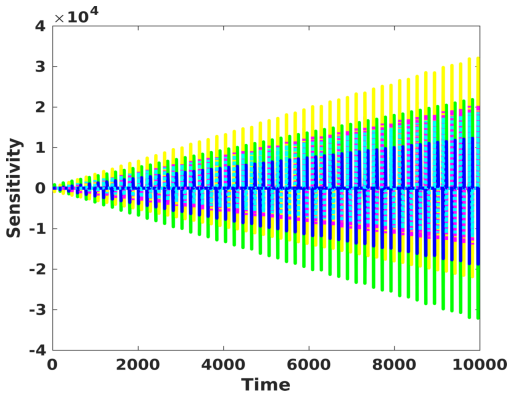

(b) Sensitivity of R to parameters in the oscillatory regime

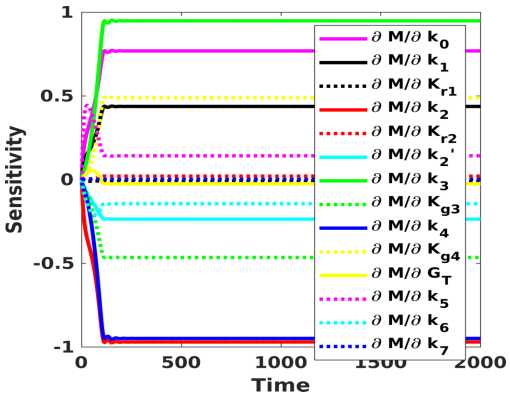

(c) Sensitivity of M to parameters in the stable region

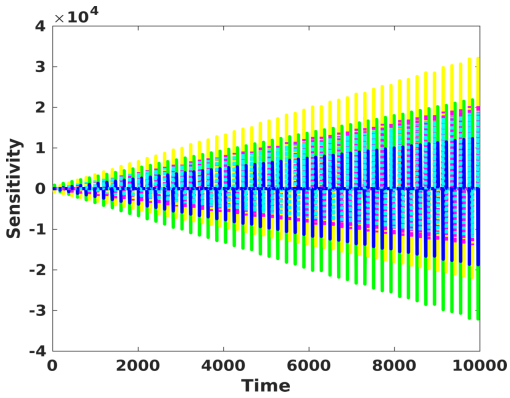

(d) Sensitivity of M to parameters in the oscillatory region

Figure 4.1: Local sensitivity profile for model GRM-1, the parameter value for G_T is selected to have either steady state or oscillatory region, other parameters are fixed as in the Table 3.1. The sensitivity matrix is bounded in the stable regime, but unbounded in the case of oscillatory dynamics.

The sensitivity profiles behaves differently in the two regimes (stable and oscillatory). In the oscillatory region the sensitivity matrix is unbounded as shown in Figures 4.1(b) and 4.1(d). This unbounded behaviour is similar to that illustrated by Equation (4.8). It is also shown (Lu and Yue, 2011; Zak et al., 2005) that the

sensitivity values for limit cycle oscillatory systems are periodic and unbounded. Since in the oscillatory regime, the sensitivity matrix is unbounded, SVD method was used to determine the period and amplitude sensitivities.

First the parameter sensitivities in the case of stable regime are shown in Figure 4.2. Since we are interested in ranking the parameters depending on their respective sensitivity indices, we normalise their sensitivity values between $[-1, 1]$. It can be shown that the most sensitive parameters are: k_2 and k_4 which have a negative effect to the output, together with k_3 which has a positive effect. This means that infinitesimal increase in k_3 increases the steady state value while infinitesimal increase in either k_2 or k_4 decreases the steady state value. The parameters K_{r1}, K_{r2}, G_T and k_7 have almost no influence or very little influence on the steady state values of both Rho and Myosin.

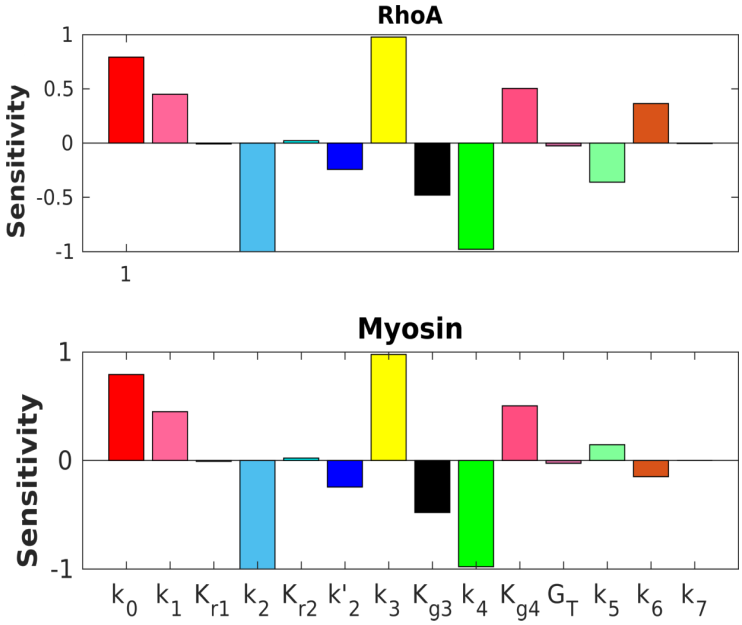

Figure 4.2: Local sensitivity results in the stable region and at time, $t = 2000$ for model GRM-1.

Figure 4.3 shows the correlations between parameter sensitivity to Rho and Myosin steady state values. Most values are distributed along the diagonal, thus these parameters affect both Rho and Myosin steady state values in the same way. Parameters k_5 and k_6 lie off the diagonal and hence their effects on Rho and Myosin steady states are different. k_5 has a positive effect to the Rho steady state value, but has a negative influence on Myosin steady state, while k_6 has an opposing influence with reference to k_5.

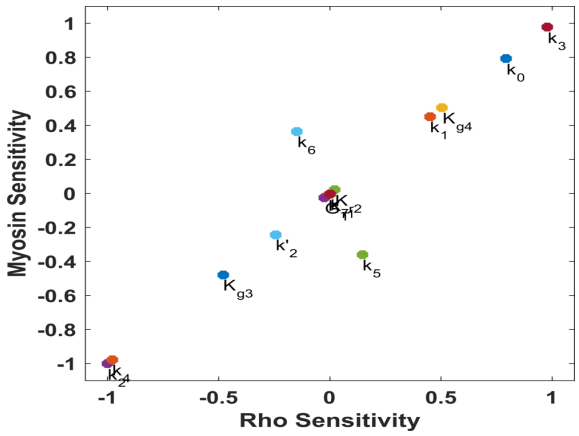

Figure 4.3: Correlations between parameters sensitivity to Rho and Myosin steady state values.

Period sensitivity results

SVD method was applied to the state sensitivity matrix in the oscillatory regime, and the period sensitivity profile obtained. The time series of period sensitivity is convergent and therefore, at large time points, we get the period sensitivity to parameters as shown in Figure 4.4. The period sensitivity is bounded and converges as time increases, as shown in Figure 4.4(a). At higher time points, fixed values are obtained from where we can extract the period sensitivity as shown in Figure 4.4(b). It is shown that the period is highly sensitive to k_3 and k_4. An increase in k_3 increases

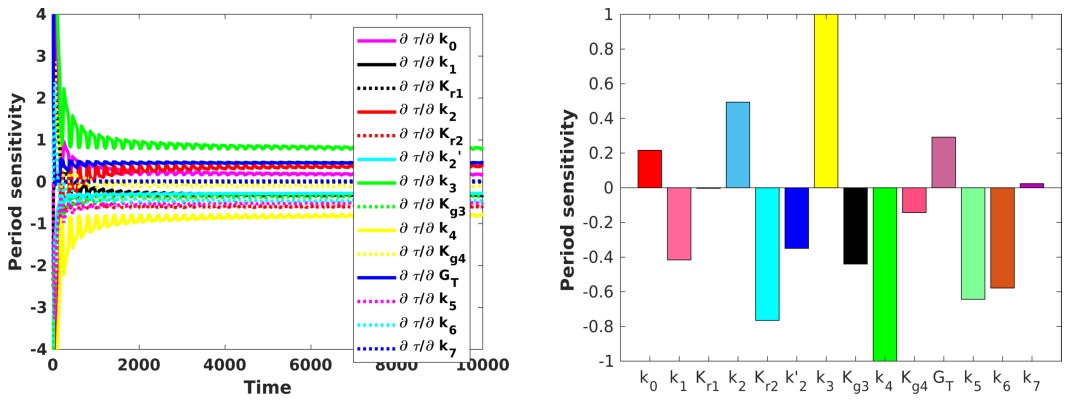

(a) (b)

Figure 4.4: Period sensitivity shown for model GRM-1

the period of oscillation while k_4 has the opposite effect. The period is least affected by K_{r1} and k_7. The oscillatory dynamics are highly sensitive to G_T than the steady state values of Rho and Myosin.

Cleaned-out and amplitude sensitivities

The period sensitivity is obtained using the largest singular value term, and then the cleaned-out sensitivity obtained using Equation (4.10), which is used to calculate the amplitude sensitivity from Equation (4.12). The cleaned-out sensitivity is bounded and periodic, while its corresponding state sensitivity is unbounded. In Figure 4.5(a), we show the plot of the cleaned-out sensitivity for only two parameters to illustrate its behaviour (*periodic and bounded*).

The results for amplitude sensitivity are shown in Figure 4.5(b). Several parameters affect the Rho and Myosin amplitudes differently. For example the Rho amplitude is highly sensitive to k_0 while Myosin amplitude is high sensitive to K_{r2}, k_3 and k_4. The parameter k_3 has a positive influence on Myosin amplitude while it has a negative influence on Rho amplitude.

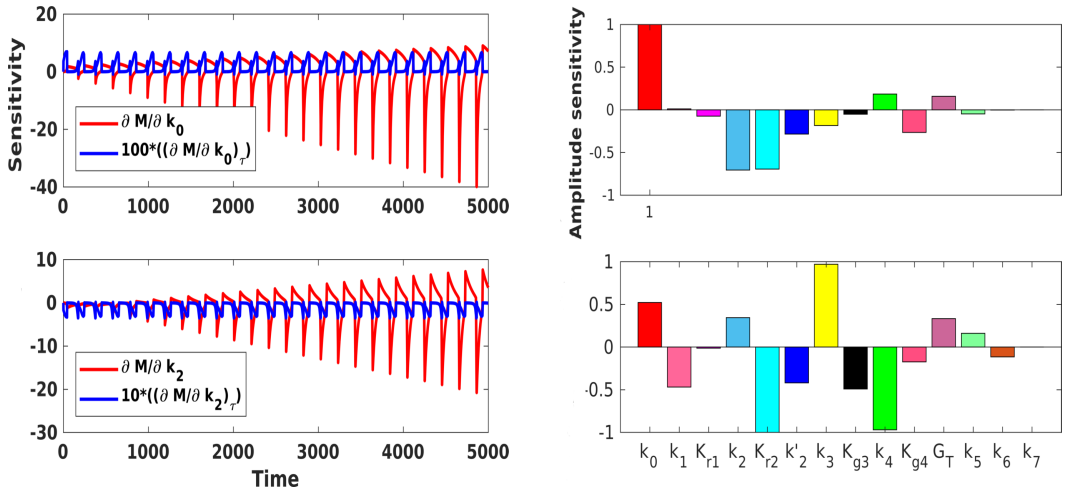

(a) (b)

Figure 4.5: Figure 4.5(a) shows cleaned-out sensitivity and the corresponding state sensitivity while 4.5(b) shows Rho and Myosin amplitude sensitivities. The cleaned-out sensitivites are periodic and bounded while their corresponding state sensitivities are unbounded.

For a model system, the sensitivity information taken from different features may be different. Figure 4.6 shows the comparison of parameters between Rho and Myosin amplitude sensitivities, and also between period and amplitude sensitivities.

The parameters are not listed alongside diagonal meaning the sensitivity rankings are different when interpreted using different features. From Figure 4.6(a), some

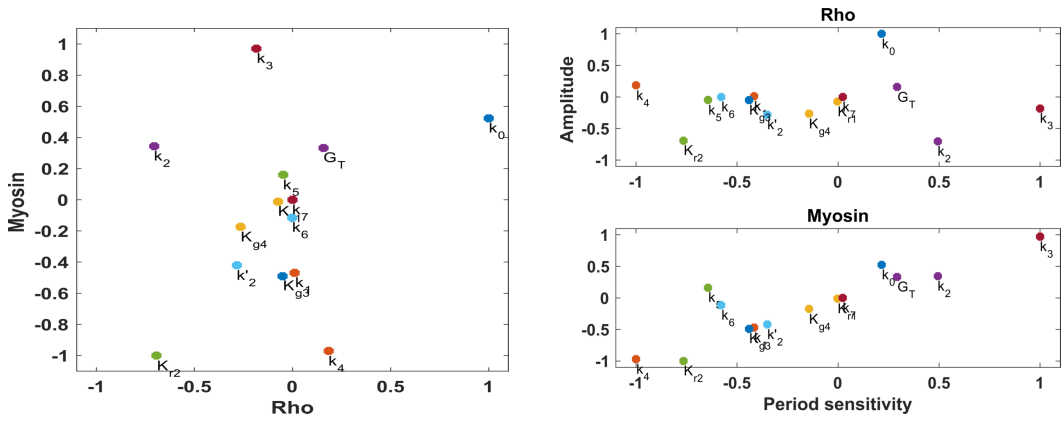

(a) (b)

Figure 4.6: Figure 4.6(a) shows correlations between Rho amplitude sensitivity and Myosin amplitude sensitivity, while 4.6(b) shows correlations between period sensitivity and Rho and amplitude sensitivities.

parameters have larger influence on Rho amplitude than Myosin amplitude, such as k_0; some have larger influence on Myosin amplitude, such as k_3 and k_4 and others such as K_{r2} have larger influence on both Rho and Myosin amplitude. From Figure 4.6(b), some parameters have lager influence on Rho amplitude than period, others have more influence on period while other parameters influence Rho amplitude and period in the same way. For example, the parameter, K_{r2} has larger influence on both Rho amplitude and period; some parameters such as k_0 and k_2 have larger influence on Rho amplitude while some such as k_3, k_4 and k_5 have larger influence on the period than Rho amplitude. Considering Myosin amplitude and period sensitivities, most parameters lie alongside the main diagonal and therefore the ranking of most parameters is fairly similar. Other parameters such as k_5 and k_6 have larger influence on the period, than Myosin amplitude.

For oscillatory dynamics, the identification of crucial parameters may depend on the feature used. Therefore, it is crucial that various features of an oscillator must be investigated in order to understand the system behaviour. The sensitivity to period is taken with more credit (Lu and Yue, 2010).

Local sensitivity results for model GRM-2

The local sensitivity analytical results for model GRM-2 are similar to those for model GRM-1. Equation (2.16) is solved simultaneously with the corresponding

sensitivity equation defined by Equation (4.4). The results are presented in Figures 4.7 and 4.8 which show local sensitivity results for model GRM-2 around the nominal parameter values. The parameters $G_T = 0.4$ and $G_T = 0.25$ were used for oscillatory and stable regimes respectively. The sensitivity profiles behave differently between the two regimes (*stable and oscillatory*) as also shown for model GRM-1. In the oscillatory regime, the sensitivity matrix is unbounded, and grows linearly with time, but it is bounded in the stable regime.

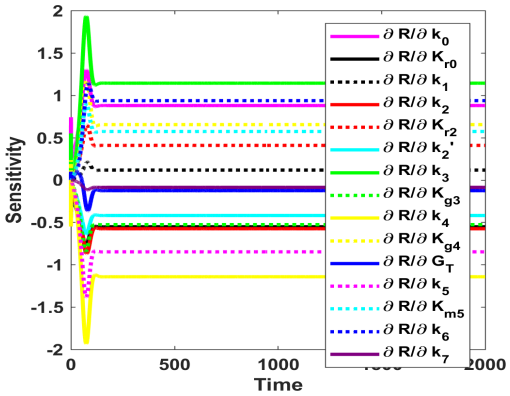

(a) Sensitivity of R to paraneters in the stable region

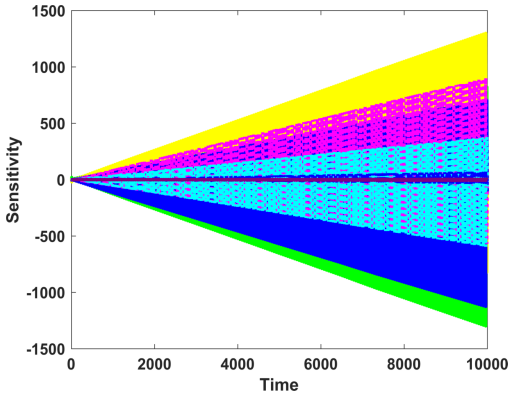

(b) Sensitivity of R to paraneters in the oscillatory regime

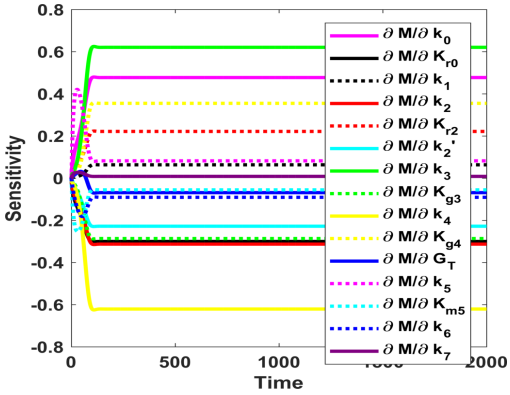

(c) Sensitivity of M to paraneters in the stable region

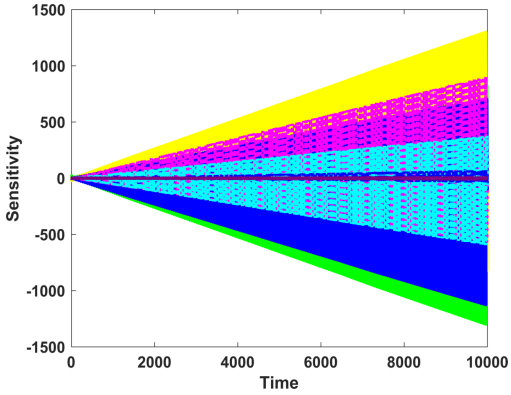

(d) Sensitivity of M to paraneters in the oscillatory region

Figure 4.7: Local sensitivity profile for model GRM-2, the parameter value for G_T is selected to have either steady state or oscillatory region, other parameters are fixed as shown in Table 3.1. The sensitivity matrix is bounded in the stable regime, but unbounded in the oscillatory regime.

In the stable regime, the steady state sensitivity to parameters is obtained and results shown in Figure 4.8. The steady state sensitivity is calculated from the results shown in Figures 4.7(a) and 4.7(c). The sensitivity values are normalised for

easier comparison. From Figure 4.8 both Rho and Myosin steady state values are highly sensitive to parameters k_3, k_4 and k_0. Some parameters have an opposite effect to Rho and Myosin steady states, for example k_5, K_{m5} and k_6. Other parameters like k_1, G_T and k_7 have very little influence on both steady state values of Rho and Myosin.

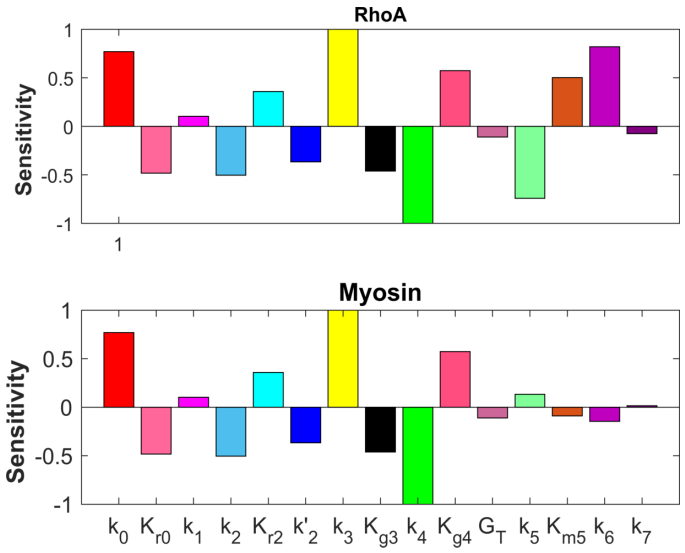

Figure 4.8: Local sensitivity results in the stable region and at time, $t = 2000$ for model GRM-2. These results are calculated from the results shown in Figures 4.7(a) and 4.7(c).

Figure 4.9 shows the correlations between parameter sensitivity to Rho and Myosin values. Most values are distributed along the diagonal, thus these parameters affect both Rho and Myosin in the same way. Parameters k_5, K_{m5} and k_6 lie off the diagonal and hence their effect on Rho and Myosin steady state values are different.

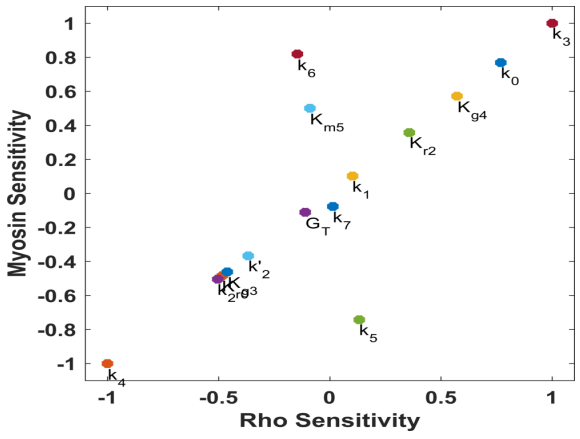

Figure 4.9: Correlations between parameters sensitivity to Rho and Myosin.

Period sensitivity

The singular value decomposition was applied to the state sensitivity matrix in the oscillatory regime. This enables the determination of period sensitivity from Equation (4.9). The period sensitivity time series is convergent, and therefore at higher time values, the sensitivity of period to parameters is calculated and results are as shown in Figure 4.10. The period is highly sensitive to k_3, k_4, G_T and k_5. An infinitesimal increase in k_3 increases the period of oscillation while k_4 has the opposite effect. Similarly an infinitesimal increase in G_T increases the period. The parameter G_T has little effect on the steady state values of Rho and Myosin, but it greatly influences its oscillatory behaviour. k_7 has very little influence on the period.

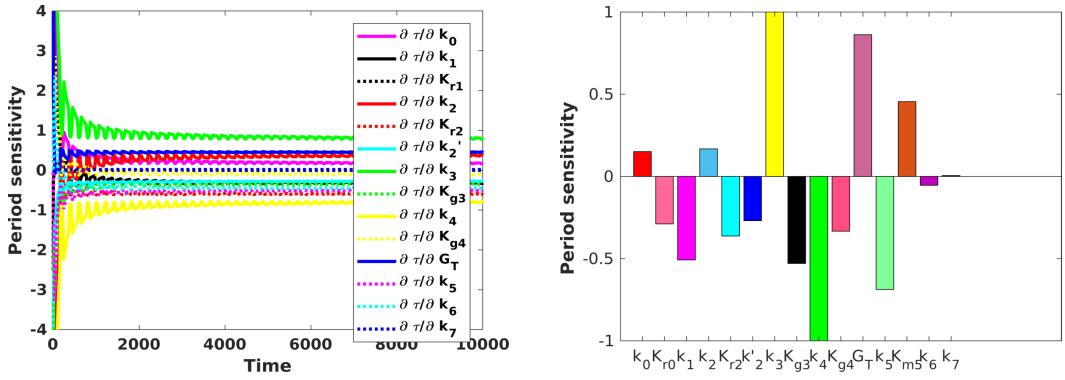

(a) (b)

Figure 4.10: Period sensitivity results for model GRM-2

Cleaned-out and amplitude sensitivities

Similarly to model GRM-1, cleaned-out sensitivity is obtained and then the sensitivity amplitude to parameters calculated. The cleaned-out sensitivity is bounded and periodic, while its corresponding state sensitivity is unbounded. Figure 4.11(a) shows the cleaned-out sensitivity for only two parameters to illustrate the behaviour. Figure 4.11(b) shows sensitivity of amplitude to parameters. Similarly to model GRM-1, several parameters affect the Rho and Myosin amplitude differently. Figure 4.12 shows the correlation of parameters between Rho and Myosin amplitude sensitivities, and also between period sensitivity and amplitudes sensitivities.

From Figure 4.12(a), we observe that some parameters such as k_0 and K_{r0} have larger

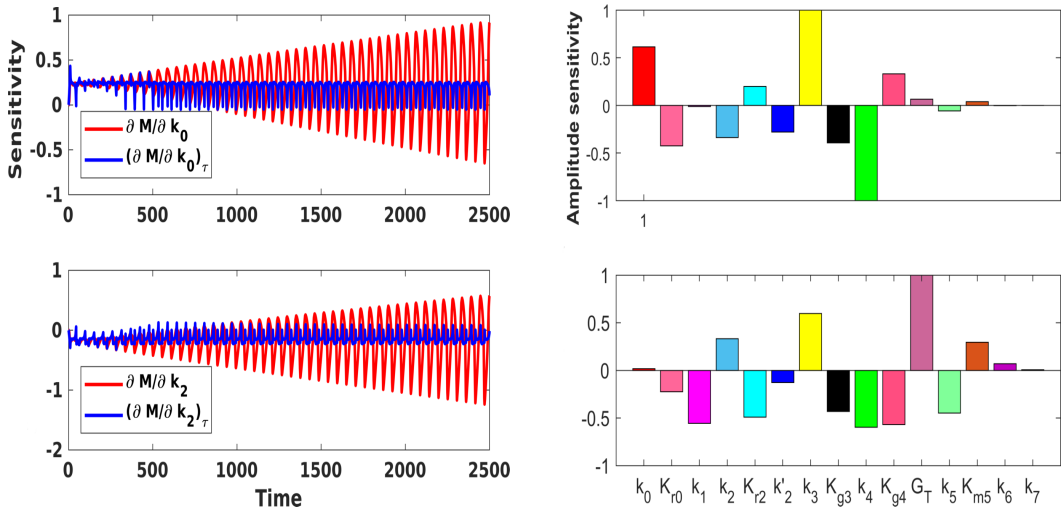

(a) (b)

Figure 4.11: Figure 4.11(a) shows cleaned-out sensitivity and the corresponding state sensitivity while 4.11(b) shows Rho and Myosin amplitude sensitivities.

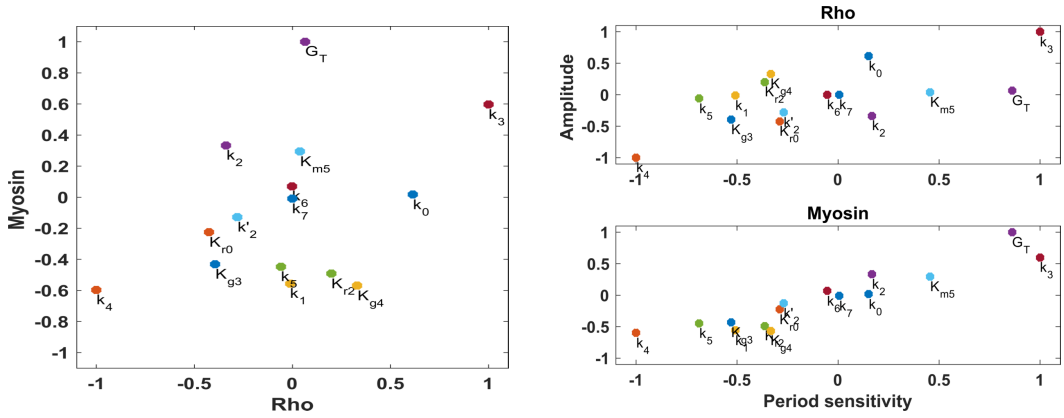

(a) (b)

Figure 4.12: Figure 4.12(a) shows correlations between Rho amplitude sensitivity and Myosin amplitude sensitivity, while 4.12(b) shows correlations between period sensitivity and Rho and amplitude sensitivities.

influence on Rho amplitude than Myosin amplitude; some such as G_T have larger influence on Myosin amplitude; while others such as k_3 and k_4 have larger influence on both Rho and Myosin amplitudes. In Figure 4.12(b), parameters k_3 and k_4 have larger influence on both Rho amplitude and period; other parameters such as k_0 and K_{r0} have larger influence on Rho amplitude while some such as G_T and k_5 have larger influence on the period than Rho amplitude. Comparing Myosin amplitude and period sensitivity, most parameters lie alongside the main diagonal and therefore

the ranking of most parameters is fairly similar when considering Myosin amplitude and period; other parameters such as k_5 has larger influence on the period, than Myosin amplitude, while K_{g4} has larger influence on Myosin amplitude than period.

Local sensitivity results for model GRM-3

The method for model GRM-3 analysis follows similar procedure to that of models GRM-1 and GRM-2. Equation (2.26) is solved simultaneously with the corresponding sensitivity equation and results are presented in Figures 4.13 and 4.14. They show local sensitivity results for model GRM-3 around the nominal parameter values. Parameters $G_T = 0.4595$ and $G_T = 0.2$ were used for oscillatory and stable regimes respectively. The behaviour of sensitivity time series is similar to that of models GRM-1 and GRM-2.

In the stable regime, the steady state sensitivity to parameters is calculated from the results shown in Figures 4.7(a) and 4.13(c) and results shown in Figure 4.14. The sensitivity values are normalised. Both GEF and Myosin steady state values are highly sensitive to parameters k_3, k_4 and k_0. Some parameters have an opposite effect to GEF and Myosin steady states, for example k_5, K_{m5}, k_6 and k_7. Other parameters like k_1, G_T and k_7 have very little effect on both steady state values. Figure 4.15 shows the correlations between parameter sensitivity to GEF and Myosin values. It is observed that most parameters influence GEF and Myosin differently. Some parameters, such as k_2, k_6 and k_1 have larger influence on both GEF and Myosin steady state values; others such as G_T have larger influence on GEF steady state value while K_{m6} and k_7 have larger influence on Myosin steady state value.

Period sensitivity

The sensitivity of period to parameters is obtained by using the SVD method on the state sensitivity matrix in the oscillatory regime. The period sensitivity time series is convergent, and therefore at higher time values, the sensitivity of period to parameters is calculated and results are as shown in Figure 4.16. The period is highly sensitive to k_2, k_1 and k_0 in the decreasing order of their influence. The effect of parameter G_T is more pronounced for the period than on the steady state values. K_{r0} and K_{m5} have very little influence on the period.

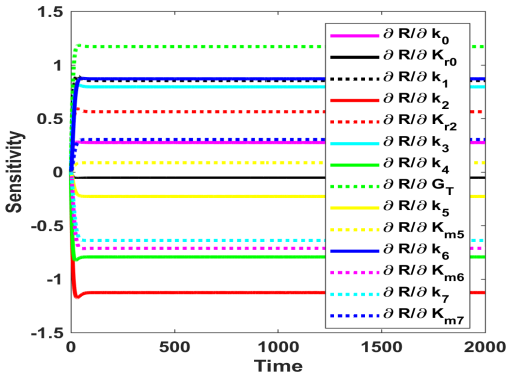

(a) Sensitivity of G to parameters in the stable region

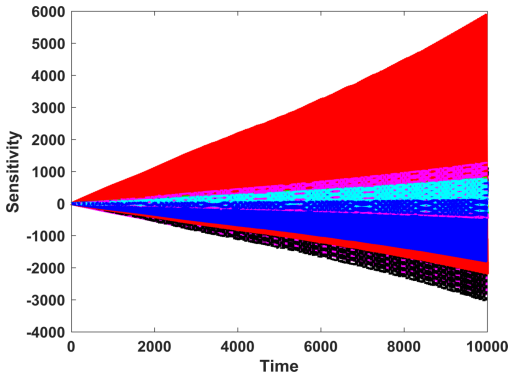

(b) Sensitivity of G to parameters in the oscillatory regime

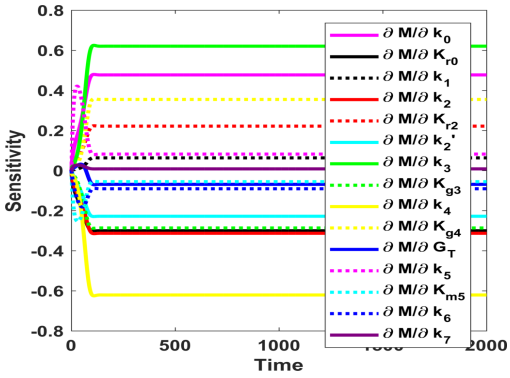

(c) Sensitivity of M to parameters in the stable region

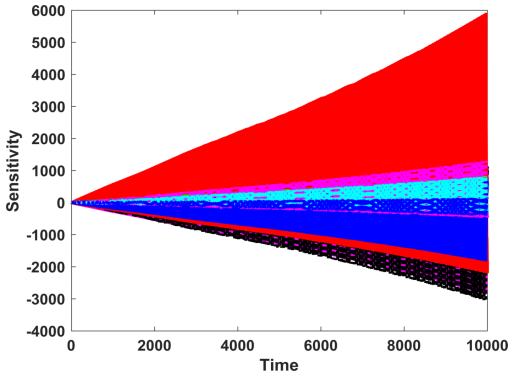

(d) Sensitivity of M to parameters in the oscillatory region

Figure 4.13: Local sensitivity profile for model GRM-3, the parameter value for G_T is selected to have either steady state or oscillatory region, other parameters are fixed as in the Table 3.1. The sensitivity matrix is bounded in the stable regime, but unbounded in the case of oscillatory dynamics.

Cleaned-out and amplitude sensitivities

Similarly to models GRM-1 and GRM-2, cleaned-out sensitivity is obtained and then the amplitude sensitivity to parameters calculated. The cleaned-out sensitivity is bounded and periodic, while its corresponding state sensitivity is unbounded. Figure 4.17(a) shows the cleaned-out sensitivity for only two parameters, while amplitude sensitivity results are shown in Figure 4.11(b). Both GEF and Myosin amplitudes are highly sensitive to G_T, and thus it affects more the oscillatory dynamics than the steady state values. Except the parameters G_T, k_0 and k_2, the rest of the parameters have very little influence on the period and some of them have opposing effect on the amplitudes.

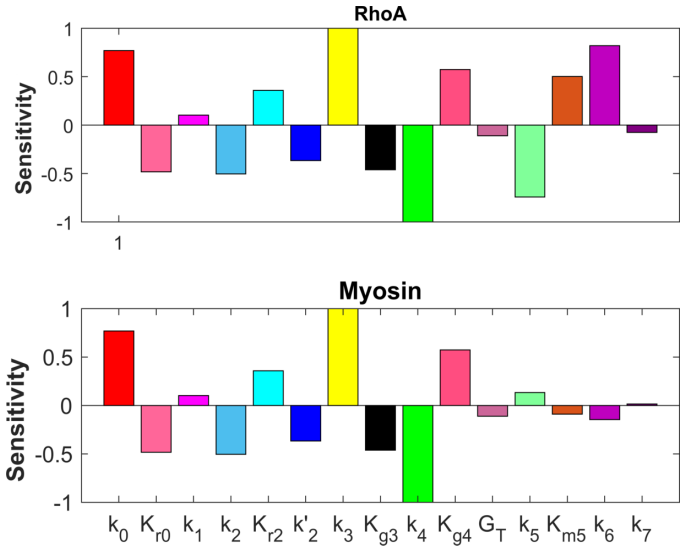

Figure 4.14: Local sensitivity results in the stable region and at time, $t = 2000$ for model GRM-2.

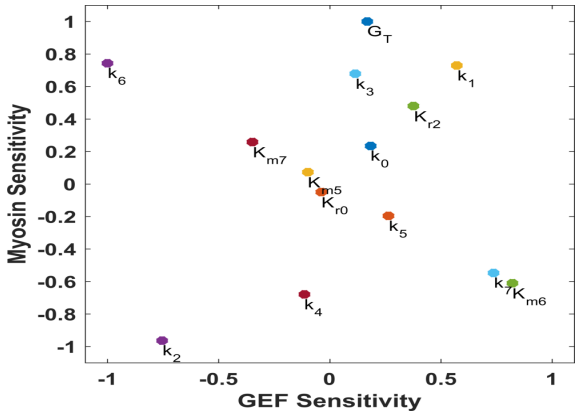

Figure 4.15: Correlations between parameter sensitivity to GEF and Myosin.

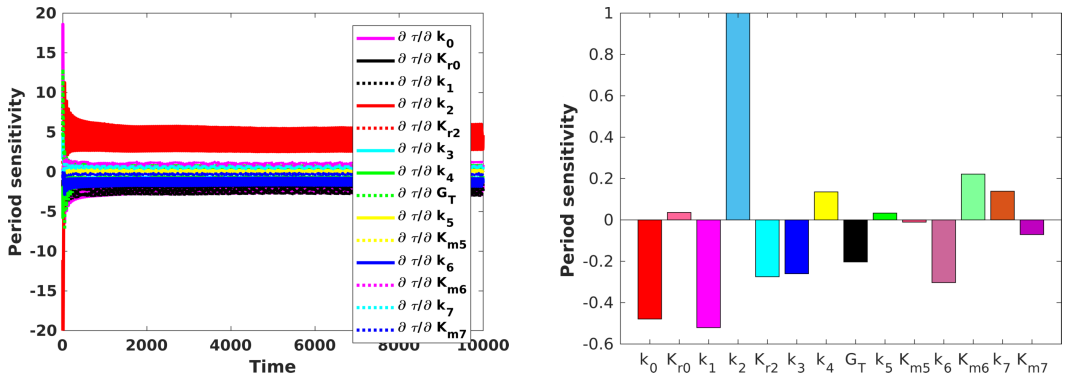

(a) (b)

Figure 4.16: Period sensitivity shown for model GRM-3.

Figure 4.18 shows the correlation of parameters between Rho and Myosin amplitude sensitivities, and also between period sensitivity and amplitudes sensitivities. In

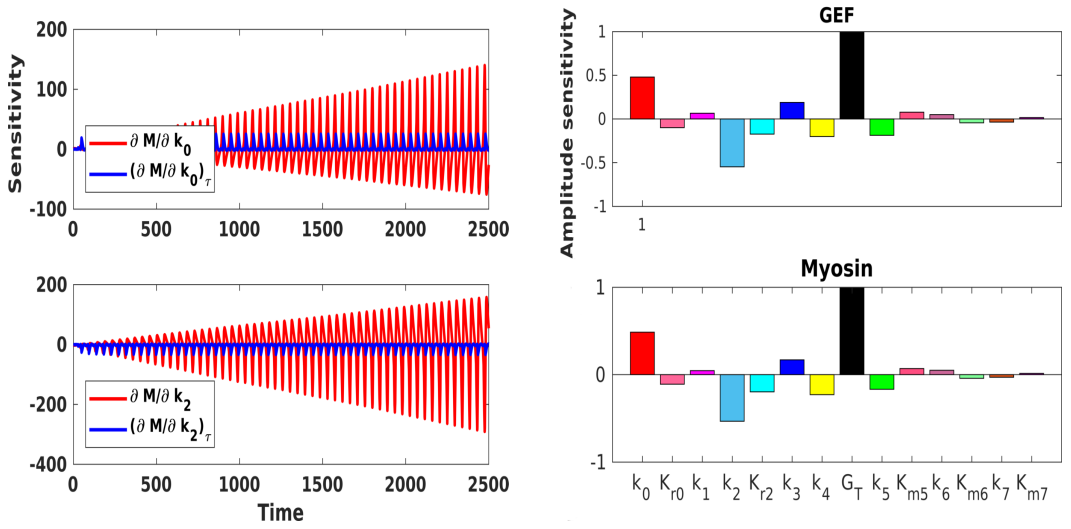

(a) (b)

Figure 4.17: Figure 4.17(a) shows cleaned-out sensitivity and the corresponding state sensitivity while 4.17(b) shows GEF and Myosin amplitude sensitivities.

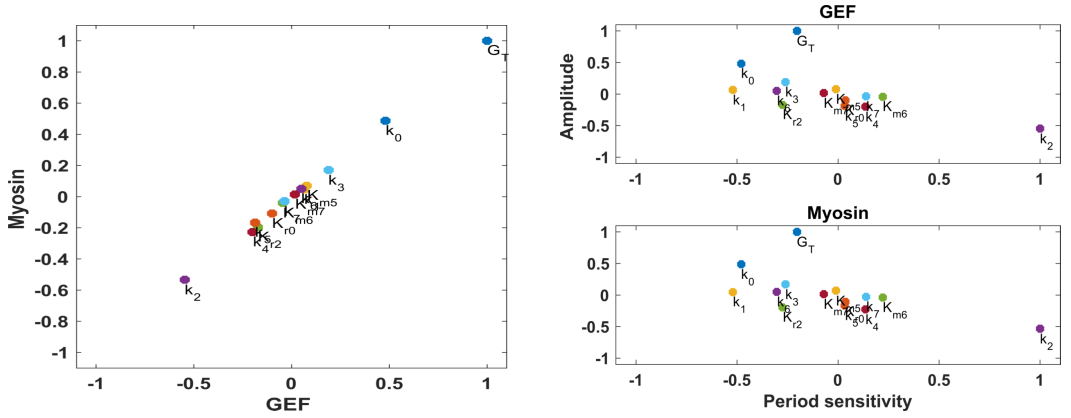

(a) (b)

Figure 4.18: Figure 4.18(a) shows correlations between Rho amplitude sensitivity and Myosin amplitude sensitivity, while 4.18(b) shows correlations between period sensitivity and Rho and amplitude sensitivities.

Figure 4.18(a), parameters lie alongside the diagonal and therefore, parameters affect GEF and Myosin amplitudes in the same way. In Figure 4.18(b), the parameters k_2, k_0 and k_4 have larger influence on both GEF amplitude and period; others such as G_T have larger influence on GEF amplitude while some such as k_1T and k_6 have larger influence on the period than Rho amplitude. The same effect is observed when comparing period and Myosin amplitude.

The local sensitivity analysis provides the influence of each parameter around the

selected nominal parameter value, and therefore its effect is local. This method is very useful to analyse the influence of different parameters on the limit cycle dynamics. We have seen that different features of an oscillatory dynamics may provide different raking of parameters. Comparison of local sensitivity for all the models will be provided in Chapter 6. Local sensitivity analysis is combined with global sensitivity analysis which is presented in the next section.

4.3 Global sensitivity analysis

To find out which input factors are more important in determining the uncertainty in the output of a model, the local techniques are not suitable in this case and therefore the *global sensitivity analysis methods* are recommended. Most of these methods are implemented using Monte Carlo simulations, and therefore, are called *Sampling-based methods* (Ekström, 2005).

For sampling-based methods, it is recommended that the starting point is to first examine the scatter plots. With these plots, non-linearities, non-monotonicity and correlation between input factors may be determined.

(i) For linear relationships between the input factor and the output, the following methods would perform well:

- Pearson product moment correlation coefficient (CC),
- Partial Correlation Coefficients (PCC),
- Standardized Regression Coefficients (SRC).

(ii) For non-linear but monotonic relationships, the following methods perform well:

- Spearman Rank Correlation Coefficient (RCC),
- Partial Rank Correlation Coefficients (PRCC),
- Standardized Rank Regression Coefficients (SRRC).

(iii) For non-linear non-monotonic relationships, the recommended methods are based on decomposition of variance, and the examples include:

- Sobol' method,

- Jansen's alternative,
- Fourier Amplitude Sensitivity Test (FAST),
- Extended Fourier Amplitude Sensitivity Test (eFAST),

The global sensitivity analysis is conducted using the Extended Fourier amplitude test (eFAST) technique. eFAST belongs to the class of variance based methods. Since the models we consider show change of dynamics when a parameter changes, we expect non-monotonic behaviour. That is why we resort to the use of variance based methods, in particular the eFAST method. This method has proven to be one of the most reliable methods among the variance-based techniques (Saltelli et al., 2004; Marino et al., 2008; Gao et al., 2016), although it is computationally expensive (Tarantola et al., 2006; Ratto et al., 2007).

Sampling-based methods for sensitivity analysis are computed on the basis of mapping between the input-output relationship generated by the Monte Carlo simulation and they evaluate the effect of a factor X_i while other factors are also allowed to vary (Ekström, 2005). Monte Carlo simulation is based on performing many model simulations where the model inputs are selected probabilistically. The results obtained may be used in testing model variations with respect to variation in the parameters (Marino et al., 2008). Variance-based methods quantify the amount of variance that each input factor X_i contributes with on the unconditional variance of the output $V(\mathbf{Y})$, (Ekström, 2005). The variance based techniques aim to rank the input factors according to the variance that is lost. The measure of the sensitivity of $\mathbf{Y}$ to X_i is defined by the formula;

$$s_i = \frac{V(E[\mathbf{Y}|X_i])}{V(\mathbf{Y})}. \tag{4.13}$$

The ratio (4.13) was named *first order sensitivity* by Sobol, (Sobol, 1993), which only measures effect of the main contribution of each parameter on the output variance and does not take into account interaction between the input factors. The sum of all order effects that a factor accounts for is called *total effect* (Homma and Saltelli, 1996; Saltelli et al., 1999). Therefore for an input X_j, the *total sensitivity index* s_{T_j} is the sum of all indices measure relating to X_j.

4.3.1 Extended Fourier amplitude test (eFAST)

eFAST method was developed by Saltelli et al. (1999, 2000) as an improvement of the Fourier amplitude test (FAST) method which was developed by Cukier et al. (1975). It is a variance based method. The technique uses a periodic sampling method together with Fourier transformation to partition the whole variance of the model output and quantify the degree to which variation in each input factor accounts for the output variance (Gao et al., 2016).

A periodic sampling approach is used to generate a search curve in the parameter space and partitioning is implemented by assigning the periodic sample of each parameter with a distinct frequency. Then a Fourier transformation is applied to the model output to measure how strongly a factor's frequency propagates from the input to the output, i.e., the variance contribution of the factor to the whole variance of the output (Saltelli and Bolado, 1998; Saltelli et al., 1999; Marino et al., 2008; Gao et al., 2016).

We make use of the dummy parameter to determine the significance of first and total order indices. This approach has been in existence in literature and was applied in the context of eFAST (Marino et al., 2008). eFAST produces small but non-zero indices even for parameters to which the model is independent. So the parameters with total-order sensitivity index less than or equal to that of dummy parameter are considered not significantly different from zero and hence not significant. The full description of eFAST method is presented in Appendix C.2.

4.3.2 Sensitivity analysis results with eFAST method

The sensitivity analysis by eFAST was performed using the parameter values listed in Table 4.1. The table also gives the range of parameters within which the sensitivity is performed. Due to lack of prior knowledge about the parameter distributions, a uniform distribution is assumed for each parameter. The range of parameters is also arbitrary, and large enough to cover all the possible dynamics. The simulations are run in MATLAB based on the code given in Ekström (2005); Marino et al. (2008). We use the sample size, $NS = 250$ and the re-sampling, $NR = 3$, and for all the models, we obtain the first order and total order sensitivities, and plot bar graph of

the same.

Parameters whose sensitivity indices are less or equal to the dummy variable are considered not sensitive, and hence do not affect the output. We also note that eFAST method produces positive sensitivity indices, and does not tell whether a parameter increases or decreases the output. Extra analysis should be performed if one wants to determine the effect of a particular parameter. The analysis here only seeks to identify the parameters which most affect the output, but not how they affect, and so we will not determine if a parameter increases or decreases the output.

Parameters	Model GRM-1		Model GRM-2		Model GRM-3	
	Range	Baseline	Range	Baseline	Range	Baseline
k_0	[0.001, 150]	4	[0.001, 150]	4	[0.001, 150]	1
k_1	[0.001, 150]	0.45	[0.001, 150]	0.1	[0.001, 150]	0.2
k_2	[0.001, 150]	1	[0.001, 150]	1	[0.001, 150]	0.5
k_2'	[0.001, 150]	1	[0.001, 150]	1	NA	NA
k_3	[0.1, 20]	1	[0.1, 20]	1	[0.1, 20]	1
k_4	[0.1, 20]	1	[0.1, 20]	1	[0.1, 20]	0.65
k_5	[0.0001, 15]	0.022	[0.0001, 15]	0.035	[0.0001, 15]	0.15
k_6	[0.0001, 15]	0.01	[0.0001, 15]	0.01	[0.0001, 15]	0.1
k_7	[0.0001, 10]	0.001	[0.0001, 15]	0.001	[0.0001, 15]	0.025
K_{r0}	NA	NA	[0.001, 50]	1	[0.001, 50]	0.051
K_{r1}	[0.001, 50]	0.05	NA	NA	[0.001, 50]	0.051
K_{r2}	[0.001, 10]	0.05	[0.001, 10]	1	[0.001, 10]	0.05
K_{m5}	NA	NA	[0.01, 5]	1	[0.01, 5]	0.5
K_{m6}	NA	NA	NA	NA	[0.01, 5]	0.75
K_{m7}	NA	NA	NA	NA	[0.01, 20]	0.75
K_{g3}	[0.01, 10]	0.3	[0.01, 10]	0.15	NA	NA
K_{g4}	[0.01, 10]	0.2	[0.01, 10]	0.1	NA	NA
G_T	[0.001, 50]	5	[0.0001, 50]	12	[0.001, 50]	12

Table 4.1: Parameter ranges and base values for models GRM-1, GRM-2 and GRM-3. NA refers for Not Applicable.

Global sensitivity results for model GRM-1

Model GRM-1 has 15 parameters together with the dummy variable. Therefore the total number of simulations performed is $15 \times 250 \times 3$. The re-sampling ensures that no parameter is sampled more than once. First and total order sensitivity indices are obtained, and results presented as shown in Figure 4.19. Figures 4.19(a) and 4.19(b) show first and total sensitivity indices for model GRM-1 computed with eFAST method. s_i only gives the effect of an input factor to the output but does not put into consideration the interaction with other input factors while s_{T_i} which is the total order index, considers interaction with other parameters. From Figure 4.19,

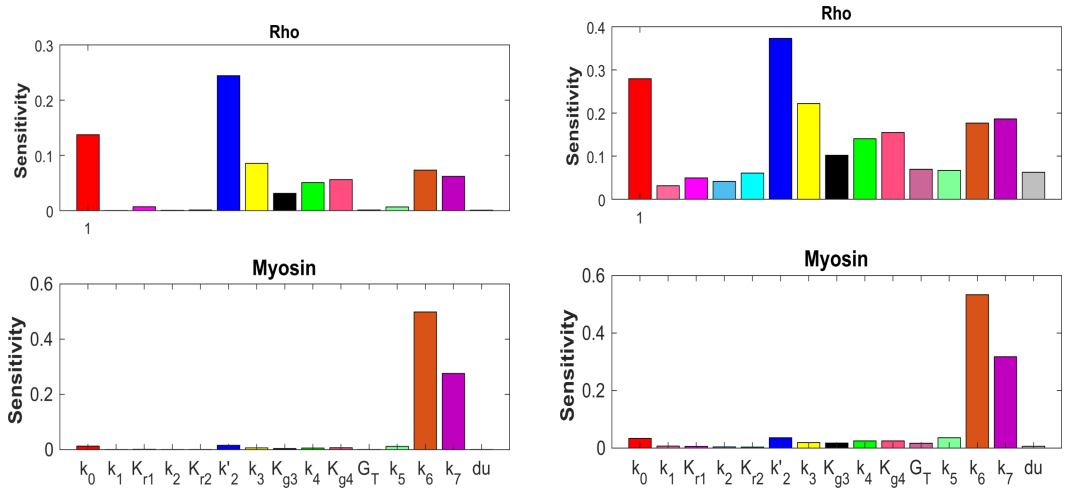

(a) s_i (b) s_{T_i}

Figure 4.19: First and total order sensitivity indices for model GRM-1, parameter values in Table 4.1 are used.

the Rho output is mostly affected by k_2', k_0, k_3. They are ranked high by both s_i or s_{T_i}. The interaction of parameter impacts more on the Rho output, since $s_{T_i} > s_i$. Similarly k_6 and k_7 affect the Rho output. The parameters k_1, K_{r1}, k_2, K_{r2}, G_T and k_5 are not significantly different from dummy and therefore considered not significant. The most sensitive parameters that affect Myosin output are k_6, k_7 and k_2'. The rest of the parameters have the sensitivity index almost equal to the dummy parameter, hence not significant. Comparing s_i and s_{T_i}, it can be concluded that the most influence is due to parameter interaction.

Global sensitivity results for model GRM-2

Model GRM-2 has a total of 16 parameters including the dummy variable, which makes the total number of simulation $16 \times 250 \times 3$. The sensitivity indices are obtained and represented on a bar plot as shown in Figure 4.20. Figures 4.20(a) and 4.20(b) show first and total sensitivity indices for model GRM-2 computed with eFAST method. From Figure 4.20, the Rho output is largely affected by k_1, k_2',

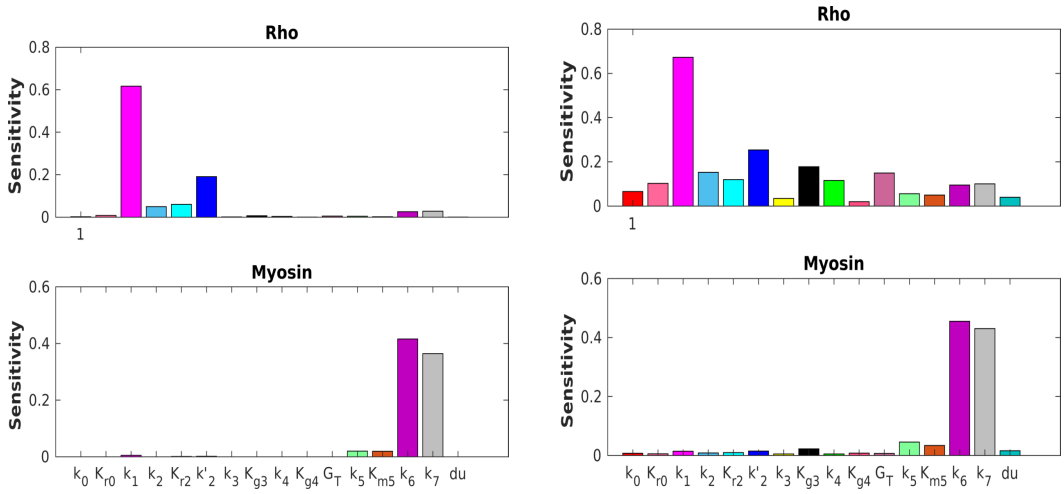

(a) s_i (b) s_{T_i}

Figure 4.20: First and total order sensitivity indices for model GRM-2, parameter values in Table 4.1 are used.

K_{g3}, k_2 and G_T. The interaction of parameter impacts more on the Rho output, for example parameters such as, k_{g3} and G_T are ranked low when considering first order sensitivity, but their ranking increases more by considering total order sensitivity. Other parameters such as k_6 and K_{m6} are ranked 6 and 5 respectively from s_i, their significance reduces to 10 and 9 respectively when we consider parameter interactions. The rest of other parameters are not significantly different from dummy and therefore considered not significant. The most sensitive parameters that affect Myosin output are k_6 and k_7, the other significant parameters are k_5, K_{m5} and K_{g3}. The rest of the parameters are ranked below the dummy variable, hence not significant. Comparing s_i and s_{T_i}, it can be concluded that the most influence is due to parameter interaction.

Global sensitivity results for model GRM-3

Model GRM-3 has a total of 15 parameters considered for sensitivity analysis. First and total order sensitivity indices are obtained and results presented using a bar plot as shown in Figure 4.21. Figures 4.21(a) and 4.21(b) show first and total sensitivity indices for model GRM-3 computed with eFAST method. s_i only gives the effect of an input factor to the output but does not put into consideration the interaction with other input factors while s_{T_i} which is the total order index considers interaction with other parameters. From Figure 4.21, the Rho output is mostly affected by G_T, k_3

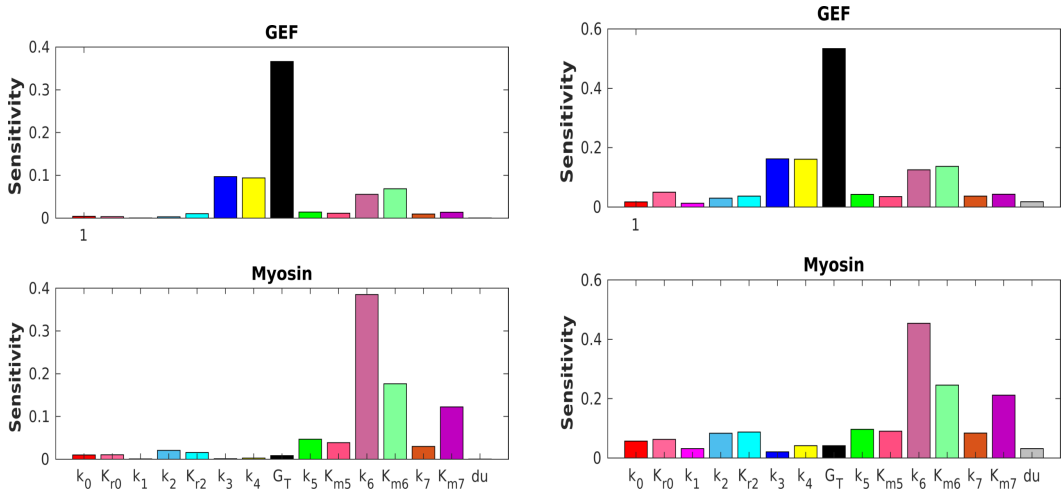

(a) s_i (b) s_{T_i}

Figure 4.21: First and total order sensitivity indices for model GRM-3, parameter values in Table 4.1 are used.

and k_4. They are ranked high by both s_i and s_{T_i}. K_{m6} also affects the Rho output, the rest of parameters are considered not significant as their sensitivity indices are almost equal to the sensitivity index of the dummy parameter. The interaction of parameter impacts more on the Rho output, since $s_{T_i} > s_i$. Similarly k_6 and k_7 affect the Rho output. Myosin output is greatly affected by the variations in k_6, K_{m6}, k_7 and K_{m7}. The rest of the parameters have the sensitivity index almost equal to the dummy parameter, hence not significant. Comparing s_i and s_{T_i}, it can be concluded that the most influence is due to parameter interaction.

4.3.3 Conclusion

In this chapter, we considered sensitivity of model output to parameters. First the local sensitivity analysis was carried out, which considered how model output is affected by an infinitesimal increase of a parameter from the nominal parameter value. With local analysis, we were able to analyse the parameter sensitivity, categorised into two regimes (stable and oscillatory). The oscillatory behaviour is one of the integral behaviour to be investigated in GEF–Rho–Myosin dynamic network. We were able to analyse period, and amplitude sensitivity to parameters. Different models are sensitive to different parameters. The comparison of models will be presented in Chapter 6. In summary, for all the models k_3 and k_4 stand out almost in every aspect as one of the most sensitive parameters.

We also carried out global sensitivity analysis using eFAST method. This is a variance based method that ranks the sensitivity of parameters depending on the variance that is lost. In general k_6, k_7, k_3, G_T stand out as some of the most influential parameters. The comparison between different models will be discussed in Chapter 6. It has been shown for all the models that the two variables are largely influenced by different parameters; for example in model GRM-1, the two most sensitive parameters that affect Rho are k_2' and k_0 while for Myosin, they are k_6 and k_7. For model GRM-2, Rho is largely affected by k_1 and k_2' while k_6 and k_7 largely affects Myosin. For model GRM-3, G_T, k_3 and k_4 largely affects GEF while k_6, K_{m6} and K_{m7} largely affects Myosin. The parameters k_6 and k_7 are associated with Myosin module, while k_3 and G_T are associated with the GEF module. Therefore, the results show that the system is more sensitive to the mechanisms which alter positive and negative feedback regulators of Rho, than those mechanisms which alter Rho module components. We also see that in general, the ranking of parameter sensitivity is fairly similar for all the models and therefore the response of GEF–Rho–Myosin system is independent on the model structure.

In the next chapter, we consider some numerical simulations relating to all the models. The chapter contains the study of the excitable dynamics and identification of excitability region for all the models. We also characterise Rho amplitude dependency on the parameter, G_T, and lastly we present time series of the molecules to

illustrate mathematical results presented in Chapter 3.

Chapter 5

Numerical simulations

5.1 Introduction

In Chapter 4, we studied the model response to parameter variations, in particular, we used local sensitivity analysis to examine the period and amplitude change with respect to parameter variations. In this chapter, we perform numerical simulations corresponding to all the three models formulated in Chapter 2. We first provide the phase-planes and temporal long term behaviours of the ODE models for different GEF concentrations (G_T), which illustrate the theoretical predictions in Chapter 3. We then investigate the Rho excitability as observed experimentally (Graessl et al., 2017) and identify the excitability region for all the three models. We also study Rho response amplitude dependency on the positive feedback mediator, GEF-H1, and also the trigger threshold that provides the maximum Rho amplitude. It was observed experimentally that Rho response amplitude increases until intermediate GEF concentration (Graessl et al., 2017).

5.2 Phase-planes and temporal analysis

We first illustrate different regime behaviour which were theoretically predicted in Chapter 3, we choose characteristic values of G_T and plot the phase-planes and temporal profiles for the variables. This is done for each model. In this case, we provide the phase-plane and temporal profile of excitability. The explicit study of

excitability region will be studied in the next section.

- In a phase-plane diagram the $R-$ and $M-$nullclines (respectively $G-$ and $M-$nullcline for model GRM-3), the direction fields, and one or two solutions are plotted.
- In the $t-$domain, the temporal evolution of the solutions is presented.

All the numerical simulations are carried out with parameter values listed in Table 3.1, unless stated otherwise. The simulations are done in MATLAB package using ode23 (Shampine and Reichelt, 1997).

5.2.1 Phase-planes and temporal analysis for model GRM-1

The bifurcation diagram in Figure 3.3 shows that as G_T increases, R slowly decreases and then at high values of G_T, the model has up to three steady states, two of which are stable, separated by an unstable (saddle) steady state. These results are illustrated by the phase-plane diagrams and temporal evolutions in Figures 5.1 and 5.2, respectively. Figure 5.1 shows different phase-planes for model GRM-1 corresponding to different GEF-H1 concentrations (as illustrated in Figure 3.3). The phase-plane diagrams also illustrate the theoretical analysis results in Figure 3.2. The phase-planes describes four dynamic regimes as G_T varies. The local intersection of the nullclines resembles the theoretically predicted shapes in Figure 3.2. In the phase-planes, R-nullcline has three branches. The middle branch is unstable, while two outer branches are stable, when the intersection occurs at the outer branches, the steady state is stable, while intersection at the middle branch implies unstable steady state, which can either be a node, spiral or a saddle depending on the local qualitative configuration at the intersection. The phase-plane illustrates that at small G_T, then we have an intersection, characterised by a stable equilibrium. As G_T increases, the system changes to oscillatory dynamics, which bifurcates to excitable dynamics and lastly at higher G_T values, the model is characterised by bistable dynamics.

The time series of Rho and Myosin for model GRM-1 are obtained for the corresponding phase-planes in Figure 5.1. The results characterise various dynamics as shown in Figure 5.2. The results illustrate the four dynamic regimes predicted for

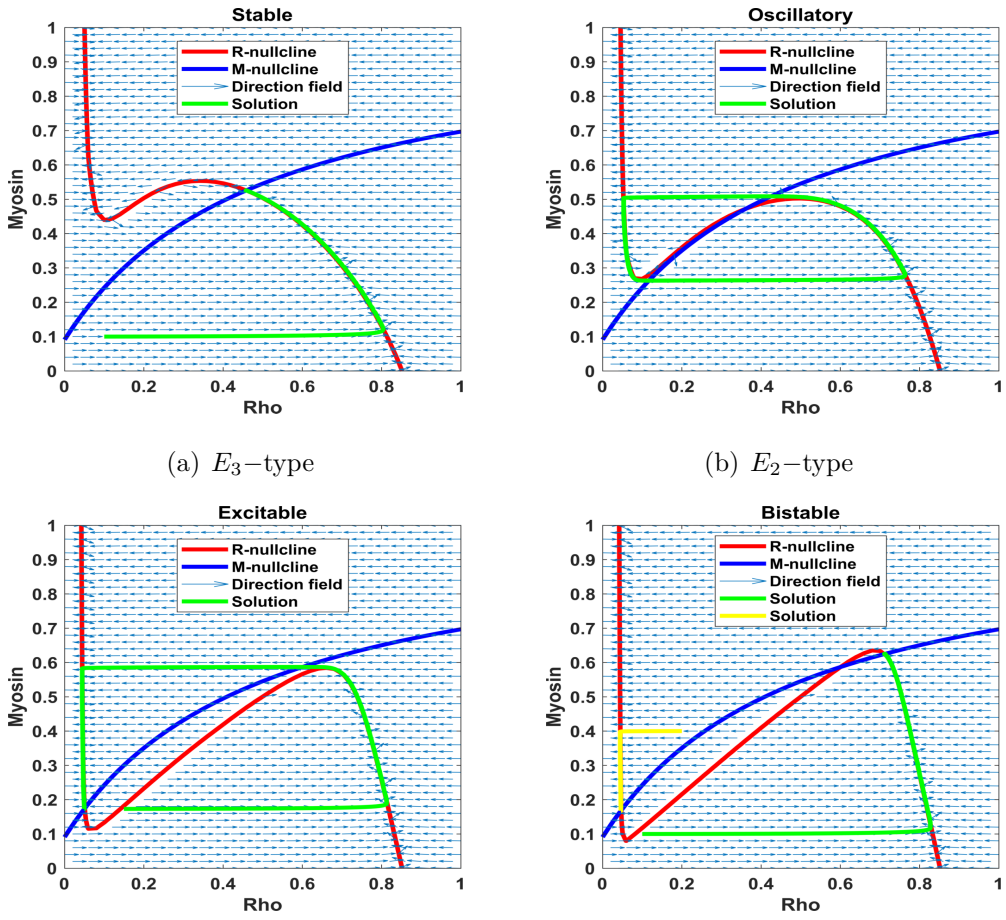

(a) E_3-type (b) E_2-type

(c) E_1-type (d) E_4-type + E_5-type + E_6-type

Figure 5.1: Phase-plane diagrams of Rho and Myosin corresponding to model GRM-1 for different values of G_T. The values of G_T are 0.1, 0.6, 5 and 16 respectively.

model GRM-1. For suitable parameter values, the model exhibit up to 4 regimes (stable, oscillatory, excitable and bistable) by changing GEF-H1 total concentration (G_T). For small values of G_T, the model has a unique steady state, which is stable (Figures 5.1(a) and 5.2(a)). AS the value of G_T increases, the stable steady state becomes unstable, and since it is unique the model oscillates around this steady state (see Figures 5.1(b) and 5.2(b)). Increasing G_T further results in the transformation of the steady state back to stable, in this case an excitable steady state (see Figures 5.1(c) and 5.2(c)). At higher G_T, the model has three equilibrium points, two are stable, separated by a saddle (see Figures 5.1(d) and 5.2(d)). The saddle steady state acts as a switch that determines to which steady state the models converges to. Both steady states can be achieved by changing initial conditions. These numerical simulation results support the theoretical findings and bifurcation analysis

results in Chapter 3.

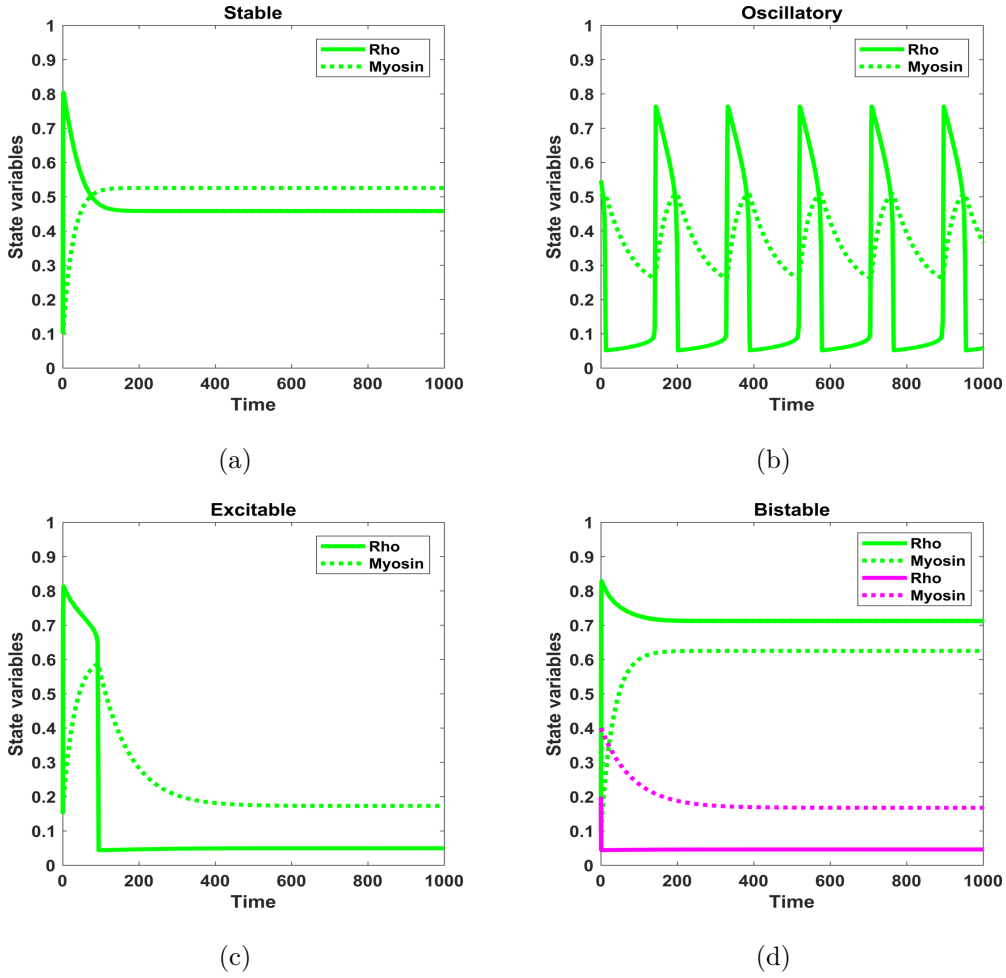

Figure 5.2: Numerical temporal evolution profiles of Rho and Myosin corresponding to model GRM-1 for different values of G_T. The values of G_T are used as in Figure 5.1. The initial conditions used for bistable regime (Figure 5.2(d)) are $(0.1, 0.1)$ and $(0.2, 0.4)$.

5.2.2 Phase-planes and temporal analysis for model GRM-2

Figure 5.3 shows different phase-planes corresponding to different values of G_T. The results illustrate theoretical predictions shown in Figure 3.4. As G_T increases, R slowly decreases and then at high values of G_T, the model has three steady states two of which are stable and separated by an unstable (saddle) steady state. It can be noted that as G_T varies, the M-nullcline remains fixed, as it is not affected by G_T. It is the R-nullcline that varies and brings different dynamic behaviours. These characteristic phase-planes are locally equivalent to the qualitative phase-planes described in Chapter 3.

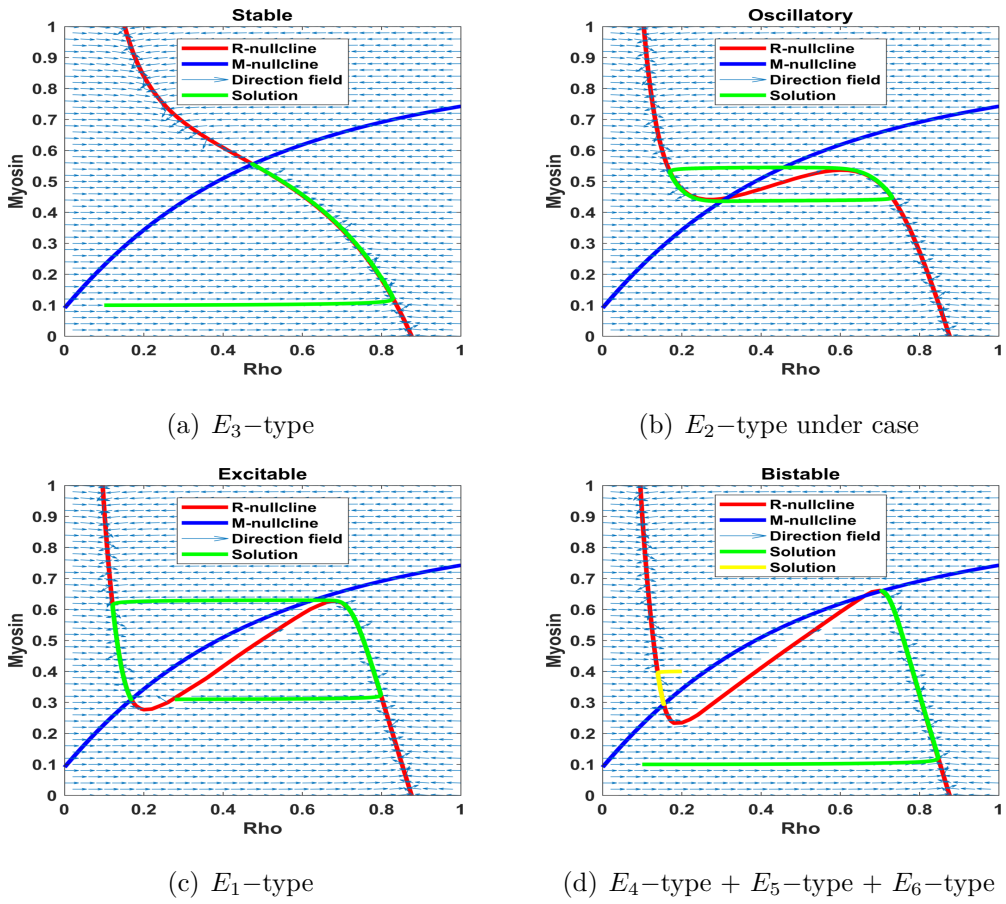

(a) E_3-type (b) E_2-type under case

(c) E_1-type (d) E_4-type + E_5-type + E_6-type

Figure 5.3: Phase-plane diagrams corresponding to Rho and Myosin for model GRM-2 for different values of G_T. The values of G_T are respectively selected as 0.1, 1, 7, 20 and $k_1 = 0.2$.

Figure 5.4 shows time series of Rho and Myosin for different values of GEF concentration. For small value of G_T, the model has a unique steady state which is globally asymptotically stable (Figure 5.4(a)). As the value of G_T increases, the steady state becomes unstable and is unique, therefore the system overshoots and undershoots between the upper and lower branches of R-nullcline in the oscillatory regime. An increase in the value of G_T makes the steady state stable, which is excitable, further increase in G_T makes the model to have three steady states. This is all illustrated by the time series behaviour.

5.2.3 Phase-planes and temporal analysis for model GRM-3

Figure 5.5 shows phase-plane analysis (5.5(a)-5.5(c)) and their corresponding temporal evolution results (5.5(d)-5.5(f)) for model GRM-3. The results illustrate various dynamic regimes of model GRM-3 (stable, excitable and oscillatory). This model

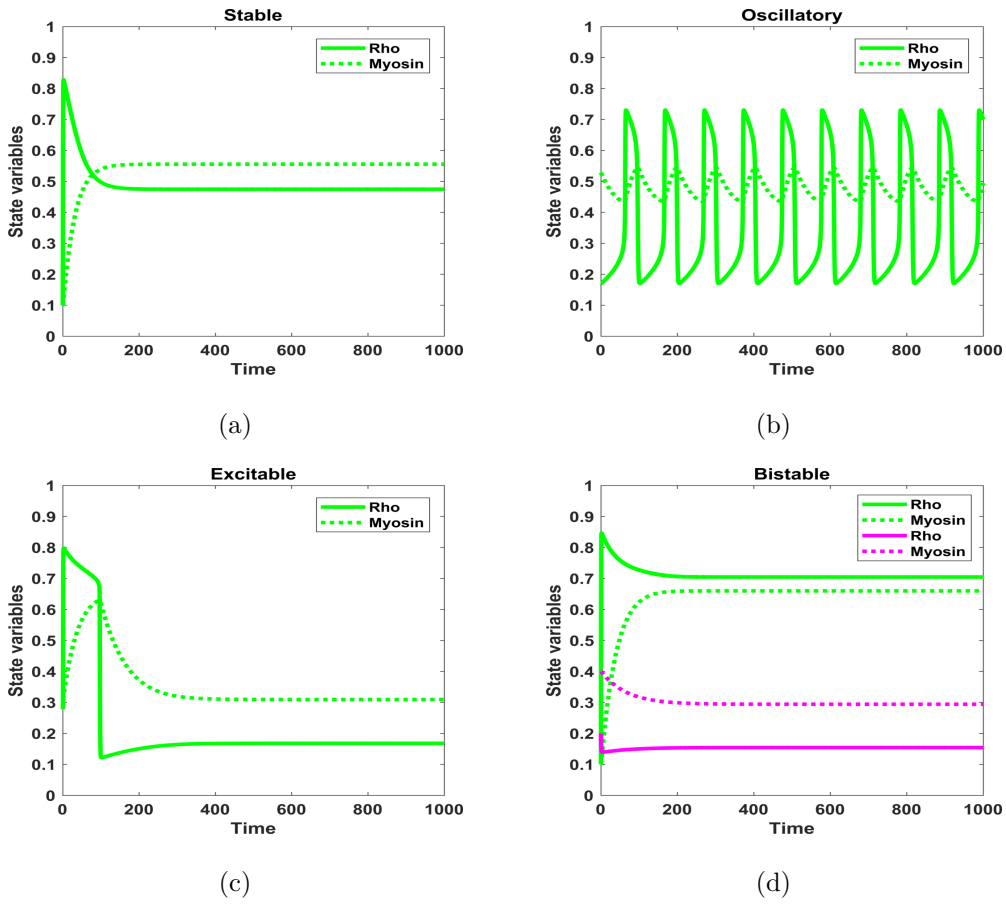

Figure 5.4: The time series of Rho and Myosin for model GRM-2. These are generated using the parameter of corresponding phase-plane diagrams in Figure 5.3. In Figure 5.2(d) we used initial conditions $(0.1, 0.1)$ and $(0.2, 0.4)$.

shows only three regimes by changing GEF total concentration. All of these regimes are illustrated. We also note that the qualitative nullclines intersection are locally similar to what was qualitatively described in Chapter 3. For small values of G_T, the steady state is stable and unique, as G_T increases, the steady state assumes excitable behaviour, further increase in G_T makes it unstable and hence periodic solutions emerge.

5.3 Rho excitability

Excitability is defined according to Allard and Mogilner (2013) as, "It results from a steady state in which small perturbation decays but perturbations larger than a threshold results in larger excursion but later returns to steady state indirectly." This is illustrated in Figure 1.4(b). It was shown that the activator-inhibitor system

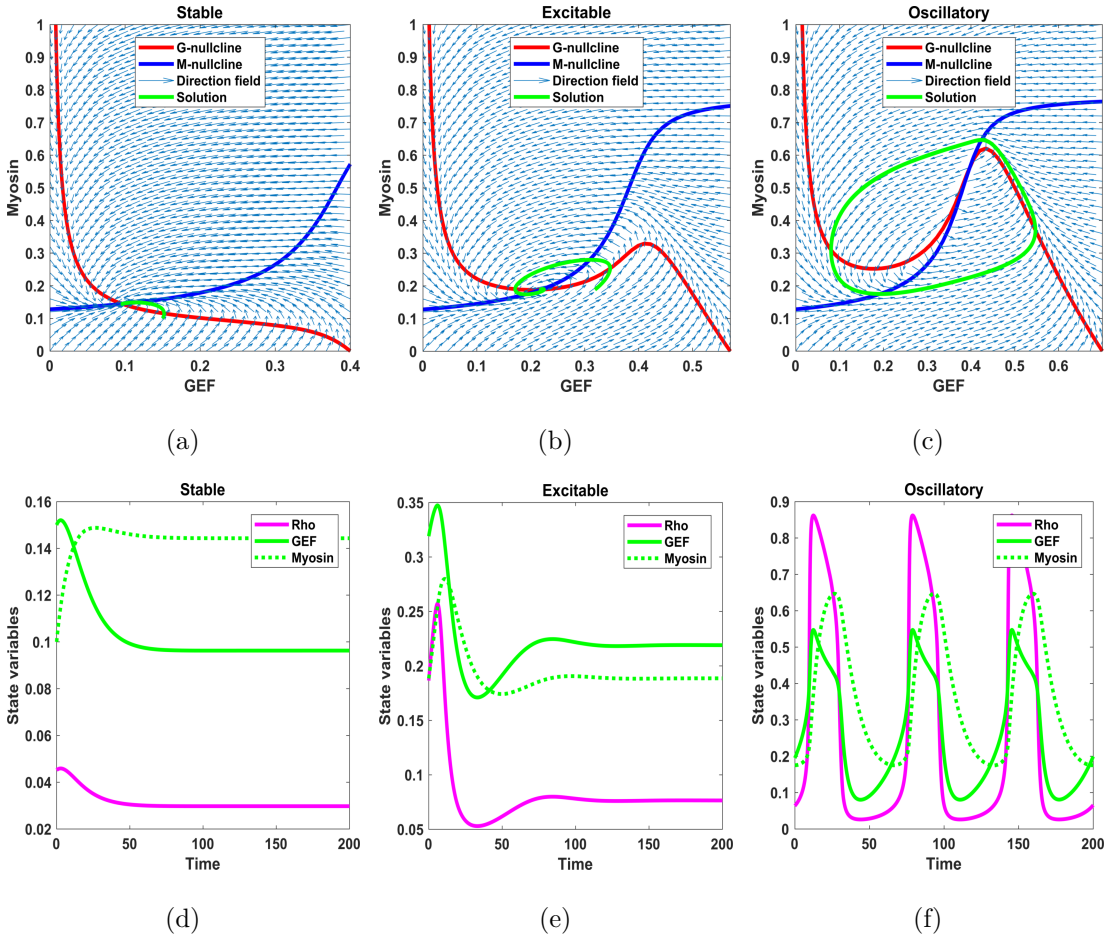

Figure 5.5: Phase-plane diagrams(5.5(a)-5.5(c)) and their corresponding numerical solutions (5.5(d)-5.5(f)) for model GRM-3 for different values of G_T. The values are $G_T = 0.4$ for stable, $G_T = 0.57$ for excitable and $G_T = 0.7$ for oscillatory, $k_1 = 0.1$.

can make cell plasma membrane and its cortex act as an excitable media (Bement et al., 2015; Barnhart et al., 2017; Miao et al., 2017). This accounts for spontaneous migration of cells (Iglesias and Devreotes, 2012). It was found that a combination of Rho self-amplification through GEF-H1 and Myosin inhibition as shown in Figure 1.3 leads to pulsatile and cell contraction dynamics (Graessl et al., 2017). This is the characteristic of an excitable medium which is composed of a component that regulates its activities by recruiting both its activator and an inhibitor (Murray, 2002; Iglesias and Devreotes, 2012). The activator provides a positive feedback loop while an inhibitor provides a slow negative feedback loop. The Hodgkin-Huxley model (Hodgkin and Huxley, 1952) forms the basis for the study of excitability. For some cells when the current/signal is too strong, the membrane potential goes through a large excursion (Sneyd and Keener, 1998). Cells which exhibit such

dynamics are said to be excitable.

Since GEF–Rho–Myosin tri-molecular interactions has been reduced to two species model, we will use phase-plane analysis to describe excitability as shown in. For some parameter values in the model, there is only one intersection of nullclines and hence one steady state for all the models. The R-nullcline has three branches and the M-nullcline is an increasing function. The intersection of the nullclines gives the steady state of the model. When the intersection of R and M-nullclines happens at the extreme branches of R-nullcline, then the steady state is stable but if the intersection happens at the middle branch, then the steady state is unstable. Consider intersection of nullclines as shown in Figure 5.6, which is similar to Figure 3.2(a) in Chapter 3. This is a typical shape of a nullcline characterised by excitable dynamics. The threshold for excitability is represented by the green line. For any perturbation below the threshold then the system decays. However if the perturbation is larger than the threshold, then we experience a large excursion of R followed by decay to the steady state.

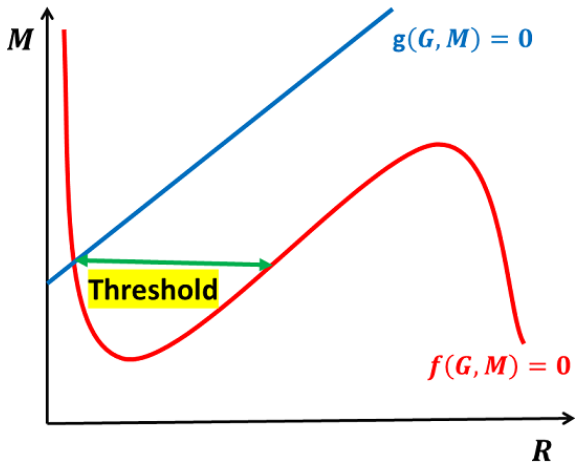

Figure 5.6: The nullcline intersection characteristic of an excitable medium. Green line is the threshold for which a large excursion is observed.

5.3.1 Excitability region for models GRM-1 and GRM-2

For models GRM-1 and GRM-2, it can be shown that as G_T increase, the nullcline configurations transition as shown in Figure 5.7. As G_T varies, M-nullcline in Figure 3.2 remains fixed while R-nullcline moves as shown in Figure 5.7, it can be

shown that excitability occurs at the values of G_T between oscillatory and bistable regimes as shown in Figure 5.8. It can be seen that models GRM-1 and GRM-2

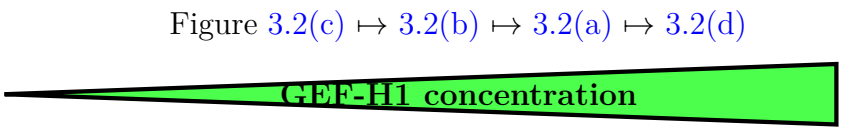

Figure 5.7: The transition of nullclines for models GRM-1 and GRM-2 as GEF-H1 concentration varies.

have the same qualitative dynamics, they have a similar defined region within which excitable dynamics occur. The dynamics transition from stable ↦ oscillatory ↦ excitable ↦ bistable. For parameter values in the green region (see Figure 5.8), if a critical threshold is exceeded, the two models show excitable behaviour. This has been illustrated in the first section, about phase-plane analysis and time series of Rho dynamics.

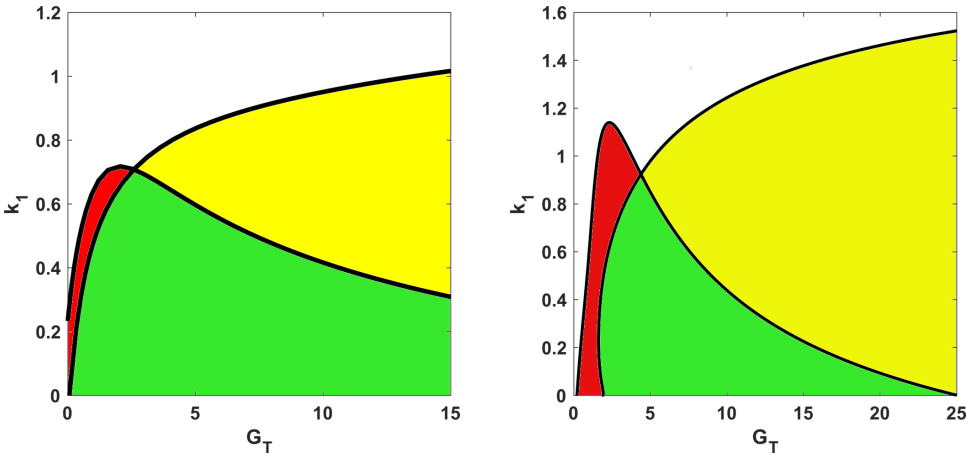

(a) Model GRM-1 (b) Model GRM-2

Figure 5.8: The green coloured region is the excitability regime in two parameters G_T and k_1. The yellow and red represents bistable and oscillatory regimes respectively

5.3.2 Excitability in model GRM-3

For model GRM-3, it can be shown that as G_T increases, the nullcline configurations transition as shown in Figure 5.9. As G_T varies, both M-nullcline and G-nullcline moves as shown, but the local configuration is equivalent to the configurations in Figures 3.2(a), 3.2(b) and 3.2(c). The excitability occurs before oscillatory region.

This model lacks a defined region within which excitable dynamics occur, and therefore, it is not easy to characterise the region within which excitable dynamics occur. This is different from models GRM-1 and GRM-2 in which we can characterise the region within which excitability occurs. The dynamics observed in model GRM-3 transition from stable ↦ excitable ↦ oscillatory ↦ stable.

Figure 3.2(a) ↦ 3.2(b) ↦ 3.2(c)

Figure 5.9: The transition of nullclines for model GRM-3 as GEF-H1 concentration varies.

Summary of excitability

All the three models GRM-1, GRM-2 and GRM-3 exhibit excitable dynamics for some parameter values. These parameters are such that the nullcline configuration is similar to the configuration shown in Figure 3.2(a). All the three models have a region within which excitable dynamics occurs. Comparison of excitability results are presented in Chapter 6.

5.4 Rho response amplitude and trigger threshold

In this section, we present the basic characterisation of dynamic states that correspond to pulsatile and excitable system dynamics. We present the results for the Rho response amplitude for models GRM-1, GRM-2 and GRM-3. The model dynamics are carried out focusing on the threshold dynamics for switching steady states, or for obtaining the maximum response amplitude. We also investigate the frequency of peaks in the oscillatory dynamics. It is observed experimentally (Graessl et al., 2017; Kamps et al., 2019) that as G_T increases, the frequency of oscillation reduces. The Rho threshold denoted, ΔRho is the perturbation from the steady state, which we define as:

$$\Delta\text{Rho} = \text{Rho}_{\text{initial}} - \text{Rho}_{\text{equilibrium}}.$$

We define the trigger threshold as the minimum ΔRho that gives rise to the maximal Rho amplitude. This formula is only valid in the case of stable steady state, oth-

erwise in the case of unstable steady states, the system is oscillatory and therefore maximum amplitude is obtained in the absence of trigger. We define Rho response amplitude as,

$$\text{Rho}_{\text{amp}} = \text{Rho}_{\text{max}} - \text{Rho}_{\text{min}} - \Delta\text{Rho}. \tag{5.1}$$

Equation (5.1) is used to calculate the Rho response amplitude and the critical threshold (ΔRho) that generates maximal Rho amplitude. First the stable steady state solutions of Rho and Myosin activities are obtained from simulations. The steady state values are then used as starting points for perturbation analyses. Next the activity of Rho response amplitude to perturbation is then calculated. The critical threshold that generates maximal Rho amplitude response is also calculated.

5.4.1 Rho response amplitude and trigger threshold for model GRM-1

First the excitability of Rho was analysed for fixed set of parameters, $G_T = 2.5$ and $k_1 = 0.5$ and other parameters fixed as in Table 3.1. The dynamic response of Rho activity is determined as shown in Figure 5.10(a). The dynamic response of Rho was then analysed in all dynamic regimes (stable, oscillatory, excitable and bistable) for G_T, k_1 parameter combinations. The results are as shown in Figures 5.10(b) and 5.10(c).

Figure 5.10 shows the results of Rho response amplitude and trigger threshold analysis. In the excitable region, corresponding to Figure 5.10(a), if the critical threshold ΔRho $= 0.075$ is exceeded, the time series shows excitable behaviour. This is characterised by rapid amplification to reach maximal Rho activity which is followed by transient minimum and return to the steady state. The maximal Rho activity amplitude for this set of parameter is 0.6725 and it occurs when the threshold, ΔRho $= 0.1$. It is also observed that the Rho response amplitude increases by increasing the threshold until its maximum value, further increasing the threshold leads to a decreases in the response amplitude. In the oscillatory regime, maximal Rho amplitude was calculated in the absence of trigger, i.e. ΔRho $= 0$, as shown in Figure 5.10(b).

In the excitable regime, the trigger threshold increases slightly by increasing G_T

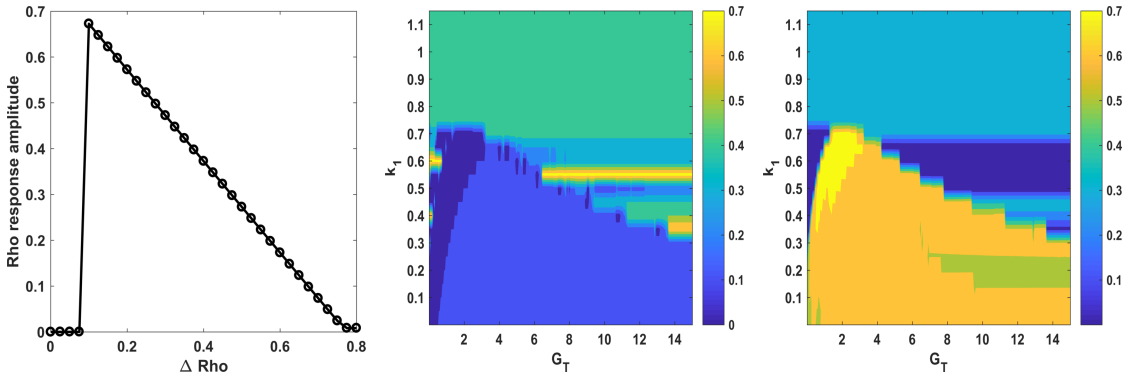

(a) (b) (c)

Figure 5.10: Figure 5.10(a) shows the dependency of Rho response amplitude on the perturbation, ΔRho for fixed parameter values in the excitable regime. 5.10(b) is the contour plot of trigger thresholds to generate the maximal Rho response amplitude for each G_T, k_1 parameter combinations. 5.10(c) is the contour plot of maximal Rho response amplitude for G_T, k_1 parameter combinations.

for any value of k_1 while in the stable and bistable regimes, the trigger threshold increases by increasing G_T or k_1. In the bistable regime, we could calculate two trigger thresholds, as well as two maximal Rho response amplitudes by switching from lower to higher steady states of Rho activity, or switching from higher to lower. The results here are shown when switching the activity of Rho to lower steady states as it requires larger threshold. From Figure 5.10(c), for smaller G_T values, the amplitude becomes larger with increasing G_T. The maximal Rho amplitude is observed in the oscillatory regime. Further increasing G_T leads to a decrease in Rho response amplitude. Figure 5.11 summarises the dynamic Rho response amplitude and the corresponding trigger threshold. In general, for fixed value of k_1 the Rho response amplitude increases by increasing G_T until the oscillatory regime. Further increasing G_T beyond the oscillatory regime decreases the response amplitude. On the other hand, the trigger threshold increases by increasing G_T, for any fixed k_1. It can also be observed that increase in k_1 value increases trigger threshold, respectively the response amplitude. These results can be compared to one parameter bifurcation diagram Figure 3.3(a) to illustrate the threshold dynamics and Rho amplitude dynamics for each regime. We also analysed the period and frequency of oscillation for model GRM-1. The results are shown in Figure 5.12. It is shown that as G_T increases in the oscillatory regime, the peak width increases, which implies

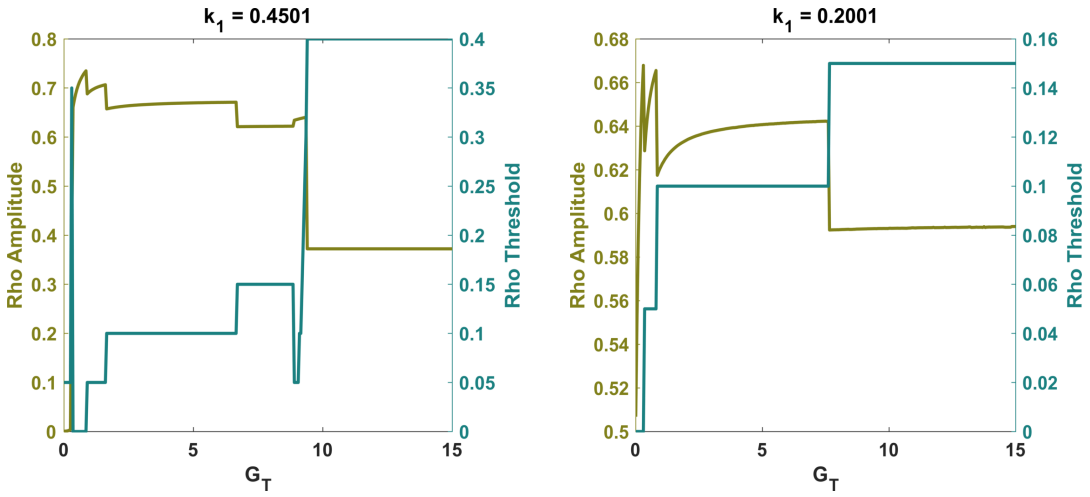

(a) (b)

Figure 5.11: Rho response amplitude and trigger threshold for model GRM-1, for fixed values of k_1 and varying G_T.

that peak frequency decreases as G_T increases. A Similar observation was made in experimental results (Graessl et al., 2017; Kamps et al., 2019), that the frequency of oscillations decreases with increasing expression levels of the positive feedback mediator, GEF-H1.

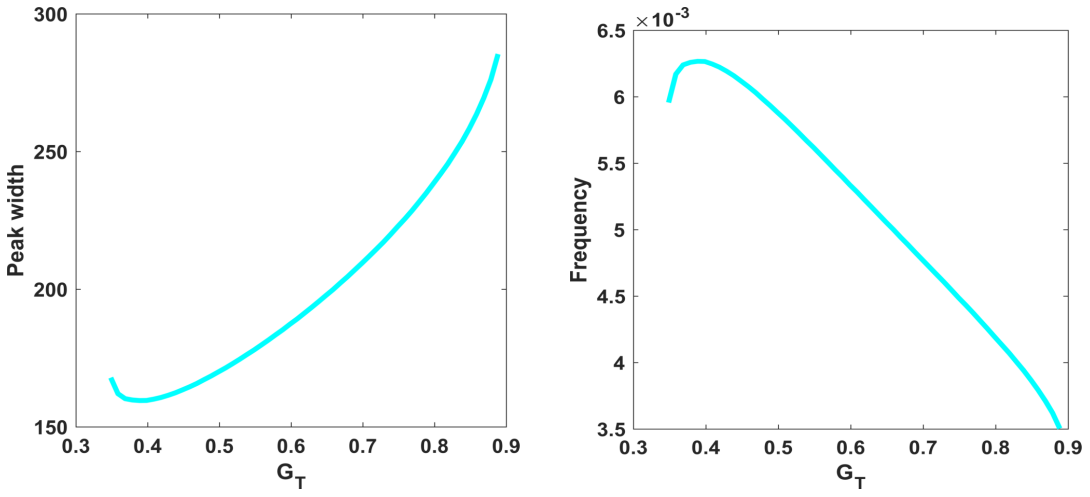

(a) (b)

Figure 5.12: Period and frequency of oscillations for model GRM-1 in the oscillatory regime.

5.4.2 Rho response amplitude and trigger threshold for model GRM-2

The analysis of model GRM-2, follows similarly to that of model GRM-1. In the excitable regime, we the take the following parameter values $G_T = 5, k_1 = 0.2$ and fix other parameters as in Table 3.1. The dynamic response of Rho activity is calculated as shown in Figure 5.13(a). The Rho response amplitude and the trigger threshold is then analysed in all dynamic regimes (stable, oscillatory, excitable and bistable) for G_T, k_1 parameter combinations. The results are presented in Figure 5.13, which shows the results of Rho response amplitude and the trigger threshold analysis. In the excitable region, Figure 5.13(a), if the critical threshold of ΔRho $= 0.45$ is exceeded, the time series shows excitable behaviour. Rho response amplitude increases by increasing the trigger threshold. Further increase in threshold beyond 0.4750 decreases the response amplitude.

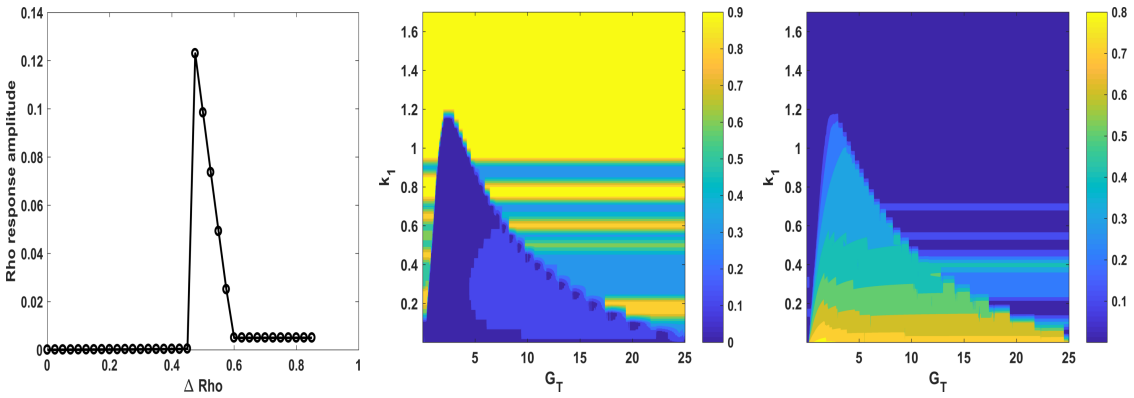

(a) (b) (c)

Figure 5.13: Figure 5.13(a) shows the dependency of Rho response amplitude on the perturbation, ΔRho for fixed parameter values in the excitable regime. 5.13(b) is the contour plot of trigger thresholds to generate the maximal Rho response amplitude for each G_T, k_1 combinations. 5.13(c) is the contour plot of maximal Rho response amplitude.

In the excitable regime, the trigger threshold increases slightly by increasing G_T for any value of k_1, it is highest in the bistable regime. From Figure 5.13(c), for smaller G_T values, the amplitude becomes larger with increasing G_T in the oscillatory and excitable regimes and finally decreases in bistable regime. The results of response amplitude as well as the trigger threshold are summarised in Figure 5.14 for fixed k_1 value. It is observed that amplitude increases and is maximal in the oscillatory

regime and then finally decreases beyond this region. The trigger threshold on the other hand increases and is maximal in the bistable regime. Beyond the oscillatory region, it can be observed that increasing k_1 values increases threshold, but decreases the amplitude. These results are similar to observations made from model GRM-1.

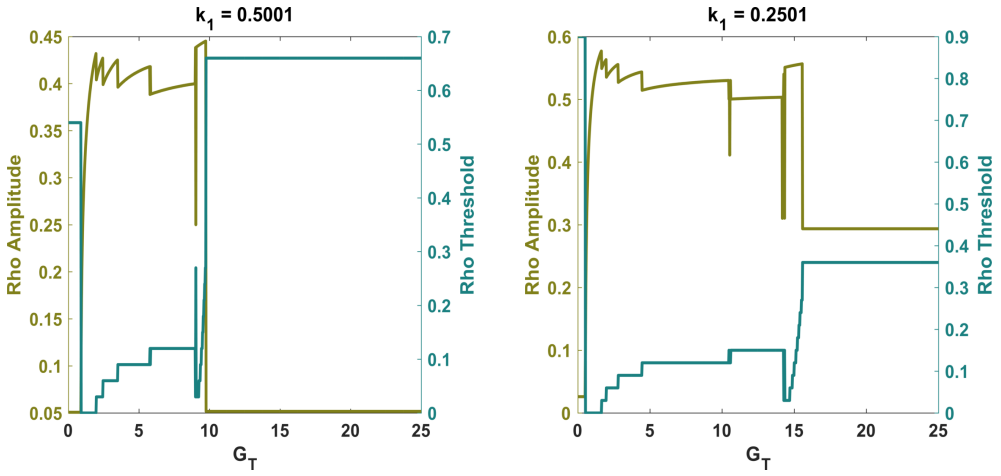

(a) (b)

Figure 5.14: Rho response amplitude and trigger threshold for model GRM-2, for fixed values of k_1 and varying G_T.

Similar to model GRM-1, the period and frequency of oscillations for model GRM-2 were analysed in oscillatory regime. The results are shown in Figure 5.15. In this figure, as G_T increases in the oscillatory regime, the peak width increases. which implies that peak frequency decreases as G_T increases. A similar observation was made in experimental results in (Graessl et al., 2017; Kamps et al., 2019) and also in model GRM-1.

5.4.3 Rho response amplitude and trigger threshold for model GRM-3

Model GRM-3 was analysed in the same way. In the excitable regime, fixed set of parameters $G_T = 0.4, k_1 = 0.15$ and other parameters fixed as in Table 3.1 were used and the dynamic response of Rho activity determined (see fig. 5.16(a)). The Rho response amplitude together with the corresponding trigger threshold were analysed in all dynamic regimes (stable, excitable and oscillatory). The results are

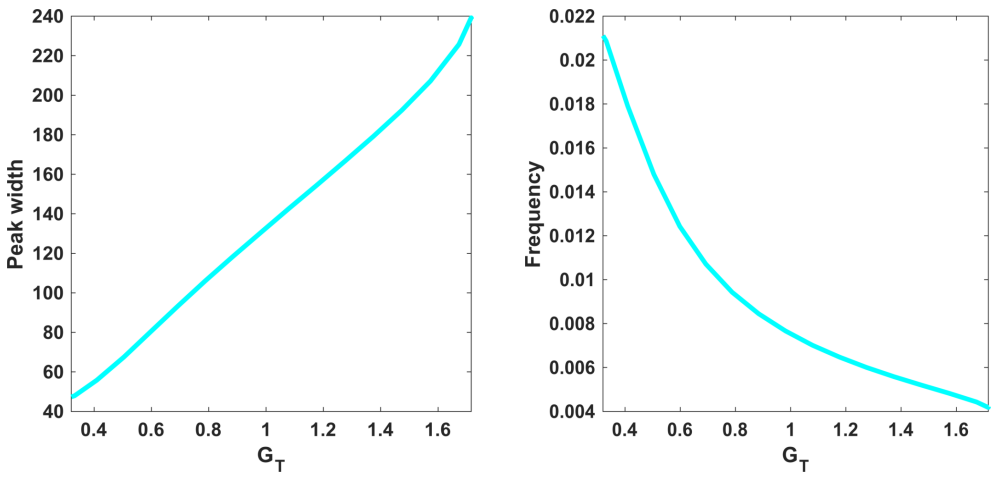

(a) (b)

Figure 5.15: Period and frequency of oscillations for model GRM-2 in the oscillatory regime.

presented in Figure 5.16, which shows the results of Rho response amplitude and trigger threshold analysis. In the excitable region, Figure 5.16(a), if the critical threshold of ΔRho = 0.15 is exceeded, the time series shows excitable behaviour which is characterised by rapid amplification to reach maximal Rho activity, followed by transient minimum and return to the steady state. In the excitable regime, a maximal amplitude of 0.451 is achieved at a threshold ΔRho = 0.225. An increase in ΔRho beyond this value further decreases the response amplitude.

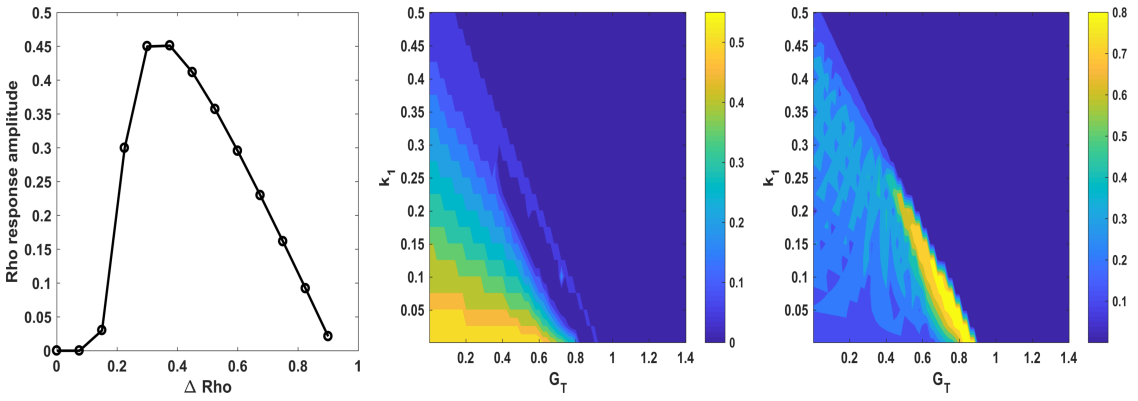

(a) (b) (c)

Figure 5.16: Figure 5.16(a) shows the dependency of Rho response amplitude on the perturbation, ΔRho for fixed parameter values in the excitable regime. 5.16(b) is the contour plot of trigger thresholds to generate the maximal Rho response amplitude for each G_T, k_1 combinations. 5.16(c) is the contour plot of maximal Rho response amplitude.

In general, the trigger threshold decreases with increasing the value of G_T, and

vanishes in the oscillatory regime and further increases in the stable and bistable regimes. From Figure 5.16(c), Rho response amplitude increases with increasing G_T. Maximum response is observed in the oscillatory regime and then finally decreases to zero in the second stable regime. Figure 5.16(a) summarises threshold and response amplitude results for fixed values of k_1. The results described the same behaviour explained before. We also observe that increasing k_1 increases Rho response amplitude. On the other hand, increasing k_1 decreases the threshold value. Similar to models GRM-1, and GRM-2 the period and frequency of oscillation for

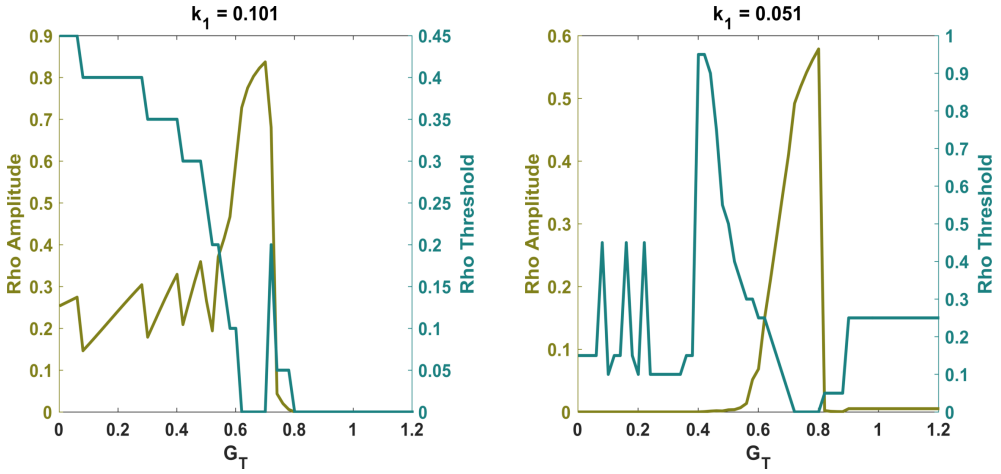

(a) (b)

Figure 5.17: Rho response amplitude and trigger threshold for model GRM-1, for fixed values of k_1 and varying G_T.

model GRM-3 were analysed in the oscillatory regime, all other parameters are fixed as shown in Table 3.1 while G_T varies. The results are shown in Figure 5.18. In Figure 5.12, as G_T increases in the oscillatory regime, the peak width first decreases and then finally increases until the Hopf bifurcation point. This implies that peak frequency first increases before decreasing as G_T increases. The experimental results Graessl et al. (2017); Kamps et al. (2019) show a similar behaviour.

5.5 Conclusion

This chapter has summarised the numerical simulations to support the mathematical analyses of all the models. We started by illustrating Rho dynamic behaviour using phase-plane analysis and time series behaviour at different G_T levels. Models GRM-1

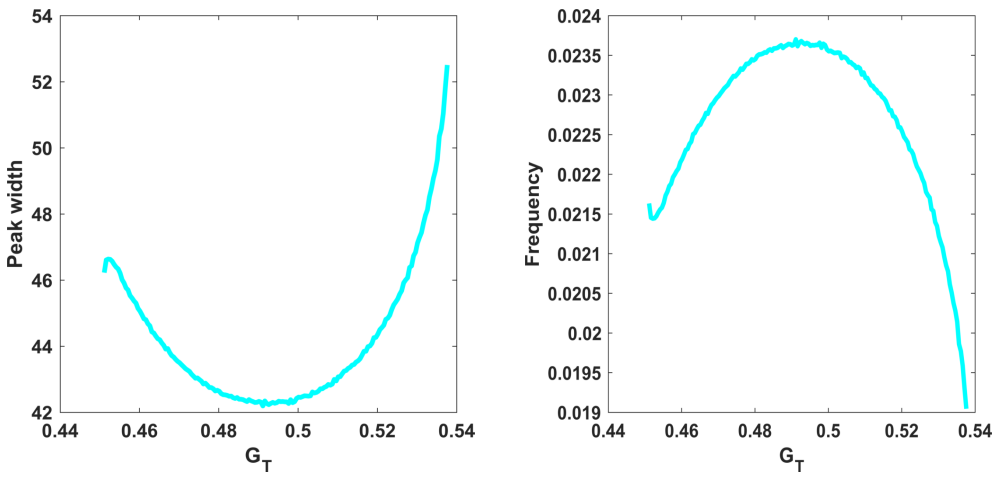

(a) (b)

Figure 5.18: Period and frequency of oscillations for model GRM-3 in the oscillatory regime.

and GRM-2 exhibit up to four regimes, while model GRM-3 has up to three regimes when G_T is varied. We then characterised the region within which excitability occurs, for models GRM-1 and GRM-2, there is a definite region within which the model shows excitable dynamics. This is different from model GRM-3 which does not have a clear defined region. We also analysed the dynamic behaviour of Rho response amplitude with G_T and k_1 parameter combinations, which has the same behaviour observed experimentally (Graessl et al., 2017; Kamps et al., 2019). It has also been shown that in the oscillatory region, increasing G_T increases the period of pulses and thus decreases the frequency. A similar observation was made with experiments. Also in the oscillatory, Myosin peaks occurs with a time delay compared to Rho or GEF. This happens for all the models. This is in agreement with experimental observations that Myosin peaks occurs with a time delay of about 3-40 seconds (Graessl et al., 2017; Kamps et al., 2019). In the next chapter, we carry out a global model comparison of all the models with an eye for model selection and rejection.

Chapter 6

An overall global comparison of all models

6.1 Introduction

In this chapter, we present comparison of the results of all the three models. First the model structure will be compared from Chapter 2, then mathematical analysis will be compared followed by sensitivity analysis results and thereafter the numerical simulation results. Models will be compared both qualitatively and quantitatively where possible, outlining clearly similarities and differences between all the models.

6.2 Comparison of model formulation

Models GRM-1, GRM-2 and GRM-3 were formulated using different mathematical assumptions. The main differences between models GRM-1 and GRM-2 to model GRM-3 is the implementation of GEF module and the quasi-equilibrium assumption. In models GRM-1 and GRM-2, the activities of GEF are implemented via enzymatic activity and also the quasi-equilibrium assumption on GEF module, while in model GRM-3, the activation and inhibition of GEF module is implemented using mass action and also quasi-equilibrium assumption on Rho module. For easier comparison of models, we re-state all the model equations here.

Equations of model GRM-1

$$\begin{aligned}\frac{dR}{dt} &= k_0 E_p\left(k_3 R, k_4 M,\ K_{g3}/G_T,\ K_{g4}/G_T\right)\left(R_T - R\right) + \frac{k_1\left(R_T - R\right)^2}{K_{r1}^2 + \left(R_T - R\right)^2} \\ &\quad - k_2' M R - \frac{k_2 R^2}{K_{r2}^2 + R^2}, \end{aligned} \tag{6.1a}$$

$$\frac{dM}{dt} = k_5 R\left(M_T - M\right) - k_6 M + k_7\left(M_T - M\right). \tag{6.1b}$$

Equations of model GRM-2

$$\begin{aligned}\frac{dR}{dt} &= k_0 E_p\left(k_3 R, k_4 M,\ K_{g3}/G_T,\ K_{g4}/G_T\right)\frac{\left(R_T - R\right)}{K_{r0} + \left(R_T - R\right)} + k_1(R_T - R) \\ &\quad - \frac{k_2 R}{K_{r2} + R} - k_2' M R, \end{aligned} \tag{6.2a}$$

$$\frac{dM}{dt} = \frac{k_5 R(M_T - M)}{K_{m5} + (M_T - M)} - k_6 M + k_7(M_T - M). \tag{6.2b}$$

The Goldbeter-Koshland function $E_p(k_3 R,\ k_4 M,\ K_{g3}/G_T,\ K_{g4}/G_T)$ is the same for both models, as defined in Equation (2.8).

Equations of model GRM-3

$$\frac{dG}{dt} = k_3 R_T E_P\left(k_0 G + k_1, k_2, \frac{K_{r0}}{R_T}, \frac{K_{r2}}{R_T}\right)\left(G_T - G\right) - k_4 M G, \tag{6.3a}$$

$$\frac{dM}{dt} = \frac{k_5 R(G, M)(M_T - M)^n}{K_{m5}^n + (M_T - M)^n} + \frac{k_7(M_T - M)}{K_{m7} + (M_T - M)} - \frac{k_6 M}{K_{m6} + M}. \tag{6.3b}$$

The Goldbeter-Koshland function is defined in Equation (2.9).

Table 6.1 contains model parameters, and their corresponding model terms for all the models. These parameters do not include Michaelis constants as well as the concentrations of molecules, we only consider reaction rates. Some kinetic parameters are absorbed into the Golbeter-Koshland function, the reaction part of these kinetic parameters are not considered in comparison and hence written as G-K.

Models GRM-1 and GRM-2 describe the same reactions presented in Figure 2.1. Since the precise mechanism is unknown for a given reaction, modelling hypotheses (plausible assumptions) were made. We considered two models GRM-1 and GRM-2 whose differences stem from the mathematical form used to translate/represent each reaction. Model GRM-3 describes the reactions presented in Figure 2.2.

The following is observed from Table 6.1:

Parameters	Ezymatic activity on GEF-H1		Mass action on GEF-H1
	Model GRM-1	Model GRM-2	Model GRM-3
k_0	$k_0 E_p\,(R_T - R)$	$k_0 E_P \frac{(R_T - R)}{K_{r0} + (R_T - R)}$	G-K
k_1	$\frac{k_1 \left(R_T - R\right)^2}{K_{r1}^2 + \left(R_T - R\right)^2}$	$k_1 (R_T - R)$	G-K
k_2	$-\frac{k_2 R^2}{K_{r2}^2 + R^2}$	$-\frac{k_2 R}{K_{r2} + R}$	G-K
k_2'	$-k_2' M R$	$-k_2' M R$	NA
k_3	G-K	G-K	$R(G, M)(G_T - G)$
k_4	G-K	G-K	$-MG$
k_5	$k_5 R(M_T - M)$	$\frac{k_5 R(M_T - M)}{K_{m5} + (M_T - M)}$	$\frac{k_5 R(G,M)(M_T - M)^n}{K_{m5}^n + (M_T - M)^n}$
k_6	$-k_6 M$	$-k_6 M$	$-\frac{k_6 M}{K_{m6} + M}$
k_7	$k_7 \left(M_T - M\right)$	$k_7 (M_T - M)$	$\frac{k_7 (M_T - M)}{K_{m7} + (M_T - M)}$

Table 6.1: Comparison between models. Reactions related to parameters k_* can be found in Figures 2.1 and 2.2. The general form of the function $E_P(R, M)$ is defined in equation (2.8) for models GRM-1 and GRM-2 while it is defined in (2.9) for model GRM-3. G-K represents the parameters absorbed into the Goldbeter-Koshland function and NA refers to Not Applicable.

1. First note that all kinetic parameters relating to Rho, are absorbed into the Goldbeter-Koshland function for model GRM-3, while in models GRM-1 and GRM-2, all reaction rates relating to GEF-H1 are also absorbed into the Goldbeter-Koshland function. We will only consider reaction rates defined explicitly for comparison purposes.

2. Consider the GEF-associated Rho activation, a reaction related to k_0. This reaction is represented by mass action for model GRM-1, while it is represented by enzymatic activity for model GRM-2.

3. The self-activation of Rho, the reaction related to k_1. This is described by Hill type equation for model GRM-1, with Hill exponent 2, while the same reaction is represented by the law of mass action for model GRM-2.

4. The self-inhibition of Rho, the reaction related to k_2 is described by Hill type equation for model GRM-1, with Hill exponent 2, while the same reaction is described by enzymatic activity for model GRM-2.

5. For model GRM-3, the reactions involving k_0, k_1 and k_2 are absorbed into the Goldbeter-Koshland function. This is one of the main differences between model GRM-3 and models GRM-1 and GRM-2.

6. Myosin-associated Rho inhibition, reaction related to k_2' is represented by mass action for both models GRM-1 and GRM-2. For model GRM-3, we only considered Myosin-IIA and therefore $k_2' = 0$.

7. Consider the Rho associated GEF activation and Myosin associated GEF inhibition, reaction related to k_3 and k_4 respectively. These reactions are represented by mass action for model GRM-3, while they are absorbed into the Goldbeter-Koshland function for models GRM-1 and GRM-2.

8. Rho-associated Myosin activation, reaction related to k_5 is represented by mass action for model GRM-1, while it is represented as an enzymatic activity (Michaelis-Menten kinetics) for model GRM-2. The same reaction is represented by a Hill function for model GRM-3.

9. Myosin self-inhibition, reaction related to k_6 is represented by mass action for models GRM-1 and GRM-2, while it is represented by enzymatic activity for model GRM-3.

10. Myosin self activation is also represented by mass action for models GRM-1 and GRM-2 while it is represented by enzymatic activity for model GRM-3.

Therefore models GRM-1 and GRM-2 are similar in reactions involving k_2', k_3, k_4, k_6 and k_7. The rest of reactions involving k_0, k_1, k_2 and k_5 are different. By considering only reactions that are not absorbed into the Goldbeter-Koshland function, then model GRM-3 has no similar reaction to model GRM-1. This model is only similar to model GRM-2 in the reaction related to k_5 when the Hill exponent, $n = 1$.

6.3 Comparison of mathematical analysis results

In this section, mathematical analysis results for all the models are compared. First the qualitative analysis results of the asymptotic behaviour are compared, followed by the bifurcation analysis results. Models GRM-1 and GRM-2 have qualitatively

similar dynamics, they admit all the nullcline configurations in Figure 3.2. The theoretical dynamics are qualitatively similar as G_T varies. As G_T is varied, the nullcline configurations transition from Figure 3.2(c) $\mapsto$ 3.2(b) $\mapsto$ 3.2(a) and then to 3.2(d). These results on the other hand differ with theoretical results of model GRM-3. This model only admits three of the nullcline configurations in Figure 3.2. As G_T varies, the dynamics transition from Figure 3.2(a) $\mapsto$ 3.2(b) and then to 3.2(c).

The same comparison is observed from bifurcation analysis results. As G_T varies, the dynamics transition from stable, oscillatory, stable and then bistability. This is observed from their bifurcation diagrams 3.3 and 3.4. For small values of G_T the steady state is stable, the steady state becomes unstable when the value of G_T increases. For the unstable steady state, the solutions to the model are periodic. Further increase in G_T changes the stability of the steady state back to stable, thereafter the models reaches a region characterised by three steady states in which two are stable, separated by a saddle. The saddle acts as a switch which determines to which steady state the model converges to. Models GRM-1 and GRM-2 have three Hopf bifurcation points. Model GRM-3 behaves differently. For small values of G_T, the steady state is stable, as the value of G_T increases, the steady state becomes unstable characterised by periodic solutions arising from Hopf bifurcation. Further increase in G_T brings the system back to another region characterised by stable steady states.

Inherent in these models is what is called *excitability*, as discussed in Chapter 5. Models GRM-1 and GRM-2 have a region characterised by excitable dynamics, which lies between the last two Hopf bifurcation points. Model GRM-3 has no clear region for excitability defined. The difference between the behaviour of Models GRM-1 and GRM-2, and model GRM-3 is attributed to the mathematical translation of GEF module, and the quasi-steady state assumption. In models GRM-1 and model GRM-2, enzymatic activity was used to translate the GEF activities, while in model GRM-3, the law of mass action was used to describe GEF module. The quasi-equilibrium kinetics are assumed on GEF module (models GRM-1 and GRM-2) or on Rho module (model GRM-3).

6.4 Comparison of sensitivity analysis results

Sensitivity analysis results for all models are compared. We show comparisons for the local and global sensitivity analyses.

6.4.1 Local sensitivity analysis

We first compare local sensitivity analysis for all the models. Table 6.2 shows the model parameters, ranked from the most sensitive to the least. In general, for models GRM-1 and GRM-2, we observe that common parameters which largely influence the steady state values are k_3, k_4 and k_0. The parameter k_2 greatly affects the steady state for model GRM-1 but not GRM-2. For model GRM-3, the most sensitive parameter is G_T which has larger influence on the GEF steady state value, but not Myosin. The other parameters are k_6 and k_1. G_T has very little effect on the steady state values for models GRM-1 and GRM-2.

Table 6.3 shows comparison of parameters for all the models in terms of their ranking. It has parameters ranked in terms of period sensitivity and Rho, GEF and Myosin amplitudes. In terms of the period, k_3 and k_4 largely influence both models GRM-1 and GRM-2; K_{r2} largely influences model GRM-1 while G_T largely influences model GRM-2. Parameters k_2 and k_1 are highly ranked in terms of period sensitivity of model GRM-3. The period is highly sensitive to the following parameters; for model GRM-1, the 5 most sensitive parameters are; k_3, k_4, K_{r2}, k_5 and k_6. For model GRM-2, the following parameters have the largest influence on the period; k_3, k_4, G_T, k_5 and K_{g3}. The period of model GRM-3 is largely affected by k_2, k_1, k_0, k_6 and K_{r2}. On the other hand, the following parameters affect Rho/GEF amplitude: for model GRM-1, we have k_0, k_2, K_{r2}, k_2' and K_{g4}. For model GRM-2, we have k_3, k_4, k_0, K_{r0} and K_{g3} while G_T, k_2, k_0 k_4 and k_3 are the most sensitive for model GRM-3.

6.4.2 Global sensitivity results

We compare global sensitivity analysis results for all the models. eFAST method only provides the absolute values of sensitivity. Table 6.4 shows parameters for all the models arranged in order of their sensitivity ranking, the ranking is based in total

Model GRM-1		Model GRM-2		Model GRM-3	
Rho	Myosin	Rho	Myosin	GEF	Myosin
$-k_2$	$-k_2$	k_3	k_3	G_T	$-k_6$
k_3	k_3	$-k_4$	$-k_4$	$-k_2$	$-K_{m6}$
$-k_4$	$-k_4$	k_6	k_0	k_6	$-k_2$
k_0	k_0	k_0	K_{g4}	k_1	k_7
$-K_{g4}$	$-K_{g4}$	$-k_5$	$-k_2$	k_3	k_1
$-K_{g3}$	$-K_{g3}$	K_{g4}	$-K_{r0}$	$-k_4$	K_{r2}
k_1	k_1	$-k_2$	$-K_{g3}$	$-K_{m6}$	$-K_{m7}$
k_6	$-k_2'$	K_{m5}	$k-_2'$	$-k_7$	k_5
$-k_5$	$-k_6$	$-K_{r0}$	K_{r2}	K_{r2}	k_0
$-k_2'$	k_5	K_{g3}	$-k_6$	K_{m7}	G_T
$-G_T$	$-G_T$	$-k_2'$	k_5	k_0	$-k_4$
K_{r2}	K_{r2}	K_{r2}	$-G_T$	$-k_5$	k_3
$-K_{r1}$	$-K_{r1}$	$-G_T$	k_1	K_{m5}	$-K_{m5}$
$-k_7$	k_7	k_1	$-K_{m5}$	$-K_{r0}$	$-K_{r0}$
		$-k_7$	$+k_7$		

Table 6.2: Comparison of ranking parameter sensitivity for all models in the case of stable regime.

sensitivity index, s_{T_i}. The three models are largely affected by different parameters, for example considering the variable Rho; Rho is largely affected by k_2', k_0, k_3 and k_7 for model GRM-1, while affected by k_1, k_2', K_{g3} and k_2 for model GRM-2. For model GRM-3, the corresponding variable GEF is largely affected by G_T, k_3, k_4 and K_{m6}. We notice that Myosin is largely affected by same parameters, k_6, k_7 and k_5 for models GRM-1 and GRM-2. In general, different parameters are ranked differently depending on the model under consideration or the variable considered. Parameters which largely affect Rho (GEF) are different from those that largely affect Myosin. This different in parameter rankings for different models may be due to differences in the mathematical assumptions used in formulating the models.

Model GRM-1			Model GRM-2			Model GRM-3		
Period	Amplitude		Period	Amplitude		Period	Amplitude	
	Rho	Myosin		Rho	Myosin		GEF	Myosin
k_3	k_0	$-K_{r2}$	k_3	k_3	G_T	k_2	G_T	G_T
$-k_4$	$-k_2$	k_3	$-k_4$	$-k_4$	$-k_4$	$-k_1$	$-k_2$	$-k_2$
$-K_{r2}$	$-K_{r2}$	$-k_4$	G_T	k_0	k_3	$-k_0$	k_0	k_0
$-k_5$	$-k_2'$	k_0	$-k_5$	$-K_{r0}$	$-K_{g4}$	$-k_6$	$-k_4$	$-k_4$
$-k_6$	$-K_{g4}$	$-K_{g3}$	$-K_{g3}$	$-K_{g3}$	$-k_1$	$-K_{r2}$	k_3	$-K_{r2}$
k_2	$-k_3$	$-k_1$	$-k_1$	$-k_2$	$-K_{r2}$	$-k_3$	$-k_5$	k_3
$-K_{g3}$	k_4	$-k_2'$	K_{m5}	K_{g4}	$-k_5$	K_{m6}	$-K_{r2}$	k_5
$-k_1$	G_T	k_2	$-K_{r2}$	$-k_2'$	$-K_{g3}$	$-G_T$	$-K_{r0}$	$-K_{r0}$
$-k_2'$	$-K_{r1}$	G_T	$-K_{g4}$	K_{r2}	k_2	k_7	K_{m5}	K_{m5}
G_T	K_{g3}	$-K_{g4}$	K_{r0}	G_T	K_{m5}	k_4	k_1	k_6
k_0	$-k_5$	$-k_5$	$-k_2'$	$-k_5$	$-K_{r0}$	$-K_{m7}$	k_6	k_1
$-K_{g4}$	k_1	$-k_6$	k_2	K_{m5}	$-k_2'$	k_5	$-K_{m6}$	$-K_{m6}$
k_7	$-k_6$	$-K_{r1}$	k_0	$-k_1$	k_6	$-K_{m5}$	$-k_7$	$-k_7$
$-K_{r1}$	$-k_7$	$-k_7$	$-k_6$	$-k_6$	k_0	$-K_{r0}$	K_{m7}	K_{m7}
			k_7	$-k_7$	$-k_7$			

Table 6.3: Comparison of parameter sensitivity for all the models in the case of oscillatory dynamics, the sign in front of the parameter indicates how a parameter affects the model output. The parameters are ranked in terms of their sensitivity

6.5 Numerical simulation results

In this section, we compare numerical results of all the models, i.e. excitability, Rho response amplitude and Phase-plane and temporal evolution of all the variables.

Excitability results

From Chapter 5, it was observed that models GRM-1 and GRM-2 have a defined region associated with excitable dynamics. The excitability region for these models lies between oscillatory and bistability regimes. This is contrary to model GRM-3 that does not have a clear region defined for excitable dynamics, and it also occurs before the oscillatory regime. All these transition dynamics are dependent on the

Model GRM-1		Model GRM-2		Model GRM-3	
Rho	Myosin	Rho	Myosin	GEF	Myosin
k_2'	k_6	k_1	k_6	G_T	k_6
k_0	k_7	k_2'	k_7	k_3	K_{m6}
k_3	k_5	K_{g3}	k_5	k_4	K_{m7}
k_7	k_2'	k_2	K_{m5}	K_{m6}	k_5
k_6	k_0	G_T	K_{g3}	k_6	K_{m5}
K_{g4}	k_4	K_{r2}	$dummy$	K_{r0}	K_{r2}
k_4	K_{g4}	k_4	k_2'	K_{m7}	k_7
K_{g3}	k_3	K_{r0}	k_1	k_5	k_2
G_T	K_{g3}	k_7	K_{r2}	K_{r2}	K_{r0}
k_5	G_T	k_6	k_2	k_7	k_0
$dummy$	k_1	k_0	K_{g4}	K_{m5}	G_T
K_{r2}	$dummy$	k_5	k_0	k_2	k_4
K_{r1}	K_{r1}	K_{m5}	G_T	$dummy$	k_1
k_2	k_2	$dummy$	K_{r0}	k_0	$dummy$
k_1	K_{r2}	k_3	k_4	k_1	k_3
		K_{g4}	k_3		

Table 6.4: Comparison of global parameter sensitivity results for all the models.

positive feedback mediator GEF-H1.

Rho response amplitude and critical threshold

We noted that models GRM-1 and GRM-2 have the same qualitative behaviour in terms of trigger threshold and Rho response amplitude dynamics, similarly to peak width and frequency. This differs from what is observed with model GRM-3. Models GRM-1 and GRM-2 have four dynamic regimes, while model GRM-3 has only three dynamic regimes. In general for all models, we observe that the amplitude increases and finally decreases for higher values of G_T. For models GRM-1 and GRM-2, in general the trigger threshold is high in the bistable regime at high values of G_T, while for model GRM-3, the critical threshold is high at low G_T values.

Regarding response amplitude and threshold analyses, we can also analyse the stability of the model in parameter combinations G_T and k_1, as shown in Figure 6.1. We are able to characterise oscillatory regimes (blue region) for all the models. This also supports the mathematical analyses in Chapter 3. Models GRM-1 and GRM-2 have similar dynamics, model GRM-1 has a narrower region associated with oscillatory dynamics than model GRM-2.

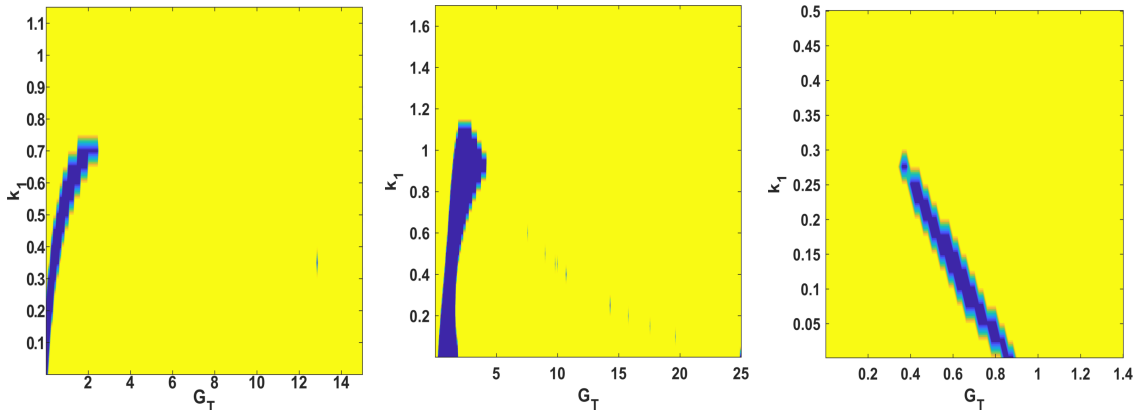

(a) Model GRM-1 (b) Model GRM-2 (c) Model GRM-3

Figure 6.1: Stability regions defined for models GRM-1, GRM-2 and GRM-3. Yellow coloured region is characterised by stable solutions of Rho, and Myosin, while blue region is characterised by periodic solutions.

Phase-planes and temporal analysis

Phase-planes and temporal analysis illustrate the mathematical analysis results. Models GRM-1 and GRM-2 exhibit up to four regimes, for suitable parameter ranges. Model GRM-1 and GRM-2 have similar qualitative dynamics. The behaviours of these models transition from stable, oscillatory, excitable and finally the bistable regime. Model GRM-3 has up to three regimes when G_T is varied while other parameters are fixed. The dynamics transition from stable, excitable, oscillatory and back to stable. The differences in dynamic behaviours of models GRM-1 and GRM-2, from model GRM-3 may be attributed to how GEF module was implemented in the two cases. The model formulation was through the positive feedback mediator whose concentration alters the system dynamics.

6.6 Conclusion

In this chapter, we have looked at the comparison of all the results corresponding to the models. In general models GRM-1 and GRM-2 are qualitatively similar with regard to their dynamics; as G_T varies, the dynamics of these two models transition from stable, oscillatory, excitability and then bistable regime. The dynamics of these two models differ from that of model GRM-3, whose dynamics transition from stable, excitable, oscillatory and then stable.

The difference of the qualitative results are due to how the GEF module was translated mathematically, and also the quasi-steady state assumption. In this thesis, models GRM-1 and GRM-2 were refined based on experimental results (Kamps et al., 2019), which resulted into model GRM-3. From here onwards, we reject models GRM-1 and GRM-2 and select only model GRM-3. This model will be used to find the optimal parameters such that the model fits data in a statistical sense. Work on rigorous model selection is omitted in this thesis, it will form the basis of our future studies. In the previous chapters, we sort to study the qualitative agreement between the mathematical models formulated and the experimental observations. Therefore in Chapter 7, we seek to link model GRM-3 to experimental observations, thus we seek to identify model parameters that satisfy the experimental observations. We will therefore apply the Bayesian paradigm to model GRM-3 with perturbation to estimate model parameters such that GRM-3 fits data in an optimal statistical sense.

Chapter 7

Parameter estimation and Bayesian approach

7.1 Introduction

In this thesis, we first started by formulating mathematical models from first principles, based on experimental observations (Graessl et al., 2017; Kamps et al., 2019). The mathematical analysis shows that model GRM-3 has similar qualitative dynamics to those observed in biological network. Therefore, in this chapter we identify optimal model parameters such that model GRM-3 best-fits experimental observations in a statistical sense.

This chapter explores the parameter identification problem by using the Bayesian approach in order for the model to fit to experimental data. Parameter estimation is the problem where the information about parameters of the model are extracted from the experimental data (Tarantola, 2005). In this study, the model is in the form of ODE for the GEF–Rho–Myosin network, whose parameters are the coefficients of the model. The data is the experimental measurements of Rho and Myosin responses to GEF-perturbation. The noise provides the experimental standard deviation. Parameter identification problem is referred to as an *inverse problem*, whereby given experimental and model solutions, what are the optimal parameters for the model to best-fit the data.

There are two main approaches for parameter identification problems. The first approach is the use of optimal control methods to find the best possible value for parameters (Aster et al., 2018). In this approach the best possible parameter is defined as one that minimises the distance from the model solution to the experimental data. In general this problem is ill-posed and therefore a regularisation term must be added and then the norm of parameter also minimised.

The second approach is the use of Bayesian methods, which consist of techniques that make use of the Bayes' theorem (Tarantola, 2005; Kaipio and Somersalo, 2006; Stuart, 2010; Campillo-Funollet et al., 2019). Bayes' theorem allows us to compute the conditional probability of parameters given data, in terms of the conditional probability of data given parameters. The amount of information obtained from the probability distribution of parameters is very large compared to a single value obtained from the optimal control methods. This probability distribution can also give information about the uncertainty of parameters (Gutenkunst et al., 2007), as well as model selection in the case where several models exist, and one needs to find one which fits better to the experimental data (Vyshemirsky and Girolami, 2007). The method can also allow one to extract information about the correlations of parameters, which may not be visible from one value computed with optimal control methods (Sutton et al., 2016). The probability distribution can also suggest a non-dimensionalised model to eliminate irrelevant parameters. The main drawback of Bayesian method is its computational cost, but the use of paralellised algorithms can help speed up the method. Given these advantages of Bayesian method over optimal control methods, we applied it to identify parameters of GEF–Rho–Myosin model such that the model best-fits experimental data.

Figure 7.1 shows a schematic representation of components that are needed for parameter identification problem. The mathematical model formulated, model GRM-3 is combined with biological data to approximate the parameters using the Bayesian technique. The goal is to obtain the set of parameters that satisfy both the perturbation kinetics and oscillatory dynamics, by changing the bifurcation parameter, G_T, while the rest of the parameters remain fixed.

We aim to extract the parameters of the model using biological data. Model GRM-

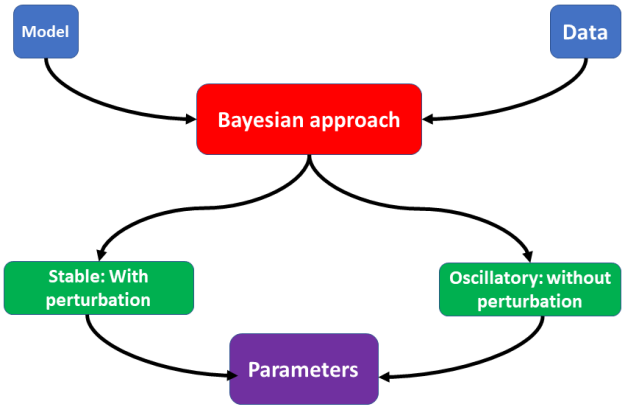

Figure 7.1: Schematic representation of parameter approximation procedure.

3 is more compatible to the experimental observations (Kamps et al., 2019), and therefore it will be fitted to the data. In this chapter, we first describe the Bayesian method for parameter identification, thereafter we describe the model with perturbation and the biological data together with normalisation process and then apply the method to the model.

NOTE: It must be noted that the content of this chapter was done in collaboration with Dr Eduard Campillo-Funollet, who was Prof. Madzvamuse's PhD student at the University of Sussex. The work here follows closely his recently published work in Campillo-Funollet et al. (2019). Eduard was in charge of the numerical implementation of the fitting algorithm.

7.2 Bayesian approach to parameter identification

In this study, a Bayesian approach for parameter identification was applied to the model of Rho-Myosin dynamics. This Bayesian approach provides a rigorous mathematical framework that allows the incorporation of the prior knowledge about the uncertainty of the observation and also the prior knowledge of the parameters (Campillo-Funollet et al., 2019). This results in the approximation of full probability distribution of the parameters given the data. The key idea in the Bayesian approach to parameter identification is to represent our knowledge about a quantity with a probability distribution. Typically, these quantities will be the parameters of the mathematical model.

Bayesian techniques have commonly been applied to parameter fitting in statistics (Ma and Leijon, 2011; Fan and Mellor, 2012; Taghia et al., 2014; Ma et al., 2015). Bayesian techniques are also used in many fields which are governed by partial differential equations (Stuart, 2010; Campillo-Funollet et al., 2019). A recent example has been the application of Bayesian technique to parameter identification of Turing systems on stationary and evolving domains (Campillo-Funollet et al., 2019). Bayesian approach treats the model as a random variable with a probability distribution. A prior distribution of model parameters is combined with data to obtain the posterior distribution of parameters (Aster et al., 2018).

Consider the set of parameters $\mathbf{p} \in \mathbb{R}^K$ of the mathematical model. Let $\mathcal{H} : \mathbb{R}^K \to \mathbb{R}^N$ be the mapping that assigns to each parameter $\mathbf{p}$ the solution to the ODE system evaluated at the observation time points. Let $y \in \mathbb{R}^N$ be the experimental measurement. We assume that y corresponds to a solution of the mathematical model with some noise η, which is naturally modelled by means of some probability distribution. Mathematically, we have;

$$y = \mathcal{H}(\mathbf{p}) + \eta. \tag{7.1}$$

Equation (7.1) gives as the probability of observing data y given a parameter $\mathbf{p}$; we are interested in the reverse condition, the probability of a parameter $\mathbf{p}$ given that we observe y. Bayes' theorem can help us obtain this using the marginal distribution for $\mathbf{p}$. This marginal distribution represents the knowledge about the parameter, called *prior*. The probability distribution of the parameter given the data is the *posterior* denoted $\mathbb{P}(\mathbf{p}|y)$. The posterior distribution encodes all the information available about a parameter estimated.

To approximate the posterior distribution we use a parallel Markov Chain Monte Carlo (MCMC) method, which generates a Markov Chain of samples distributed as the posterior. The method is implemented to run in parallel using multiple processors. The posterior distribution provides information not only about the best parameter, but also about possible correlations between parameters, and credible regions. In particular, when it is possible to make plausible assumptions on the experimental noise, the method provides robust error bars for the parameters.

Applying Bayes' formula to Equation (7.1), we obtain;

$$\pi^y(\mathbf{p}) \propto \rho(y - \mathcal{H}(\mathbf{p}))\, \pi_0(\mathbf{p}), \tag{7.2}$$

where $\pi^y(\mathbf{p})$ denote the probability density function of the probability measure $\mathbb{P}(\mathbf{p}|y)$, $\pi_0(\mathbf{p})$ is the probability measure of the prior. The probability of data given parameters has density $\rho(y|\mathbf{p}) := \rho(y - \mathcal{H}(\mathbf{p}))$, which is referred to as the *data likelihood*. The constant of proportionality in Equation (7.2) depends only on the data y. Equation (7.2) is in finite dimensional setting, this can be extended to infnite dimensional setting by using Radon-Nikodym derivative (Stuart, 2010). We thus obtain;

$$\frac{d\mathbb{P}^y}{d\mathbb{P}_0}(\mathbf{p}) \propto \exp(-\phi((\mathbf{p}); y)). \tag{7.3}$$

The potential $\phi((\mathbf{p}); y)$ corresponds to the negative log-likelihood. Equation (7.3) generalises Bayes' theorem to infinite dimensional setting. A useful approach to extracting information from posterior distribution is to find a *maximum posterior estimator*, or MAP estimator. This is a parameter set $\mathbf{p}$ which maximizes the posterior probability density function $\pi^y(\mathbf{p})$ (Stuart, 2010), or alternatively produce samples from posterior distribution, by using Markov Chain Monte Carlo methods. In particular, we use Parallel Metropolis-Hastings method to sample from a posterior distribution. The full description of Bayesian method and MCMC methods are provided in Appendix D.

The implementation by Eduard Campillo Funollet was done in Python, using the module Scipy (Johansson et al., 2014). I implemented the solver for the model solution in Python, which was incorporated into the Bayesian method code. The numerical results about fitting are provided in a later section. In the next section, we first discuss the experimental data, and how it was normalised. The experimental data was normalised, since the goal was to fit the model parameters to the shape of response curves, rather than the values themselves. The model simulations were also normalised in a similar fashion.

7.3 Experimental data and the model with perturbation

The experimental data is in two forms: First, for small G_T values in the stable regime, a light is used to induce a perturbation of GEF-H1. The response of Rho and respectively Myosin is then recorded against the corresponding GEF-H1 (perturbation). In this section, we describe the model with perturbation, and then the normalisation of experimental data. The normalisation will be done for data in the stable regime only (responses of Rho and Myosin to GEF perturbation), but not in the oscillatory regime. In the oscillatory regime, we fit the scalar values, period and time-shifts between GEF, Rho and Myosin, and therefore, there is no need to normalise the period and time-shifts.

7.3.1 Formulation of model with perturbation

Model GRM-3 was modified to include GEF-H1 (perturbation). To experimentally incorporate perturbation, Kamps et al. (2019) uses a light pulse to trigger a perturbation of GEF-H1, based on a method provided in Chen et al. (2017). This experimental set-up generates data of GEF perturbation as shown in Figures 7.2(b) and 7.3(b). We observe from the data shown that GEF perturbation recruitment follows single association kinetics, and therefore we mathematically model this as:

$$\frac{dG_{p,\text{vis}}}{dt} = k_{GP} - k_{GP}G_{p,\text{vis}}. \tag{7.4}$$

Equation (7.4) describes the observed recruitment of GEF-H1 perturbation, where the constant k_{GP} can be obtained by fitting this equation to the data shown in Figures 7.2(b) and 7.3(b). We obtain two distinct k_{GP} corresponding to GEF perturbation with respect to Rho and Myosin responses.

It is expected that GEF perturbation follows the same kinetics as the normal GEF-H1. Therefore, GEF perturbation is inhibited by Myosin, and it also activates Rho in the same way as normal GEF. Therefore, Equation (7.4) is modified by including a term with Myosin inhibition, which leads to Equation (7.5) as shown

$$\frac{dG_{p,\text{Active}}}{dt} = k_{GP} - k_{GP}G_{p,\text{Active}} - k_4 G_{p,\text{Active}} M. \tag{7.5}$$

Equation (7.5) describes the activity of GEF perturbation, which includes the inhibition by Myosin in the same way as normal GEF-H1 and it also activates Rho. This perturbation activity is then added to the term that describes Rho activity, with a perturbation strength denoted, G_{pt} as shown in Equation (7.6).

$$R(G,M) = R_T E_P \left(k_0(G + G_{pt}G_{p,\text{Active}}) + k_1, k_2, \frac{K_{r0}}{R_T}, \frac{K_{r2}}{R_T} \right). \tag{7.6}$$

The full model with perturbation is then stated by the three ODEs of the form:

$$\frac{dG}{dt} = k_3 R(G,M)(G_T - G) - k_4 MG, \tag{7.7a}$$

$$\frac{dM}{dt} = \frac{k_5 R(G,M)(M_T - M)^n}{K_{m5}^n + (M_T - M)^n} + \frac{k_7(M_T - M)}{K_{m7} + (M_T - M)} - \frac{k_6 M}{K_{m6} + M}, \tag{7.7b}$$

$$\frac{dG_{p,\text{Active}}}{dt} = k_{GP} - k_{GP}G_{p,\text{Active}} - k_4 G_{p,\text{Active}} M, \tag{7.7c}$$

where $R(G,M)$ is given in Equation (7.6). We remark that the values of G_{pt} and k_{GP}, are dependent on the Rho response data, or Myosin response data, and therefore they are different for each case. In the oscillatory regime, we consider the model without perturbation, therefore $G_{pt} = 0$. This recovers the original model GRM-3, that is used to analyse system dynamics.

Model Equations (7.7) quantitatively describe the perturbation, and can be used to fit the unknown model parameters. We also remark that this does not affect the mathematical analysis of the original model, as the unperturbed model is considered for analysing the dynamics. The model we have described only fits the parameters to the perturbation kinetics. The goal is to obtain parameters that provide predictions about changes in dynamic state depending on the concentration of GEF-H1. Therefore the perturbation kinetics will be combined with the oscillatory dynamics data to approximate parameters that simultaneously satisfy the two regimes. In the next section, we first describe the biological data and how it was normalised.

7.3.2 Normalisation of biological data and model simulations

For the data and simulations to be compatible, both of them are normalised between 0 and 100%. We are only interested in fitting the qualitative dynamics and shape

of response curves, and that is why both model simulations and the biological data are normalised. The experimental data was normalised as follows:

Consider the raw fluorescence intensity (camera count) for a single cell given by $I^{(i)}(t),\ i \in \{1, \cdots, N\}$ at a time, t where N is the total cell population. The value at $t = 0$ is given by $I^{(i)}(0)$. For simplicity we shall denote $I^{(i)}(0)$ as $I_0^{(i)}$. The percentage increase in the camera count of cell i from $I_0^{(i)}$, at time t is given by:

$$I_{\%\text{inc}}^{(i)}(t) = \frac{100\, I^{(i)}(t)}{I_0^{(i)}} - 100.$$

The raw camera count contains the background activity, which is defined as,

$$I_{\%\text{inc},b}^{(i)} = \frac{1}{N} \sum_{i=1}^{N} I_{\%\text{inc},c,t_1}^{(i)},$$

where $I_{\%\text{inc},c,t_1}^{(i)}$ is the first measurement, $I_{\%\text{inc}}^{(i)}(t_1)$ for the control measurement without GEF-H1 (control perturbation), i.e. the first measurement after photo activation. The values were corrected by removing the background measurement to obtain

$$I_{\%\text{inc},bc}^{(i)}(t) = \begin{cases} I_{\%\text{inc}}^{(i)}(t), & \text{for } t \leq 0 \\ I_{\%\text{inc}}^{(i)}(t) - I_{\%\text{inc},b}^{(i)}(t), & \text{otherwise.} \end{cases}$$

The background corrected values are then normalised to max = 100, i.e.

$$I_{\text{norm}}^{(i)}(t) = \frac{100\, I_{\%\text{inc},bc}^{(i)}(t)}{\max(I_{\%\text{inc},bc}^{(i)}(t))}.$$

From the normalised values, we can find the mean and standard deviation. The mean of the normalised data is also normalised to maximum, 100. This normalised mean, denoted $I_{\text{norm, avg}}^{(i)}(t)$ and the corresponding standard deviation of the data will be used in fitting the parameters. For each data set, and for each time point, we compute the mean and standard deviation of the measurement. In each data set, there are N different measurements for each time point, corresponding to the cell population. The mean is the data to fit the model (y), and we assume that the experimental standard deviation is a good approximation of the standard deviation of the experimental noise η.

A plot of raw data (mean± standard deviation) is shown in Figures 7.2 and 7.3. Figure 7.2(a) shows the percentage increase in Rho response corresponding to the

percentage increase in GEF-H1 perturbation (Figure 7.2(b)), while Figure 7.3(a) shows the percentage increase in Myosin response corresponding to the percentage increase in GEF-H1 perturbation (Figure 7.3(b)).

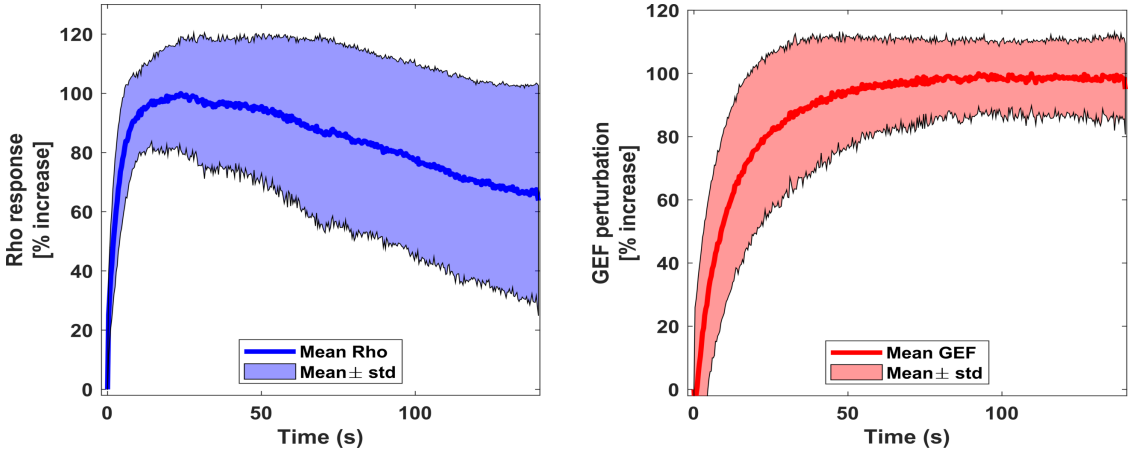

(a) (b)

Figure 7.2: Figure 7.2(a) represents Rho response induced by GEF-H1 perturbation (Figure 7.2(b)).

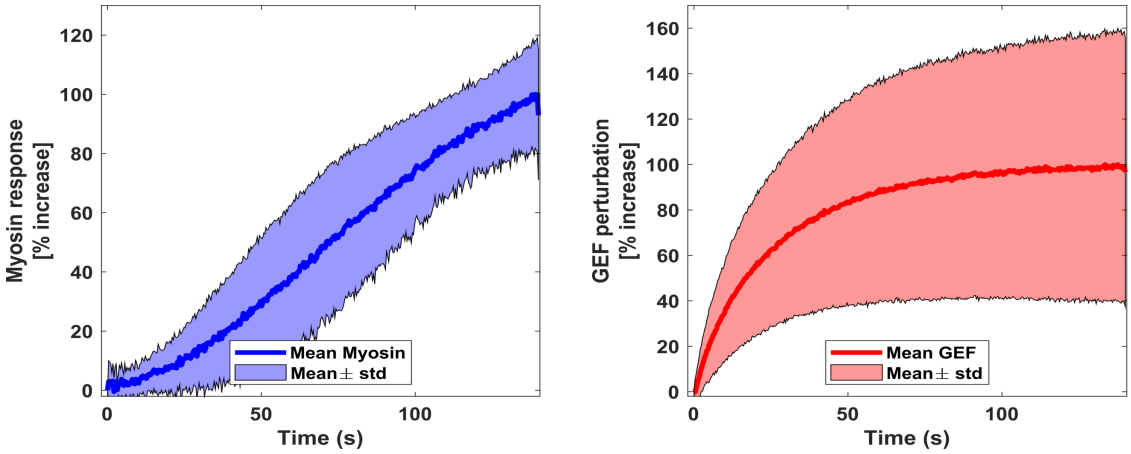

(a) (b)

Figure 7.3: Figure 7.3(a) represents Myosin response induced by GEF-H1 perturbation (Figure 7.3(b)).

The second set of data describes the cross-correlation of each pair of GEF, Rho and Myosin, which describes the dynamics in the oscillatory regime that is used to fit the period and amplitude of the model to data. Due to the irregularity of pulses in the experimental data, the cross-correlation and autocorrelation of peaks are blurred after the main peak. Therefore after the main peak, little information

may be provided by the cross-correlation data. It was therefore suggested that a better way to represent information in the oscillatory regime is the use of time shifts between variables and the pulse period. This is used to fit kinetics that satisfy the oscillatory dynamics.

The period was determined by fast Fourier transform. To remove cells with irregular periods from the analysis, only cells in which the main frequency has an amplitude that is larger than 5% of the sum of all amplitudes was considered. The time shifts were obtained as the maximum of the cross correlation curve for an individual cell. The sign of the time shift is according to the text labels. These data is shown in Table 7.3.

7.4 Numerical implementation of Bayesian algorithm and results

The implementation was done in python, by Campillo-Funollet et al. (2019). The following experimental prior was used for the parameters.

7.4.1 Description of prior

In total, there are 25 parameters in the system. 8 of them are known or given by other parameters, hence we do not fit them to data. For the rest of the parameters, we define the prior as a uniform distribution. The other parameters such as G_T, G_{pt}, and k_{GP} are split in order to characterise different regimes, and also to differentiate between Rho response values from Myosin response data. For the terms involving enzymatic activity, we use the following ratio $k_* = \frac{k'_*}{K_M}$. The parameter k_* represents the reaction speed at saturation while k'_* represents the reaction speed at negligible saturation as defined in Koshland Jr (2002) and is commonly referred to as *performance ratio* of an enzyme (Koshland Jr, 2002). The prior of k'_* may be found from experimental assumption and so will be used in fitting, and not k_*.

For the prior, we assume that the parameters are independent of each other. We also impose, in the prior definition, a restriction on the parameters given by the dynamics that the parameters exhibits in the reduced (G, M) model. To validate if

parameters	Fitting Rho perturbation response	Fitting Myosin perturbation response	Fitting Rho and Myosin oscillations
K'_0	0.316049632 to 31.60496324		
K_{r0}	0.0474609 to 47.4609		
k_1	0 (fixed)		
K_{r1}	$=K_{r0}$		
K'_2	0.15 to 150		
K_{r2}	0.01 to 10		
k_3	0.15 to 15		
k_4	0.015 to 15		
K'_5	0.0049943397 to 4.994339748		
K_{m5}	0.0030034 to 3.0034		
K'_6	0.0008444444444 to 2.666666667		
K_{m6}	0.05625 to 5.625		
k_7	0 (fixed)		
K_{m7}	Not relevant, since $k_7 = 0$		
G_T	0.00142 to 1		0.1 to 20
G_{pt}	0.01 to 1	0.01 to 1	0 (fixed)
k_{GP}	data (fixed)	data (fixed)	Not relevant, since $G_{pt} = 0$
R_T	0.443 (fixed)		
M_T	1.24 (fixed)		
n	1 to 5		

Table 7.1: Lower and upper bounds for prior.

a parameter exhibits the right dynamics, we vary G_T from 0.0142 to 20, leaving the rest of parameters fixed, and compute the steady state solution for each G_T using a continuation method. A parameter is valid if the dynamics at the steady state are stable for small G_T, and they become unstable at some point. The continuation method for the fixed points is a predictor-corrector algorithm. The prediction step is a linear approximation of the curve of steady states, whilst the correction step is performed by means of a truncated Newton algorithm.

We have three different datasets; the first data set is for Rho response to GEF perturbation, the second dataset is for Myosin response to GEF perturbation, and the third data set if for the period and time shits. In each data set for the perturbation

response, there are different measurements corresponding to different cells, for each time point. For each data set, and for each time point, we compute the mean and standard deviation of the measurement. The normalised mean is the data to fit the model (y), and we assume that the experimental standard deviation is a good approximation of the standard deviation of the experimental noise η. A plot of normalised data (mean$\pm$ standard deviation) is shown in Figures 7.2 and 7.3. With the assumption that the experimental noise η is Gaussian, the negative log-likelihood is the squared distance between the data and the solution to the model, with weights given by the standard deviation.

The posterior distribution does not provide what is considered a single solution. However we can estimate the optimum parameter values that corresponds to the largest values of the likelihood. This value which maximises log-likelihood is referred to as the maximum posterior (MAP) value (Aster et al., 2018). The following values in Table 7.2 were identified as the ones which maximise the likelihood, and therefore, they are the best approximate values that best connects the model to the data. These approximated parameter values are used to study model dynamics.

The parameters in Table 7.2 were used to generate the results, shown in Figures 7.4 and 7.5. The Rho response to GEF perturbation fits better at higher values, where the model simulation lies within the range of experimental data as shown in Figure 7.4(a). The model simulation corresponding to Myosin response fits better, the model simulation lies within the data range at all time points, see Figure 7.5(a). The fit is even better, for GEF perturbations, see Figures 7.4(b) and 7.5(b).

This provides the optimal parameter values that describe the experimental data. Therefore the model represents the experimental data, with parameter values in Table 7.2. We also investigate how well the model describes biological data, in the oscillatory regime.

We further illustrated how the estimated parameters best fit to the experimental data in the case of oscillatory dynamics. Figure 7.6 represents GEF, Rho and Myosin in the oscillatory regime. The values are normalised between 0 and 100%. Based on these values, we obtain the period and time shifts for oscillatory dynamics. The period and time shifts are shown in Table 7.3. Model simulation using the approx-

parameters	Fitting Rho perturbation response	Fitting Myosin perturbation response	Fitting Rho and Myosin oscillations
K_0'	2.0029821110183295		
K_{r0}	0.37480474714530848		
k_1	0		
K_{r1}	0.37480474714530848		
K_2'	2.0537442837103903		
K_{r2}	0.093132809252206558		
k_3	1.3350504567204298		
k_4	1.9336450919021999		
K_5'	0.43171212210802096		
K_{m5}	0.026557314554939367		
K_6'	0.004848137676027436		
K_{m6}	0.47961927660495896		
k_7	0		
K_{m7}	Not relevant, since $k_7 = 0$		
G_T	0.0098222719379802131		0.73099999999999987
G_{pt}	0.13825057594065401	0.100009699822926	0
k_{GP}	0.078907890789078908	0.039703970397039705	Not relevant, since $G_{pt} = 0$
R_T	0.443 (fixed)		
M_T	1.24 (fixed)		
n	1.0818412088003961		

Table 7.2: Best fit parameters from the Bayesian method.

imated parameter values produces period and time shifts that lie within the range of biological data.

	Period	Rho shift after GEF	Myosin shift after Rho
Data	248.324989 ± 90.128913	2.51470588 ± 5.57961797	39.4864865 ± 14.5055844
Model	240.1479	0	39.8027

Table 7.3: Period and time shifts in the oscillatory regime, using parameter values in Table 7.2.

We have already shown that the approximated parameter values satisfy experimental data, both perturbation kinetics and oscillatory dynamics. In the next section, we therefore, illustrate the dynamics of the model, by using parameters in Table 7.2 and plotting one and two parameter bifurcation diagrams.

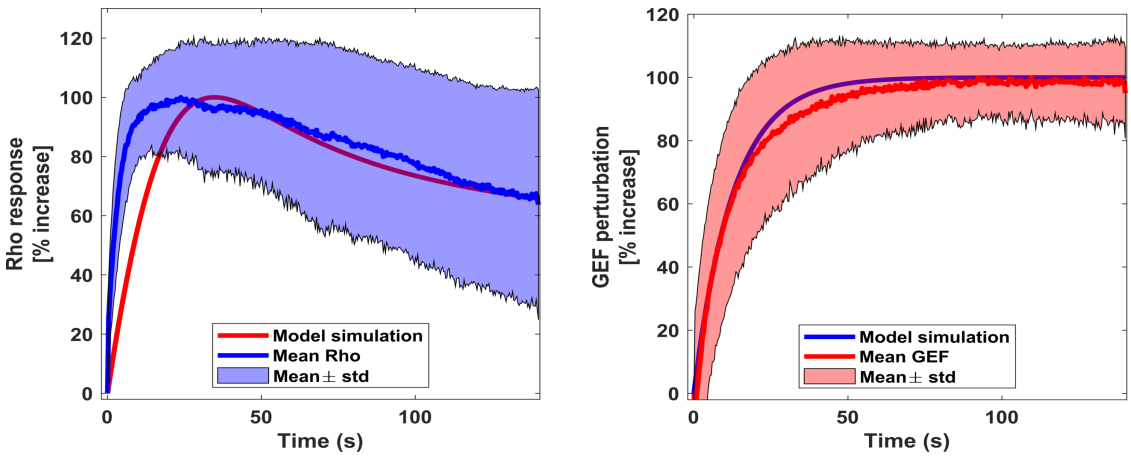

(a) (b)

Figure 7.4: Figure 7.4(a) represents Rho response induced by GEF-H1 perturbation (Figure 7.4(b)).

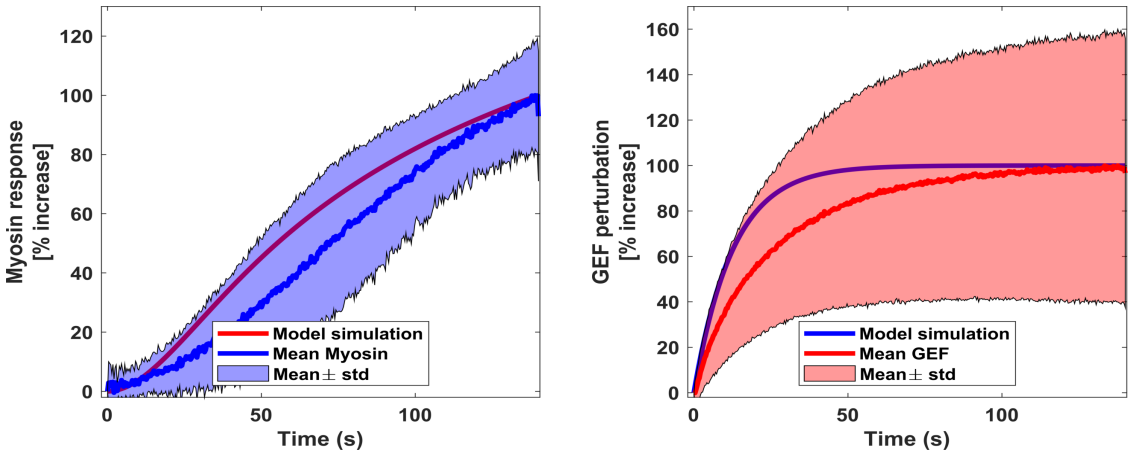

(a) (b)

Figure 7.5: Figure 7.5(a) represents Myosin response induced by GEF-H1 perturbation (Figure 7.5(b)).

7.5 Bifurcation analysis of model GRM-3 using estimated parameter values

In this section, we perform bifurcation analysis of model GRM-3 with parameter values listed in Table 7.2. The bifurcation parameter is G_T, and we want to illustrate that we still obtain the same model dynamics as illustrated theoretically in Chapter 3. Bifurcation analysis of model GRM-3 was carried out with approximated parameter values listed in Table 7.2. The Rho activity is defined implicitly by $R(G, M)$ in the form of Goldbeter-Koshland function and therefore we shall derive

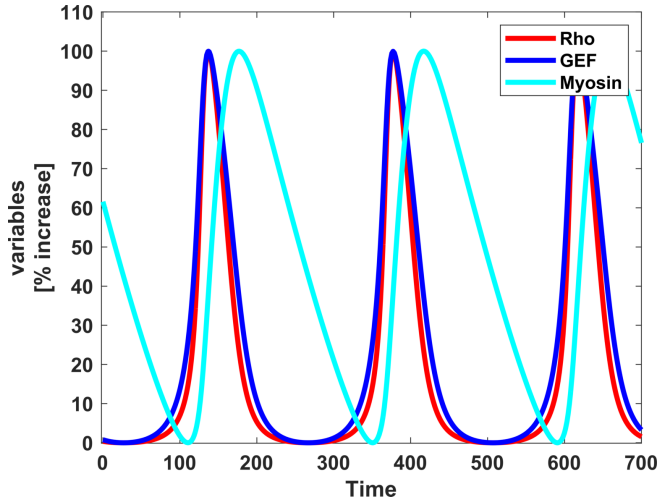

Figure 7.6: Normalised time series of GEF, Rho and Myosin, using parameter values in Table 7.2 to illustrate the behaviour in the oscillatory regime.

its bifurcation diagram from GEF and Myosin bifurcation diagrams. One parameter bifurcation diagrams were obtained by taking G_T as the bifurcation parameter, they represent the value of equilibria of Rho and Myosin as G_T varies, as shown in Figures 7.7(a) and 7.7(b). As G_T varies, the following can be deduced:

1. $G_T < 0.605942$ similar to $4.231679 < G_T$: Situation as in Figure 3.2(a) or 3.2(c), a unique equilibrium state which is G.A.S. (*stable regime*).

2. $0.605942 < G_T < 4.231679$: Situation as in Figure 3.2(b), there is a unique equilibrium state which is unstable and therefore existence of a stable limit cycle (*oscillatory regime*).

A two-parameter bifurcation diagram was derived from one parameter diagrams by considering GEF concentration and Rho constant activation parameter defined by k_1. This defines a region of plane where the model exhibit different dynamics as shown in Figure 7.7(c). We observe that the model exhibits all the dynamics for small values of k_1. At higher values of k_1, the model show stable dynamics everywhere, see Figure 7.7(c). The following regions are defined:

1. The red region is characterised by unstable steady state (node or spiral). The steady state is unique and therefore there exits a stable periodic obit (limit cycle). This region corresponds to red dashed lines in Figures 7.7(a) and 7.7(b).

2. The uncoloured region is characterised by the steady state which is unique and stable, and therefore globally asymptotically stable.

The results are summarised in Figure 7.7 and the bifurcation parameters listed in Table 7.4.

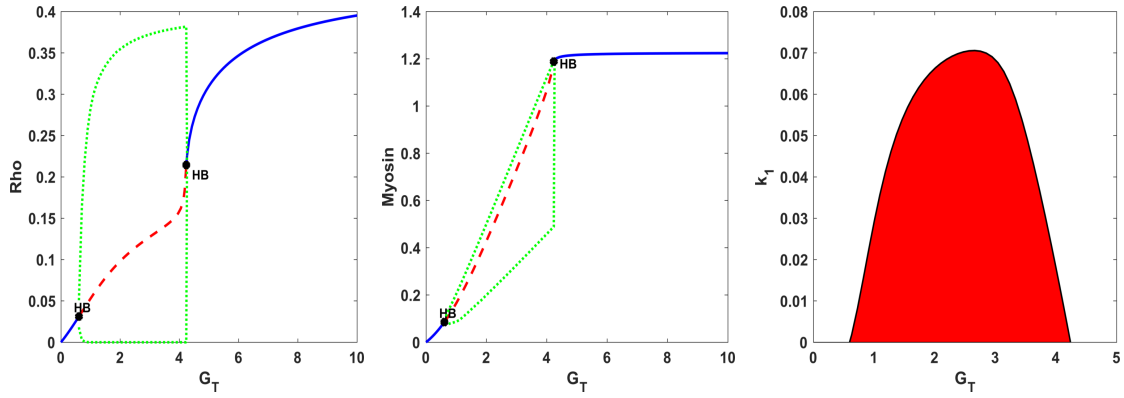

(a) (b) (c)

Figure 7.7: Bifurcation diagrams corresponding to model equations (2.26). G_T is the bifurcation parameter. In Figure 7.7(a), **HB** are Hopf bifurcation points, red dashed line represents respectively values of R and M in the unstable region while blue line represent their values in the stable region. Green dotted line is the maximum and minimum values of Rho and Myosin in the oscillatory regime. Figure 7.7(c) represents two-parameter bifurcation diagram, bifurcation parameters are G_T and k_1. The red region is the unstable region, where the model exhibits oscillatory dynamics.

	Bifurcation points	
	HB	**HB**
G_T	0.605942	4.231679
Rho	0.0312	0.468786
Myosin	0.0.2144	1.188030

Table 7.4: Hopf bifurcation (**HB**) parameter values for model GRM-3.

The Bifurcation analysis of the model produces results which are similar to those observed experimentally (Kamps et al., 2019). For small values of G_T, the model shows stable dynamics of Rho activity. As values of G_T increases, the dynamics changes and periodic pulses of Rho activity are observed. These pulses disappear again at higher G_T values. This is similar to the dynamics of model GRM-3. It was

also shown that the peak width of periodic pulses increases as the expression levels of GEF increases (Graessl et al., 2017; Kamps et al., 2019). We also analysed period and frequency of the oscillatory dynamics, results are shown in Figure 7.8. As G_T increases in the oscillatory regime, the peak width also increases, this implies that the frequency of oscillations decreases. These results are in line with experimental observations.

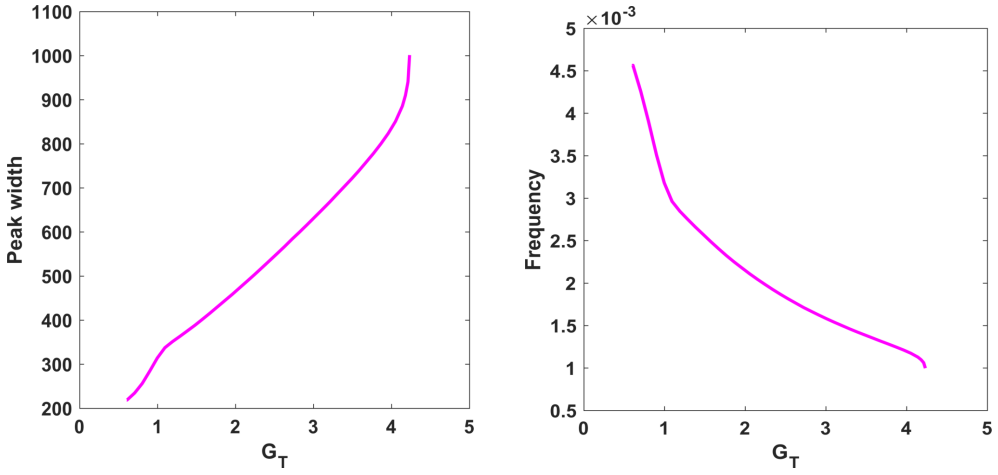

(a) (b)

Figure 7.8: Period and frequency of oscillations for model GRM-3 in the oscillatory regime, with parameter values in Table 7.2.

7.6 Conclusion

In this chapter, we employed the full Bayesian parameter identification approach to estimate model parameters from experimental data. This method allows the incorporation of our knowledge about the parameters (prior) into the parameter identification problem. First the model with perturbation was formulated from first principles based on the experimental observations. This model is used to fit the unknown parameters, but does not affect the model dynamics, as the dynamics are analysed on the model without perturbation. The parameters approximated by Bayesian algorithm are in the form of distribution, called the *posterior* distribution. In this work, we approximated the parameters that maximises the log-likelihood, that is the maximum posterior (MAP) value. We performed bifurcation analysis with the approximated parameters, to illustrate that they satisfy experimental res-

ults.

We also note that in this chapter, we only fitted to the shape of curves (biological experimental data) and thus both experimental data and model solutions were normalised between 0 to 100%. Therefore the approximated parameters represent the qualitative dynamics of biological experimental data, but not the quantitative results. The results in this chapter will be extended to analyse the posterior distribution, and identify correlation between parameters and credible regions given 95% confidence intervals, such work is beyond the scope of this thesis.

Chapter 8

Mathematical formulation and analysis of spatially inhomogeneous models

This chapter explores the effect of spatial inhomogeneity to models GRM-1 (2.11), GRM-2 (2.16) and GRM-3 (2.26), formulated in Chapter 2. We therefore formulate and analyse spatially extended models. Mathematical analysis for the possibility of Turing instability is performed in general, and then the results are illustrated numerically using the kinetic equations corresponding to model GRM-3. Finally, numerical simulations for the full reaction-diffusion models are presented for the parameters corresponding to stable, excitable, oscillatory and bistable regimes, to investigate the effect of adding diffusion to spatially homogeneous models in various dynamics regimes corresponding to stable, oscillatory, excitable and bistable.

8.1 Mathematical formulation of spatial model

Consider the general model describing the reactions given by:

$$\frac{dR}{dt} = f(R, M), \tag{8.1a}$$

$$\frac{dM}{dt} = g(R, M). \tag{8.1b}$$

System (8.1) represents the temporal activities of R and M corresponding to models GRM-1 (2.11), GRM-2 (2.16) and GRM-3 (2.26), which were formulated in Chapter 2. The variable R represents Rho in models GRM-1 and GRM-2 and GEF in model GRM-3. The variable M represents Myosin in the three models. It is known that these molecules diffuse within the cell, and hence in this chapter we consider both temporal and spatial activities, which lead to reaction-diffusion system given as:

$$\frac{\partial R}{\partial t} = f(R, M) + D_R \nabla^2 R, \tag{8.2a}$$

$$\frac{\partial M}{\partial t} = g(R, M) + D_M \nabla^2 M. \tag{8.2b}$$

The functions $f(R, M)$ and $g(R, M)$ correspond to the right hand sides of the ODE models in Chapter 2. The parameters D_R and D_M represent respectively the diffusion coefficients of R and M. We define the Laplace operator ∇^2 as;

$$\nabla^2 = \sum_{i=1}^{n} \frac{\partial^2}{\partial x_i^2},$$

where n is the space dimension. The system (8.2) is defined on a spatial domain which represents the cell. In this chapter, we describe the cell as 1-D domain such that:

$$\Omega = \{x,\ 0 \leq x \leq L\},$$

where L is the cell diameter.

We assume that the proteins (Rho, GEF and Myosin) do not leave or enter the cell, and therefore system (8.2) is defined subject to no-flux boundary conditions, which in 1-D are written as

$$\left.\frac{\partial R}{\partial x}\right|_{\partial\Omega} = \left.\frac{\partial M}{\partial x}\right|_{\partial\Omega} = 0, \tag{8.3}$$

where $\partial\Omega$ represents the cell boundary. We define initial conditions as:

$$R(x, 0) = R_0 \text{ and } M(x, 0) = M_0,\ \forall x \in \Omega. \tag{8.4}$$

8.2 Turing instability

We want to analyse system (8.2) for the existence of spatial patterns. These patterns arise when the steady state which is stable in the absence of diffusion becomes unstable to small perturbations in the presence of diffusion. This phenomenon is called Turing instability or diffusion-driven instability (Turing, 1952; Murray, 2003). Turing (1952) suggested that under certain conditions, chemical components can react and diffuse in such a way that they produce spatial patterns. Sarfaraz and Madzvamuse (2017) explored the bifurcation analysis of reaction-diffusion system with Schnakenberg reaction kinetics. Their analysis relates the domain-size with reaction-diffusion rates to the type of diffusion-driven instability (Turing, Hopf and Transcritical type bifurcations).

8.2.1 Mathematical analysis

For the mathematical analysis, we adimensionalise time and space variables in the system (8.2) by introducing a typical length scale L and setting $t^* = \frac{D_R t}{L^2}$, $\gamma = \frac{L^2}{D_R}$, $d = \frac{D_M}{D_R}$ and $x^* = \frac{x}{L}$. On dropping $*$, the new system becomes

$$\frac{\partial R}{\partial t} = \gamma f(R, M) + \nabla^2 R, \tag{8.5a}$$

$$\frac{\partial M}{\partial t} = \gamma g(R, M) + d\nabla^2 M. \tag{8.5b}$$

The adimensionalisation of t and x allows us to work with the ratio d and not the diffusion coefficients D_R and D_M. Moreover, it also allows us to use the mathematical analysis already presented in Chapter 3 for spatially homogeneous models, as illustrated below. The reaction kinetics in this model are just a multiple of original reaction kinetics $f(R, M)$ and $g(R, M)$ with the same positive scalar γ.

Therefore, we investigate the existence of Turing patterns in relation to the ratio d. We present the analysis of system (8.5) subject to boundary conditions (8.3) and initial condition (8.4) for the existence of Turing type instability, based on the approach presented in Murray (2003). The reaction-diffusion system (8.5) exhibit diffusion-driven instability if the homogeneous steady state is stable to small perturbations, in the absence of diffusion, but unstable to small spatial perturbations in the presence of diffusion.

We are interested in the positive steady state of (8.5) which is stable. This steady state denoted $E_i = (R^*, M^*)$, where E_i, $i = 1, \cdots, 9$ is the steady state described in Chapter 3, and it satisfies the algebraic equations

$$f(R^*, M^*) = 0 \quad \text{and} \quad g(R^*, M^*) = 0. \tag{8.6}$$

In the absence of diffusion, this steady state must be linearly asymptotically stable. The conditions of stability of the steady state of the homogeneous system were derived in Chapter 3. These conditions are such that given the linearised system

$$\mathbf{u}_t = \gamma A\mathbf{u}, \quad \text{where} \quad A = \begin{pmatrix} f_R & f_M \\ g_R & g_M \end{pmatrix}, \tag{8.7}$$

then the steady state is linearly stable if

$$trA = f_R + g_M < 0, \quad |A| = f_R g_M - f_M g_R > 0. \tag{8.8}$$

These two conditions are satisfied when nullclines are in the configurations shown in Figure 8.1. Therefore, to investigate for Turing instability, we only consider a steady state which is in the form of E_1 or E_2. The equilibrium E_1 and E_2 have Jacobian matrices with the respective sign patterns of the form

$$\mathcal{J}_{E_1} = \begin{bmatrix} - & - \\ + & - \end{bmatrix} \quad \text{and} \quad \mathcal{J}_{E_2} = \begin{bmatrix} + & - \\ + & - \end{bmatrix}. \tag{8.9}$$

The steady state in the form of E_2 is linearly stable if $f_R + g_M < 0$, otherwise it is unstable.

The interest here is to find conditions under which a steady state that satisfies condition (8.8) will loose its stability in the presence of diffusion. We now linearise the full reaction-diffusion system (8.2) around the steady state $E_i = (R^*, M^*)$. We introduce new variable $\mathbf{u} = (u, v)$ which is slightly perturbed from the steady state. That is $u = R - R^*$ and $v = M - M^*$, where u and v are very small. We therefore substitute the perturbed variables $u + R^*$ and $v + M^*$ in (8.5) and expand using Taylor's series of two variables. We obtain the linearised system written as

$$\mathbf{u}_t = \gamma A\mathbf{u} + D\nabla^2\mathbf{u}, \quad \text{where} \quad A = \begin{pmatrix} f_R & f_M \\ g_R & g_M \end{pmatrix}, \; D = \begin{pmatrix} 1 & 0 \\ 0 & d \end{pmatrix}. \tag{8.10}$$

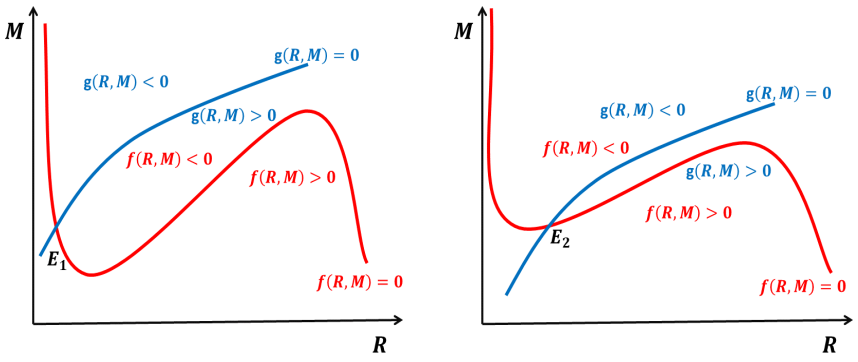

(a) (b)

Figure 8.1: Qualitative forms of nullcline intersection that may satisfy the above two conditions. All the steady states in the form of E_1 are linearly stable while the stability of E_2 depends on the trA.

To complete the linearisation of the reaction-diffusion system, we find the eigenfunctions of the Laplace operator which satisfy the homogeneous Neumann boundary conditions. Eigenfunctions of the Laplace operator on planar domains are well-studied in the literature (Benedetto, 1996; Madzvamuse, 2000). The eigenfunctions for the Laplace operator are found by solving an eigenvalue problem that satisfy the given boundary conditions of (8.5). The eigenvalue problem takes the form

$$\nabla^2\tilde{\mathbf{u}} + k^2\tilde{\mathbf{u}} = 0, \quad (\mathbf{n}\cdot\nabla)\tilde{\mathbf{u}} = 0 \quad \text{on} \quad \partial\Omega, \tag{8.11}$$

where k is the eigenvalue of Laplace operator.

In this case, we solve the problem in 1-D, say if we have $0 \leq x \leq l$. With this we can easily solve the eigenvalue problem whose general solution is given by

$$\tilde{\mathbf{u}} = a\sin kx + b\cos kx.$$

Imposing the boundary conditions give the eigenvalue $k = n\pi/l$ and $a = 0$, which give the solutions to the eigenvalue problem as

$$\tilde{\mathbf{u}}_n(x) = \cos(n\pi x/l), \quad n \in \mathbb{N}.$$

Since problem (8.10) is linear, we seek solutions of the form

$$\mathbf{u}(x,t) = \sum_n c_n\mathbf{u}_n(x,t), \quad \text{where} \quad \mathbf{u}_n(x,t) = \exp(\lambda t)\tilde{\mathbf{u}}_n(x). \tag{8.12}$$

The constants c_n are determined by Fourier expansion of the initial conditions in terms of $\tilde{\mathbf{u}}_n(x)$. Substitute this solution into (8.10), we get for each n

$$\begin{aligned}\lambda \mathbf{u}_n =& \gamma A \mathbf{u}_n + D\nabla^2 \mathbf{u}_n, \\ =& \gamma A \mathbf{u}_n - D\left(\tfrac{n\pi}{l}\right)^2 \mathbf{u}_n.\end{aligned}$$

Since we are interested in the non-trivial solutions, we determine the nature of eigenvalues, which are the roots of characteristic polynomial

$$|\gamma A - D\left(\tfrac{n\pi}{l}\right)^2 - \lambda I| = 0.$$

Using Equation (8.10), we therefore find the trace and determinant of the matrix

$$A' = \gamma A - D\left(\tfrac{n\pi}{l}\right)^2.$$

We have

$$A' = \begin{pmatrix} \gamma f_R - \left(\tfrac{n\pi}{l}\right)^2 & \gamma f_M \\ \gamma g_R & \gamma g_M - d\left(\tfrac{n\pi}{l}\right)^2 \end{pmatrix}. \tag{8.13}$$

We can easily find that A' has trace and determinant given by:

$$trA' = \gamma trA - \left(\tfrac{n\pi}{l}\right)^2 (1+d), \quad |A'| = \gamma^2 |A| + d\left(\tfrac{n\pi}{l}\right)^4 - \gamma\left(\tfrac{n\pi}{l}\right)^2 (df_R + g_M). \tag{8.14}$$

Therefore, we analyse linear stability by considering the trace and determinant. For pattern formation, we expect the steady state to be unstable in the presence of diffusion, that is $Re(\lambda(n)) > 0$ for some $n \neq 0$. $Re(\lambda(n)) > 0$ is only possible if we either have

$$trA' > 0 \quad \text{or} \quad |A'| < 0.$$

Recall that we required the steady state to be linearly stable in the absence of diffusion, resulting in conditions (8.8). This implies that $trA < 0$ and therefore also $trA' < 0$ for all values of n. The only possibility left for Turing instability is that $|A'| < 0$ for some n. Recall that $|A| > 0$ and therefore from Equation (8.14), the only possibility for $|A'| < 0$ is when we have

$$df_R + g_M > 0.$$

From the analysis, since $f_R + g_M < 0$ for stable steady state, we cannot have a situation where $d = 1$. This implies that the activator and inhibitor must have

different diffusion coefficients. Furthermore we must have that f_R and g_M have opposite signs. This condition excludes equilibrium of the form E_1 in Figure 3.2(a), since in that case we have $f_R < 0$ and $g_M < 0$. Therefore, for the equilibrium in the form of E_1, we can never have Turing instability.

We are therefore only left to check for the existence of diffusion-driven instability in the case of steady state in the form E_2. Also from Equation (8.9), we have that $f_R > 0$ and $g_M < 0$ for E_2. Therefore $df_R + g_M > 0$ is only possible when $d > 1$ meaning that the inhibitor must diffuse faster than the activator. Therefore, we conclude that the system (8.2) can exhibit Turing patterns if the following conditions are satisfied:

i) $f_R + g_M < 0$ and $f_R g_M - g_R f_M > 0$

ii) The steady is in the form of E_2

iii) $df_R + g_M > 0$ for some $d > 1$

iv) $f_R > 0$.

We first find the minimum d that can allow Turing patterns to occur. To do this, consider $|A'|$ as a function say $T((\frac{n\pi}{l})^2)$. We therefore write

$$T((\tfrac{n\pi}{l})^2) = \gamma^2|A| + d\left(\tfrac{n\pi}{l}\right)^4 - \gamma\left(\tfrac{n\pi}{l}\right)^2(df_R + g_M)\,. \tag{8.15}$$

To find the minimum of (8.15), we differentiate and find the value of $(\frac{n\pi}{l})^2$ that minimises it. Therefore at the minimum, we obtain:

$$(\tfrac{n\pi}{l})^2_{\min} = \frac{\gamma(df_R + g_M)}{2d}. \tag{8.16}$$

Using this value we get from (8.15)

$$T_{\min} = \gamma^2\left[|A| - \frac{(df_R + g_M)^2}{4d}\right]. \tag{8.17}$$

Equation (8.17) must also be negative to satisfy the conditions for Turing instability. From this we can therefore calculate the critical d that will make $T_{\min} < 0$. We find the critical d labelled d_c that satisfy

$$|A| - \frac{(df_R + g_M)^2}{4d} = 0.$$

Simplifying this we find that the critical value d_c is the positive root of the quadratic equation

$$d^2 f_R^2 + 2d(2f_M g_R - f_R g_M) + g_M^2 = 0. \tag{8.18}$$

This critical value d_c gives us the minimum value of d for diffusion-driven instability to occur.

8.2.2 Numerical simulations

We illustrate Turing instability numerically, using reaction kinetics of model GRM-3 (2.26). We first find parameters which give the steady state of the form E_2. Using this steady state, we compute the corresponding Jacobian matrix, and find its determinant. From there we compute the critical value d_c for Turing instability to occur. We then compute the solution to the reaction-diffusion system with two different values of d, one greater than d_c and the second one less than d_c. The reaction-diffusion system (8.2) together with the boundary conditions (8.3) and given initial conditions (8.4) is solved using MATLAB package pdepe.

Using parameter values in Table 3.1, and select $G_T = 0.5327$ and $k_1 = 0.1206$. We obtain numerically the steady state in the form E_2 given by $(0.2140, 0.1983)$. Figure 8.2 shows numerical simulation of model GRM-3 (2.26) with parameter values listed in Table 3.1. The solution converges to a homogeneous steady state $(0.2140, 0.1983)$.

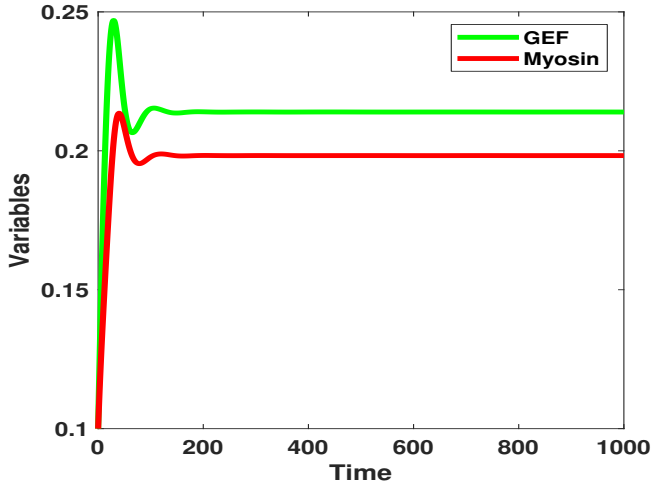

Figure 8.2: Numerical solution of the ODE model GRM-3 (2.26), with parameter values in Table 3.1 with $G_T = 0.5327$ and $k_1 = 0.1206$.

We obtain the Jacobian matrix, J_{E_2} evaluated at the steady state $(0.2140, 0.1983)$ given as:

$$J_{E_2} = \begin{bmatrix} 0.0066 & -0.1391 \\ 0.0643 & -0.0950 \end{bmatrix}. \tag{8.19}$$

This Jacobian matrix has the sign matrix $\mathcal{J}_{E_2}$, negative trace and positive determinant. It therefore satisfies conditions (8.8) which are necessary for investigation of Turing instability. Using Equation (8.18), we obtain $d_c = 789.3031$.

Figure 8.3 shows simulations corresponding to $d = 100$. The activator diffuses slower than the inhibitor, but there are no Turing patterns which are formed, since $d < d_c$. With the initial condition of GEF and Myosin randomly selected around the uniform steady state, no Turing patterns are observed, and the solution converges to a uniform spatially homogeneous solution. We also compute the discrete L_2 norms of the errors at each time point as shown in Figure 8.3(c). The errors converge to zero as time increases which means we converge to temporally stable solution.

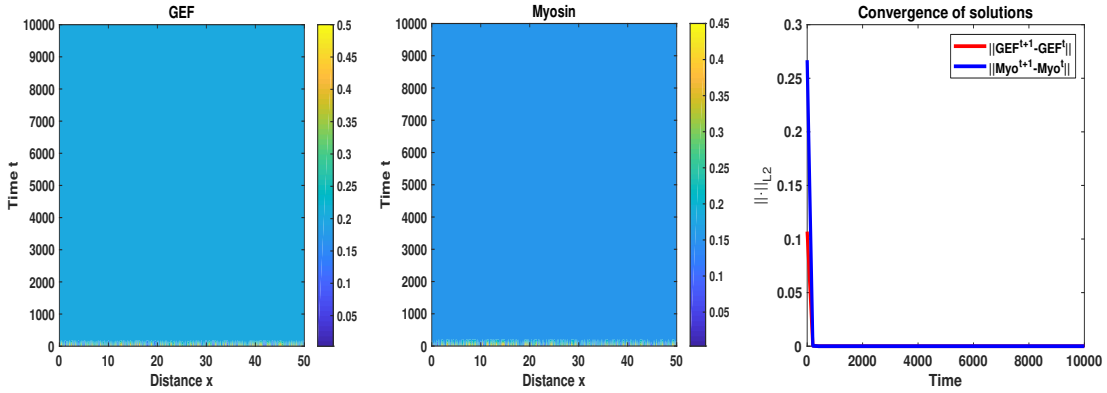

(a) (b) (c)

Figure 8.3: Numerical solution of the reaction-diffusion system (8.2) with reaction kinetics corresponding to model GRM-3. We use parameters in Table 3.1. We take $G_T = 0.5327$, $k_1 = 0.1206$ and $d = 100$. Figures 8.3(a) and 8.3(b) show respective solutions of GEF and Myosin in time and space, where the colour code represents the concentrations of GEF and Myosin. 8.3(c) shows the discrete L_2 norms of the errors computed at each time point. There are no Turing patterns formed.

In the second case, we pick $d = 1000$ such that $d > d_c$. The simulation results are shown in Figure 8.4. As expected, spatial patterns emerges since conditions for Turing instability are satisfied. The solutions of GEF and Myosin are shown in Figures 8.4(a) and 8.4(b). The discrete L_2 norms of the errors converge to zero (see

Figure 8.4(c)) and therefore the patterns formed are stable in time. Figure 8.4(d) shows spatial profile of patterns of GEF and Myosin in space at $t = 999.8$. For this simulation, we also used initial random conditions around the steady state at each spatial location x.

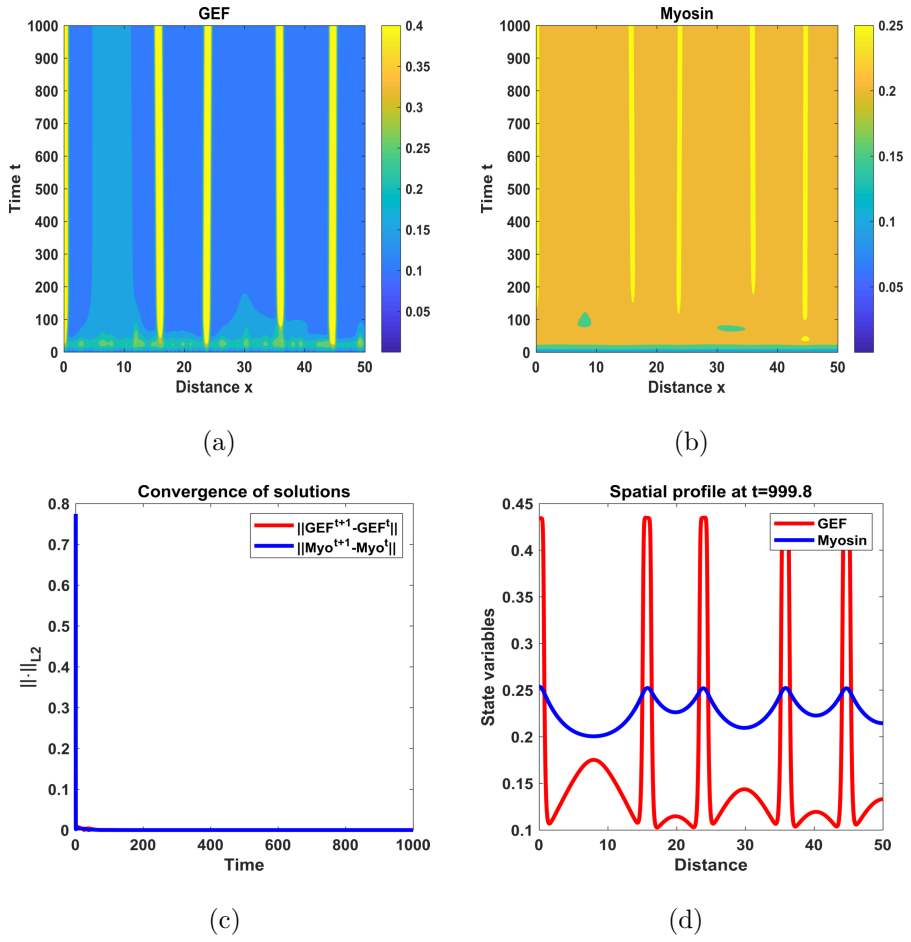

Figure 8.4: Numerical simulation of system (8.2) with reaction kinetics corresponding to model GRM-3 and parameters in Table 3.1. We take $G_T = 0.5327$, $k_1 = 0.1206$ and $d = 1000$. Figures 8.4(a) and 8.4(b) respectively show solutions of Turing patterns of GEF and Myosin in time and space, while 8.4(c) shows the discrete L_2 norms of the errors computed at each time point. Initial conditions are taken as random perturbations around uniform steady state. Turing patterns are formed.

We have derived conditions necessary for diffusion-driven instability for a reaction-diffusion system of two species. Using these conditions, we have shown that the reaction kinetics defined in the system (2.26) are capable of generating Turing patterns, given that the conditions for Turing instability are satisfied.

In the numerical simulations in Figures 8.3 and 8.4, we assumed that $d > 1$ to mean

that Myosin diffuses much faster than GEF. However, Myosin is known to diffuse much slower than GEF and therefore we do not expect to get Turing patterns with this two species model in the realistic biological case. In the next section we perform numerical simulations of the full reaction-diffusion system in various dynamical regimes corresponding to stable, oscillatory, excitable and bistable.

8.3 Numerical investigation of spatial models

In this section, we provide numerical solutions of the full reaction-diffusion model with parameter values corresponding to different dynamical regimes (stable, excitable, bistable and oscillatory). The results will be as follows: using model GRM-3, we provide numerical simulations corresponding to stable and oscillatory regimes. Since this model lacks bistability, and also there is no clear region defined for excitable dynamics, we also provide numerical simulations using the reaction terms corresponding to model GRM-2 to show the effect of diffusion in various dynamical regimes.

Table 8.1 summarises the different simulations carried out in the different regimes with the parameter values, initial conditions and models used. For the numerical simulations henceforth, we use biological diffusion coefficients of Rho (GEF) and Myosin, given by $D_R = 0.28\mu m^2/s$ and $D_M = 0.005\mu m^2/s$ (Petrášek et al., 2008; Weitzman, 2013).

8.3.1 Numerical simulations in the stable regime

We show numerical simulation results with parameter values corresponding to a stable regime for models GRM-2 (2.16) and GRM-3 (2.26). Figure 8.5 shows numerical solution results of system (8.2) with reaction kinetics corresponding to model GRM-3, while Figure 8.6 shows the results with reaction kinetics corresponding to model GRM-2. The parameter values and initial conditions used are as shown in Table 8.1. In both scenarios, the solutions to the system (8.2) are spatially homogeneous. The L_2 norms of errors converges to zeros, showing that the solutions are stable in time.

Regime	Model	Parameter	Initial conditions (R_0, M_0)
Stable	GRM-2, Figure 8.6	$G_T = 0.1,\ k_1 = 0.2$	random initial conditions
	GRM-3, Figure 8.5	$G_T = 0.4,\ k_1 = 0.1$	
Oscillatory	GRM-2, Figure 8.8	$G_T = 0.66,\ k_1 = 0.1$	$\begin{cases}(0.1747, 0.5158),\ 245 < x < 255\\(0.95, 0.5),\ \text{elsewhere}\end{cases}$
	GRM-3, Figure 8.7	$G_T = 1,\ k_1 = 0.2$	$\begin{cases}(0.2, 0.2),\ 190 < x < 210\\(0.3, 0.5),\ \text{elsewhere}\end{cases}$
Excitable	GRM-2, Figures 8.9 and 8.10	$G_T = 7,\ k_1 = 0.2$	$\begin{cases}(0.33, 0.3093),\ 245 < x < 255\\(0.1680, 0.3093),\ \text{elsewhere}\end{cases}$
Bistable		$G_T = 20,\ k_1 = 0.2$	$\begin{cases}(0.2, 0.4),\ x < 400\\(0.4, 0.2),\ \text{elsewhere}\end{cases}$

Table 8.1: Table showing different regimes in which we carry out numerical simulations, the corresponding parameter values and initial condition used, the other parameter values used are listed in Table 3.1. The table also gives reference to each figure showing numerical simulations.

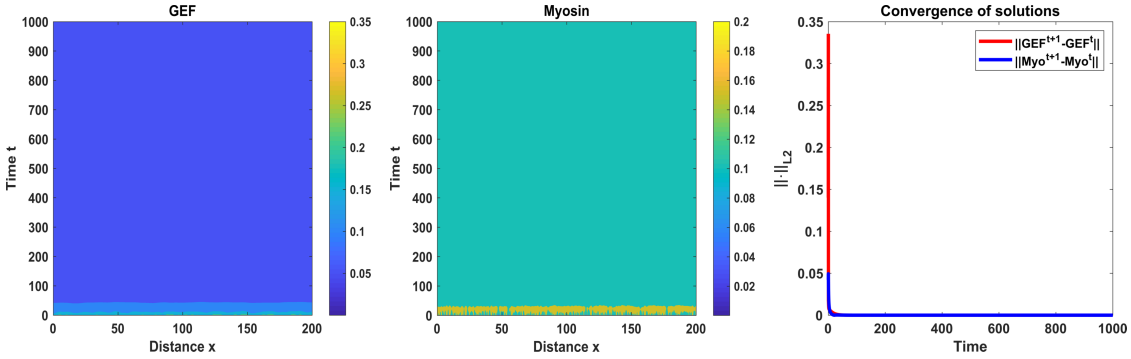

(a) (b) (c)

Figure 8.5: Numerical solution of the reaction-diffusion system (8.2) with reaction kinetics corresponding to model GRM-3. We use parameters in Table 3.1 with $G_T = 0.4$ and $k_1 = 0.1$. We use $L = 200$.

8.3.2 Numerical simulations in the oscillatory regime

Here we provide numerical simulation results for the system (8.2) with reaction kinetics corresponding to models GRM-2 (2.16) in Figure 8.8 and GRM-3 (2.26) in Figure 8.7 and parameter values selected in the oscillatory regime. The initial conditions and parameter values used are as shown in Table 8.1. In both simulation results, the solutions are periodic in time, which is illustrated by the discrete L_2 norms of the errors shown in Figure 8.7(d) and Figure 8.8(d) respectively. For the simulations, we used $L = 500$.

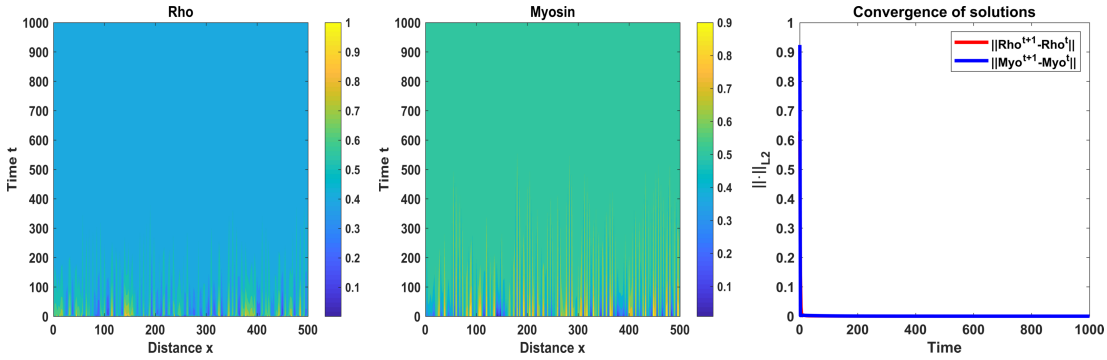

(a) (b) (c)

Figure 8.6: Numerical solution of system (8.2) with reaction kinetics corresponding to model GRM-2 and parameter values in Table 3.1 with $G_T = 0.1$ and $k_1 = 0.2$. $L = 500$.

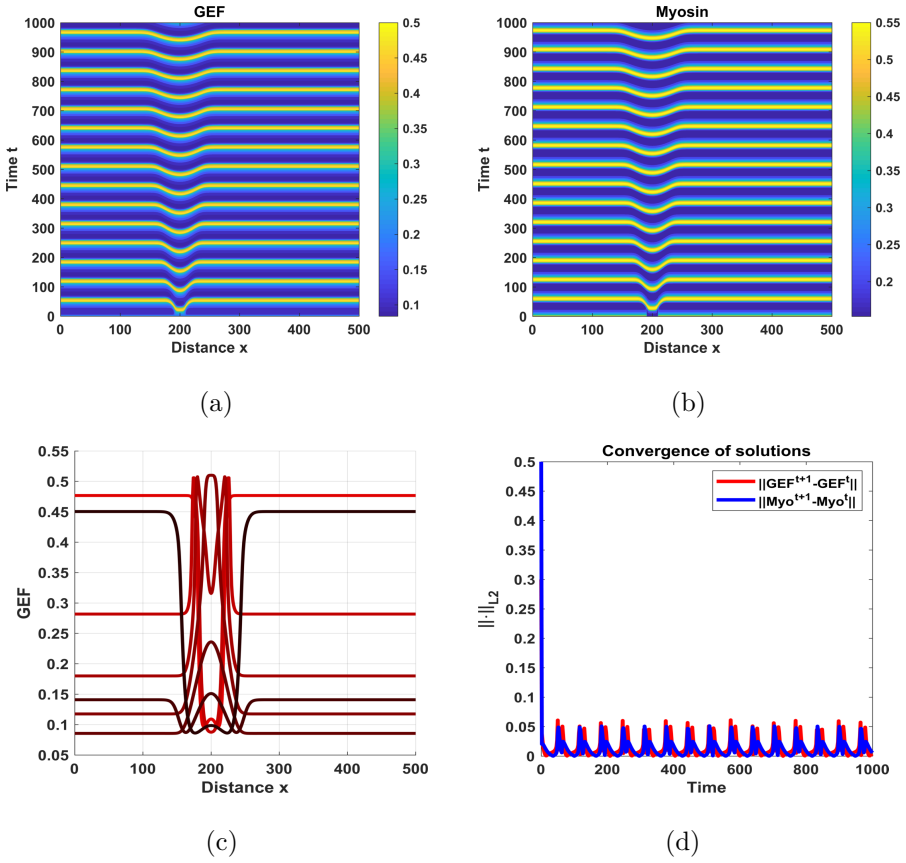

(a) (b)

(c) (d)

Figure 8.7: Numerical simulation results for system (8.2) with reaction kinetics corresponding to model GRM-3. Parameters are taken from Table 3.1, with $G_T = 0.66$ and $k_1 = 0.1$. Figures 8.7(a) and 8.7(b) show respectively solutions of GEF and Myosin in time and space, while Figure 8.7(c) shows the spatial profiles of GEF at different time points. Figure 8.7(d) shows the discrete L_2 norms of the errors of GEF and Myosin at each time point. In Figure 8.7(c) the sequence of colours starts from red indicating the spatial profile at the initial time and finishes with black for the spatial profile at the final time.

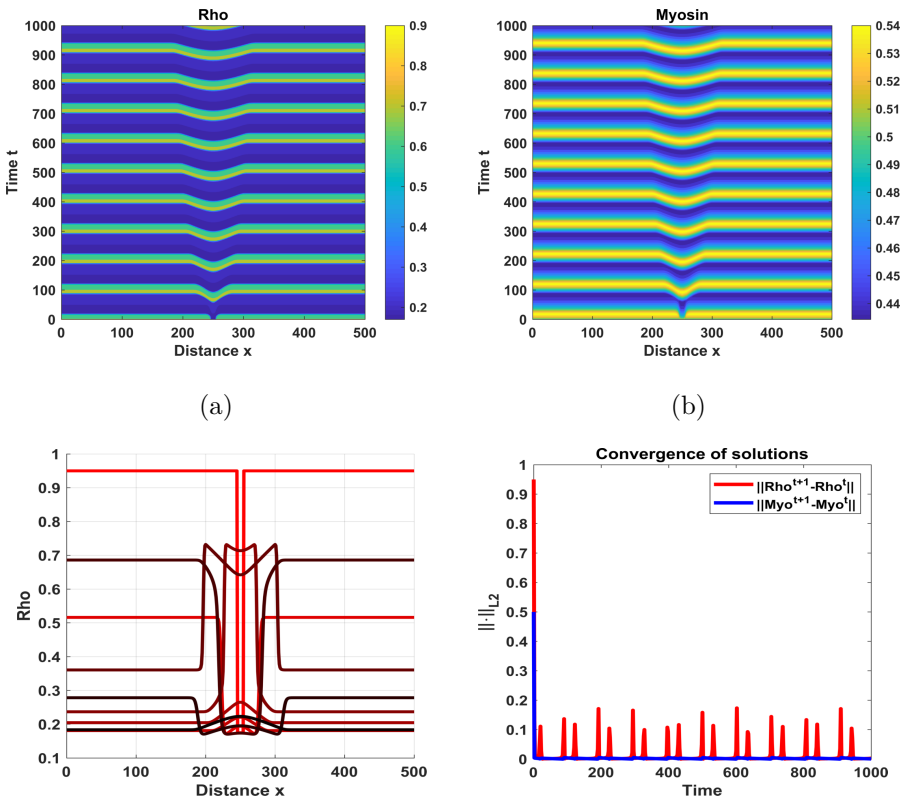

Figure 8.8: Numerical simulation results for system (8.2) with reaction kinetics corresponding to model GRM-2 and parameter values in the Table 3.1 with $G_T = 1$ and $k_1 = 0.2$. Figures 8.8(a) and 8.8(b) show respectively solutions of Rho and Myosin in time and space, while Figure 8.8(c) shows the spatial behaviour of GEF at different time points. Figure 8.8(d) shows the L_2 norm of GEF and Myosin at each time point. Figure 8.8(c) shows the spatial profile of Rho at different time points. The sequence of colours starts from red, indicating the spatial profile at the initial time and finishes with black for the spatial profile at the final time.

8.3.3 Numerical simulations in the excitable regime

We next investigate the numerical solutions in the region characterised by excitable dynamics. We used kinetic equation corresponding model GRM-2 and results are shown in Figure 8.9. Parameter values used and initial conditions are as listed in Table 8.1. In the small interval of x such that $x \in (245, 255)$, we use initial conditions such that the threshold for excitable dynamics is exceeded, and in the rest of the interval we used the steady state values of the ODE system as the initial conditions. A pulse is formed in the small region, and then it is propagated in the domain as time increases. This is shown in Figures 8.9(a), 8.9(b) and 8.9(c). The discrete L_2 norms of the errors forms a peak value and then vanishes as shown in Figure 8.9(d).

The solutions are stable in time.

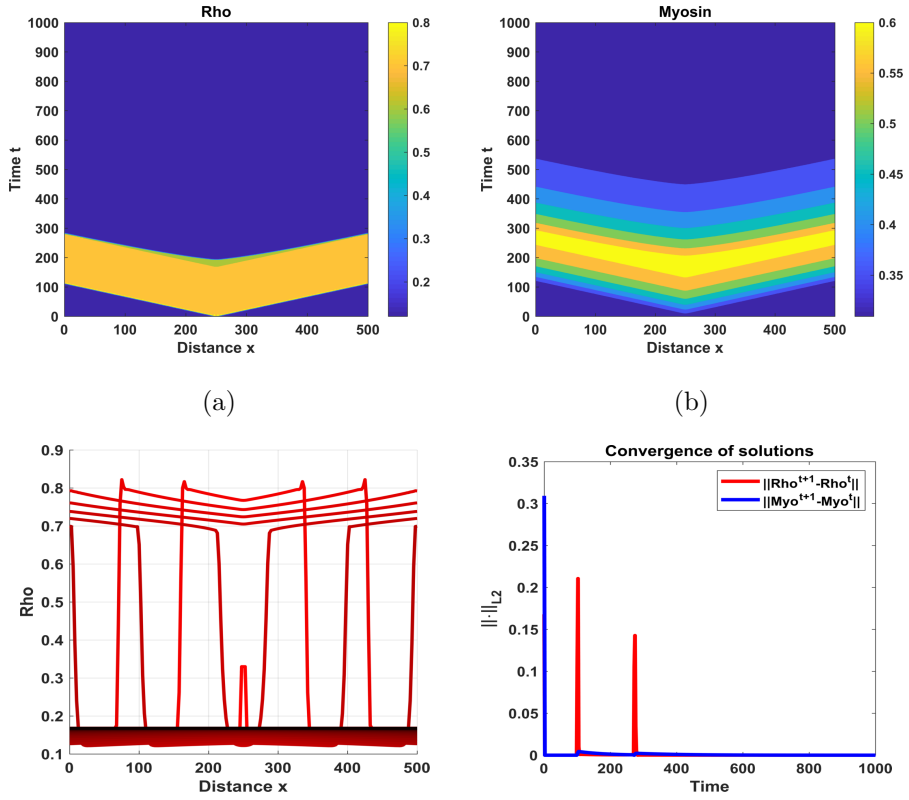

(a) (b)

(c) (d)

Figure 8.9: Numerical simulation results for system (8.2) with reaction kinetics corresponding to model GRM-2 with excitable dynamics. Figure 8.9(c) shows the pulses of Rho at different time points. The colour red indicates spatial profile at the initial time point while black shows the spatial profile at the final time point.

8.3.4 Numerical simulations in the bistable regime

Lastly, Figure 8.10 shows numerical simulation results for the system (8.2) with kinetic reaction terms corresponding to model GRM-2 with parameter values and initial conditions as listed in Table 8.1. We observe travelling wave fronts moving from right to left as shown in Figures 8.10(a), 8.10(b) and 8.10(c). For the numerical simulation, we use the distance, $L = 500$. Diffusion induces a travelling wave from one locally stable steady state of the ODE model to another, in a bistable region. The solutions are stable in time as shown by the discrete L_2 norms of the errors at different time points in Figure 8.10(d).

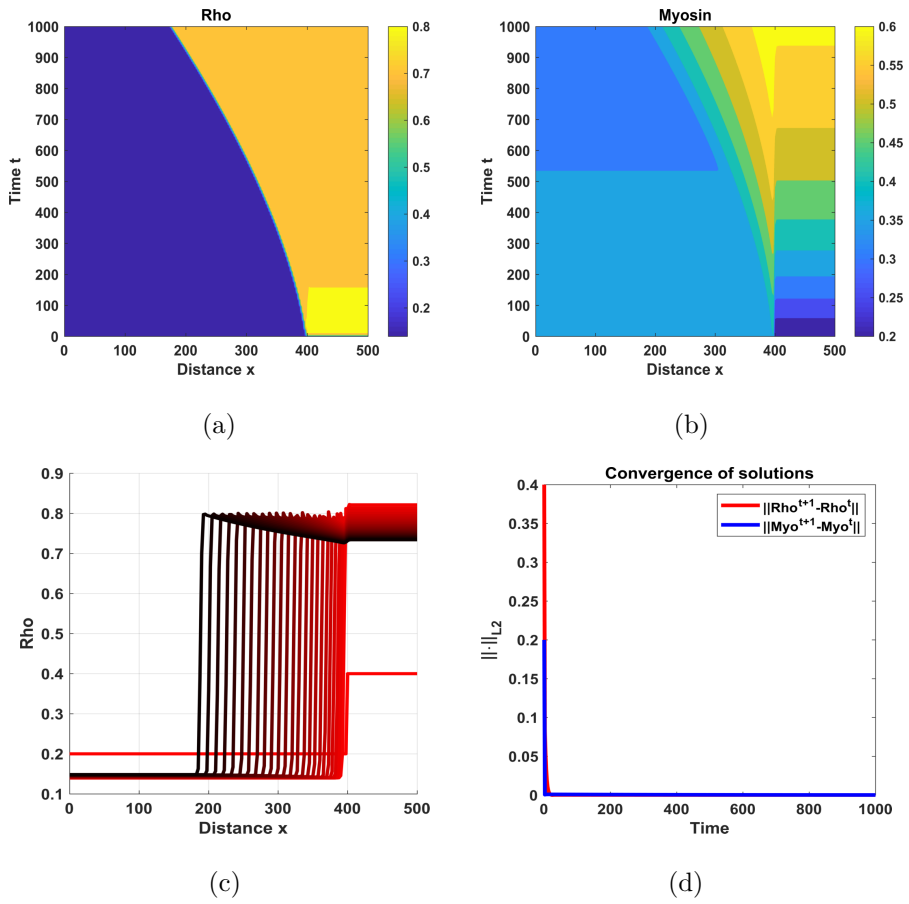

Figure 8.10: Numerical simulation results for system (8.2) with reaction kinetics corresponding to model GRM-2 in bistable regime. In Figure 8.10(d), the red line shows the spatial behaviour at $t = 0$. The sequence finishes in black which shows spatial profile at the final time point.

8.4 Conclusion

In this chapter we explored the effect of adding diffusion to the ODE models formulated in Chapter 2. We first investigated the existence of Turing instability in the spatially inhomogeneous models. Mathematical analysis were illustrated by numerical simulations.

Then, we numerically investigated the effect of adding diffusion when the ODE model dynamics lie in distinct dynamical regimes corresponding to stable, oscillatory, excitability and bistable. In general we observe that for most of the parameters selected, the temporal dynamics related to reaction kinetics are dominant over the spatial dynamics induced by diffusion. In order to fully characterise the behaviour of solution in various regimes, rigorous mathematical analysis needs to be done and the parameter space characterised. In this chapter, we have not done the mathem-

atical analysis for the emergence of travelling waves, we refer the interested reader to some of the articles published (Keener, 1980; Jones, 1984; Tyson and Keener, 1988; Wang et al., 2008).

The choice of d used to illustrate Turing instability is not realistic biologically, since Myosin diffuses much slower than GEF (Rho) (Petrášek et al., 2008; Weitzman, 2013). Model GRM-3 exhibits spatial patterns for a given set of parameters in the stable region. Although the results are not biologically supported, this is because our model does not take into account the inactive molecules that would enrich the model to be of the form of long-range inhibition via activator-depletion provided by the inactive molecules and short range negative feedback mechanism provided by Myosin (Turing, 1952).

Chapter 9

Conclusions

In the previous chapters, a conclusion was provided at the end of each chapter, summarising the focus of that particular chapter, and the results. In this chapter, we therefore focus on the overall conclusion of the thesis and some possible extensions.

9.1 Conclusion and Discussion

This thesis studies the full cycle of GEF–Rho–Myosin temporal dynamics linked to cellular contractility from experimental observations, to formulation of mathematical models from first principles based on data and their analysis. Finally closing the cycle is the rigorous sensitivity analysis and parameter estimation. Three models were formulated from first principles based on the experimental data. The formulation depended on different mathematical assumptions used to translate the experimental observations. These models were referred to as: *GRM-1*, *GRM-2* and *GRM-3*. They are represented in the form of activator-inhibitor regulatory network. The main assumptions of models GRM-1 and GRM-2 is the use of enzymatic activity to implement GEF reaction and quasi-equilibrium assumption on GEF module while for model GRM-3, the main assumption is the use of the law of mass action to implement GEF module and quasi-equilibrium assumption on Rho module.

Asymptotic analyses of models provides the range of parameter, G_T for which the models exhibit different type of dynamics. The use of G_T was biologically motivated. Experimentally Rho activity dynamics change at different expression levels

of the positive feedback mediator, GEF and therefore the total GEF concentration becomes the bifurcation parameter. We characterised mathematically different dynamic states of each model, by use of nullcline theory, linear stability theory and sign pattern analysis. Numerical bifurcation analysis was used to complement theoretical findings. These results were illustrated numerically and showed that the models have the same nullcline configuration as the ones obtained through mathematical analysis. Models GRM-1 and GRM-2 exhibit the four dynamics (stable, excitable, oscillatory and bistable) while model GRM-3 exhibit only three regimes as the bifurcation parameter G_T varies. These regimes were illustrated by plotting the time evolution of Rho and Myosin and their corresponding phase-planes.

It was shown that model GRM-1 has the same qualitative behaviour to model GRM-2, for suitable parameter ranges, both models exhibit up to four regimes (stable, oscillatory, excitable and bistable). Their qualitative results differ from the results of model GRM-3, which show up to three distinct dynamic regimes (stable, excitable, oscillatory). We hypothesised that these differences come because of the way GEF module was translated mathematically. Taking G_T as bifurcation parameter, it has been shown that models GRM-1 and GRM-2 exhibit bistability without hysteresis, in which one of the limit points goes to infinity (Guidi and Goldbeter, 1997), the change in the steady states is achieved by changing initial conditions.

Local and global sensitivity analysis were performed for all the models. Local sensitivity analysis allowed us to study amplitude and period sensitivities to parameters. The period is largely affected by k_3, k_4 and K_{r2} for model GRM-1; while k_3, k_4 and G_T for model GRM-2 and then k_2, k_1 and k_0 for model GRM-3. For model GRM-3, G_T, k_2, k_0 and k_4 commonly affects both GEF and Myosin amplitudes. The rank of parameters for all the models is listed in Tables 6.2, 6.3 and 6.4. In general Rho and Myosin amplitudes are sensitive to different parameters. In this thesis, the nominal parameter set for local sensitivity analysis was selected arbitrarily such that the model satisfies either stability condition or the limit cycle case, in future studies, this could be taken as values estimated/obtained from experiments as a justifiable nominal parameter set for analysis. We also have to incorporate the prior knowledge about the parameters, to find the range for sensitivity analysis.

Comparisons between models provides premises for critical model analysis and possible elimination or selection based on raw experimental data and also understanding differences that may exist with certain mathematical assumptions. Model GRM-3 was refined from models GRM-1 and GRM-2, based on experimental observations. This model was used in parameter estimation, using the biological data both in the stable regime (Rho and Myosin responses to GEF perturbation) and the data in the oscillatory regime. We employed the Bayesian method to define parameters which link model GRM-3 to experimental data. This method allows the inclusion of prior knowledge about the parameters. We then identified maximum posterior (MAP) parameter that we used to verify the applicability of the model to experimental data. With these MAP parameters, model GRM-3 exhibit the experimentally observed dynamic regimes. The parallel Metropolis-Hastings method was used to speed up the computations in the Bayesian method.

In Chapter 8, we explored effects of adding diffusion to the ODE models formulated. We provided conditions for diffusion-driven instability and numerical simulations to illustrate mathematical analysis. We later provided numerical simulations for the full reaction-diffusion model for various dynamical regimes corresponding to stable, oscillatory, excitable and bistable. The reaction-diffusion models formulated do not produce realistic biological scenario of GEF–Rho–Myosin dynamics, since it does not account for spatial inhomogeneity of inactive species corresponding to GEF, Rho and Myosin.

9.2 Future work and possible extensions

There are several research strands this current research may be extended, which include:

The modelling approach in this thesis considered only the interaction of Rho with its positive and negative regulators, GEF and Myosin. However, it has been shown that the cross-talk between small G-proteins (Cdc42, Rho and Rac) contribute to cell polarity and motility (Marée et al., 2006; Jilkine et al., 2007; Marée et al., 2012). Therefore in a future study, the models formulated in this thesis can be coupled to include Rho GTPases' interactions.

The models derived in this thesis may be extended to include diffusion, in the form of reaction-diffusion models, without compartmentalisation. This follows a similar approach as the work done in Goryachev and Pokhilko (2008), where it is assumed that all the molecules are in the same planar domain. Due to different regions within which the molecules reside, the equations in the cytosol will be multiplied by the scaling factor $\eta = V_m/V_c$, where V_m is the cortex volume and V_c is the volume of the cytosol.

The other possible extension is the improved coupling of diffusion molecules with compartmentalisation of the domain in a bulk-surface model type setting. Here we shall couple a reaction diffusion in the cytosol (bulk) to the reaction-diffusion on the membrane (surface) as in Rätz and Röger (2012, 2014) and recently published work by Cusseddu et al. (2018). The flux condition and attachment and detachment law can be incorporated as in Rätz and Röger (2012, 2014). The models formed will be studied on various bulk-surface geometries. We can also study the presence of propagating wave fronts in the case of parameters where the models exhibit excitable dynamics.

The network dynamics of Rho-Myosin signalling pathways are modulated by the expression levels of the associated regulators, and the elasticity of the ECM to control the cell contractility dynamics. In the work of Graessl et al. (2017), the pulses of Rho activity were modulated by the mechanical properties of the surrounding environment. It has also been shown that GEF-H1 is regulated by the microtubules. Therefore in these models, we can introduce the microtubule assembly and disassembly which regulate GEF-H1, and also introduce the ECM. The dynamic properties of the resulting models will be studied and compared to experimental observations.

It has also been shown experimentally that the Rho activities are affected by random processes (Graessl et al., 2017; Kamps et al., 2019). These models can therefore be extended to include random process, i.e. the stochastic differential equation system will be formed, and analysed. The question is to determine compatibility between the two models (PDE model and stochastic model) and experimental results.

In this thesis, we also studied the local sensitivity analysis, where the nominal

parameter set was selected randomly to illustrate various regimes. This may be extended to include several nominal parameter values. Statistical techniques may be applied to the resulting sensitivity indexes to rank the parameters. This approach may be equivalent to using global sensitivity analysis.

Bibliography

Allard, J. and Mogilner, A. (2013). Traveling waves in actin dynamics and cell motility. *Current Opinion in Cell Biology*, 25(1):107–115. 11, 14, 94

Andrew, N. and Insall, R. H. (2007). Chemotaxis in shallow gradients is mediated independently of ptdins 3-kinase by biased choices between random protrusions. *Nature Cell Biology*, 9(2):193–200. 1

Aster, R. C., Borchers, B., and Thurber, C. H. (2018). *Parameter estimation and inverse problems*, volume 2. Elsevier. 119, 121, 129, 205, 206

Bagheri, N., Stelling, J., and Doyle III, F. J. (2006). Quantitative performance metrics for robustness in circadian rhythms. *Bioinformatics*, 23(3):358–364. 64

Barnhart, E. L., Allard, J., Lou, S. S., Theriot, J. A., and Mogilner, A. (2017). Adhesion-dependent wave generation in crawling cells. *Current Biology*, 27(1):27–38. 10, 14, 15, 95

Bement, W. M., Leda, M., Moe, A. M., Kita, A. M., Larson, M. E., Golding, A. E., Pfeuti, C., Su, K.-C., Miller, A. L., Goryachev, A. B., et al. (2015). Activator–inhibitor coupling between Rho signalling and actin assembly makes the cell cortex an excitable medium. *Nature Cell Biology*, 17(11):1471–1483. 14, 15, 95

Benais-Pont, G., Punn, A., Flores-Maldonado, C., Eckert, J., Raposo, G., Fleming, T. P., Cereijido, M., Balda, M. S., and Matter, K. (2003). Identification of a tight junction–associated guanine nucleotide exchange factor that activates Rho and regulates paracellular permeability. *The Journal of Cell Biology*, 160(5):729–740. 7

Benedetto, J. J. (1996). *Harmonic analysis and applications*, volume 23. CRC Press. 140

Bodine, E., Deaett, L., McDonald, J., Olesky, D., and van den Driessche, P. (2012). Sign patterns that require or allow particular refined inertias. *Linear Algebra and its Applications*, 437(9):2228–2242. 42, 43, 48, 50, 185, 186

Boer, E. F., Howell, E. D., Schilling, T. F., Jette, C. A., and Stewart, R. A. (2015). Fascin1-Dependent Filopodia are Required for Directional Migration of a Subset of Neural Crest Cells. *PLOS Genetics*, 11(1):1–25. 5

Bornschlögl, T. (2013). How filopodia pull: what we know about the mechanics and dynamics of filopodia. *Cytoskeleton*, 70(10):590–603. 4

Boureux, A., Vignal, E., Faure, S., and Fort, P. (2006). Evolution of the Rho family of ras-like GTPases in eukaryotes. *Molecular Biology and Evolution*, 24(1):203–216. 2

Bray, D. (1995). Protein molecules as computational elements in living cells. *Nature*, 376(6538):307–312. 10

Burnette, D. T., Manley, S., Sengupta, P., Sougrat, R., Davidson, M. W., Kachar, B., and Lippincott-Schwartz, J. (2011). A role for actin arcs in the leading-edge advance of migrating cells. *Nature Cell Biology*, 13(4):371–382. 10

Byrne, K. M., Monsefi, N., Dawson, J. C., Degasperi, A., Bukowski-Wills, J.-C., Volinsky, N., Dobrzyński, M., Birtwistle, M. R., Tsyganov, M. A., Kiyatkin, A., et al. (2016). Bistability in the Rac1, PAK, and RhoA signaling network drives actin cytoskeleton dynamics and cell motility switches. *Cell Systems*, 2(1):38–48. 12

Cai, D., Chen, S.-C., Prasad, M., He, L., Wang, X., Choesmel-Cadamuro, V., Sawyer, J. K., Danuser, G., and Montell, D. J. (2014). Mechanical feedback through e-cadherin promotes direction sensing during collective cell migration. *Cell*, 157(5):1146–1159. 5

Calderhead, B. (2014). A general construction for parallelizing Metropolis-Hastings

algorithms. *Proceedings of the National Academy of Sciences*, 111(49):17408–17413. 207

Campillo-Funollet, E., Venkataraman, C., and Madzvamuse, A. (2019). Bayesian parameter identification for Turing systems on stationary and evolving domains. *Bulletin of Mathematical Biology*, 81(1):81–104. 119, 120, 121, 127, 206, 207, 208

Charras, G. and Paluch, E. (2008). Blebs lead the way: how to migrate without lamellipodia. *Nature Reviews Molecular Cell Biology*, 9(9):730–736. 5

Chen, X., Venkatachalapathy, M., Kamps, D., Weigel, S., Kumar, R., Orlich, M., Garrecht, R., Hirtz, M., Niemeyer, C. M., Wu, Y.-W., et al. (2017). "Molecular Activity Painting": Switch-like, Light-Controlled Perturbations inside Living Cells. *Angewandte Chemie International Edition*, 56(21):5916–5920. 123

Cotter, S. L., Roberts, G. O., Stuart, A. M., White, D., et al. (2013). Mcmc methods for functions: modifying old algorithms to make them faster. *Statistical Science*, 28(3):424–446. 208

Csikász-Nagy, A., Battogtokh, D., Chen, K. C., Novák, B., and Tyson, J. J. (2006). Analysis of a generic model of eukaryotic cell-cycle regulation. *Biophysical Journal*, 90(12):4361–4379. 10

Cukier, R., Schaibly, J., and Shuler, K. E. (1975). Study of the sensitivity of coupled reaction systems to uncertainties in rate coefficients. III. Analysis of the approximations. *The Journal of Chemical Physics*, 63(3):1140–1149. 82, 199

Culos, G., Olesky, D., and van den Driessche, P. (2016). Using sign patterns to detect the possibility of periodicity in biological systems. *Journal of Mathematical Biology*, 72(5):1281–1300. 42, 48, 184, 185

Cusseddu, D., Edelstein-Keshet, L., Mackenzie, J., Portet, S., and Madzvamuse, A. (2018). A coupled bulk-surface model for cell polarisation. *Journal of Theoretical Biology*. 1, 15, 21, 61, 156

Das, M., Drake, T., Wiley, D. J., Buchwald, P., Vavylonis, D., and Verde, F. (2012). Oscillatory dynamics of Cdc42 GTPase in the control of polarized growth. *Science*, 337(6091):239–243. 64

Dashti, M. and Stuart, A. M. (2016). *The Bayesian approach to inverse problems*, volume 319, pages 1–118. Springer. 204, 208

DerMardirossian, C. and Bokoch, G. M. (2005). GDIs: central regulatory molecules in Rho GTPase activation. *Trends in Cell Biology*, 15(7):356–363. 3

Devreotes, P. and Horwitz, A. R. (2015). Signaling networks that regulate cell migration. *Cold Spring Harbor Perspectives in Biology*, 7(8):a005959. 12

Dhooge, A., Govaerts, W., and Kuznetsov, Y. A. (2003). MATCONT: a MATLAB package for numerical bifurcation analysis of odes. *ACM Transactions on Mathematical Software (TOMS)*, 29(2):141–164. 53

Dhooge, A., Govaerts, W., Kuznetsov, Y. A., Meijer, H., and Sautois, B. (2008). New features of the software Matcont for bifurcation analysis of dynamical systems. *Mathematical and Computer Modelling of Dynamical Systems*, 14(2):147–175. 53

Drew, J., Johnson, C., Olesky, D., et al. (2000). Spectrally arbitrary patterns. *Linear Algebra and its Applications*, 308(1-3):121–137. 43

Drubin, D. G. and Nelson, W. J. (1996). Origins of cell polarity. *Cell*, 84(3):335–344. 1

Edelstein-Keshet, L. (1988). *Mathematical models in biology*, volume 46. Siam. 10

Edelstein-Keshet, L., Holmes, W. R., Zajac, M., and Dutot, M. (2013). From simple to detailed models for cell polarization. *Philosophical Transactions of the Royal Society of London B: Biological Sciences*, 368(1629):20130003. 13

Ekström, P.-A. (2005). *A simulation toolbox for sensitivity analysis*. PhD thesis, Faculty of Science and Technology, Uppsala Universitet. 62, 63, 80, 81, 82, 198, 199, 200

Etienne-Manneville, S. (2004). Cdc42-the centre of polarity. *Journal of Cell Science*, 117(8):1291–1300. 4

Etienne-Manneville, S. (2014). Neighborly relations during collective migration. *Current Opinion in Cell Biology*, 30:51–59. 5

Etienne-Manneville, S. and Hall, A. (2002). Rho GTPases in cell biology. *Nature*, 420(6916):629–635. 2

Even-Ram, S., Doyle, A. D., Conti, M. A., Matsumoto, K., Adelstein, R. S., and Yamada, K. M. (2007). Myosin IIA regulates cell motility and actomyosin–microtubule crosstalk. *Nature Cell Biology*, 9(3):299–309. 5

Fan, L. and Mellor, H. (2012). The small Rho GTPase Rif and actin cytoskeletal remodelling. *Biochemical Society Transactions*, 40(1):268–272. 4, 121

Faroudi, M., Hons, M., Zachacz, A., Dumont, C., Lyck, R., Stein, J. V., and Tybulewicz, V. L. (2010). Critical roles for rac gtpases in t-cell migration to and within lymph nodes. *Blood*, 116(25):5536–5547. 3

Ferrell Jr, J. E. (2002). Self-perpetuating states in signal transduction: positive feedback, double-negative feedback and bistability. *Current Opinion in Cell Biology*, 14(2):140–148. 20

FitzHugh, R. (1961). Impulses and physiological states in theoretical models of nerve membrane. *Biophysical Journal*, 1(6):445–466. 11

FitzHugh, R. (1969). Mathematical models of excitation and propagation in nerve. *Biological Engineering*, 1(6):1–85. 11

Friedl, P. and Alexander, S. (2011). Cancer invasion and the microenvironment: plasticity and reciprocity. *Cell*, 147(5):992–1009. 1

Friedl, P., Locker, J., Sahai, E., and Segall, J. E. (2012). Classifying collective cancer cell invasion. *Nature Cell Biology*, 14(8):777–783. 2

Gad, A. K., Nehru, V., Ruusala, A., and Aspenström, P. (2012). Rhod regulates cytoskeletal dynamics via the actin nucleation–promoting factor wasp homologue associated with actin golgi membranes and microtubules. *Molecular Biology of the Cell*, 23(24):4807–4819. 4

Gao, L., Bryan, B. A., Nolan, M., Connor, J. D., Song, X., and Zhao, G. (2016). Robust global sensitivity analysis under deep uncertainty via scenario analysis. *Environmental Modelling & Software*, 76:154–166. 81, 82, 199

Garcia-Mata, R., Boulter, E., and Burridge, K. (2011). The 'invisible hand': reg-

ulation of Rho GTPases by RhoGDIs. *Nature Reviews Molecular Cell Biology*, 12(8):493–504. 3

Gardner, T. S., Cantor, C. R., and Collins, J. J. (2000). Construction of a genetic toggle switch in escherichia coli. *Nature*, 403(6767):339–342. 13

Garnett, C., Olesky, D., and van den Driessche, P. (2014). A note on sign patterns of order 3 that require particular refined inertias. *Linear Algebra and its Applications*, 450:293–300. 184, 187

Goldbeter, A. (1995). A model for circadian oscillations in the drosophila period protein (per). *Proceedings of the Royal Society of London. Series B: Biological Sciences*, 261(1362):319–324. 64

Goldbeter, A. and Koshland, D. E. (1981). An amplified sensitivity arising from covalent modification in biological systems. *Proceedings of the National Academy of Sciences*, 78(11):6840–6844. 19, 27, 31, 35

Golub, G. H. and Van Loan, C. F. (2012). *Matrix computations*, volume 3. Johns Hopkins University Press. 191, 196

Gonze, D. and Goldbeter, A. (2001). A model for a network of phosphorylation–dephosphorylation cycles displaying the dynamics of dominoes and clocks. *Journal of Theoretical Biology*, 210(2):167–186. 11

Goryachev, A. B. and Pokhilko, A. V. (2008). Dynamics of Cdc42 network embodies a Turing-type mechanism of yeast cell polarity. *FEBS Letters*, 582(10):1437–1443. 15, 156

Graessl, M., Koch, J., Calderon, A., Kamps, D., Banerjee, S., Mazel, T., Schulze, N., Jungkurth, J. K., Patwardhan, R., Solouk, D., et al. (2017). An excitable Rho GTPase signaling network generates dynamic subcellular contraction patterns. *Journal of Cell Biology*, 216(12):4271–4285. 1, 6, 8, 9, 10, 13, 15, 16, 20, 21, 22, 24, 26, 30, 31, 34, 35, 39, 45, 54, 61, 89, 95, 98, 101, 103, 105, 106, 118, 134, 156

Graziano, B. R. and Weiner, O. D. (2014). Self-organization of protrusions and polarity during eukaryotic chemotaxis. *Current Opinion in Cell Biology*, 30:60–67. 11

Guidi, G. M. and Goldbeter, A. (1997). Bistability without hysteresis in chemical reaction systems: a theoretical analysis of irreversible transitions between multiple steady states. *The Journal of Physical Chemistry A*, 101(49):9367–9376. 154

Guilluy, C., Garcia-Mata, R., and Burridge, K. (2011). Rho protein crosstalk: another social network? *Trends in Cell Biology*, 21(12):718–726. 1, 12

Gutenkunst, R. N., Waterfall, J. J., Casey, F. P., Brown, K. S., Myers, C. R., and Sethna, J. P. (2007). Universally sloppy parameter sensitivities in systems biology models. *PLoS Computational Biology*, 3(10):1871–78. 119

Hanley, P. J., Xu, Y., Kronlage, M., Grobe, K., Schön, P., Song, J., Sorokin, L., Schwab, A., and Bähler, M. (2010). Motorized RhoGAP myosin IXb (Myo9b) controls cell shape and motility. *Proceedings of the National Academy of Sciences*, 107(27):12145–12150. 5, 6, 21, 22

Hartwell, L. H., Hopfield, J. J., Leibler, S., and Murray, A. W. (1999). From molecular to modular cell biology. *Nature*, 402(6761):C47–C52. 20

Heasman, S. J., Carlin, L. M., Cox, S., Ng, T., and Ridley, A. J. (2010). Coordinated Rhoa signaling at the leading edge and uropod is required for T cell transendothelial migration. *The Journal of Cell Biology*, 190(4):553–563. 4

Heasman, S. J. and Ridley, A. J. (2008). Mammalian Rho GTPases: new insights into their functions from in vivo studies. *Nature Reviews Molecular Cell Biology*, 9(9):690–701. 2

Hodge, R. G. and Ridley, A. J. (2016). Regulating Rho GTPases and their regulators. *Nature Reviews Molecular Cell Biology*, 17(8):496–510. 3

Hodgkin, A. L. and Huxley, A. F. (1952). A quantitative description of membrane current and its application to conduction and excitation in nerve. *The Journal of Physiology*, 117(4):500–544. 95

Holmes, W. R. and Edelstein-Keshet, L. (2016). Analysis of a minimal Rho-GTPase circuit regulating cell shape. *Physical Biology*, 13(4):046001. 12, 13, 15

Holmes, W. R., Mata, M. A., and Edelstein-Keshet, L. (2015). Local perturbation

analysis: a computational tool for biophysical reaction-diffusion models. *Biophysical Journal*, 108(2):230–236. 53

Holmes, W. R., Park, J., Levchenko, A., and Edelstein-Keshet, L. (2017). A mathematical model coupling polarity signaling to cell adhesion explains diverse cell migration patterns. *PLoS Computational Biology*, 13(5):1–22. 12, 13, 15

Homma, T. and Saltelli, A. (1996). Importance measures in global sensitivity analysis of nonlinear models. *Reliability Engineering & System Safety*, 52(1):1–17. 81, 198

Hu, D. and Yuan, J.-M. (2006). Time-dependent sensitivity analysis of biological networks: coupled mapk and pi3k signal transduction pathways. *The Journal of Physical Chemistry A*, 110(16):5361–5370. 64

Huang, B., Lu, M., Jolly, M. K., Tsarfaty, I., Onuchic, J., and Ben-Jacob, E. (2014). The three-way switch operation of Rac1/Rhoa GTPase-based circuit controlling amoeboid-hybrid-mesenchymal transition. *Scientific Reports*, 4. 12

Huang, C.-H., Tang, M., Shi, C., Iglesias, P. A., and Devreotes, P. N. (2013). An excitable signal integrator couples to an idling cytoskeletal oscillator to drive cell migration. *Nature Cell Biology*, 15(11):1307–1316. 14

Iglesias, P. A. and Devreotes, P. N. (2012). Biased excitable networks: how cells direct motion in response to gradients. *Current Opinion in Cell Biology*, 24(2):245–253. 9, 10, 14, 95

Inagaki, N. and Katsuno, H. (2017). Actin waves: Origin of cell polarization and migration? *Trends in Cell Biology*. 11

Jaffe, A. B. and Hall, A. (2005). Rho GTPases: biochemistry and biology. *Annual Review of Cell and Developmental Biology*, 21:247–269. 2

Jilkine, A., Marée, A. F., and Edelstein-Keshet, L. (2007). Mathematical model for spatial segregation of the rho-family gtpases based on inhibitory crosstalk. *Bulletin of Mathematical Biology*, 69(6):1943–1978. 155

Johansson, J. R., Nation, P., and Nori, F. (2014). QuTiP: An open-source Py-

thon framework for the dynamics of open quantum systems. *Computer Physics Communications*, 183(8):1760–1772. 122

Johnson, K. A. and Goody, R. S. (2011). The original Michaelis constant: translation of the 1913 Michaelis–Menten paper. *Biochemistry*, 50(39):8264–8269. 180

Jones, C. K. (1984). Stability of the travelling wave solution of the fitzhugh-nagumo system. *Transactions of the American Mathematical Society*, 286(2):431–469. 152

Jordan, D. W. and Smith, P. (1999). *Nonlinear ordinary differential equations: an introduction to dynamical systems*, volume 2. Oxford University Press, USA. 47, 49, 50, 52

Kaipio, J. and Somersalo, E. (2006). *Statistical and computational inverse problems*, volume 160. Springer Science & Business Media. 119

Kamps, D., Koch, J., Juma, V., Graessl, M., Banerjee, S., Mazel, T., Koseska, A., Schmick, M., Chen, X., Yaowen, W., Portet, S., Madzvamuse, A., Nalbant, P., and Dehmelt, L. (2019). Reaction-diffusion based focusing of local cell contraction pulses. *In Preparation*, -(-):–. 8, 10, 19, 20, 21, 22, 24, 26, 30, 31, 34, 35, 39, 45, 54, 61, 98, 101, 103, 105, 106, 117, 118, 120, 123, 133, 134, 156

Keener, J. P. (1980). Waves in excitable media. *SIAM Journal on Applied Mathematics*, 39(3):528–548. 152

Keener, J. P. and Sneyd, J. (1998). *Mathematical physiology*, volume 1. Springer. 179, 181, 183

Khurana, S. and George, S. P. (2011). The role of actin bundling proteins in the assembly of filopodia in epithelial cells. *Cell Adhesion & Migration*, 5(5):409–420. 4

Kim, D., Kwon, Y.-K., and Cho, K.-H. (2007). Coupled positive and negative feedback circuits form an essential building block of cellular signaling pathways. *BioEssays*, 29(1):85–90. 20

Kim, I.-J., Olesky, D. D., Shader, B. L., Van Den Driessche, P., Van Der Holst, H., and Vander Meulen, K. N. (2009). Generating potentially nilpotent full sign patterns. *Electron Journal of Linear Algebra*, 18(1):162–175. 184

Kong, R., Yi, F., Wen, P., Liu, J., Chen, X., Ren, J., Li, X., Shang, Y., Nie, Y., Wu, K., et al. (2015). Myo9b is a key player in SLIT/ROBO-mediated lung tumor suppression. *The Journal of Clinical Investigation*, 125(12):4407–4420. 5

Koshland Jr, D. E. (2002). The application and usefulness of the ratio kcat/KM. *Bioorganic Chemistry*, 30(3):211–213. 127

Krendel, M., Zenke, F. T., and Bokoch, G. M. (2002). Nucleotide exchange factor gef-h1 mediates cross-talk between microtubules and the actin cytoskeleton. *Nature Cell Biology*, 4(4):294–301. 7

Kruse, K. and Jülicher, F. (2005). Oscillations in cell biology. *Current opinion in cell biology*, 17(1):20–26. 64

Kühn, S. and Geyer, M. (2014). Formins as effector proteins of Rho GTPases. *Small GTPases*, 5(3):e983876. 4

Larter, R. (1983). Sensitivity analysis of autonomous oscillators. separation of secular terms and determination of structural stability. *The Journal of Physical Chemistry*, 87(16):3114–3121. 65, 189

Lee, C.-S., Choi, C.-K., Shin, E.-Y., Schwartz, M. A., and Kim, E.-G. (2010). Myosin II directly binds and inhibits Dbl family guanine nucleotide exchange factors: a possible link to Rho family GTPases. *The Journal of Cell Biology*, 190(4):663–674. 6, 7, 8, 21, 22

Lu, B. and Yue, H. (2010). Sensitivity analysis of oscillatory biological systems with a SVD-based algorithm. *Systemics and Informatics World Network*, 10:85–92. 63, 65, 71, 189, 190, 191, 193, 194

Lu, Y. and Yue, H. (2011). Objective sensitivity analysis of biological oscillatory systems. *IFAC Proceedings Volumes*, 44(1):10466–10471. 63, 65, 66, 67, 190, 191, 192

Ma, Z. and Leijon, A. (2011). Bayesian estimation of beta mixture models with variational inference. *IEEE Transactions on Pattern Analysis and Machine Intelligence*, (11):2160–2173. 121

Ma, Z., Teschendorff, A. E., Leijon, A., Qiao, Y., Zhang, H., and Guo, J. (2015).

Variational bayesian matrix factorization for bounded support data. *IEEE Transactions on Pattern Analysis and Machine intelligence*, 37(4):876–889. 121

Machacek, M., Hodgson, L., Welch, C., Elliott, H., Pertz, O., Nalbant, P., Abell, A., Johnson, G. L., Hahn, K. M., and Danuser, G. (2009). Coordination of rho gtpase activities during cell protrusion. *Nature*, 461(7260):99–103. 4, 12

Madzvamuse, A. (2000). *A numerical approach to the study of spatial pattern formation*. PhD thesis, University of Oxford. 140

Marée, A. F., Grieneisen, V. A., and Edelstein-Keshet, L. (2012). How cells integrate complex stimuli: the effect of feedback from phosphoinositides and cell shape on cell polarization and motility. *PLoS Computational Biology*, 8(3):e1002402. 155

Marée, A. F., Jilkine, A., Dawes, A., Grieneisen, V. A., and Edelstein-Keshet, L. (2006). Polarization and movement of keratocytes: a multiscale modelling approach. *Bulletin of Mathematical Biology*, 68(5):1169–1211. 155

Marino, S., Hogue, I. B., Ray, C. J., and Kirschner, D. E. (2008). A methodology for performing global uncertainty and sensitivity analysis in systems biology. *Journal of Theoretical Biology*, 254(1):178–196. 81, 82, 199

Mayor, R. and Carmona-Fontaine, C. (2010). Keeping in touch with contact inhibition of locomotion. *Trends in Cell Biology*, 20(6):319–328. 2

Mayor, R. and Theveneau, E. (2013). The neural crest. *Development*, 140(11):2247–2251. 5

McRae, G. J., Tilden, J. W., and Seinfeld, J. H. (1982). Global sensitivity analysis—a computational implementation of the fourier amplitude sensitivity test (fast). *Computers & Chemical Engineering*, 6(1):15–25. 201

Medina, F., Carter, A. M., Dada, O., Gutowski, S., Hadas, J., Chen, Z., and Sternweis, P. C. (2013). Activated RhoA is a positive feedback regulator of the Lbc family of Rho guanine nucleotide exchange factor proteins. *Journal of Biological Chemistry*, 288(16):11325–11333. 21, 31

Meller, N., Merlot, S., and Guda, C. (2005). CZH proteins: a new family of Rho-GEFs. *Journal of Cell Science*, 118(21):4937–4946. 7

Miao, Y., Bhattacharya, S., Edwards, M., Cai, H., Inoue, T., Iglesias, P. A., and Devreotes, P. N. (2017). Altering the threshold of an excitable signal transduction network changes cell migratory modes. *Nature Cell Biology*, 19(4):329–340. 10, 14, 15, 95

Montell, D. J., Yoon, W. H., and Starz-Gaiano, M. (2012). Group choreography: mechanisms orchestrating the collective movement of border cells. *Nature Reviews Molecular Cell Biology*, 13(10):631. 3

Mori, Y., Jilkine, A., and Edelstein-Keshet, L. (2008). Wave-pinning and cell polarity from a bistable reaction-diffusion system. *Biophysical Journal*, 94(9):3684–3697. 13, 15, 21

Mori, Y., Jilkine, A., and Edelstein-Keshet, L. (2011). Asymptotic and bifurcation analysis of wave-pinning in a reaction-diffusion model for cell polarization. *SIAM Journal on Applied Mathematics*, 71(4):1401–1427. 13, 15

Moshfegh, Y., Bravo-Cordero, J. J., Miskolci, V., Condeelis, J., and Hodgson, L. (2014). A Trio–Rac1–Pak1 signalling axis drives invadopodia disassembly. *Nature Cell Biology*, 16(6):571. 4

Murray, J. (2003). Mathematical biology II 3 ed., 536. 10, 11, 138

Murray, J. D. (2002). Mathematical biology I: an introduction, vol. 17 of interdisciplinary applied mathematics. 10, 11, 45, 95

Nalbant, P., Chang, Y.-C., Birkenfeld, J., Chang, Z.-F., and Bokoch, G. M. (2009). Guanine nucleotide exchange factor-H1 regulates cell migration via localized activation of Rhoa at the leading edge. *Molecular Biology of the Cell*, 20(18):4070–4082. 5, 7, 8, 21

Norris, J. R. (1998). *Markov chains*. Number 2. Cambridge University Press. 205, 206

Novak, B. and Tyson, J. J. (1993). Numerical analysis of a comprehensive model of m-phase control in xenopus oocyte extracts and intact embryos. *Journal of Cell Science*, 106(4):1153–1168. 11

Novak, B. and Tyson, J. J. (1995). Quantitative analysis of a molecular model of

mitotic control in fission yeast. *Journal of Theoretical Biology*, 173(3):283–305. 11

Ohashi, K., Fujiwara, S., and Mizuno, K. (2017). Roles of the cytoskeleton, cell adhesion and rho signalling in mechanosensing and mechanotransduction. *The Journal of Biochemistry*, 161(3):245–254. 2

Park, J., Holmes, W. R., Lee, S.-H., Kim, H.-N., Kim, D.-H., Kwak, M. K., Wang, C. J., Suh, K.-Y., Edelstein-Keshet, L., and Levchenko, A. (2016). A mechanochemical feedback underlies co-existence of qualitatively distinct cell polarity patterns within diverse cell populations. *ArXiv E-prints*. 13

Petrášek, Z., Hoege, C., Mashaghi, A., Ohrt, T., Hyman, A. A., and Schwille, P. (2008). Characterization of Protein Dynamics in Asymmetric Cell division by Scanning Fluorescence Correlation Spectroscopy. *Biophysical Journal*, 95(11):5476–5486. 146, 152

Raftopoulou, M. and Hall, A. (2004). Cell migration: Rho GTPases lead the way. *Developmental Biology*, 265(1):23–32. 2

Ratto, M., Pagano, A., and Young, P. (2007). State dependent parameter metamodelling and sensitivity analysis. *Computer Physics Communications*, 177(11):863–876. 81

Rätz, A. and Röger, M. (2012). Turing instabilities in a mathematical model for signaling networks. *Journal of Mathematical Biology*, 65(6-7):1215–1244. 21, 156

Rätz, A. and Röger, M. (2014). Symmetry breaking in a bulk–surface reaction–diffusion model for signalling networks. *Nonlinearity*, 27(8):1805–1827. 156

Redheffer, R. (1972). The theorems of Bony and Brezis on flow-invariant sets. *The American Mathematical Monthly*, 79(7):740–747. 37

Ren, Y., Li, R., Zheng, Y., and Busch, H. (1998). Cloning and characterization of GEF-H1, a microtubule-associated guanine nucleotide exchange factor for Rac and Rho GTPases. *Journal of Biological Chemistry*, 273(52):34954–34960. 7

Ridley, A. J. (2015). Rho GTPase signalling in cell migration. *Current Opinion in Cell Biology*, 36:103–112. 2, 3, 4, 5

Ridley, A. J., Comoglio, P. M., and Hall, A. (1995). Regulation of scatter factor/hepatocyte growth factor responses by Ras, Rac, and Rho in MDCK cells. *Molecular and Cellular Biology*, 15(2):1110–1122. 2

Ridley, A. J., Schwartz, M. A., Burridge, K., Firtel, R. A., Ginsberg, M. H., Borisy, G., Parsons, J. T., and Horwitz, A. R. (2003). Cell migration: integrating signals from front to back. *Science*, 302(5651):1704–1709. 1

Ross, R. J., Baker, R. E., Parker, A., Ford, M., Mort, R., and Yates, C. (2017). Using approximate bayesian computation to quantify cell–cell adhesion parameters in a cell migratory process. *NPJ Systems Biology and Applications*, 3(9):9–18. 208

Rossman, K. L., Der, C. J., and Sondek, J. (2005). Gef means go: turning on Rho GTPases with guanine nucleotide-exchange factors. *Nature Reviews Molecular Cell Biology*, 6(2):167–180. 7

Row, R. H., Maître, J.-L., Martin, B. L., Stockinger, P., Heisenberg, C.-P., and Kimelman, D. (2011). Completion of the epithelial to mesenchymal transition in zebrafish mesoderm requires spadetail. *Developmental Biology*, 354(1):102–110. 5

Rowlands, A., Panniers, R., and Henshaw, E. (1988). The catalytic mechanism of guanine nucleotide exchange factor action and competitive inhibition by phosphorylated eukaryotic initiation factor 2. *The Journal of Biological Chemistry*, 263(12):5526–5533. 25

Rozenwasser, E. and Yusupov, R. (1999). *Sensitivity of automatic control systems*. CRC press. 189

Ryan, G. L., Watanabe, N., and Vavylonis, D. (2012). A review of models of fluctuating protrusion and retraction patterns at the leading edge of motile cells. *Cytoskeleton*, 69(4):195–206. 11

Sakumura, Y., Tsukada, Y., Yamamoto, N., and Ishii, S. (2005). A molecular model for axon guidance based on cross talk between Rho GTPases. *Biophysical Journal*, 89(2):812–822. 25

Saltelli, A., Annoni, P., Azzini, I., Campolongo, F., Ratto, M., and Tarantola, S. (2010). Variance based sensitivity analysis of model output. design and estimator

for the total sensitivity index. *Computer Physics Communications*, 181(2):259–270. 200

Saltelli, A. and Bolado, R. (1998). An alternative way to compute fourier amplitude sensitivity test (fast). *Computational Statistics & Data Analysis*, 26(4):445–460. 82, 199, 201

Saltelli, A., Chan, K., Scott, E. M., et al. (2000). *Sensitivity analysis*, volume 1. Wiley New York. 62, 82, 199, 201

Saltelli, A., Tarantola, S., Campolongo, F., and Ratto, M. (2004). *Sensitivity analysis in practice: a guide to assessing scientific models*. John Wiley & Sons. 81, 201

Saltelli, A., Tarantola, S., and Chan, K.-S. (1999). A quantitative model-independent method for global sensitivity analysis of model output. *Technometrics*, 41(1):39–56. 81, 82, 198, 199, 201

Sandquist, J. C., Swenson, K. I., DeMali, K. A., Burridge, K., and Means, A. R. (2006). Rho kinase differentially regulates phosphorylation of nonmucle myosin II isoforms A and B during cell rounding and migration. *Journal of Biological Chemistry*, 281(47):35873–35883. 6

Sarfaraz, W. and Madzvamuse, A. (2017). Classification of parameter spaces for a reaction-diffusion model on stationary domains. *Chaos, Solitons & Fractals*, 103:33–51. 138

Schaibly, J. H. and Shuler, K. E. (1973). Study of the sensitivity of coupled reaction systems to uncertainties in rate coefficients. ii applications. *The Journal of Chemical Physics*, 59(8):3879–3888. 199

Shampine, L. F. and Reichelt, M. W. (1997). The matlab ode suite. *SIAM Journal on Scientific Computing*, 18(1):1–22. 90

Shi, C., Huang, C.-H., Devreotes, P. N., and Iglesias, P. A. (2013). Interaction of motility, directional sensing, and polarity modules recreates the behaviors of chemotaxing cells. *PLoS Computational Biology*, 9(7):e1003122. 14

Simon, C. M., Vaughan, E. M., Bement, W. M., and Edelstein-Keshet, L. (2013).

Pattern formation of Rho GTPases in single cell wound healing. *Molecular Biology of the Cell*, 24(3):421–432. 25, 53

Simons, M., Wang, M., McBride, O., Kawamoto, S., Yamakawa, K., Gdula, D., Adelstein, R. S., and Weir, L. (1991). Human nonmuscle myosin heavy chains are encoded by two genes located on different chromosomes. *Circulation Research*, 69(2):530–539. 5

Skogestad, S. and Postlethwaite, I. (2000). *Multivariate Feedback control.* Chichester, UK: John Wiley and Sons. 193

Sneyd, J. and Keener, J. (1998). *Mathematical Physiology II: Systems Physiology*, volume 1. Springer New York. 95

Sobol, I. M. (1993). Sensitivity estimates for nonlinear mathematical models. *Mathematical Modelling and Computational Experiments*, 1(4):407–417. 81, 198, 201

Somlyo, A. P. and Somlyo, A. V. (2000). Signal transduction by g-proteins, rho-kinase and protein phosphatase to smooth muscle and non-muscle myosin II. *The Journal of Physiology*, 522(2):177–185. 6

Stelling, J., Sauer, U., Szallasi, Z., Doyle III, F. J., and Doyle, J. (2004). Robustness of cellular functions. *Cell*, 118(6):675–685. 20

Stuart, A. M. (2010). Inverse problems: a bayesian perspective. *Acta Numerica*, 19:451–559. 119, 121, 122, 203, 204, 205, 206, 208

Sutton, J. E., Guo, W., Katsoulakis, M. A., and Vlachos, D. G. (2016). Effects of correlated parameters and uncertainty in electronic-structure-based chemical kinetic modelling. *Nature Chemistry*, 8(4):331–337. 119

Taghia, J., Ma, Z., and Leijon, A. (2014). Bayesian estimation of the von-mises fisher mixture model with variational inference. *IEEE Transactions on Pattern Analysis and Machine Intelligence*, 36(9):1701–1715. 121

Tarantola, A. (2005). *Inverse problem theory and methods for model parameter estimation*, volume 89. SIAM. 118, 119

Tarantola, S., Gatelli, D., and Mara, T. A. (2006). Random balance designs for

the estimation of first order global sensitivity indices. *Reliability Engineering & System Safety*, 91(6):717–727. 81

Tjelmeland, H. (2004). Using all metropolis–hastings proposals to estimate mean values. Technical report. 207

Togo, T. and Steinhardt, R. A. (2004). Nonmuscle myosin IIA and IIB have distinct functions in the exocytosis-dependent process of cell membrane repair. *Molecular Biology of the Cell*, 15(2):688–695. 5

Tomovic, R. and Vukobratovic, M. (1972). *General sensitivity theory*, volume 1 of *Mod. Analytic Comput. Methods Sci. Math. ; 35*. New York, NY: North-Holland. 65, 189, 190

Turing, A. M. (1952). The chemical basis of morphogenesis. *Philosophical Transactions of the Royal Society of London. Series B, Biological Sciences*, 237(641):37–72. 11, 138, 152

Tyson, J. J., Chen, K., and Novak, B. (2001). Network dynamics and cell physiology. *Nature Reviews Molecular Cell Biology*, 2(12):908–916. 10

Tyson, J. J., Chen, K. C., and Novak, B. (2003). Sniffers, buzzers, toggles and blinkers: dynamics of regulatory and signaling pathways in the cell. *Current Opinion in Cell Biology*, 15(2):221–231. x, 10, 11, 13, 15, 19, 20, 21, 30, 34, 54, 181

Tyson, J. J. and Keener, J. P. (1988). Singular perturbation theory of traveling waves in excitable media (a review). *Physica D: Nonlinear Phenomena*, 32(3):327–361. 152

van Haastert, P. J., Keizer-Gunnink, I., and Kortholt, A. (2017). Coupled excitable ras and f-actin activation mediates spontaneous pseudopod formation and directed cell movement. *Molecular Biology of the Cell*, 28(7):922–934. 10

Varma, A., Morbidelli, M., and Wu, H. (2005). *Parametric sensitivity in chemical systems*. Cambridge University Press. 63, 189

Vega, F. M., Fruhwirth, G., Ng, T., and Ridley, A. J. (2011). Rhoa and rhoc have

distinct roles in migration and invasion by acting through different targets. *The Journal of Cell Biology*, 193(4):655–665. 4

Vyshemirsky, V. and Girolami, M. A. (2007). Bayesian ranking of biochemical system models. *Bioinformatics*, 24(6):833–839. 119

Wakayama, Y., Fukuhara, S., Ando, K., Matsuda, M., and Mochizuki, N. (2015). Cdc42 mediates bmp-induced sprouting angiogenesis through fmnl3-driven assembly of endothelial filopodia in zebrafish. *Developmental Cell*, 32(1):109–122. 5

Wang, M., Li, X., and Zhang, J. (2008). The (G G)-expansion method and travelling wave solutions of nonlinear evolution equations in mathematical physics. *Physics Letters A*, 372(4):417–423. 152

Weitzman, M. D. (2013). *Single molecule dynamics of the Rho GTPase spatial cycle in living cells*. PhD thesis, University of Delaware. 146, 152

Weyl, H. (1938). Mean motion. *American Journal of Mathematics*, 60(4):889–896. 199

Wirth, J., Jensen, K., Post, P., Bement, W., and Mooseker, M. (1996). Human myosin-IXb, an unconventional myosin with a chimerin-like rho/rac gtpase-activating protein domain in its tail. *Journal of Cell Science*, 109(3):653–661. 6

Wolf, K., Te Lindert, M., Krause, M., Alexander, S., Te Riet, J., Willis, A. L., Hoffman, R. M., Figdor, C. G., Weiss, S. J., and Friedl, P. (2013). Physical limits of cell migration: control by ecm space and nuclear deformation and tuning by proteolysis and traction force. *Journal of Cell Biology*, 201(7):1069–1084. 1

Wu, J., Mao, Z., Tan, H., Han, L., Ren, T., and Gao, C. (2012). Gradient biomaterials and their influences on cell migration. *Interface Focus*, 2(3):337–355. 2

Xiong, Y., Huang, C.-H., Iglesias, P. A., and Devreotes, P. N. (2010). Cells navigate with a local-excitation, global-inhibition-biased excitable network. *Proceedings of the National Academy of Sciences*, 107(40):17079–17086. 10, 14

Yang, H. W., Collins, S. R., and Meyer, T. (2015). Locally excitable cdc42 signals steer cells during chemotaxis. *Nature Cell Biology*, 18(2):191–201. 10

Yi, F., Kong, R., Ren, J., Zhu, L., Lou, J., Wu, J. Y., and Feng, W. (2016). Non-canonical Myo9b-RhoGAP accelerates RhoA GTP hydrolysis by a dual-arginine-finger mechanism. *Journal of Molecular Biology*, 428(15):3043–3057. 2, 5

Yue, H., Brown, M., He, F., Jia, J., and Kell, D. B. (2008). Sensitivity analysis and robust experimental design of a signal transduction pathway system. *International Journal of Chemical Kinetics*, 40(11):730–741. 64

Zak, D. E., Stelling, J., and Doyle, F. J. (2005). Sensitivity analysis of oscillatory (bio) chemical systems. *Computers & Chemical Engineering*, 29(3):663–673. 63, 65, 66, 67, 189, 190, 191, 192, 193

Appendix A

Law of mass action, enzyme kinetics and Hill function

In this appendix, we introduced the law of mass action, Michaelis-Menten kinetics and the Hill function that are used in Chapter 2 to derive from first principles the mathematical models to describe GEF-H1–Rho–Myosin signalling network.

A.1 Law of mass action

This is the fundamental law of chemical reactions. It describes the rate at which chemicals whether large macromolecules or simple ions collide and interact to form different products.

Suppose that two chemical compounds, say X and Y react upon collision to form the a compound Z described by the formulation,

$$X + Y \xrightarrow{k} Z. \tag{A.1}$$

Let $[X]$ $[Y]$ and $[Z]$ denotes the concentration of the chemical compounds X, Y and Z respectively, then the rate of reaction (A.1) is the rate of accumulation of the product, i.e. $\frac{d[Z]}{dt}$. This rate is the product of number of collisions per unit time between the two reactants and the probability that a collision is sufficiently energetic to overcome free energy of activation of the reaction. This number of collisions per unit time is taken to be proportional to the product of $[X]$ and $[Y]$

with a factor of proportionality (this factor of proportionality may depend upon the geometrical shapes and sizes of reactant molecules or temperature of the mixture). Mathematically, this law is expressed as,

$$\frac{d[Z]}{dt} = k\,[X]\,[Y]\,, \tag{A.2}$$

where k is the rate constant of the reaction, it accounts for the probability that the molecules are well oriented and have sufficient energy to react. The units of k depend on the order of the reaction, this is a second order equation with the unit being $(concentration \times Time)^{-1}$.

Now let us consider a more general case for an elementary reaction in which a molecules of X react with b molecules of Y to produce c molecules of Z and d molecules of D given by the formulation:

$$aX + bY \xrightarrow{k} cZ + dD. \tag{A.3}$$

The mass action law provides that the rate, $v = k\,[X]^a\,[Y]^b$ and the order of this reaction is $a + b$. The unit of k is $(concentration)^{-b-a+1} \times (time)^{-1}$.
The evolution of different species is given by:

$$\begin{aligned}
\frac{d[X]}{dt} &= -k(a)\,[X]^a\,[Y]^b\,,\\
\frac{d[Y]}{dt} &= -k(b)\,[X]^a\,[Y]^b\,,\\
\frac{d[Z]}{dt} &= k(c)\,[X]^a\,[Y]^b\,,\\
\frac{d[D]}{dt} &= k(d)\,[X]^a\,[Y]^b\,.
\end{aligned} \tag{A.4}$$

In general case for the reaction in which n molecules of X transformed, b molecules are recovered at the end:

$$nX + \cdots \xrightarrow{k} bX + \cdots\,;$$

Then the evolution equation for the concentration of X is

$$\frac{d\,[X]}{dt} = \eta V, \tag{A.5}$$

where $\eta = b - n$ is called the **stoichiometric coefficient** and $V = k\,[X]^n\,[\cdot]$. The sign of η depends on the global behaviour of the species i.e. $\eta > 0$ if globally the species X is produced, and $\eta < 0$ if it is consumed globally.

A.1.1 Systems of chemical reactions

We want to consider a system of coupled chemical reactions:

$$\begin{aligned} n_{11}X_1 + n_{21}X_2 + \cdots &\xrightarrow{k_1} b_{11}X_1 + b_{21}X_2 + \cdots, \\ n_{12}X_1 + n_{22}X_2 + \cdots &\xrightarrow{k_2} b_{12}X_1 + b_{22}X_2 + \cdots, \\ \vdots \qquad\qquad &\quad \vdots \qquad\qquad \vdots \\ n_{1R}X_1 + n_{2R}X_2 + \cdots &\xrightarrow{k_R} b_{1R}X_1 + b_{2R}X_2 + \cdots. \end{aligned} \tag{A.6}$$

Here the evolution of a given compound X_i involved in R reactions is defined by

$$\frac{d[X_i]}{dt} = \sum_{r=1}^{R} \eta_{ir} V_r = \eta_{i1}V_1 + \eta_{i2}V_2 + \cdots + \eta_{iR}V_R, \tag{A.7}$$

where V_r is the rate of reaction r $(r = 1, 2, \cdots R)$, $V_r = k_r \pi_i [X_i]^{n_{ir}}$.
$\eta_{ir} = b_{ir} - n_{ir}$ is the stoichiometric coefficient of the compound X_i in the reaction r.

NB: Mass action law is limited and is not valid for all the reactions, for example at high concentrations, doubling the concentrations of one reactant need not double the overall reaction rate, and at extremely very low concentrations, it may not be appropriate to present the concentration as a continuous variable (Keener and Sneyd, 1998).

A.2 Michaelis-Menten kinetics

Michaelis-Menten kinetics results in the case where a reaction is catalysed by an enzyme. "Enzymes are proteins that help convert substrates into products, but they remain unchanged in the reaction" (Keener and Sneyd, 1998).

In an enzyme-catalysed reaction, the enzyme binds itself to the substrate (one of the reactants) to form an enzymes-substrate complex denoted ES. This formation of complex leads to the formation of transition-state species, which then forms the product. We denote an enzyme E, substrate S and V_0 the initial rate of reaction, and their concentrations given by $[E]$ and $[S]$ respectively. The curve expressing the relationship between the $[S]$ and V_0 has a general shape for most enzymes, it approaches a rectangular hyperbola. This curve can be expressed algebraically by

Michaelis-Menten equation.

$$V_0 = \frac{V_{\max}\,[S]}{K_m + [S]}. \tag{A.8}$$

This model that deviates from the law of mass action was first proposed by Michaelis and Menten in 1913 (Johnson and Goody, 2011). They derived this equation by using the basic hypothesis that the rate limiting step in an enzymatic reaction is the breakdown of the ES complex into the product and free enzymes.

To derive Equation (A.8), we start from the formation and breakdown of enzyme-substrate complex ES, with its concentration denoted $[ES]$ i.e

$$E + S \underset{k_{-1}}{\overset{k_1}{\rightleftharpoons}} ES, \tag{A.9}$$

$$ES \underset{k_{-2}}{\overset{k_2}{\rightleftharpoons}} E + P. \tag{A.10}$$

We ignore the reverse reaction, $P \longrightarrow ES$, since early in the reaction, the concentration of $[P]$ is negligible. Therefore the overall reaction reduces to:

$$E + S \underset{k_{-1}}{\overset{k_1}{\rightleftharpoons}} ES \xrightarrow{k_2} E + P. \tag{A.11}$$

V_0 is determined by the breakdown of ES to form product, this is determined by, $[ES]$

$$V_0 = k_2\,[ES]\,, \tag{A.12}$$

where V_0 is the initial rate of production of the product. We introduce another term $[E_0]$ which represents the total concentration of the enzymes. Therefore the unbound enzymes can be represented by:

$$[E] = [E_0] - [ES]\,.$$

Now the rate of accumulation of ES is:

$$\frac{d\,[ES]}{dt} = k_1\,[E]\,[S] - (k_{-1} + k_2)\,[ES]\,, \tag{A.13}$$

or equivalently

$$\frac{d\,[ES]}{dt} = k_1([E_0] - [ES])\,[S] - (k_{-1} + k_2)\,[ES]\,. \tag{A.14}$$

Enzymes are capable of processing the substrate very efficiently, and a steady-state is soon reached in which the rate of formation of the enzyme-substrate complex equals

the rate of its breakdown. Very little complex is present and it turns out over rapidly but the concentration stays the same over time. Therefore according to the quasi-steady-state approximation (Keener and Sneyd, 1998), then the rate of formation of the enzyme-substrate complex equals its breakdown hence from equation (A.14) we obtain

$$k_1([E_0] - [ES])\,[S] = (k_{-1} + k_2)\,[ES]\,. \tag{A.15}$$

Solving for $[ES]$ and dividing through by k_1, we obtain

$$[ES] = \frac{[E_0]\,[S]}{[S] + (k_2 + k_{-1})/k_1}. \tag{A.16}$$

The term $(k_2+k_{-1})/k_1$ is the Michaelis constant denoted by K_M. One interpretation of K_M is that it equals the concentration of substrate at which 50% of the enzyme active sites are occupied by substrate, it has units of concentration (Tyson et al., 2003).

$$[ES] = \frac{[E_0]\,[S]}{[S] + K_M}, \tag{A.17}$$

using equation (A.12) in (A.17) we obtain

$$V_0 = \frac{k_2\,[E_0]\,[S]}{[S] + K_M}, \tag{A.18}$$

Now the maximum velocity occurs when the enzyme is saturated, $V_{\max}$ can be defined as $k_2\,[E_0]$. Substituting this in (A.18) we get

$$V_0 = \frac{V_{\max}\,[S]}{[S] + K_M}. \tag{A.19}$$

Equation (A.19) is the Michaelis-Menten kinetics, the rate equation for a one-substrate enzyme-catalysed reaction.

A.3 Hill equation

Consider the case where the reaction velocity is not a simple hyperbolic curve as predicted by Michaelis-Menten model, but rather follows the shape of a sigmoid curve. This results from cooperative behaviour in which an enzyme can bind more than one substrate, but the binding of one affects the binding of subsequent ones.

For the simplest case, consider the case where an enzyme can bind two substrate molecules. It therefore can exist in one of the forms as a free molecule E, or as

complex with one occupied centre ES or as complex with two occupied centres denoted ESS. The reaction mechanism for this case is represented by;

$$E + S \underset{k_{-1}}{\overset{k_1}{\rightleftharpoons}} ES \xrightarrow{k_2} E + P,$$
$$S + ES \underset{k_{-3}}{\overset{k_3}{\rightleftharpoons}} ESS \xrightarrow{k_4} E + P.$$

Denote the concentrations of enzymes by $s = [S]$, $e = [E]$, $c_1 = [ES]$, $c_2 = [ESS]$ and $p = [P]$ and also consider that the total amount of enzyme is conserved, i.e $c_1 + c_2 + e = e_0$. We use the law of mass action to write down rate equations for the concentrations as:

$$\frac{ds}{dt} = -k_1 se + k_{-1}c_1 - k_3 sc_1 + k_{-3}c_2, \tag{A.21a}$$
$$\frac{dc_1}{dt} = k_1 se - (k_{-1} + k_2)c_1 - k_3 sc_2 + (k_4 + k_{-3})c_2, \tag{A.21b}$$
$$\frac{dc_2}{dt} = k_3 sc_1 - (k_4 + k_{-3})c_2, \tag{A.21c}$$
$$\frac{dp}{dt} = k_2 c_1 + k_4 c_2. \tag{A.21d}$$
$$\tag{A.21e}$$

Due to the conservation of mass of enzyme concentration, we do not formulate an equation for e, as this may be expressed in terms of c_1 and c_2. Using quasi-steady state assumption on Equation (A.21b) and Equation (A.21c), we solve for c_1 and c_2 to obtain

$$c_1 = \frac{K_2 e_0 s}{K_1 K_2 + K_2 S + S^2}, \tag{A.22a}$$
$$c_2 = \frac{e_0 s^2}{K_1 K_2 + K_2 S + S^2}, \tag{A.22b}$$

with $K_1 = \frac{k_{-1}+k_2}{k_1}$ and $K_2 = \frac{k_{-3}+k_4}{k_3}$.

Therefore, the reaction velocity, $\frac{dp}{dt}$ is given by

$$\frac{dp}{dt} = \frac{(K_1 k_2 + k_4 s)e_0 s}{K_1 K_2 + K_2 s + s^2}. \tag{A.23}$$

Consider one extreme case where it is assumed that the binding of the first substrate molecule is slow but with one site bound, the binding of the second increases and hence fast. This is modelled by letting $k_3 \mapsto \infty$ and $k_2 \mapsto 0$ while keeping $k_1 k_3 =$

constant (Keener and Sneyd, 1998). This case means $K_1 \mapsto \infty$ and $K_2 \mapsto 0$ while $K_1 K_2 =$ constant.

Using these limits in the velocity reaction, Equation (A.23), we obtain the reaction velocity

$$V = \frac{V_{\max} s^2}{K_h^2 + s^2}, \; K_h^2 = K_1 K_2 \text{ and } V_{\max} = k_4 e_0. \tag{A.24}$$

This can be generalised to the case where n substrate molecules can bind to the enzyme, and hence there are n equilibrium constants K_i, $i = 1, \cdots, n$. In the limiting case where $K_1 \mapsto \infty$ and $K_n \mapsto 0$ while $K_1 K_n =$ constant, we obtain

$$V = \frac{V_{\max} s^n}{K_h^n + s^n}, \quad K_h^n = \prod_{i=1}^{n} K_i. \tag{A.25}$$

Equation (A.25) is known as *Hill equation*. It is used to model reactions whose detailed intermediate steps are not known but in which cooperativity is suspected. The parameters n, $V_{\max}$ and K_h are usually determined from the experimental data.

Appendix B

Sign pattern and the stability analysis

B.1 Introductory concepts about sign pattern

Definition B.1.1 (**Sign pattern (Garnett et al., 2014; Culos et al., 2016)**). *An $n \times n$ sign pattern is a matrix with entries in $\{+, -, 0\}$. For a real matrix J, $\mathcal{J}$ is the sign pattern with each entry equal to the sign of the corresponding entry of J.*

Definition B.1.2 (**Equivalent sign patterns (Culos et al., 2016)**). *A sign pattern $\mathcal{J}$ is equivalent to $\mathcal{J}'$, denoted by $\mathcal{J} \sim \mathcal{J}'$ if*

(i) $\mathcal{J} = \mathcal{J}'^T$,

(ii) *Permutation similarity; $\mathcal{J}$ is obtained from $\mathcal{J}'$ by simultaneous row and column permutations.*

(iii) *Signature similarity; $\mathcal{J}$ is obtained from $\mathcal{J}'$ by negating same set of rows and columns.*

(iv) *Any combination of (i), (ii) or (iii).*

Definition B.1.3 (**Refined inertia (Kim et al., 2009)**). *The refined inertia of an $n \times n$ real matrix J is an ordered 4-tuple $ri(J) = (n_+, n_-, n_z, 2n_p)$ where n_+ is the number of eigenvalues with positive real part, n_- is the number with negative real part, n_z number of zero eigenvalues and $2n_p$ the number of pure imaginary*

eigenvalues (all counted with multiplicities) and $n_+ + n_- + n_z + 2n_p = n$.

The concept of refined inertia splits the number of zero eigenvalues from the number of other eigenvalues on the imaginary axis, which allows the study of existence of periodic solutions in a dynamical system. The sign pattern allows or requires a certain property if respectively some or every realization of that sign pattern has that property. We are interested in the refined inertia

$$\mathbb{H}_n = \{(0,\, n, 0, 0),\, (0, n-2, 0, 2),\, (2, n-2, 0, 0)\}.$$

$\mathbb{H}_n$ which was introduced by (Bodine et al., 2012) corresponds to the transition of eigenvalues as pair of eigenvalues with negative real part crosses the imaginary axis to have positive real parts, and therefore it is used in investigating the existence of periodic solutions as a parameter is varied. If a matrix has this property as certain parameter changes then there is a Hopf bifurcation at some parameter value and hence the possibility of linearly stable periodic solutions. A sign pattern is said to be sign definite if the sign of the entries are not parameter dependent.

Theorem B.1.4 (**Stability of sign matrix (Culos et al., 2016)**). *Let* E *be the steady state value and* $\mathbf{p}$ *represent the parameter values, suppose that the Jacobian matrix,* $J(\mathbf{p})$ *is sign-definite at a positive steady state* E *with the corresponding sign pattern* $\mathcal{J}(\mathbf{p})$ *then,*

(i) *if* $\mathcal{J}(\mathbf{p})$ *requires the refined inertia* $(0,\, n, 0, 0)$, *then the steady state is linearly stable for all* $\mathbf{p}$.

(ii) *if* $\mathcal{J}(\mathbf{p})$ *does not allow* $\mathbb{H}_n$, *then the model does not have periodic solutions around the steady state arising from a Hopf bifurcation.*

(iii) *If the entries of* $J(\mathbf{p})$ *have or have no magnitude restrictions and if the restricted or unrestricted sign pattern allows* $\mathbb{H}_n$ *then the model gives rise to a Hopf bifurcation at a certain parameter value.*

Definition B.1.5 (**Restricted sign pattern (Culos et al., 2016)**). *If there is an algebraic relationship between some of the entries of a real matrix* J, *then these are called magnitude restrictions on the entries of the matrix and the sign matrix* $\mathcal{J}$ *is called a restricted sign pattern; otherwise it is unrestricted sign pattern.*

Definition B.1.6 (**Superpattern (Bodine et al., 2012)**). *A sign pattern* $\mathcal{J}' = [a'_{ij}]$ *is a superpattern of* $\mathcal{J} = [a_{ij}]$ *if* $a'_{ij} = a_{ij}\ \forall\ a_{ij} \neq 0$.

Theorem B.1.7 (**Superpattern of sign patterns with negative diagonal entries (Bodine et al., 2012)**). *If an* $n \times n$ *sign pattern* $\mathcal{J}$ *allows* $\mathbb{H}_n$ *and has all the diagonal entries negative, then any superpattern of* $\mathcal{J}$ *allows* $\mathbb{H}_n$.

Since in this thesis, we study 2×2 sign pattern, I illustrate these concepts and how they can applied in an example of 3×3 matrix.

Example B.1.1. *The Jacobian matrix, Equation (B.1), where* (g^*, r^*, m^*) *is the steady state value of Equation (B.2) does not allow* $\mathbb{H}_3$ *due to magnitude restrictions. In particular, it only allows the refined inertia* $(0, 3, 0, 0)$.

$$\mathbf{J} = \begin{bmatrix} -a_1 r^* - a_2 m^* & a_1 - a_1 g^* & -a_2 g^* \\ b_1 - b_1 r^* & -b_1 g^* - b_2 m^* - b_3 - b_4 & -b_2 r^* \\ 0 & c_1 - c_1 m^* & -c_1 r^* - 1 - c_2 \end{bmatrix}. \tag{B.1}$$

This Jacobian matrix corresponds to the model equations (B.2) below:

$$\frac{dg}{d\tau} = f_1 = a_1 r(1-g) - a_2 m \cdot g, \tag{B.2a}$$
$$\frac{dr}{d\tau} = f_2 = b_1 g(1-r) - b_2 m \cdot r - b_3 r + b_4(1-r), \tag{B.2b}$$
$$\frac{dm}{d\tau} = f_3 = c_1 r(1-m) - m + c_2(1-m). \tag{B.2c}$$

Proof. The Jacobian matrix (B.1) is sign definite, since the sign of all entries are not parameter dependent, therefore we let the sign pattern of (B.1) be given by:

$$\mathcal{S} = \begin{bmatrix} - & + & - \\ + & - & - \\ 0 & + & - \end{bmatrix}. \tag{B.3}$$

By applying transposition we find that $\mathcal{S}$ is equivalent to the sign pattern

$$\mathcal{S}^T = \begin{bmatrix} - & + & 0 \\ + & - & + \\ - & - & - \end{bmatrix}. \tag{B.4}$$

The sign pattern $\mathcal{S}^T$ is a superpattern of the sign pattern

$$\mathcal{S}' = \begin{bmatrix} - & + & 0 \\ 0 & - & + \\ - & 0 & - \end{bmatrix}. \tag{B.5}$$

By (Garnett et al., 2014), $\mathcal{S}'$ requires and hence allows $\mathbb{H}_3$ and has all the diagonal entries negative. Therefore, by Theorem B.1.7 we have that $\mathcal{S}^T$ allows $\mathbb{H}_3$ and hence also $\mathcal{S}$ allows $\mathbb{H}_3$. We show that the unrestricted sign pattern $\mathcal{S}$ does not require $\mathbb{H}_3$, and therefore we just show that $\mathcal{S}$ is not sign non-singular. Without loss of generality take a realization of (B.3) be given by:

$$\mathbf{S} = \begin{bmatrix} -a & 1 & -b \\ 1 & -c & -d \\ 0 & 1 & -e \end{bmatrix}, \tag{B.6}$$

The determinant of $\mathbf{S}$ is

$$-a(ce + d) + (e - d)$$

and hence the sign pattern $\mathcal{S}$ is sign singular and hence does not require $\mathbb{H}_3$. Therefore the unrestricted sign pattern (B.3) allows $\mathbb{H}_3$. The possible refined inertia of (B.6) is presented in Table B.1.

Refined inertia	**Values of** b
(0, 3, 0, 0)	$0 < b < 8$
(0, 1, 0, 2)	$b = 8$
(2, 1, 0, 0)	$8 < b < \infty$

Table B.1: Refined inertias of (B.6) with parameters $a, c, d, e = 1$

We are only left to check whether the sign pattern with magnitude restrictions as in Equation (B.1) allows $\mathbb{H}_3$. If we consider magnitude restrictions then we find (0, 3, 0, 0) as the only refined inertia of (B.1), which shows that the matrix has all eigenvalues negative and therefore the steady state (g^*, r^*, m^*) is linearly stable for all parameter values, by Theorem B.1.4. □

Appendix C

Local and global sensitivity analysis

This appendix contains the derivation of equations used in the sensitivity analysis in Chapter 4.

C.1 Local sensitivity analysis

Here we consider a general ordinary differential equation (ODE) model of the form:

$$\dot{\mathbf{x}}(t) = \mathbf{f}\left(\mathbf{x}(t),\ \mathbf{p}\right), \qquad \mathbf{x}(t_0) = \mathbf{x}_0, \tag{C.1}$$

where $\mathbf{x} \in \mathbb{R}^{m_s}$ is the vector of dependent variables and $\mathbf{p} \in \mathbb{R}^{m_p}$ are the parameters of the model. It is assumed in this case that the system of ODEs depend on the variables themselves, as well as model parameters.

Assuming that the solution for ODE system (C.1) exists, the sensitivity matrix of Equation (C.1) is the matrix denoted $\mathbf{S}(t)$. It describes how the parameter variations around the nominal parameter space, $\mathbf{p}_0$ influences the variations in the model state variables. The sensitivity matrix is defined by:

$$\mathbf{S}(t) = \left(\frac{\partial \mathbf{x}}{\partial \mathbf{p}}\right)_{(\mathbf{x}(t,\mathbf{p}_0),\mathbf{p}_0)} = \{s_{ij}\}\,. \tag{C.2}$$

The simplest way to estimate sensitivities from Equation (C.2) is by finite differences

(Zak et al., 2005). This method is computationally tedious and inaccurate since it may lead to numerical instabilities (Zak et al., 2005).

Another approach to finding the sensitivity matrix (C.2) is by differentiating (C.1) with respect to parameter, $\mathbf{p}$. This gives

$$\begin{aligned} \frac{\partial \dot{\mathbf{x}}}{\partial \mathbf{p}} &= \frac{\partial}{\partial \mathbf{p}} \left(\mathbf{f}(\mathbf{x}, \mathbf{p}) \right) \\ \frac{\partial}{\partial t} \underbrace{\left(\frac{\partial \mathbf{x}}{\partial \mathbf{p}} \right)}_{\mathbf{S}} &= \underbrace{\frac{\partial \mathbf{f}}{\partial \mathbf{x}}}_{A(t,\mathbf{p}_0)} \cdot \underbrace{\frac{\partial \mathbf{x}}{\partial \mathbf{p}}}_{\mathbf{S}} + \underbrace{\frac{\partial \mathbf{f}}{\partial \mathbf{p}}}_{B(t,\mathbf{p}_0)} \end{aligned} \tag{C.3}$$

Therefore;

$$\dot{\mathbf{S}} = A(t, \mathbf{p}_0)\mathbf{S} + B(t, \mathbf{p}_0), \tag{C.4}$$

$$\mathbf{S}(t_0, \mathbf{p}_0) = \mathbf{S}_0.$$

We note that the initial sensitivity to parameters is always zero, unless we consider sensitivity to initial conditions (Rozenwasser and Yusupov, 1999; Varma et al., 2005; Lu and Yue, 2010).

Equations (C.1) and (C.4) can be solved simultaneously to obtain the sensitivity matrix $\mathbf{S}$ given initial conditions $\mathbf{x}(t_0) = \mathbf{x_0}$, nominal parameter values $\mathbf{p}(t_0) = \mathbf{p_0}$, and initial sensitivity, $\mathbf{S}(t_0) = \mathbf{S}_0$. This method is what is called the DDM. The DDM is achieved by first obtaining the system Jacobian matrix $A(t, \mathbf{p}_0)$ and parameter Jacobian matrix $B(t, \mathbf{p}_0)$. For an ODE system with convergent steady state, the DDM solution is also convergent.

Now consider a system of differential equations that is periodic in time with period τ, we have:

$$\mathbf{x}(t + \tau) = \mathbf{x}(t). \tag{C.5}$$

From (C.5), it is possible to express each of the state variables of $\mathbf{x}(t)$ expanded in Fourier series, (Tomovic and Vukobratovic, 1972; Larter, 1983; Zak et al., 2005; Lu and Yue, 2010) and we obtain:

$$x_i(t) = \sum_{n=0}^{\infty} \left[a_{n_i} \cos \frac{2n\pi t}{\tau} + b_{n_i} \sin \frac{2n\pi t}{\tau} \right]. \tag{C.6}$$

Fourier coefficients a_{n_i} and b_{n_i} are functions of parameters. Time derivative of state variables can be obtained by differentiating equation (C.6). This gives:

$$\dot{x}_i(t) = \frac{2\,\pi}{\tau} \sum_{n=0}^{\infty} \left[-n\, a_{n_i} \sin \frac{2n\pi t}{\tau} + n\, b_{n_i} \cos \frac{2n\pi t}{\tau} \right]. \tag{C.7}$$

Here we assume that the period of oscillation is dependent on at least one parameter and its sensitivity, $\mathbf{S}_\tau$ may be defined as:

$$\mathbf{S}_\tau = \left[\frac{\partial \tau}{\partial p_1}, \cdots, \frac{\partial \tau}{\partial p_{m_p}} \right]. \tag{C.8}$$

$\mathbf{S}_\tau$ contains individual sensitivity parameters and is a vector independent of time. From equation (C.6) and using the fact that τ depends on $\mathbf{p}$, the sensitivity, s_{ij} may be calculated as:

$$\begin{aligned} s_{ij} = & \sum_{n=0}^{\infty} \left[\frac{\partial a_{n_i}}{\partial p_j} \cos \frac{2n\pi t}{\tau} + \frac{\partial b_{n_i}}{\partial p_j} \sin \frac{2n\pi t}{\tau} \right] \\ & - \frac{2\,\pi t}{\tau^2} \frac{\partial \tau}{\partial p_j} \sum_{n=0}^{\infty} \left[-n\, a_{n_i} \sin \frac{2n\pi t}{\tau} + n\, b_{n_i} \cos \frac{2n\pi t}{\tau} \right]. \end{aligned} \tag{C.9}$$

Using Equations (C.6) and (C.7), Equation (C.9) may be written as:

$$s_{ij} = -\frac{t}{\tau} s_{\tau j} f_i + \left[\frac{\partial x_i}{\partial p_j} \right]_\tau.$$

In vector form, this is written as:

$$\mathbf{S} = -\frac{t}{\tau} \mathbf{f}\, \mathbf{S}_\tau + \mathbf{S}_c. \tag{C.10}$$

$\mathbf{S}_c$ is evaluated at constant period, it is periodic in time and is an $m_s \times m_p$ matrix called *Cleaned out sensitivity matrix* (Tomovic and Vukobratovic, 1972). This matrix captures how parameter variations affect the shape of trajectory when period is constant (Zak et al., 2005; Lu and Yue, 2010, 2011).

From equation (C.10) it can be clearly seen that when $\mathbf{f} \neq 0$ and $\mathbf{S}_\tau \neq 0$, then the first term will grow unbounded as time increases and it will become the dominant term.

There are different methods for calculating period sensitivities, among these methods include an algorithm based singular value decomposition (SVD) of the state sensitivity matrix $\mathbf{S}$. This method which can determine all the period sensitivities

at ones and without concern about numerical stability (Zak et al., 2005) is based on the fact that at large time point, the first term in (C.10) will dominate and therefore,

$$\mathbf{S} \approx -\frac{t}{\tau}\mathbf{f}\,\mathbf{S}_\tau.$$

Based on this decomposition, a method which is based on singular value decomposition (SVD) is proposed to determine all the period sensitivities (Lu and Yue, 2011; Zak et al., 2005).

C.1.1 Singular value decomposition (SVD)

In this work we want to consider the SVD method for raw sensitivity matrix $\mathbf{S}(t)$ used in (Zak et al., 2005; Lu and Yue, 2010, 2011), for determining period sensitivities.

Theorem C.1.1 (**The singular value decomposition** (Golub and Van Loan, 2012))**.** *Suppose that A is a real m-by-n matrix. If there exist orthogonal matrices U and V such that*

$$U = [u_1, \cdots, u_m] \in \mathbb{R}^{m\times m} \quad \text{and} \quad V = [v_1, \cdots, v_n] \in \mathbb{R}^{n\times n},$$

then we have

$$U^T A\, V = \text{diag}(\sigma_1, \cdots, \sigma_p) \in \mathbb{R}^{m\times n} \quad p = \min\{m, n\},$$

where

$$\sigma_1 \geq \cdots \geq \sigma_p \geq 0.$$

If we define the Matrix Σ which is an $m \times n$ diagonal matrix of non-negative singular values $\sigma_i,\ i = 1, \cdots, p$, which are the square root of the eigenvalues of $A^T A$, given V is an $n \times n$ matrix whose columns are the unit eigenvectors of $A^T A$ while U is an $m \times m$ matrix whose columns are the unit eigenvectors of AA^T, then

$$A = U\Sigma V^T = \sum_{i=1}^{r} \sigma_i u_i v_i^T. \tag{C.11}$$

Equation (C.11) is the singular value decomposition of the matrix A. The matrices U and V are called unitary matrices and the vectors which comprise them are respectively called output and input vectors.

It can be easily seen from Theorem C.1.1 that

$$Av_i = \sigma_i u_i.$$

The aim is to apply SVD to the state sensitivity matrix (C.10) and approximate the period sensitivity to parameters. Since in equation (C.10), the state sensitivity grows with time, at large time point, it will be dominated by the first tern on the right hand side and the cleaned out sensitivity $\mathbf{S}_c$ becomes negligible (Zak et al., 2005; Lu and Yue, 2011). We therefore use the following approximation:

$$\mathbf{S} = -\frac{t}{\tau}\mathbf{f}\,\mathbf{S}_\tau. \tag{C.12}$$

For Equation (C.12) to be valid, it is required that both $\mathbf{f} \neq 0$ and $\mathbf{S}_\tau \neq 0$. Due to the periodicity of the system, the first condition is guaranteed, otherwise will be in stable steady state. We also assume that the period is sensitive to at least one parameter and this guarantees that all components of $\mathbf{S}_\tau$ cannot simultaneously be zero.

Therefore applying SVD to Equation (C.12) we have

$$\mathbf{S} = U\Sigma V^T. \tag{C.13}$$

From equation (C.12) we have:

$$\begin{aligned}
\mathbf{S}^T\mathbf{S} &= (-\frac{t}{\tau}\mathbf{f}\,\mathbf{S}_\tau)^T(-\frac{t}{\tau}\mathbf{f}\,\mathbf{S}_\tau) \\
&= \frac{t^2}{\tau^2}\mathbf{S}_\tau^T\,\mathbf{f}^T\mathbf{f}\,\mathbf{S}_\tau \\
&\text{Let} \quad \phi^2 = \mathbf{f}^T\mathbf{f} \\
&\text{Therefore} \\
\mathbf{S}^T\mathbf{S} &= \frac{t^2}{\tau^2}\phi^2\,\mathbf{S}_\tau^T\,\mathbf{S}_\tau.
\end{aligned} \tag{C.14}$$

Finding the eigenvalues we have that:

$$eig(\mathbf{S}^T\mathbf{S}) = \frac{t^2}{\tau^2}\phi^2\,eig(\mathbf{S}_\tau^T\,\mathbf{S}_\tau). \tag{C.15}$$

When $\mathbf{S}$ is approximated as in Equation (C.12), it has only one non-zero singular value. The non-zero eigenvalues of a matrix $\mathbf{S}^T\mathbf{S}$ are equivalent to the eigenvalues of $\mathbf{S}\,\mathbf{S}^T$, (Zak et al., 2005; Skogestad and Postlethwaite, 2000) and therefore the non-zero eigenvalue of $\mathbf{S}_\tau^T\,\mathbf{S}_\tau$ is $\mathbf{S}_\tau\,\mathbf{S}_\tau^T$.

Note that when $\mathbf{S}$ has more than one eigenvalues, at large, t, the singular value σ_1 will dominate other by several orders of magnitude (Lu and Yue, 2010).

Therefore we obtain the non-zero eigenvalue given by:

$$eig(\mathbf{S}^T\mathbf{S}) = \lambda = \frac{t^2}{\tau^2}\phi^2\,\mathbf{S}_\tau\,\mathbf{S}_\tau^T. \tag{C.16}$$

To find the eigenvector of $\mathbf{S}^T\mathbf{S}$ we require that if $\mathbf{v}$ is the eigenvector of $\mathbf{S}^T\mathbf{S}$, then we have that

$$\mathbf{S}^T\mathbf{S}\,\mathbf{v} = \lambda\mathbf{v}. \tag{C.17}$$

Using equations (C.14) and (C.16) in (C.17) we obtain;

$$\frac{t^2}{\tau^2}\phi^2\,\mathbf{S}_\tau\,\mathbf{S}_\tau^T\mathbf{v} = \frac{t^2}{\tau^2}\phi^2\,\mathbf{S}_\tau^T\,\mathbf{S}_\tau\,\mathbf{v}. \tag{C.18}$$

Equation (C.18) hold for any value of $\mathbf{v}$ and therefore without loss of generalisation we can assume it is a scalar multiple of $\mathbf{S}_\tau$ and therefore we have that:

$$\mathbf{v} = \alpha\mathbf{S}_\tau, \quad \alpha \in \mathbb{R} \setminus \{0\}\,. \tag{C.19}$$

From the above we observe that SVD of raw sensitivity matrix at large time points, t will yield scalar multiple of $\mathbf{S}_\tau$ as the input vector. We now have to determine the magnitude of period sensitivities.

Since $\mathbf{v}$ has to be a unit vector (it is usually normalised), the arbitrary scalar will be such that the resulting vector is a unit and therefore we have

$$\alpha = \pm\frac{1}{\sqrt{\mathbf{S}_\tau^T\,\mathbf{S}_\tau}}. \tag{C.20}$$

Substituting (C.20) into (C.19) we obtain an input vector corresponding to the largest singular value as:

$$\mathbf{v} = \pm\frac{\mathbf{S}_\tau}{\sqrt{\mathbf{S}_\tau\,\mathbf{S}_\tau^T}}. \tag{C.21}$$

Using the singular value obtained in equation (C.16) we can obtain the magnitudes of period sensitivities using the singular values given by

$$\sigma = \frac{t}{\tau}\phi\,\sqrt{\mathbf{S}_\tau\,\mathbf{S}_\tau^T}, \tag{C.22}$$

therefore from (C.21) and (C.22) we can obtain the period sensitivities as:

$$\mathbf{S}_\tau \approx \pm\frac{\sigma\tau}{\phi\,t}\mathbf{v}. \tag{C.23}$$

Equation (C.23) provides only the relative sign of sensitivity components but not the absolute signs and therefore a small perturbation to each parameter need to be calibrated in order to determine if that parameter increases of decreases the period. To solve this issue, an alternative formulation was given in (Lu and Yue, 2010) based on the following Theorem.

Theorem C.1.2 (Lu and Yue (2010))**.** *Consider*

$$A = \sum_{i=1}^{r}\sigma_i u_i v_i^T,$$

denote $\tilde{\mathbf{S}}_i = \sigma_i\,\mathbf{u}_i\,\mathbf{v}_i^T$ $(i = 1, 2, \cdots, r)$*, where* $\tilde{\mathbf{S}}_i$ *are matrices of rank 1. At large time t, the first term in* (C.10) *can be described by the first SVD term of* $\mathbf{S}$*. That is*

$$-\frac{t}{\tau}\mathbf{f}\,\mathbf{S}_\tau = \tilde{\mathbf{S}}_1. \tag{C.24}$$

Proof. The proof of Theorem C.1.2 can be found in (Lu and Yue, 2010). The idea of the proof is to show that $\mathbf{S}_p = -\frac{t}{\tau}\mathbf{f}\,\mathbf{S}_\tau$ is a matrix of rank 1 and its eigenvalue is linearly increasing in time by multiples of period. The second part clarifies that $\mathbf{S}_p = -\frac{t}{\tau}\mathbf{f}\,\mathbf{S}_\tau$ is one of the SVD components of $\mathbf{S}$.

Note that when $\mathbf{f} \neq 0$ and also $\mathbf{S}_\tau \neq 0$, then $\mathbf{S}_p$ is a matrix of rank 1. Any of its columns can be expressed as a linear of combination of all the remaining columns. It has also one singular value, denoted as σ_p. Write the SVD for $\mathbf{S}_p$

$$\mathbf{S}_p = -\frac{t}{\tau}\mathbf{f}\,\mathbf{S}_\tau = \sigma_p\mathbf{u}_p\,\mathbf{v}_p^T. \tag{C.25}$$

At a time point say $t_i \in (0,\ \tau]$, then we have

$$-\frac{t_i}{\tau}\mathbf{f}(t_i)\,\mathbf{S}(t_i)_\tau = \sigma(t_i)_p\mathbf{u}(t_i)_p\,\mathbf{v}(t_i)_p^T. \tag{C.26}$$

After a number of periods, say k periods, we then have $t = t_i + k \cdot \tau$, $\mathbf{S}(t) = \mathbf{t_i}$ and $\mathbf{S}_\tau(t) = \mathbf{S}_\tau(t_i)$.

Therefore $\mathbf{S}_p$ can be described by:

$$-\frac{t}{\tau}\mathbf{f}(t)\,\mathbf{S}(t)_\tau = -\frac{t_i + k \cdot \tau}{\tau}\mathbf{f}(t_i)\,\mathbf{S}(t_i)_\tau. \tag{C.27}$$

Using Equation (C.26), Equation (C.27) can be written as

$$(1 + k \cdot \frac{\tau}{t_i})\sigma(t_i)_p \mathbf{u}(t_i)_p\,\mathbf{v}(t_i)_p^T. \tag{C.28}$$

Equations (C.28) shows that after k periods, the singular value for $\mathbf{S}_p$ increases to $\sigma_p(t) = (1 + k \cdot \frac{\tau}{t_i})\sigma(t_i)_p$ which is a linear increase to the number of periods (time).

Lastly, we shows that $\mathbf{S}_p$ is one of the SVD components of $\mathbf{S}$. We know that $\mathbf{S}_p$ contains information about period variations to parameter changes and increases with $\mathbf{fS}_\tau$ after each period at all time points in a period. $\mathbf{S}_c$ represents the state variations to parameter changes at constant period, and therefore its trajectory in one period is exactly the same as in all other periods. This shows that $\mathbf{S}_p$ and $\mathbf{S}_c$ are orthogonal components of $\mathbf{S}$. From the SVD expansion theory, the terms $\tilde{\mathbf{S}}_i$ are orthogonal and this decomposition is unique. This concludes that $\mathbf{S}_p$ is one of the $\tilde{\mathbf{S}}_i$.

We have also shown that the singular value of $\mathbf{S}_p$ increases with time scaled by multiples of period while on the other hand, the singular values of $\mathbf{S}_c$ oscillate with constant peak values in amplitude. We therefore have that at large time point t, only σ_p will be the dominant singular value. That is $\sigma_p = \sigma_1$ and $\mathbf{S}_p = \tilde{\mathbf{S}}_1$. This proves the theorem.

□

From Equation (C.24) and since $\mathbf{f} \neq 0$, multiply both sides by $\mathbf{f}^T$ and simplify to obtain

$$\mathbf{S}_\tau \approx -\frac{\tau}{\phi^2\, t}\mathbf{f}^T\,\tilde{\mathbf{S}}_1, \tag{C.29}$$

where the term $\tilde{\mathbf{S}}_1 = \sigma_1\,\mathbf{u}_1\,\mathbf{v}_1^T$ is the largest Singular value decomposition term of the state sensitivity matrix $\mathbf{S}$. Equation (C.29) is used to calculate the period sensitivities together with their corresponding signs, depending on the effect of particular parameter to the output.

To obtain the cleaned out sensitivities, consider the SVD expansion of a matrix. If r is the rank of a matrix $\mathbf{S}$, we then have by (Golub and Van Loan, 2012) that:

$$\mathbf{S} = \sum_{i=1}^{r} \sigma_i \mathbf{u}_i \mathbf{v}_i^T. \tag{C.30}$$

Define $\tilde{\mathbf{S}}_i = \sigma_i \, \mathbf{u}_i \, \mathbf{v}_i^T$, therefore (C.30) can be written as:

$$\mathbf{S} = \tilde{\mathbf{S}}_1 + \sum_{i=2}^{r} \tilde{\mathbf{S}}_i. \tag{C.31}$$

Therefore from equations (C.10) and (C.31) we obtain cleaned-out sensitivity can be approximated by the sum of all the remaining SVD terms, i.e.,

$$\mathbf{S}_c \approx \sum_{i=2}^{r} \tilde{\mathbf{S}}_i. \tag{C.32}$$

C.1.2 Amplitude sensitivity

The amplitude of an oscillation is the maximum displacement from the mean position. This is proportional to the difference between the peaks (difference between maximum and minimum values of the oscillatory trajectory).

For the purpose of sensitivity analysis, we define amplitude for each state as:

$$A_{mi} = \max(x_i) - \min(x_i). \tag{C.33}$$

Let us define $t_{\max_i}$ and $t_{\min_i}$ as the points where the local maximum and minimum occurs within the period, then Equation (C.33) is written as:

$$A_{mi} = x_i(t_{\max_i}) - x_i(t_{\min_i}). \tag{C.34}$$

From Equation (C.34) we define amplitude sensitivity as:

$$\mathbf{S}_{A_{mi}} = \frac{\partial A_{mi}}{\partial \mathbf{p}}. \tag{C.35}$$

Using Equation (C.34), this can be written as:

$$\mathbf{S}_{A_{mi}} = \frac{\partial x_i(t_{\max_i})}{\partial \mathbf{p}} - \frac{\partial x_i(t_{\min_i})}{\partial \mathbf{p}}. \tag{C.36}$$

Using equation (4.2) we get amplitude sensitivity given by:

$$\mathbf{S}_{A_{mi}} = \mathbf{S}_i(t_{\max_i}) - \mathbf{S}_i(t_{\min_i}). \tag{C.37}$$

Having obtained the cleaned out sensitivity, we can use the fact that at the local extrema of x_i, $f_i = 0$, and therefore from Equation (C.10) we have that $\mathbf{S}_i = \mathbf{S}_{ci}$. From that we can therefore define amplitude sensitivity as:

$$\mathbf{S}_{A_{mi}} = \mathbf{S}_{ci}(t_{\max_i}) - \mathbf{S}_{ci}(t_{\min_i}). \tag{C.38}$$

C.2 Variance based methods for sensitivity analysis

Consider p input parameters, $\mathbf{X} = (X_1, X_2, \cdots, X_p)$, which are independent and each one varying over its own probability density function. The output $\mathbf{Y}$ is defined as

$$\mathbf{Y} = \mathbf{f}(\mathbf{X}).$$

The variance based techniques aim to rank the input factors according to the variance that is lost. Assume that the true value x_i^* for a given input parameter X_i is known. The conditional variance of $\mathbf{Y}$ given $X_i = x_i^*$ is defined by

$$V(\mathbf{Y}|X_i = x_i^*), \tag{C.39}$$

this is obtained by taking the variance over all input parameters except x_i^*.

In most cases, the true value x_i^* of each X_i, $i = 1, 2, \cdots p$, is not known. Therefore, in place of Equation (C.39), we use the average of the conditional variance for all possible values X_i. That is, we evaluate

$$E(V(\mathbf{Y}|X_i)). \tag{C.40}$$

Since we want to find the variance of the conditional expectation, consider the following property of variance

$$V(\mathbf{Y}) = V(E[\mathbf{Y}|X_i]) + E[V(\mathbf{Y}|X_i)]. \tag{C.41}$$

Having the unconditional variance of output $V(\mathbf{Y})$, variance of the conditional expectation is obtained from Equation (C.40) and Equation (C.41). This is defined as:

$$v_i = V(E[\mathbf{Y}|X_i]), \tag{C.42}$$

v_i in (C.42) is sometimes called main effect (Ekström, 2005). It is used as a measure of the sensitivity of $\mathbf{Y}$ to X_i. Equation (C.42) is normalised by $V(\mathbf{Y})$ to obtain

$$s_i = \frac{V(E[\mathbf{Y}|X_i])}{V(\mathbf{Y})}. \tag{C.43}$$

The ratio (4.13) was named *first order sensitivity* by Sobol, (Sobol, 1993). This index only measures the main effect contribution of each parameter on the output variance and does not take into account interaction between the input factors.

In terms of conditional variances, the interaction of two orthogonal factors X_i and X_j on the output $\mathbf{Y}$ is given by:

$$v_{ij} = V(E[\mathbf{Y}|X_i, X_j]) - V(E[\mathbf{Y}|X_i]) - V(E[\mathbf{Y}|X_j]). \tag{C.44}$$

The quantity $V(E[\mathbf{Y}|X_i, X_j])$ which is known as the *second-order effect* describes the joint effect of the pair (X_i, X_j) on the output. Higher order effects can be obtained in a similar fashion.

The sum of all order effects that a factor accounts for is called *total effect* (Homma and Saltelli, 1996; Saltelli et al., 1999). Therefore for an input X_j, the *total sensitivity index* s_{T_j} is the sum of all indices measure relating to X_j.

Therefore for a model with two, three and four input factors ($p = 2, 3, 4$), the total sensitivity index for an input X_2 would respectively be:

$$p = 2 \text{ implies } s_{T_2} = s_2 + s_{21},$$

$$p = 3 \text{ implies } s_{T_2} = s_2 + s_{21} + s_{23} + s_{213},$$

and

$$p = 4 \text{ implies } s_{T_2} = s_2 + s_{21} + s_{23} + s_{24} + s_{213} + s_{214} + s_{234} + s_{2134}.$$

The number of terms to be evaluated is 2^{p-1}. All the variance-based method listed above except FAST method can compute both s_i and s_{T_i}.

Here the input factor space Ω^p is assumed to be p-dimensional hypercube (Ekström, 2005):

$$\Omega^p = (\mathbf{X}|\, 0 \leq X_i \leq 1;\, i = 1, \cdots, p).$$

The input factors are assumed to be orthogonal hence no correlation structure can be induced by the input factors. The expected value of the output $E(\mathbf{Y})$ can be evaluated by the p-dimensional integral:

$$E(\mathbf{Y}) = \int_{\Omega^p} \mathbf{f}(\mathbf{X}) p(\mathbf{X}) d\mathbf{X} = \int_{\Omega^p} \mathbf{f}(\mathbf{X}) d\mathbf{X}, \tag{C.45}$$

where $p(\mathbf{X})$ is joint probability density function assumed to be uniform for each input factor.

C.2.1 Extended Fourier amplitude test (eFAST)

eFAST method was developed by (Saltelli et al., 1999, 2000) as an improvement of the Fourier amplitude test (FAST) method, which was developed by (Cukier et al., 1975). It is a variance based method.

The technique uses a periodic sampling method together with Fourier transformation to partition the whole variance of the model output and quantify the degree to which variation in each input factor accounts for the output variance, (Gao et al., 2016).

A periodic sampling approach is used to generate a search curve in the parameter space and partitioning is implemented by assigning the periodic sample of each parameter with a distinct frequency. Then a Fourier transformation is applied to the model output to measure how strongly a factor's frequency propagates from the input to the output, i.e., the variance contribution of the factor to the whole variance of the output (Saltelli and Bolado, 1998; Saltelli et al., 1999; Marino et al., 2008; Gao et al., 2016)

Fourier amplitude test (FAST)

FAST is sensitivity analysis method developed by (Cukier et al., 1975; Schaibly and Shuler, 1973) and it was successfully applied to two sets of coupled non-linear chemical rate equations. The main idea of FAST method is to convert the p-dimensional integral equation (C.45) into a one dimensional equation (Weyl, 1938). In FAST

method each input (uncertain) X_i is related to a frequency ω_i and transformed as

$$x_i(s) = G_i(sin(\omega_i s)), \tag{C.46}$$

where G_i is defined parametric equation which allows each input factor to be varied in its range as we vary s. The parametric equation (C.46) defines a curve that explores the whole input factor space Ω^p.

The p-dimensional integral (C.45) can be estimated by integrating over the curve (Saltelli et al., 2010; Ekström, 2005):

$$\hat{E}(\mathbf{Y}) = \frac{1}{2\,\pi}\int_{-\pi}^{\pi}\mathbf{f}(s)ds, \tag{C.47}$$

where

$$\mathbf{f}(s) = \mathbf{f}(G_1(sin(\omega_1 s)), G_2(sin(\omega_2 s)), \cdots, G_k(sin(\omega_k s))).$$

The output variance may be approximated by performing Fourier analysis as shown below and using the fact that the expected value is given by the initial value of $\mathbf{f}$:

$$\begin{aligned}\hat{V}^{\text{FAST}}(\mathbf{Y}) &= \frac{1}{2\,\pi}\int_{-\pi}^{\pi}\mathbf{f}^2(s)ds - \hat{E}^2(\mathbf{Y}),\\ &\approx \sum_{j=-\infty}^{\infty}(A_j^2 + B_j^2) - (A_0^2 + B_0^2),\\ &\approx 2\sum_{j=1}^{N}(A_j^2 + B_j^2).\end{aligned} \tag{C.48}$$

The Fourier coefficients A_j and B_j are defined by:

$$\begin{aligned}A_i &= \frac{1}{2\,\pi}\int_{-\pi}^{\pi}\mathbf{f}(s)\cos(js)ds,\\ B_j &= \frac{1}{2\,\pi}\int_{-\pi}^{\pi}\mathbf{f}(s)\sin(js)ds.\end{aligned} \tag{C.49}$$

The partial variances are finally calculated by:

$$\hat{V}_i^{\text{FAST}}(\mathbf{Y}) = 2\sum_{j=1}^{M}(A_{pwj}^2 + B_{pwj}^2), \tag{C.50}$$

where M is the maximum number of Fourier coefficients that may be retained in calculating the partial variances without interferences between the assigned frequencies and it is usually 4 or 6, (Ekström, 2005).

To approximate the Fourier coefficients for the partial variances, (McRae et al., 1982) proposed the following expression:

$$A_j = \begin{cases} 0 & \text{if } j \text{ is odd} \\ \frac{1}{N}\left(y_0 + \sum_{p=1}^{q}(y_p + y_{-p})\cos(\frac{\pi jp}{N})\right), & \text{if } j \text{ is even} \end{cases}$$
$$B_j = \begin{cases} 0 & \text{if } j \text{ is even} \\ \frac{1}{N}\left(\sum_{p=1}^{q}(y_p - y_{-p})\sin(\frac{\pi jp}{N})\right), & \text{if } j \text{ is odd} \end{cases} \tag{C.51}$$

where $q = (N-1)/2$. In (Saltelli et al., 1999; Saltelli and Bolado, 1998; Saltelli et al., 2004) a better transformation for G_i is recommended that could provide a uniformly distributed samples for each input factor in the hypercube and is given by:

$$x_i(s) = G_i(\sin(w_i s)) = \frac{1}{2} + \frac{1}{\pi}\arcsin(\sin(w_i s)). \tag{C.52}$$

Saltelli proved in (Saltelli and Bolado, 1998) that the ratio $\hat{V}_i^{FAST}/\hat{V}^{FAST}$ computed with FAST method is equivalent to first order sensitivity indices proposed by Sobol, (Sobol, 1993). This method does not calculate the total index and thus an improvement was done to obtain eFAST method.

eFAST method is able to calculate the total order index by estimating the variance in the complementary set $\hat{V}_{ci}^{FAST}$ which is done by assigning a frequency ω_i for the factor X_i very high and almost identical frequencies to the rest $\omega_{\sim i}$ very low. They then compute the partial variance of the complementary set as:

$$\hat{V}_{ci}^{FAST} = 2\sum_{j=1}^{M}(A_{\sim j}^2 + B_{\sim j}^2). \tag{C.53}$$

In FAST method, equation (C.52) always returns exactly the same factor in Ω^p and so in (Saltelli et al., 1999, 2000) a more flexible sampling scheme was introduced by adding a random phase-shift φ_i. The new equation now becomes:

$$x_i(s) = G_i(\sin(w_i s)) = \frac{1}{2} + \frac{1}{\pi}\arcsin(\sin(w_i s + \varphi_i)), \tag{C.54}$$

and the curve is sampled over the interval $(-\pi, \pi)$ due to symmetry. This idea of generating many different curves in Ω^p, doing dependent Fourier analysis over them and finally finding their average is called *re sampling*.

In eFAST method, the computation cost to obtain all first and total indices are $k(2M\omega_{max})N_r$, where N_r is the number of re samples.

Appendix D

Bayesian method to parameter identification

D.1 Introduction to Bayesian method

To introduce the Bayesian setting of the problem, let $\mathbf{p} \in \mathbb{R}^K$ be the set of parameters of the mathematical model. Let $\mathcal{H} : \mathbb{R}^K \to \mathbb{R}^N$ be the mapping that assigns to each parameter $\mathbf{p}$ the solution to the ODE system evaluated at the observation time points. Let $y \in \mathbb{R}^N$ be the experimental measurement. We assume that the measurement y corresponds to a solution of the mathematical model perturbed by some noise η, which is naturally modelled by means of some probability distribution. Mathematically, we have:

$$y = \mathcal{H}(\mathbf{p}) + \eta, \tag{D.1}$$

for a certain parameter $\mathbf{p}$.

In terms of probability distributions, the parameter identification can be stated as follows: (D.1) gives as the probability of observing y given a parameter $\mathbf{p}$; we are interested in the reverse condition, the probability of a parameter $\mathbf{p}$ given that we observe y. The Bayes' theorem characterizes the latter in terms of the former together with the marginal distribution for $\mathbf{p}$. This marginal distribution represents the knowledge about the parameter, called *a prior*. The probability distribution of the parameter given the data is the *posterior* denoted $\mathbb{P}(\mathbf{p}|y)$.

The prior encodes assumptions about the parameter such as positivity or bounds and even more complex information, such as that the parameter exhibits certain dynamics in a reduced system of equations and the range of parameter to be considered; while the posterior distribution encodes all the information available about a parameter estimated.

To approximate the posterior distribution we use parallel Markov Chain Monte Carlo (MCMC) method. The method generates a Markov Chain of samples distributed as the posterior. The method is implemented to run in parallel using multiple processors.

The posterior distribution provides information not only about the best parameter, but also about possible correlations between parameters, and credible regions. In particular, when it is possible to make plausible assumptions on the experimental noise, the method provides robust error bars for the parameters.

In order to calculate the posterior probability, we shall apply Bayes' formula to (D.1). First consider the following definition:

Definition D.1.1. *Consider the probability space* $(\Omega, \mathcal{F}, \mathbb{P})$ *and two sets* $A, B \in \mathcal{F}$ *with* $\mathbb{P}(A), \mathbb{P}(B) > 0$. *We define the probability of* A *given* B *and that of* B *given* A *by;*

$$\mathbb{P}(A|B) = \frac{\mathbb{P}(A \cap B)}{\mathbb{P}(B)},$$
$$\mathbb{P}(B|A) = \frac{\mathbb{P}(A \cap B)}{\mathbb{P}(A)}.$$

Combining the two gives Bayes' formula

$$\mathbb{P}(A|B) = \frac{\mathbb{P}(B|A)}{\mathbb{P}(B)}\mathbb{P}(A). \tag{D.2}$$

Applying Bayes' formula to (D.1). Let $\pi^y(\mathbf{p})$ denote the probability density function of the probability measure $\mathbb{P}(\mathbf{p}|y)$, then the probability density function of the prior distribution is $\pi_0(\mathbf{p})$. If we assume that the noise $\eta \in \mathbb{R}^N$ is a random variable with density ρ, then the probability of data given parameters has density $\rho(y|\mathbf{p}) := \rho(y - \mathcal{H}(\mathbf{p}))$, which is referred to as the *data likelihood* (Stuart, 2010). Therefore by Bayes' formula, we obtain

$$\pi^y(\mathbf{p}) = \frac{\rho(y - \mathcal{H}(\mathbf{p}))\, \pi_0(\mathbf{p})}{W}, \tag{D.3}$$

where

$$W = \int_{\mathbb{R}^N} \rho(y - \mathcal{H}(\mathbf{p}))\, \pi_0(\mathbf{p}).$$

Thus

$$\pi^y(\mathbf{p}) \propto \rho(y - \mathcal{H}(\mathbf{p}))\, \pi_0(\mathbf{p}), \tag{D.4}$$

where in Equation (D.4), the constant of proportionality depends only on the data, y.

Consider the Radon-Nikodym Theorem below:

Theorem D.1.2 (Radon–Nikodym Theorem (Stuart, 2010))**.** *Let μ and ν be two measures on the same measure space $(\Omega, \mathcal{F})$. $\mu \ll \nu$ and ν is σ-finite then there exists ν-measurable function $f : \Omega \mapsto [0, \infty]$ such that, for all ν-measurable sets $A \in \mathcal{F}$,*

$$\mu(A) = \int_A f(x) d\nu(x).$$

The function f is known as the Radon–Nikodym derivative of μ with respect to ν, which is written as

$$\frac{d\mu}{d\nu}(x) = f(x).$$

From Theorem D.1.2, (D.4) expresses the fact that the posterior measure, $\mathbb{P}(\mathbf{p}|y)$ and prior measure $\mathbb{P}_0(\mathbf{p}|y)$ are related through the Radon-Nikodym derivative (Stuart, 2010). Therefore denoting $\mathbb{P}(\cdot|y) = \mathbb{P}^y(\cdot)$ from the theorem we have

$$\frac{d\mathbb{P}^y}{d\mathbb{P}_0}(\mathbf{p}) \propto \rho(y - \mathcal{H}(\mathbf{p})). \tag{D.5}$$

The right hand side of Equation (D.5) can be written as an exponential of a negative potential $\phi((\mathbf{p}); y)$ to obtain,

$$\frac{d\mathbb{P}^y}{d\mathbb{P}_0}(\mathbf{p}) \propto \exp(-\phi((\mathbf{p}); y)). \tag{D.6}$$

The potential $\phi((\mathbf{p}); y)$ corresponds to the negative log-likelihood. Equation (D.6) generalises Bayes' theorem to infinite dimensional setting, and thus Bayesian approach to parameter identification can be applied to infinite dimensional problems using this formulation. This results can be summarised in the theorem below (Dashti and Stuart, 2016)

Theorem D.1.3 (Bayes' Theorem). *Assume that the potential $\phi : A \times B \mapsto \mathbb{R}$ is measurable with respect to the product measure $\mathbb{P}_0 \times \mathbb{Q}_0$, where $\mathbb{Q}_0$ is a probability distribution and η is a realisation of $\mathbb{Q}_0$. Also assume that*

$$W = \int_A \exp(-\phi((\mathbf{p}); y))\mathbb{P}_0(d\mathbf{p}) \geq 0.$$

Then the posterior distribution, $\mathbb{P}(\mathbf{p}|y)$ exists, and it is absolutely continuous with respect to the prior distribution. Furthermore, $\mathbb{P}^y \ll \mathbb{P}_0$ and

$$\frac{d\mathbb{P}^y}{d\mathbb{P}_0}(\mathbf{p}) = \frac{1}{W}\exp(-\phi((\mathbf{p}); y)).$$

Bayes' theorem characterises the posterior probability distribution, which involves determining the normalization constant, W. This process is expensive to evaluate. Therefore in general it is not easy to get information from a posterior probability measure in high dimensions. One useful approach to extracting information is to find a *maximum posteriori estimator*, or MAP estimator. This is a parameter set $\mathbf{p}$ which maximizes the posterior probability density function $\pi^y(\mathbf{p})$ (Stuart, 2010).

Another alternative is not to compute the posterior probability distribution, but rather produce samples from it, by using Markov Chain Monte carlo methods.

D.2 Markov Chain Monte carlo methods (MCMC)

Markov Chain Monte carlo methods (MCMC) are a family of sampling methods that can produce Markov chain with a given distribution (Norris, 1998). They are used to sample from posterior distribution. Given a sufficient good number of such samples, the solution of the Bayesian problem can be characterised. MCMC are easily applied to linear and non linear problems, since they only depend on the forward problem and the associated likelihood (Aster et al., 2018).

A Markov chain is a sequence of random variables, $X^0, X^1, \cdots$, where the probability distribution of X^{n+1} depends solely on the previous value, X^n and not on the other previous sequence values. That is,

$$\mathbb{P}(X^{n+1}|X^0, X^1, \cdots, X^n) = \mathbb{P}(X^{n+1}|X^n).$$

We consider time-invariant Markov chains so that the *transition kernel* is independent of n. That is

$$\mathbb{P}(X^{n+1}, X^n) = \mathbb{P}(X^{n+1}|X^n), \quad \text{is independent of n.}$$

Not all Markov chains have a limiting distribution (Aster et al., 2018), here we are interested in Markov chains that have a limiting distribution, $\pi^y(\mathbf{p})$ such that

$$\lim_{n\to\infty} \mathbb{P}(X^{n+1}|X^n) = \pi^y(\mathbf{p}).$$

In general, for any multivariate model, suppose that $q(\mathbf{x})$ and $k(\mathbf{x}, \mathbf{y})$ are the target distribution and transition kernel respectively. $q(\mathbf{x})$ is a limiting distribution if the following local balance equation is satisfied;

$$q(\mathbf{x})\, k(\mathbf{x}, \mathbf{y}) = q(\mathbf{y})\, k(\mathbf{y}, \mathbf{x}). \tag{D.7}$$

Equation (D.7) states that the rate of transition from from $q(\mathbf{x})$ to $q(\mathbf{y})$ equals the rate from $q(\mathbf{y})$ to $q(\mathbf{x})$.

MCMC methods have the advantage of sampling from a probability measure only known up to a normalizing constant (Stuart, 2010). They are robust but slow, and the distribution of Markov chain converges to the target(posterior) distribution under general conditions, but long chains are needed to obtain good approximations (Norris, 1998; Campillo-Funollet et al., 2019). *Metropolis-Hastings sampler* will be used to simulate Markov chain with a specified limiting or target distribution.

D.2.1 Metropolis-Hastings sampler

Metropolis-Hastings method produces samples from posterior distribution that tend to densely sample its higher likelihood regions. With many of these samples, we can characterise the posterior distribution.

In implementing Metropolis-Hastings method, first pick a proposal distribution, which will facilitate random selection in the target distribution (posterior). These samples are subjected to a likelihood based test.

The proposal distribution selected cannot be implemented as transition kernel directly since it does not satisfy the local balance equation (D.7). To overcome this a ratio called the *acceptance ratio* is introduced such that

$$a(\mathbf{x}, \mathbf{y}) = \min\{1, s\}, \tag{D.8}$$

where

$$s = \frac{q(\mathbf{y})\, k(\mathbf{y}, \mathbf{x})}{q(\mathbf{x})\, k(\mathbf{x}, \mathbf{y})}. \tag{D.9}$$

We therefore have that

$$a(\mathbf{y}, \mathbf{x}) = \min\left\{1, s^{-1}\right\}. \tag{D.10}$$

The choice of the acceptance probability (acceptance ratio) a depends on the proposal kernel in order to ensure that the Markov chain is reversible with respect to the target probability. That is, the local balance equation (D.7) is satisfied. This reversibility ensures that the Markov chain preserves the target (posterior) probability. For simplicity, consider the proposal kernels that are symmetric, i.e. $k(\mathbf{y}, \mathbf{x}) = k(\mathbf{x}, \mathbf{y})$. Applying this then Equation (D.9) simplifies to

$$s = \frac{q(\mathbf{y})}{q(\mathbf{x})}, \tag{D.11}$$

and therefore

$$a(\mathbf{x}, \mathbf{y}) = \min\left\{1, \frac{q(\mathbf{y})}{q(\mathbf{x})}\right\}. \tag{D.12}$$

Using the negative log likelihood, we have $q(\cdot) = \exp(-\phi(\cdot))$ in Equation (D.12), we obtain;

$$a(\mathbf{x}, \mathbf{y}) = \min\{1, \exp(\phi(\mathbf{x}) - \phi(\mathbf{y}))\}. \tag{D.13}$$

Therefore for standard Metropolis-Hastings method, we take a proposal kernel equal to the prior distribution such that,

$$k(\mathbf{x}, \cdot) = \mathbb{P}_0(\cdot).$$

Together with the acceptance ratio defined in Equation (D.13). In a parameter identification problem, evaluation of acceptance probability involves at least one evaluation of the potential, ϕ and therefore one evaluation of the observation operator $\mathcal{H}$, which makes this operation very expensive with regard to the computation time. To overcome this problem, we used *parallel Metropolis-Hastings* algorithm (Tjelmeland, 2004; Calderhead, 2014; Campillo-Funollet et al., 2019).

The implementation of this method is credited to Eduard Campillo Funollet and his published work in (Campillo-Funollet et al., 2019). The key idea behind parallel Metropolis-Hastings algorithm is to generate an N-dimensional Markov chain such, such that its distribution is N copies of the target distribution, which is the posterior distribution. This is done such that the potential ϕ is evaluated in parallel. The type of Metropolis-Hastings implemented in this work is known as the *independence sampler*. Cotter *et al.* (Cotter et al., 2013) derived this and other proposal kernels by discretising the Langevin-type stochastic differential equation.

The parallel Metropolis-Hastings is implemented as follows: Generate N new proposals, $\bar{x}_{j=1}^{N}$ from the proposal kernel $k(x_k, x^j)$. Take $x^0 = x^j$ and then evaluate the potentials $\phi(x^j)$, $j = 1, \cdots N$ in parallel. The values of $\phi(x^j)$ are used to compute the acceptance probability for each proposal, by finding the stationary distribution of a Markov chain with $N + 1$ states, given by the transition matrix

$$A(i,j) = \begin{cases} \frac{1}{N} a(x^i, x^j), & \text{if } i \neq j, \\ 1 - \sum_{j \neq i} A(i,j), & \text{if } i = j. \end{cases} \tag{D.14}$$

We again sample N times from the stationary distribution to produce N new states.

The parallel Metropolis-Hastings method does not require modification of solver for the model, and hence suited when the solver is already available, and then aim is just to speed up the computations without modifying the solver, and it also works well for problems with infinite dimensional parameters (Stuart, 2010; Dashti and Stuart, 2016; Campillo-Funollet et al., 2019).

In this formulation, we can compute the likelihood, ϕ as a consequence of Equation (D.1), which allows us to incorporate information about the experimental noise. In the cases where the likelihood cannot be computed, or when the distribution is not known, one can resort to Approximate Bayesian methods (Ross et al., 2017).